Technische Universität München

Lehrstuhl für Thermodynamik

Analysis and Improvement of Rocket Engine Combustion Stability Simulations

Alexander Chemnitz

Vollständiger Abdruck der von der TUM School of Engineering and Design der Technischen Universität München zur Erlangung des akademischen Grades eines

DOKTOR – INGENIEURS

genehmigten Dissertation.

Vorsitzender:
Prof. Dr.-Ing. Oskar Haidn
Prüfer der Dissertation:
Prof. Dr.-Ing. Thomas Sattelmayer
Prof. Dr. rer. nat. Michael Oschwald

Die Dissertation wurde am 15.10.2021 bei der Technischen Universität München eingereicht und durch die TUM School of Engineering and Design am angenommen.

Abstract

A hybrid methodology for the efficient assessment of liquid rocket engines' thermoacoustic stability is analyzed. Approaches to overcome identified deficiencies are proposed and evaluated. Building on that, the soundness and perspectives of the procedure are discussed.

To provide a basis for the study, a validation of rocket single flame simulations, which the methodology relies on, is performed. This includes the development and application of an approach to obtain representative OH* radiation images from the numerical results.

A revised procedure for the calculation of the quasi one-dimensional mean flow that is used in the acoustic simulations is developed. It retains certain characteristics of the single flames while being consistent with the Euler Equations. Several variants of the mean flow calculation are tested, showing minor differences compared to other modeling uncertainties. An investigation of the impact of radial mean flow stratification on the stability predictions reveals that while oscillation frequencies are reproduced well with a quasi one-dimensional mean flow, damping rates are severely changed by radial gradients.

A modification of the flame response simulations is proposed to suppress the eigenacoustics of the reduced simulation domain. A significant impact of the simulation approach and the modeling details of the Flame Transfer Function on the stability predictions is found.

Due to the high uncertainties in both, the mean flow related damping and the flame response, it is concluded that no sound validation based on the overall stability behavior can be conducted. Further development of the procedure requires additional validation data.

Zusammenfassung

Ein hybrider Ansatz zur effizienten Vorhersage der thermoakustischen Stabilität von Flüssigraketentriebwerken wird untersucht. Lösungsansätze für gefundene Defizite werden entwickelt und es erfolgt eine Einschätzung von Belastbarkeit und Potential der Methode.

Als Grundlage für die Untersuchungen werden die Einzelflammenberechnungen, denen eine hohe Bedeutung in der Prozedur zukommt, validiert. Dies umfasst die Entwicklung eines Ansatzes zur Berechnung von OH^*-Bildern aus den numerischen Ergebnissen.

Eine verbesserte Prozedur zur Berechnung der quasi-eindimensionalen Grundströmung für die akustischen Simulationen wird entwickelt. Der Ansatz erhält charakteristische Eigenschaften der Einzelflammen und erfüllt die Euler Gleichungen. Verschiedene Grundströmungsvarianten werden verglichen, die Unterschiede sind vernachlässigbar gegenüber anderen Modellierungsunsicherheiten. Eine Untersuchung radial stratifizierter Grundströmungen zeigt, dass die Schwingungsfrequenzen mit dem quasi-eindimensionalen Ansatz gut getroffen, die Dämpfungsraten aber stark von radialen Gradienten beeinflusst werden.

Die Methode zur Berechnung der Flammenantwort wird modifiziert, um die Eigenakustik der Rechendomäne zu unterdrücken. Der Simulationsansatz sowie die Modellierungsdetails der Flammentransferfunktion wirken sich deutlich auf die Stabilitätsvorhersagen aus.

Aufgrund der hohen Unsicherheiten in der passiven Dämpfung wie auch der Flammenantwort kann eine Validierung der Methodik nicht allein anhand des Stabilitätsverhaltens erfolgen. Zur weiteren Entwicklung werden zusätzliche Validierungsdaten benötigt.

Contents

List of Figures

List of Tables

Nomenclature

Roman Letters

A	area	m^2
A_{ex}	excitation pressure amplitude	Pa
A_s	surface area	m^2
A^θ	amplitude of circumferential mode	$-$
A_ψ	stratification amplitude	
b	parameter of cubic EOS	$\mathrm{m}^3\,\mathrm{kg}^{-1}$
C_μ	k-ϵ model constant	
c	sound speed	$\mathrm{m\,s}^{-1}$
	parameter of cubic EOS	$\mathrm{m}^3\,\mathrm{kg}^{-1}$
c_l	light speed	$\mathrm{m\,s}^{-1}$
c_u	constant for equalizing momentum source $-$	
c_v	specific isochoric heat capacity	$\mathrm{J\,kg}^{-1}\,\mathrm{K}^{-1}$
c_p	specific isobaric heat capacity	$\mathrm{J\,kg}^{-1}\,\mathrm{K}^{-1}$
c_a	coefficient for absorption description	$-$
c_e	coefficient for emission description	$-$
D	mass diffusion coefficient	$\mathrm{kg\,m}^{-1}\,\mathrm{s}^{-1}$
D'	acoustic energy dissipation	$\mathrm{W\,m}^{-3}$
D_H	hydraulic diameter	m
E	specific total energy	$\mathrm{J\,kg}^{-1}$
e	emissivity	$\mathrm{W\,m}^{-3}$
e_s	sensible internal energy	$\mathrm{J\,kg}^{-1}$
f	mixture fraction	$-$
	frequency	Hz

F	amplitude of right running wave	$\mathrm{m\,s^{-1}}$
FTF	flame transfer function	$\mathrm{W\,s^{-1}}$, –
G	amplitude of left running wave	$\mathrm{m\,s^{-1}}$
H	specific total enthalpy	$\mathrm{J\,kg^{-1}}$
h	Planck constant	$\mathrm{m^2\,kg\,s^{-1}}$
	characteristic size	m
h_f^0	enthalpy of formation	$\mathrm{J\,kg^{-1}}$
h_s	sensible internal enthalpy	$\mathrm{J\,kg^{-1}}$
I	identity	–
	radiation intensity	$\mathrm{W\,m^{-2}}$
	turbulent intensity	–
J_m	m^{th} Bessel function	–
k	acoustic wave number	$\mathrm{rad\,m^{-1}}$
	absorption coefficient	$\mathrm{m^{-1}}$
	turbulent kinetic energy	$\mathrm{m^2\,s^{-2}}$
k_B	Boltzmann Constant	$\mathrm{m^2\,kg\,s^{-2}\,K^{-1}}$
L	domain length	m
l	length	m
Ma	Mach number	–
m	transverse mode order	–
$\dot{m}$	mass flow	$\mathrm{kg\,s^{-1}}$
N_A	Avogadro constant	$\mathrm{mol^{-1}}$
n	surface unit normal	–
	number	–
	radial mode order	–
P	axial pressure ansatz function	Pa
Pr	Prandtl number	–
PSD	Power Spectral Density	a.u.
p	pressure	Pa
q	volumetric heat release	$\mathrm{W\,m^{-3}}$
$q_{\Delta x,rel}$	normalized integral heat release fluctuations	–
q_x	heat release per axial distance	$\mathrm{W\,m^{-1}}$
	heat flux	$\mathrm{W\,m^{-2}}$

R	specific gas constant	$\mathrm{J\,kg^{-1}\,K^{-1}}$
	radial pressure/velocity ansatz function	–
	outer radius	m
R_m	universal gas constant	$\mathrm{J\,mol^{-1}\,K^{-1}}$
Ry	Response factor	–
r	radial coordinate	m
S	strain rate	$\mathrm{s^{-1}}$
Sc	Schmidt number	–
s	spectral variable (optical wave length/number)	m, $\mathrm{m^{-1}}$
	entropy	$\mathrm{J\,K^{-1}}$
s_{mn}	n^{th} root of derivative of m^{th} Bessel function	–
T	temperature	K
t	time	s
u	velocity	$\mathrm{m\,s^{-1}}$
U	axial velocity ansatz function	$\mathrm{m\,s^{-1}}$
V	volume	$\mathrm{m^3}$
W'	acoustic energy flux	$\mathrm{W\,m^{-2}}$
x	axial coordinate	m
	mole fraction	–
y	mass fraction	–
Z	real gas factor	–

Greek Letters

α	parameter of cubic EOS	$\mathrm{J\,kg^{-1}}$
	damping rate	$\mathrm{rad\,s^{-1}}$
	radiation transmission factor	–
Γ	heat capacity-temperature integral term	$\mathrm{J\,kg^{-1}}$
Δ	difference	–
δ	parameter of cubic EOS	$\mathrm{m^3\,kg^{-1}}$
ϵ	parameter of cubic EOS	$\mathrm{m^6\,kg^{-2}}$
	turbulence dissipation	$\mathrm{m^2\,s^{-3}}$

$\zeta^{\pm}$	parameters for velocity fluctuations in duct flow acoustics	$-$
η_i	field impedance	$\mathrm{m^2\,kg^{-1}\,s^{-1}}$
η_s	isentropic compressibility	$\mathrm{m\,kg^{-1}\,s^{-2}}$
Θ	tangential pressure/velocity ansatz function	$-$
θ	circumferential coordinate	rad
κ	isentropic coefficient	$-$
λ	thermal conductivity	$\mathrm{W\,m^{-1}\,K}$
	optical wave length	m
μ	dynamic viscosity	Pa s
μ^0	standard stare Gibbs free energy	$\mathrm{J\,mol^{-1}}$
ν	optical wave number	$\mathrm{m^{-1}}$
ξ	dimensionless ray coordinate	$-$
	linearized circumferential coordinate	m
ρ	density	$\mathrm{kg\,m^{-3}}$
σ_ϕ	standard deviation of ϕ	$[\phi]$
τ	shear stress	Pa
	finite element stabilization distribution	s
τ_s	finite element stabilization parameter	$-$
ϕ	generic quantity	a.u.
φ	angular coordinate in single flame domain	rad
ψ	stratification function	$-$
ω	angular frequency	$\mathrm{rad\,s^{-1}}$
Ω	complex eigenfrequency	$\mathrm{rad\,s^{-1}}$
Ω^e	finite element	$-$

Symbols

$\mathfrak{A}$	boundary flow of enthalpy of formation	$\mathrm{W\,m^{-3}}$
$\mathfrak{E}$	relative error	$-$
$\mathcal{E}_{net}$	Spectral net emission	$\mathrm{W\,m^{-2}}$
$\mathcal{I}^+$	function returning radiation intensity that leaves computational cell	$\mathrm{W\,m^{-2}}$

$\mathcal{L}$	differential equation operator	s^{-1}
$\mathcal{P}$	probability density function	–
$\mathfrak{q}$	specific heat source	$\mathrm{J\,kg}^{-1}$
$\mathcal{R}$	residual	s^{-1}[1]
$\mathcal{S}_\phi$	voluemtric source term of ϕ	$[\phi]\mathrm{m}^{-3}\,\mathrm{s}^{-1}$
$\mathcal{T}$	finite element stabilization term	$[\mathcal{W}]\mathrm{m}^{3}\,\mathrm{s}^{-12}1$
	radiation transmission term	$\mathrm{W\,m}^{-2}$
$\mathcal{V}$	Voigt profile	–
$\mathcal{W}$	weighting function	a.u.

Subscripts

b	black body radiation
bd	spectral band
	FTF zone boundary
$blue$	blue radiation
c	center
	chamber
	critical point
$cells$	computational cells
co	cut-on
eff	effective
f	final
fl	flame
	flamelet
$ideal$	ideal gas
inj	injector
m	mass
max	maximum
mol	per molecule
n	normalized
ox	oxidizer
r	reduced

---

[1] for normalized solution variables

rec	recirculation zone
s	per spectral variable
$real$	real gas
ref	reference value
rel	relative
$stoich$	stoichiometric
s	start
sf	single flame
t	turbulent
	total
	target
λ	thermal diffusion
ϕ	vector component in ϕ-direction
0	reference
	entrance/inlet
$1D$	axial reference profile for mean flow calculation
$2D$	two-dimensional reference distribution for mean flow calculation

Superscripts

x	axial
r	radial
$\bar{\ }$	Reynolds average
	mean value
$'$	fluctuation value
$'^2$	variance
$\tilde{\ }$	Favre average
	amplitude in reference plane
$\hat{\ }$	complex amplitude
$\pm$	right/left running
	counterclockwise/clockwise
	entry/exit

Scalars, Vectors and Matrices

ϕ	scalar
ϕ_i	i component of vector $\boldsymbol{\phi}$
$\boldsymbol{\phi}$	vector
$\underline{\boldsymbol{\phi}}$	Matrix

Abbreviations

exp	experimental
ox	oxidizer
rec	recess
thr	throttle

Acronyms

BKD	Combustion Chamber D
DLR	German Aerospace Center
EFRM-A	Equilibrium Filtered Radiation Model with self-Absorption
EOS	Equation Of State
EWT	Enhanced Wall Treatment
FTF	Flame Transfer Function
LP	Load Point
ML	Menter Lechner near wall treatment
NIST	National Institute of Standards and Technology
O/F	Oxidizer to Fuel mass flow ratio
PSD	Power Spectral Density
PDF	Probability Density Function
RHS	Right Hand Side
SRK	Soave Redlich Kwong
SWF	Scalable Wall Functions
TCD	Thrust Chamber Demonstrator
TCI	Turbulence Chemistry Interaction

1 Introduction

Since the early days of space flight [2] thermoacoustic instabilities have been a crucial issue in the design of liquid rocket engines. The interaction of the combustion chamber acoustics with the combustion process may lead to mutual amplification with the possible consequences ranging up to engine breakdown and mission failure. An instability arises if a feedback loop is formed by the oscillations of the flow fields in the combustor and heat release fluctuations. There are many different coupling mechanisms leading to a specific flame response, like an impact of the acoustics on the propellant mass flows entering the chamber from the feeding system as well as modifications of mixing or evaporation [3]. Being a necessary prerequisite for the design of reliable engines, the avoidance or suppression of combustion instabilities is of major technical interest. In the following, an outline of the characteristics (Sec. 1.1) and the classification of combustion instabilities (Sec. 1.2) is given in order to clarify the scope of the present work. The goal and structure of the thesis are given thereafter in Sec. 1.3.

1.1 Characteristics of Combustion Instabilities

The basic principle of thermoacoustic combustion instabilities is shown in Fig. 1.1. A feedback loop is formed between the eigenacoustics of the chamber and the flame's response to these perturbations. If the energy fed to the oscillations by the flame dynamics exceeds the damping capabilities of the chamber, an instability arises and amplitudes increase. Eventually non-linear behavior e.g. flame response, wave propagation or flow dynamics may cause the formation of a limit cycle where the amplitudes reach an upper limit. Possible consequences of combustion instabilities reach up to the destruction of the engine due to increased thermal or mechanical loads.

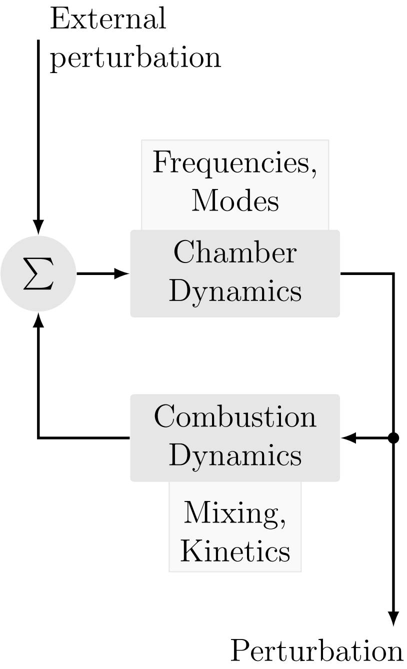

Figure 1.1: Feedback loop (based on [1])

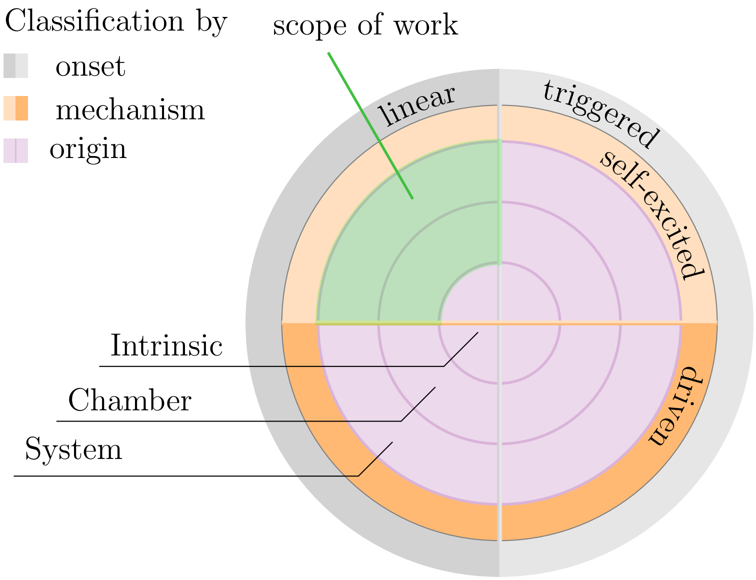

Figure 1.2: Classification of combustion instabilities

To suppress combustion instabilities manipulations of any of the involved processes is performed. The most common approach is the application of damping devices that dissipate fluctuation energy. A change of the flame response by modifying the combustion process is usually more complex as it involves e.g. modifications of the injectors or operating conditions. To efficiently apply any of the above measures to an engine, a numerical prediction of the system's stability is desirable. This is particularly relevant as an experimental determination of the stability behavior requires full scale testing of the design.

The detailed mechanisms leading to the feedback loop described above are highly case dependent. A review of the processes relevant for the test cases in the present work is given in Sec. 3.1.2. In the following, a more general view is taken. First, the basic characteristics of combustion instabilities are introduced. Then different classification systems for combustion instabilities from literature are presented and used to identify the types of instabilities the present work focuses on.

The mere occurrence of oscillations in the combustion chamber is not a sufficient criterion for a combustion instability [4]. A certain level of perturbations is always present due to the turbulent nature of the flow-processes. For small fluctuations (pressure amplitudes typical smaller than 5% of the mean value [5]), combustion is considered to be smooth as opposed to rough combustion. Rough combustion is further distinguished into a non-detrimental type, which is characterized by rather uncorrelated fluctuations, and a detrimental type, which is considered a combustion instability. It is constituted by the presence of a coordinating process that feeds organized oscillations which in turn sustain the process. As pointed out by Culick [1] the term combustion instability does not mean that the combustion process itself is unstable but that the coupled system of combustion and gas-dynamics in the chamber is unstable, as described by a feedback loop (cf. Fig. 1.1).

A common approach to assess the thermoacoustic stability of a system is the Rayleigh criterion. It is based on the concept that the effect of heat release fluctuations on the combustor's acoustics depends on the phase offset between both processes. To get a quantitative measure of this phase relation the product of heat release (q') and pressure fluctuations (p') are integrated over one oscillation period and the combustor volume:

$$\int_V \int_{f^{-1}} q' p' dt d\check{V} \begin{cases} < 0 & \text{stable} \\ > 0 & \text{unstable} \end{cases} \quad . \tag{1.1}$$

If the integral in Eq. 1.1 is negative, the combustor is expected to be stable, while for a positive value the heat release fluctuations have an destabilizing effect on the system. The actual stability of the chamber then depends on whether the energy fed to the oscillations exceeds the available damping capabilities. This criterion despite its simplicity is rather useful for the quick assessment of processes' tendencies regarding stability. It considers only the driving part. It requires knowledge of the heat release response to pressure perturbations. The exact mechanisms that lead to a combustion instability take many forms.

1.2 Classification of Combustion Instabilities

As the field of thermoacoustics is wide, a classification of the present work's topic within the different types of combustion instabilities is given. In literature, different approaches to subdivide instabilities can be found. The most general one is a rather coarse differentiation according to principal mechanisms [5] and typical associated frequencies: *Chugging* (10–400 Hz) describes low frequency fluctuations, mainly due to a coupling of feed system or structure and combustion chamber. *Buzzing* (400–1000 Hz) refers to an interaction of combustion and flow in the feed system. *Screeching* (>1000 Hz) comprises instabilities that arise from acoustical resonance of the chamber and its interaction with the combustion. However, the categorization based on the combination of frequency ranges and mechanism is not unambiguous. So the type of instabilities covered in the present work would be usually considered as high frequency screeching but the feed system is involved in the driving mechanim as well. For this reason, alternate classification approaches are considered in the following. These are not to be seen as contradiction to each other but łfocus on different aspects for classification as shown in Fig. 1.2.

Depending of the onset of an instability [1]: *Linear Instabilities* develop from an infinitesimal disturbance that grows in time whereas *Triggered Instabilities* require a certain level of initial perturbation in order to form. An example for linear instabilities is the combustion chamber D (BKD) [6] which is studied in the present work.

A different classification criterion is the way the instability is sustained [7]. A *Driven Instability* is not the result of a feedback loop but rather a response to some external mechanism. It fades, once the forcing stops. An example for this type of instability are artificially excited experiments [8] used to study the reacting flow's response to acoustic perturbations. In contrast, *Self-Excited Instabilities* are self-sustaining with the oscillations directly leading to an energy gain from the combustion response. Strictly speaking, the definition of forced instabilities does not match the above concept of the oscillations being sustained by a feedback loop between flame and acoustics.

Nevertheless, this type of instability is commonly referred to as combustion instability.

The extent of the system that is involved in the instability is taken as distinctive feature by Barrère et al. [9]. Like the classification based on principal mechanisms introduced at the beginning of this section, the approach by Barrère et al. is not able to account for the huge variety of instability mechanisms. However, two of the proposed categories cover the majority of relevant cases: *Combustion Chamber Instabilities* are related to the flow processes in the combustor alone, *System Instabilities* involve additional components like the feed system. The sub-categories given for these classes [9] are defined too narrow to be of use for a general classification and not considered here. For the sake of completeness only the third class, *Inctrinsic Instabilities* is mentioned, where the combustion process itself becomes unstable instead of the coupled system of acoustics and heat release.

1.3 Thesis Objective and Structure

To efficiently predict the stability behavior of an engine already in early design stages, numerical methods are essential, especially as robust experimental studies require full scale testing of the system with all its acoustically relevant components. To allow for numeric stability studies applicable within industrial development processes, a hybrid methodology has been under development for several years [3, 10–12]. It combines linear perturbation analyses with flame response characterizations based on single flame simulations. The different components of the procedure have been assembled in a previous study [13] to obtain stability predictions of a cryogenic H_2/O_2 engine. The present work covers the consolidation and validation of both the overall methodology and its components. On this basis revisions are proposed to address potential weaknesses. Finally, an assessment of the method's soundness and capabilities is given. The approach followed in the present work relies on three steps:

1. First, the previous developments of the methodology's different aspects are discussed. Weaknesses are identified and a revised version of the procedure is proposed.
2. The components of the stability assessment procedure are validated both by studying their sensitivity towards modeling uncertainties as well as by comparison to experimental findings.
3. The consequences that the considering modeling options have on the stability calculations are evaluated. The soundness of the predictions is discussed critically and suggestions for subsequent research activities are derived.

The thesis is structured as follows: First, the theoretical background for the subsequent methodology analysis and development is introduced in Chap. 2. An overview over basic modeling aspects from literature and previous studies is given. The information in this chapter will be referred to during the analyses and model derivations in the remainder of the work, in favor of a clear separation between background and new findings. Thereupon (Chap. 3) the experimental and theoretical reference cases that will be used for the later application and validation of the stability prediction approach are introduced. This includes a review of previous findings regarding the occurring instability mechanisms, which will be useful for the assessment of the numerical results' plausibility. Based on the fundamentals and the knowledge of the target configurations, Chap. 4 addresses the stability analysis procedure. After an overview of the overall concept, its components are considered separately. For each part of the procedure, the previous development and the state that the present work starts from are outlined, shortcomings and necessary analyses are identified. On this basis a revised version of the stability assessment procedure is developed along with approaches to conduct the analyses. The chapter provides the basis for the subsequent analysis and validation of the stability assessment approach. As the methodology relies heavily on simulations of a single rocket engine flame, these are the starting point of the subsequent application of the procedure. In Chap. 5 the numerical setup for the simulations is specified. An approach to obtain flame radiation images in a way that is consistent with the single flame simulation setup and allows for the validation of the numerical results is developed and applied in the subsequent validation. Taking the validated CFD approach for single flame simulations the componentwise evaluation of the stability assessment procedure is started with the passive chamber acoustics in Chap. 6. The modeling of the flame feedback is addressed subsequently in Chap. 7. Combining the findings and approaches from the previous two chapters, the role of the different modeling choices in the context of the overall stability assessment is conducted in Chap. 8. The findings are used to assess reliability and prospects of the approach. Finally in Chap. 9 the conclusions of the work are given.

2 Fundamentals

The analysis and further development of the rocket engine thermoacoustic stability assessment procedure relies on several fundamental principles ranging from engine design to flow and radiation modeling. In this chapter the basic concepts from literature and previous studies that the remainder of this work relies on are introduced. Starting point is a survey of the thrust chambers' basic configuration (Sec. 2.1) and the associated flow patterns. The equations used to model the flow fields are introduced thereafter (Sec. 2.2). These equations are mainly applied in the context of single flame (cf. Sec. 5.1) and mean flow calculations (cf. Sec. 4.2.5) as well as the development of the stability assessment procedure (Chap. 4). To describe small perturbations from a flow mean state, the Linearized Euler Equations (LEE) are employed (Sec. 2.3). They are used for the acoustic analyses in this work (cf. Sec. 4.1). When applied to the case of a uniform cylindrical duct flow, an analytical solution of the isentropic LEE can be obtained, which allows for the basic explanation of a thrust chamber's acoustic behavior (Sec. 2.4) and is of relevance for the design of the stability assessment procedure (Chap. 4). Finally, the computation of flame radiation is addressed (Sec. 2.5). This topic is a necessary prerequisite for the radiation-based single flame validation, which is outlined in Sec. 5.2 and performed in Sec. 5.3.

2.1 Thrust Chamber Structure and Flow Fields

The basic design of rocket thrust chambers influences the engines' acoustic behavior (cf. Sec. 2.4) and sets the framework for the discussion and further development of the stability assessment procedure in Chap. 4. In the following, an introduction to the system and its components is given. Further information can be found e.g. in the book of Sutton and Biblarz [5].

Rocket engines convert the energy chemically stored in the propellants to kinetic energy of the flow whose exit impulse provides the thrust. This conversion occurs in the thrust chamber. Depending on the type of application, a wide range of designs exists. For the present work main and upper stage liquid rocket engines for space launchers are of relevance. A representative configuration of this engine type is shown in Fig. 2.1a. The release of chemical energy occurs in the combustion chamber by multiple diffusion flames, forming in the mixing region between the fuel and oxidizer mass flows. In the convergent-divergent nozzle the heated flow is accelerated to supersonic velocities to convert the thermal into kinetic energy. As the convergent nozzle part can cover a substantial portion of the combustor, the combination of cylindrical part and convergent nozzle region is referred to as combustion chamber in the remainder of this work. Its downstream boundary is defined by the sonic line associated with the choked nozzle flow, which acoustically

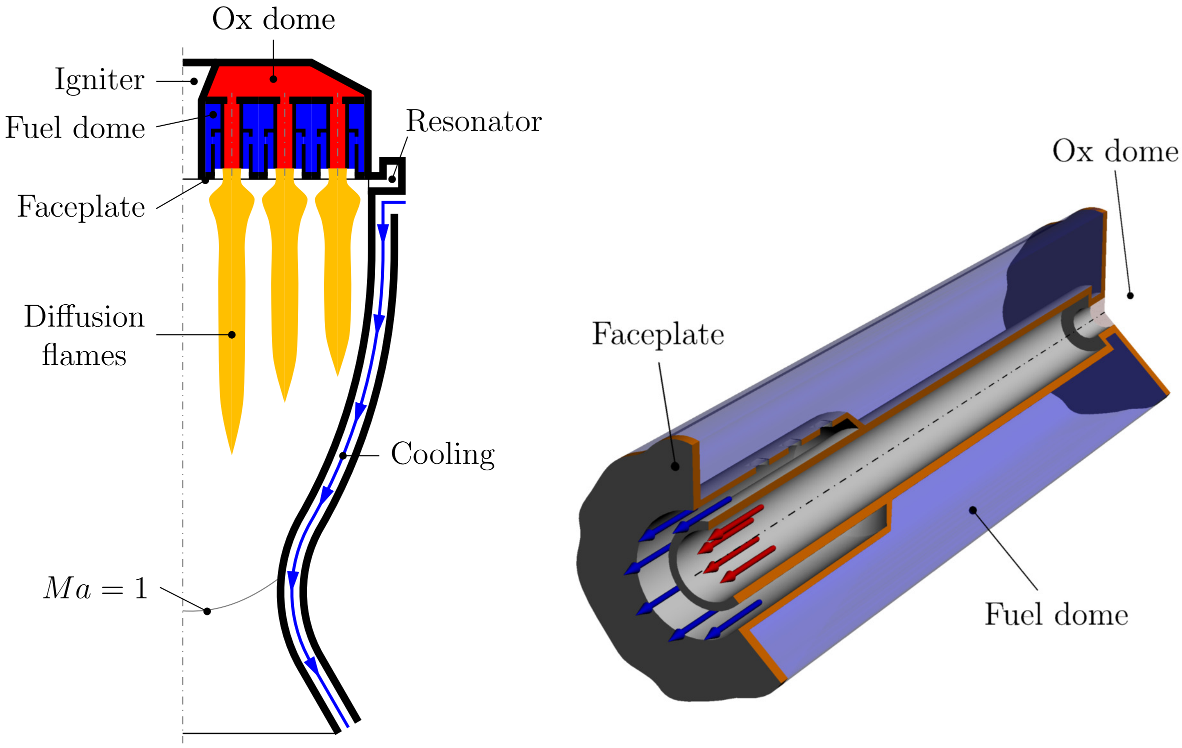

(a) Overview **(b)** Injection element

Figure 2.1: Thrust chamber structure

decouples the chamber from its surroundings. The propellants are injected via multiple (up to several hundreds) injection elements. Together with the face plate they form the upstream boundary of the combustion chamber.

A typical injector configuration is shown in Fig. 2.1b with the fuel being injected concentrically around the oxidizer. At the upstream end of the oxidizer injector there is a throttle to induce a pressure loss for decoupling the chamber from the dome and the upstream feed system. The propellants are distributed to the injection elements by their respective domes, which again are fed by a supply system containing turbopumps to raise the propellants' pressure from storage to pre-injection conditions. The actual cycle type used for the propellant feed system is not of relevance in the current work and the reader is referred to other publications [5] for further information. To ensure the thermal integrity of the chamber walls, regenerative cooling can be applied, usually using the fuel mass flow as coolant. Resonators may be included in the design to modify the chamber acoustics in order to suppress combustion instabilities. They are placed close to the faceplate to avoid exposure to the hot combustion gases. Finally, the igniter is integrated in the injection head at the centerline of the chamber.

Propellants are typically injected cryogenic at supercritical pressures and low temperatures (around 100 K, cf. Chap. 3). The mixture ratio is slightly fuel rich as the optimum for the achievable exit velocity is located there.

The acoustic behavior of the chamber is strongly influenced by the fluid flow. Its principal structure is shown in Fig. 2.2 for a single flame and its associated injection element. The color code represents the temperature distribution. Constantly low temperatures are present in the injection system. In the chamber, after an initially strongly stratified diffusion flame with a distinct hot gas zone, the flow homogenizes further downstream at a combustion temperature of more than 3000 K. The underlying mixing structure is shown in detail view B by means of the mixture fraction f, i.e. the local fraction of mass originating from fuel (cf. Sec. 5.1.3). After injection, the fuel spreads towards the chamber wall, dominating the composition inside the recirculation zone. The oxidizer forms a dense core at the centerline of the flame. Between both components a mixing region develops, where the

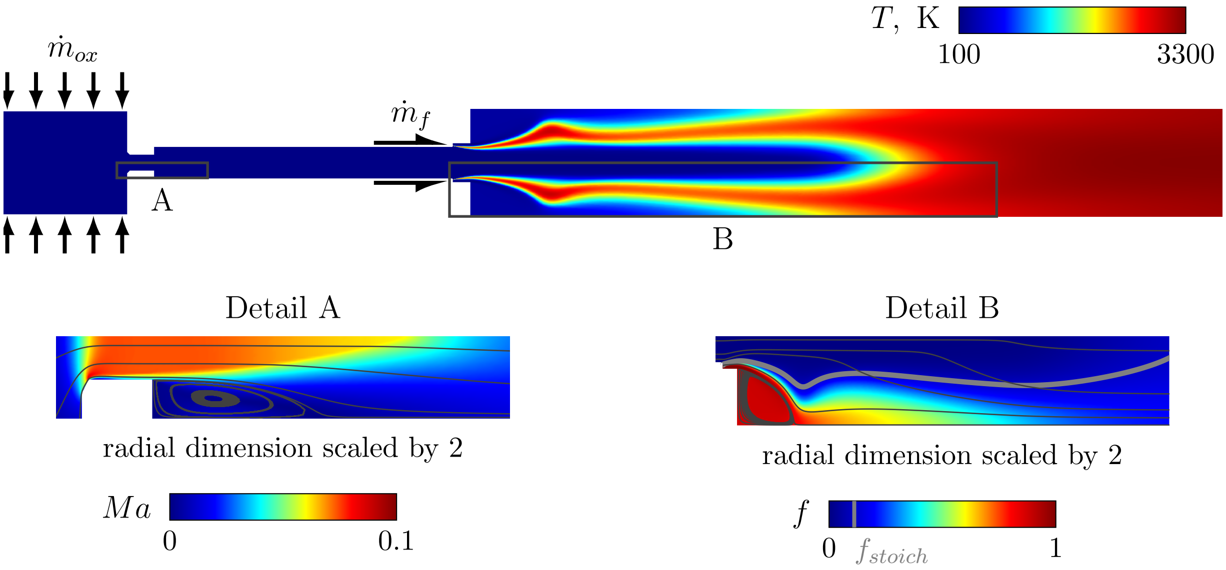

Figure 2.2: Flow fields of a single flame

combustion occurs. It can be characterized by the iso-line of stoichiometric mixture fraction, f_{stoich}. Emanating from the small gap between fuel and oxidizer injection, the stoichiometric line first bends outwards, then inwards, forming a bulb. After a region of nearly constant radius, the flame contour closes towards the centerline due to the fuel rich operating conditions. The initial bulb results from the strong volumetric expansion of the cryogenic oxidizer core and is considerably weaker for ideal gas injection conditions. Aside of the dominant recirculation zone originating from the backward facing step formed at the transition from injector to chamber, the flow direction is mainly axial. Mixing occurs via turbulent exchange between oxidizer and fuel rich regions, which is sufficient to ensure a rather homogeneous flow at the chamber end.

In the oxygen injector, the throttle at the connection to the dome causes a disturbance of the pipe flow (Fig. 2.2, Detail A). The contraction from the dome to the throttle leads to a local flow acceleration followed by a deceleration once the injector diameter increases again. This area jump causes the formation of a recirculation zone at the downstream side of the throttle. The flow in the fuel injector is of minor relevance in this study and not covered here.

2.2 Fluid Dynamic Equations

The acoustic characterization of the configuration outlined in Sec. 2.1 requires knowledge of the flow fields inside the rocket combustion chamber. The equations governing the numerical simulations of a single flame (cf. Sec. 5.1) as well as the calculation of perturbations for the acoustic analysis (cf. Sec. 2.3 and 4.1) are each derived from a common set of equations describing the dynamics of the flow. These equations are introduced in the following. In the beginning, basic concepts for the description of mixtures and turbulence are introduced (Sec. 2.2.1) along with the relevant equations of state and the concept of incompressibility (Sec. 2.2.2). Thereafter, mass and momentum conservation are addressed in Sec. 2.2.3. As a detailed discussion of the Navier-Stokes equations can be found in an abundance of sources (see e.g. [14]), their outline is kept short here. Energy conservation is covered separately (Sec. 2.2.4). It is introduced as conservation of total energy, forming the basis for the derivation of any other form of this principle used in the current work. The enthalpy equation, which is used for the single flame calculations (Sec. 5.1.3), is developed from the total energy equation afterwards, followed by the chemical enthalpy balance equation used for heat release calculations as described in Sec. 5.1.3.

2.2.1 Basic Concepts

As prerequisites for the introduction of the equations of state (Sec. 2.2.2) and the fluid dynamic equations (Sec. 2.2.3 and 2.2.4) the concepts of mixture properties and turbulence treatment are introduced in the following.

The fluid inside the rocket combustion chamber is composed of multiple species, whose concentrations vary across the flow. The equations presented in the following sections 2.2.2 to 2.2.4 are formulated for the mixture as opposed to its components. This approach requires to calculate the mixture properties from those of the individual species. In general, a generic fluid property ϕ is composed of an ideal part and a real gas correction (cf. Sec.

2.2.2):

$$\begin{gathered}\phi = \phi_{ideal} + \phi_{real} = \sum_i \phi_i y_i + \Delta\phi_{real} \qquad . \\ \phi = h_f^0,\ c_v,\ c_p,\ \Delta e_s,\ H,\ E\end{gathered} \tag{2.1}$$

The different variables that ϕ represents (2^{nd} line in Eq. 2.1) are introduced later, upon use. Their ideal part can be calculated from the species mass fractions y_i while the real gas correction depends on the used equation of state and the mixing law (see Sec. 2.2.2 and 5.1.2). For the enthalpy of formation h_f^0 only the ideal part in Eq. 2.1 is considered. So any enthalpy of mixing is neglected for this property. As the dominating species in the fluid composition can be approximated as an ideal gas at standard state conditions this approach is justified. The further use of this concept is addressed in Sec. 5.1.3. The transport properties (thermal conductivity λ and dynamic viscosity μ) are subject to more complex mixing laws [15]. The specification of these properties is addressed in Sec. 5.1.2.

Aside of the just discussed multicomponent composition, high turbulence is another characteristic trait of the flow in a rocket combustion chamber. For the numerical description of the turbulent flow fields, ensemble averaging of Reynolds or Favre type is applied. In this concept the field variables ϕ are decomposed in their mean ($\bar{\ }$) and turbulent fluctuating part ($'$)

$$\phi = \bar{\phi} + \phi' \quad . \tag{2.2}$$

The overbar denotes Reynolds averaging, i.e. an unweighted ensemble average. However, in order to retain the structure of the equations that are introduced in the subsequent sections 2.2.3 and 2.2.4, only the mean density $\bar{\rho}$ and pressure $\bar{p}$ are Reynolds averaged. The other variables are replaced by their Favre averages

$$\tilde{\phi} = \frac{1}{\bar{\rho}}\overline{\rho\phi} \quad . \tag{2.3}$$

That way, the Reynolds averaged product of density and another variable can be replaced according to

$$\overline{\rho\phi} = \bar{\rho}\tilde{\phi} \quad , \tag{2.4}$$

thus allowing to separate the fields. The practical application of this modeling concept is addressed within the discussion of the respective equations in Sec. 2.2.3 and 2.2.4.

2.2.2 Equations of State and Incompressibility

In general, there are two types of equations of state (EOS), thermal and caloric. The thermal EOS relates local pressure p, temperature T and density ρ of the fluid, whereas the caloric EOS describes the dependence of the sensible energy e_s or enthalpy h_s on the state variables. If not specified otherwise, the term equation of state in this work refers to both the thermal and caloric EOS. So if e.g. the use of a cubic EOS is stated, this means that not only the cubic thermal EOS is used but also the corresponding caloric one. Two different sets of EOS are of relevance here (cf. Sec. 2.3 and 5.1.2), the common ideal EOS and a cubic real gas EOS. They are introduced in the following. Moreover, the concept of incompressible flow is used for certain simulation types in this work (cf. Sec. 4.3.1.3), which is addressed thereafter.

The ideal gas EOS neglects any interactions between the molecules of the fluid. The corresponding thermal and caloric EOS read

$$p = \rho R T \tag{2.5a}$$

$$\Delta e_s = \Delta h_s - \frac{p}{\rho} = \int_{T_{ref}}^{T} c_v d\check{T} = \int_{T_{ref}}^{T} (c_p - R) d\check{T} \tag{2.5b}$$

with Δe_s denoting the difference of sensible energy, T_{ref} a fixed reference temperature, c_v the specific isochoric heat capacity and c_p the specific isobaric heat capacity. Their ratio gives the isentropic coefficient of an ideal gas

$$\kappa = \frac{c_p}{c_v} \tag{2.6}$$

or

$$c_p = R \frac{\kappa}{\kappa - 1}, \quad c_v = \frac{R}{\kappa - 1} \quad . \tag{2.7}$$

For detailed flow simulations under rocket combustion chamber conditions, the ideal gas assumption is in general not appropriate to describe the low temperature-high pressure propellant streams at injection conditions (cf. Sec. 3). The thermal equation of state does not follow Eq. 2.5a but deviates by a real gas factor Z

$$Z = \frac{p}{\rho R T} \quad . \tag{2.8}$$

For these cases a cubic real gas EOS is used. The corresponding thermal EOS has the general form

$$p = \frac{RT}{1/\rho - b + c} - \frac{\alpha}{1/\rho^2 + \delta/\rho + \varepsilon} \quad . \tag{2.9a}$$

The definition of the parameters b, c, α, δ and ε depends on the exact choice of the EOS. The same applies to the caloric EOS, which includes a correction term $\Delta e_{s,real}$ analogous to Eq. 2.1 to extend the caloric ideal gas equation 2.5b:

$$\Delta e_s = \int_{T_{ref}}^{T} c_v d\check{T} + \Delta e_{s,real} \quad . \tag{2.9b}$$

For details, see the references given in Sec. 5.1.2.

The thermal equations of state 2.5a and 2.9a provide a coupling between the local pressure and density, describing the general case of a compressible flow. Compressibility is a necessary prerequisite to capture acoustic waves. In the present work, the suppression of acoustics is desirable in certain cases (cf. Sec. 4.3.1.3). Therefore incompressibility is employed. In an incompressible flow, density is decoupled from pressure:

$$\left.\frac{\partial \rho}{\partial p}\right|_{T,y_i} = 0 \quad . \tag{2.10}$$

However, density variations can still occur due to a change of temperature or flow composition. Thus, the often used modeling of incompressible flow via a divergence-free velocity field does not apply here. To close the flow equations introduced in the following sections 2.2.3 and 2.2.4, a relation between density, temperature and flow composition is required. In the present work, this coupling is achieved by evaluating the thermal EOS 2.9a at a fixed reference pressure, as will be discussed in Sec. 5.1.2.

2.2.3 Mass and Momentum Conservation

For the fluid mixture the conservation of mass and momentum is described by the Navier-Stokes equations, reading

$$\frac{\partial \rho}{\partial t} + \nabla \cdot (\rho \boldsymbol{u}) = 0 \tag{2.11}$$

and

$$\frac{\partial}{\partial t}\boldsymbol{u} + (\boldsymbol{u} \cdot \nabla)\,\boldsymbol{u} = -\frac{1}{\rho}\nabla p + \frac{1}{\rho}\nabla \cdot \underline{\boldsymbol{\tau}} \quad , \tag{2.12}$$

respectively. Here ρ denotes the density, $\boldsymbol{u}$ the velocity vector, p the pressure and $\underline{\boldsymbol{\tau}}$ is the shear stress tensor

$$\underline{\boldsymbol{\tau}} = \mu\left(\underline{\boldsymbol{S}} - \frac{2}{3}\nabla \cdot \boldsymbol{u}\underline{\boldsymbol{I}}\right) \tag{2.13}$$

with the dynamic viscosity μ, the strain rate tensor $\underline{\boldsymbol{S}}$ and the identity matrix $\underline{\boldsymbol{I}}$. For turbulent flow, the Reynolds Averaged Navier-Stokes (RANS) equations are solved. These provide directly the results for the ensemble averaged flow fields (Sec. 2.2.1) and are obtained by averaging Eq. 2.11 and 2.12. The resulting equations retain their original structure but density and pressure are replaced by their ensemble and velocity by its Favre average. However, averaging Eq. 2.12 leads to unclosed Reynolds stresses τ_t that are subtracted from the RHS:

$$\frac{\partial}{\partial t}\tilde{\boldsymbol{u}} + (\tilde{\boldsymbol{u}} \cdot \nabla)\,\tilde{\boldsymbol{u}} = -\frac{1}{\rho}\nabla \bar{p} + \frac{1}{\rho}\nabla \cdot (\underline{\bar{\boldsymbol{\tau}}} - \underline{\bar{\boldsymbol{\tau}}}_t) \tag{2.14}$$

with

$$\bar{\tau}_t = \overline{\boldsymbol{u}' \cdot \boldsymbol{u}'} \quad . \tag{2.15}$$

The Reynolds stresses are modeled via the Boussinesq approximation: The viscosity in Eq. 2.13 is replaced by an effective viscosity

$$\mu_{eff} = \mu + \mu_t \tag{2.16}$$

with the turbulent viscosity μ_t accounting for the increased momentum transport due to turbulence. More information on the applied turbulence closure is given in Sec. 5.1.1.

2.2.4 Energy Conservation

In addition to mass and momentum, energy is conserved in the flow as well. In the following, this principle is formulated by means of the total energy E (Eq. 2.17). The corresponding equation 2.18 is the common starting point for the derivation of any other description of energy conservation in this work, be it the subsequently derived enthalpy equation 2.21 that is used for the single flame simulations (Sec. 5.1.2) or the pressure equation of the Euler Equations (Sec. 2.3). A different energy balance that will be of relevance later is the chemically bound energy h_f^0, which will be used for heat release calculations (cf. Sec. 5.1.3). The corresponding equation is introduced at the end of the current section.

The total energy E is composed of three components:

$$E = h_f^0 + \Delta e_s + \frac{1}{2} u^2 \quad . \tag{2.17}$$

The enthalpy of formation h_f^0 is the chemically bound energy, the sensible energy difference is in general calculated according to Eq. 2.9b and the last term in Eq. 2.17 is the kinetic contribution. Neglecting viscous dissipation, the total energy conservation equation reads

$$\frac{\partial \rho E}{\partial t} + \nabla \cdot \left[\boldsymbol{u} \left(\rho E + p \right) \right] = -\nabla \cdot \left(\boldsymbol{q}_\lambda + \boldsymbol{q}_m \right) \tag{2.18}$$

with the diffusive fluxes due to heat conduction $\boldsymbol{q}_\lambda$ and mass transfer $\boldsymbol{q}_m$. According to Fourier's and Fick's laws these are calculated as

$$\boldsymbol{q}_\lambda = -\lambda \nabla T \tag{2.19}$$

$$\boldsymbol{q}_m = -\sum_i D_i E_i \nabla y_i \tag{2.20}$$

with the thermal conductivity λ and the mass diffusion coefficient of species i, D_i. Note that Eq. 2.20 neglects explicit real-gas mixture effects.

In the single flame simulations (Sec. 5.1.2) a different formulation of the energy conservation principle Eq. 2.18 is used. For unity turbulent and molecular Lewis numbers along with Reynolds averaging to handle turbulence, the energy equation 2.18 can be rearranged as

$$\frac{\partial \bar{\rho}\tilde{H}}{\partial t} + \nabla \cdot \left(\tilde{\boldsymbol{u}} \bar{\rho} \tilde{H} \right) = \frac{\partial \bar{p}}{\partial t} + \nabla \cdot \left(\frac{\lambda_{eff}}{c_p} \nabla \tilde{H} \right) \quad . \tag{2.21}$$

Here the total enthalpy

$$H = E + \frac{p}{\rho} \tag{2.22}$$

is used as conservation variable. The effective thermal conductivity is composed of the molecular value and the turbulent contribution:

$$\lambda_{eff} = \lambda + \frac{\mu_t}{Sc_t} \quad . \tag{2.23}$$

The turbulent part covers turbulent enthalpy transport associated with temperature gradients as well as turbulent flow due to species diffusion. For approximately isobaric flows Eq. 2.21 is often simplified by dropping the first term on the RHS.

In contrast to the total energy that sums up all relevant energy forms, the enthalpy of formation h_f^0 represents the chemically bound part alone. Its source term $\mathcal{S}_{h_f^0}$ is directly linked to the volumetric heat release due to combustion, q, via

$$q = -\mathcal{S}_{h_f^0} \quad . \tag{2.24}$$

By combining the transport equations of the different species, an equation describing the mixture enthalpy of formation as defined in Sec. 2.2.1 is obtained:

$$\frac{\partial \bar{\rho}\tilde{h}_f^0}{\partial t} + \nabla \cdot \left(\bar{\rho} \tilde{\boldsymbol{u}} \tilde{h}_f^0 \right) = \nabla \cdot \left(\frac{\mu}{Sc} + \frac{\mu_t}{Sc_t} \nabla \tilde{h}_f^0 \right) + \tilde{\mathcal{S}}_{h_f^0} \tag{2.25}$$

with the Schmidt number Sc and its turbulence counterpart Sc_t.

2.3 Linearized Euler Equations

The Linearized Euler Equations (LEE) are used to describe the acoustic perturbations in the combustion chamber as discussed further in Sec. 4.1.

They are the basis of the acoustic analyses presented in Chap. 6 and 8. Moreover, the analytic solution for duct flow acoustics discussed in Sec. 2.4 is obtained for a special case of the LEE. For linear rocket engine acoustics viscous and turbulence effects can be considered secondary. Thus the flow equations describing momentum and energy conservation (Eq. 2.12, Eq. 2.18) can be simplified by dropping the diffusion terms. In combination with the continuity equation 2.11, the Euler Equations are obtained. If deviations from the mean state are small, the perturbations induced by the chamber acoustics can be described by linearization, leading to the Linearized Euler Equations. In their general form, the LEE model the linear temporal perturbations of a non-isentropic, frictionless, three-dimensional flow. In this section their basic form, covering the fluctuations of the primitive flow variables density, velocity and pressure, is introduced. Starting point are the basic assumptions going into derivation of the form of the LEE used in the present work (Sec. 2.3.1). Thereupon the actual equations are discussed (Sec. 2.3.2), with focus on the pressure fluctuation equation. Finally, the general structure of the LEE solution is addressed (Sec. 2.3.3).

2.3.1 Basic Concepts

In the following, the assumptions and simplifications that underlie the LEE as used in the present work are outlined. This concerns the perturbation approach, the used EOS and the modeling of fluid property fluctuations.

The LEE describe the linear perturbations from a reference state, the mean flow. This corresponds to the decomposition of the flow fields into a steady mean ($\bar{}$) and a significantly smaller transient perturbation ($'$):

$$\phi = \bar{\phi} + \phi', \quad |\phi'| << \left|\bar{\phi}\right| \quad . \tag{2.26}$$

This approach is formally similar to the turbulence modeling concept described in Sec. 2.2.1 (Eq. 2.2). However, the LEE are used to calculate the fluctuating part instead of the mean, as it is done in the context of turbulence modeling.

The form of the LEE used in this work is based on the assumption that the fluid behaves like an ideal gas (Eq. 2.5). Despite the local relevance of real gas effects in the chamber (cf. Sec. 2.2.2, Sec. 5.1.2) the simplification is justified due to the way the mean flow is calculated. This will be discussed in Sec. 4.2.

For an ideal gas, the isentropic coefficient κ depends on temperature and local fluid composition. Its temperature dependence is usually small and thus the influence of T' on κ is neglected. Moreover, it is assumed that the impact of fluctuations in the local flow composition on κ and molar mass are of minor relevance. So the isentropic coefficient κ and specific gas constant R are modeled as constant in time, i.e.

$$\kappa = \bar{\kappa}, \quad R = \overline{R} \quad . \tag{2.27}$$

From Eq. 2.27 together with Eq. 2.7 the stationarity of the specific isochoric and isobaric heat capacities follows directly:

$$c_v = \bar{c}_v, \quad c_p = \bar{c}_p \quad . \tag{2.28}$$

Note that Eq. 2.27 does not imply a temporally constant speed of sound c since for an ideal gas

$$c' = \sqrt{\kappa R T}' = \frac{1}{2}\sqrt{\frac{\kappa R}{\overline{T}}}T' \quad , \tag{2.29}$$

i.e. the sound speed fluctuates with the local flow temperature. In contrast to the aforementioned properties, fluctuations of the enthalpy of formation cannot be neglected in general. These go directly into the flame response, which is an essential part of the thermoacoustic characterization of a combustion chamber (cf. Sec. 4.1). Finally, the simplification of a temperature independent isentropic coefficient is applied to the mean flow in the derivation of the pressure fluctuation equation as well. Usually, an effective value of κ corresponding to a representative specific heat capacity would be used in this context. However, in this work the isentropic coefficient is used to achieve certain acoustic characteristics of the mean flow. The details including the exact calculation procedure used to obtain the isentropic coefficient are subject of Sec. 4.2 and not considered further at this point.

2.3.2 Perturbation Equations

With the prerequisites given in Sec. 2.3.1 the LEE are introduced. Focus is placed on the pressure fluctuation equation, which represents the energy conservation principle in the LEE. Thereafter, the solution structure of the presented equations is shortly addressed.

To derive the LEE, first the Euler Equations are obtained from the conservation Equations given in Sec. 2.2 by dropping the diffusive terms. Then the perturbation approach (Eq. 2.26) is inserted into the Euler Equations and only linear terms are kept. For the mass (Eq. 2.11) and momentum (Eq. 2.12) equations the result is straightforward:

$$\frac{\partial \rho'}{\partial t} + \nabla \cdot \bar{\boldsymbol{u}}\rho' + \bar{\boldsymbol{u}} \cdot \nabla \rho' + \nabla \bar{\rho} \cdot \boldsymbol{u}' + \bar{\rho} \nabla \cdot \boldsymbol{u}' = 0 \tag{2.30}$$

and

$$\frac{\partial \boldsymbol{u}'}{\partial t} + \left(\bar{\boldsymbol{u}} \cdot \nabla\right) \boldsymbol{u}' + \left(\boldsymbol{u}' \cdot \nabla\right) \bar{\boldsymbol{u}} = -\frac{1}{\bar{\rho}} \nabla p' + \frac{1}{\bar{\rho}^2} \nabla \bar{p} \rho' \quad . \tag{2.31}$$

To complete the description of the flow perturbations, a pressure equation is required. Starting point for its derivation is the energy equation 2.18. Dropping diffusive transport terms in accordance with the basic assumptions of the LEE leads to

$$\frac{\partial \left(\rho E\right)}{\partial t} + \nabla \cdot \left[\boldsymbol{u}\left(\rho E + p\right)\right] = 0 \quad . \tag{2.32}$$

Inserting the definition of the total energy, Eq. 2.17, rearranging under usage of a vector identity[1] and employing Eq. 2.11 and 2.12 gives (cf. App. A)

$$\rho \frac{\partial \Delta e_s}{\partial t} + \rho \boldsymbol{u} \cdot \nabla \Delta e_s + p \nabla \cdot \boldsymbol{u} = -\left(\frac{\partial \rho h_f^0}{\partial t} + \nabla \cdot \left(\rho \boldsymbol{u} h_f^0\right)\right) \quad . \tag{2.33}$$

This equation is completely equivalent to the total energy conservation Equation 2.18 as no simplifications have been introduced so far. Linearization of Eq. 2.33 under usage of the assumptions from Sec. 2.3.1 results in

---

[1] The identity $\nabla\left(\boldsymbol{\phi} \cdot \boldsymbol{\phi}\right) = 2\left(\boldsymbol{\phi} \cdot \nabla\right)\boldsymbol{\phi} + 2\boldsymbol{\phi} \times \left(\nabla \times \boldsymbol{\phi}\right)$ is combined with $\boldsymbol{\phi} \cdot \left(\boldsymbol{\phi} \times \left(\nabla \times \boldsymbol{\phi}\right)\right) = 0$.

(cf. App. A)

$$\begin{aligned}\frac{\partial p'}{\partial t} &+ \overline{\boldsymbol{u}} \cdot \nabla p' + \boldsymbol{u}' \cdot \nabla \overline{p} + \kappa \left(\overline{p} \nabla \cdot \boldsymbol{u}' + p' \nabla \cdot \overline{\boldsymbol{u}} \right) - \frac{1}{\kappa - 1} \left(\boldsymbol{u}' \overline{p} + \overline{\boldsymbol{u}} p' \right) \cdot \nabla \kappa \\ &= -T_{ref} \left(\boldsymbol{u}' \overline{\rho} + \overline{\boldsymbol{u}} \rho' \right) \cdot \left(\frac{R}{\kappa - 1} \nabla \kappa - \nabla R \right) - (\kappa - 1) \left[\frac{\partial (\rho h_f^0)}{\partial t} + \nabla \cdot \left(\rho \boldsymbol{u} h_f^0 \right) \right]' \quad . \end{aligned} \tag{2.34}$$

To interpret the right-hand side (RHS) of Eq. 2.34 it is rewritten as

$$\begin{aligned} RHS &= -(\kappa - 1) \left[\left(\frac{\partial (\rho h_f^0)}{\partial t} + \nabla \cdot \left(\rho \boldsymbol{u} h_f^0 \right) \right)' - (\rho \boldsymbol{u})' \nabla \frac{R}{\kappa - 1} T_{ref} \right] \\ &= -\left(\kappa - 1 \right) \left[\frac{\partial (h_f^0 - c_v T_{ref})}{\partial t} + \rho \boldsymbol{u} \cdot \nabla \left(h_f^0 - c_v T_{ref} \right) \right]' \end{aligned} \quad . \tag{2.35}$$

For the last transform in Eq. 2.35 it has been used that $\partial(c_v T_{ref})/\partial t = 0$ due to the time-independent c_v assumption (Eq. 2.28). The term in square brackets in Eq. 2.35 is similar to the transport equation for the enthalpy of formation (Eq. 2.25). It can be represented as the fluctuating heat release due to combustion q' (Eq. 2.24) along with a modification that accounts for the reference sensible energy at T_{ref}. This modification effectively moves the reference temperature for the calculations on the left hand side (LHS) of Eq. 2.34 to 0 K. However, in the remainder of this work it is neglected to ensure consistency with the form of the LEE used in previous works [12]. This simplification is justified since for the majority of the mean flow (cf. Sec. 6.1.1) T_{ref} is significantly lower than the local flow temperature T. Thus, recalling Eq. 2.9b it can be considered to be of minor importance. Adapting the notation of the heat release from Eq. 2.24 and 2.25 the final form of the pressure fluctuation equation reads

$$\frac{\partial p'}{\partial t} + \bar{\boldsymbol{u}} \cdot \nabla p' + \boldsymbol{u}' \cdot \nabla \bar{p} + \kappa \left(\bar{p} \nabla \cdot \boldsymbol{u}' + p' \nabla \cdot \bar{\boldsymbol{u}} \right) - \frac{1}{\kappa - 1} \left(\boldsymbol{u}' \bar{p} + \bar{\boldsymbol{u}} p' \right) \cdot \nabla \kappa = (\kappa - 1) q' \quad . \tag{2.36}$$

Eq. 2.30, 2.31 and 2.36 together constitute the Linearized Euler Equations as used in the present work. Their application in the context of the stability assessment procedure is addressed in Sec. 4.1.

2.3.3 Solution Structure

For the stability analysis eigensolutions of the LEE (Eq. 2.30, 2.31 and 2.36) are calculated (cf. Sec. 4.1). The solution structure consists of three contributions [16]:

- Acoustic perturbations propagate as waves. They are isentropic and associated with irrotational velocity perturbations.
- Vortical, solenoidal velocity perturbations are convected with the mean flow.
- Entropy perturbations are convectively transported as well but are not associated with a velocity amplitude.

Strictly speaking, only the first one is of acoustic nature. However, all three parts contribute to the fluctuation energy in the chamber and thus the stability behavior. Thus, if not stated explicitly otherwise, the term acoustics is used to refer to the superposition of all three perturbation classes in the following. This also seems appropriate as the eigenfrequencies of interest are clearly dominated by the acoustic mode, which is accompanied by the other two perturbation types.

2.4 Analytical Cylinder Acoustics

As outlined in Sec. 2.1, the basic design of a rocket combustion chamber is composed of a cylindrical section ending in a convergent nozzle. Although neglecting the nozzle contraction may appear as a somewhat crude geometrical approximation, it has been found [12] that the chamber's basic acoustic behavior can be well characterized by analyzing isentropic perturbations in a uniform, one-dimensional cylinder flow. The governing principles of such a configuration are of major importance in the design of the stability assessment procedure (Sec. 2.3.3). In the following, the equation describing the acoustic perturbations for the above flow type is introduced (Sec. 2.4.1). Thereupon its analytical solution is outlined (Sec. 2.4.2) along with the description of the associated perturbation energy. Finally, a discussion of the consequences for rocket combustion chamber acoustics is given in Sec. 2.4.3.

2.4.1 Pressure Perturbation Equation

The differential equation describing the acoustic perturbations in a uniform, one-dimensional cylindrical duct is obtained by combining the mass (Eq. 2.30) and momentum (Eq. 2.31) equations of the LEE with the isentropic relation between pressure p and density ρ:

$$p' = c^2 \rho' \quad . \tag{2.37}$$

Along with the uniformity of the mean flow,

$$\nabla \bar{\phi} = \mathbf{0}, \quad \boldsymbol{u} = u_x \quad , \tag{2.38}$$

the partial differential equation

$$\frac{1}{c^2}\frac{\overline{D}^2 p'}{Dt^2} - \frac{\partial^2 p'}{\partial x^2} + \frac{\partial^2 p'}{\partial r^2} + \frac{1}{r}\frac{\partial p'}{\partial r} + \frac{1}{r^2}\frac{\partial^2 p'}{\partial \theta^2} = 0 \tag{2.39}$$

is obtained. The mean flow material derivative of a scalar reads

$$\frac{\overline{D}}{Dt} = \frac{\partial}{\partial t} + \bar{\boldsymbol{u}} \cdot \nabla \quad . \tag{2.40}$$

The analytical solution of this equation is outlined in the following section 2.4.2.

2.4.2 Analytical Solution

The analytical solution for the pressure perturbation equation 2.39 at an oscillation frequency of interest ω is the superposition of an, in general infinite, number of modes. Modes can be categorized in three types, longitudinal, tangential and radial, corresponding to the dimension along which their amplitude distribution varies primarily[2]. Each mode potentially contributes to the pressure fluctuations p' via its complex amplitude distribution, resulting in

$$p' = \sum_{m=0}^{\infty} \sum_{n=0}^{\infty} \hat{p}_{mn} \exp(i\omega t) \quad . \tag{2.41}$$

The index m denotes the tangential order of a mode, n is its radial order. The associated amplitude patterns will be addressed further below.

The complex pressure amplitude distribution in Eq. 2.41 is given by

$$\hat{p}_{mn} = P_{mn}(x) R_{mn}(r) \Theta_{mn}(\theta) \tag{2.42}$$

with its axial, radial and circumferential shape functions

$$P_{mn} = \bar{\rho} c \left(\hat{F}_{mn} \exp\left(-ik_{mn}^{x+} x\right) + \hat{G}_{mn} \exp\left(-ik_{mn}^{x-} x\right) \right) \tag{2.43a}$$

$$R_{mn} = J_m\left(k_{mn}^{r} r\right) \tag{2.43b}$$

$$\Theta_{mn} = A_{mn}^{\theta-} \exp\left(im\theta\right) + A_{mn}^{\theta+} \exp\left(-im\theta\right) \quad . \tag{2.43c}$$

$\hat{F}$ and $\hat{G}$ denote the complex amplitudes of the right and left running plane waves, J_m is the m^{th} Bessel function of first kind and $A_{mn}^{\pm}$ are the amplitudes of the counterclockwise and clockwise rotating circumferential contributions respectively.

The scalar wave number known from the one-dimensional solution of the non-convective Helmholtz Equation

$$k = \frac{\omega}{c} \tag{2.44}$$

is replaced by separate axial and radial wave numbers

$$k_{mn}^{x\pm} = \frac{k}{1 - Ma^2} \left(-Ma \pm \sqrt{1 - \left(\frac{k_{mn}^{r}}{k}\right)^2 \left(1 - Ma^2\right)} \right) \tag{2.45a}$$

$$k_{mn}^{r} = \frac{s_{mn}}{R} \quad . \tag{2.45b}$$

---

[2] As discussed later, the amplitudes of e.g. a cut-off tangential mode decreases in axial direction. However, within each cross-section the circumferential amplitude distribution is scaled by a constant factor and does not change qualitatively.

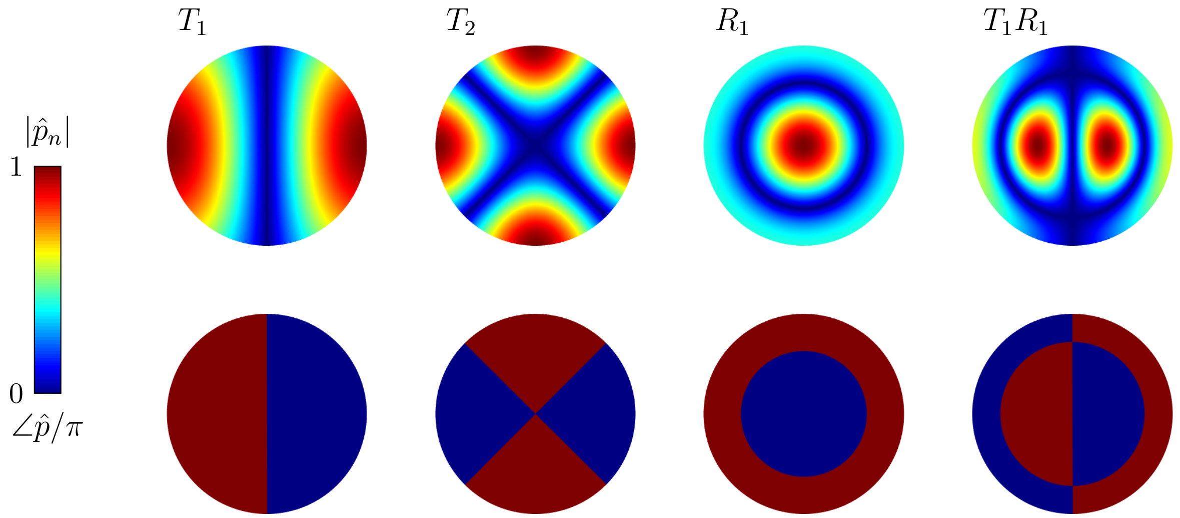

Figure 2.3: Cross-sectional complex pressure amplitude distribution; absolute value (top) and phase (bottom)

Ma denotes the Mach number of the mean flow, R is the duct radius and s_{mn} is the n^{th} root of the first derivative of J_m. For $Ma = 0$, the norm of the vector formed by these two wave numbers amounts to the value given by Eq. 2.44.

In this work the longitudinal, radial and transverse eigenmodes are referred to as L_i, R_n and T_m respectively with i, n and m the associated mode order. Besides the pure modes, combinations of all three can occur. The normalized cross-sectional pressure amplitude distributions are given by Eq. 2.42 and 2.43, independent of the up-and downstream boundary conditions. For selected pure and combined modes they are shown in Fig. 2.3.

The velocity fluctuations are obtained by inserting Eq. 2.41 into the linearized momentum equations. The solution structure follows Eq. 2.41 with

$$\hat{u}_{x,mn} = U_{x,mn}(x) R_{mn}(r) \Theta_{mn}(\theta) \tag{2.46a}$$

$$\hat{u}_{r,mn} = U_{r,mn}(x) \frac{dR_{mn}(r)}{dr} \Theta_{mn}(\theta) \tag{2.46b}$$

$$\hat{u}_{\theta,mn} = U_{\theta,mn}(x) \frac{R_{mn}(r)}{r} \frac{d\Theta_{mn}(\theta)}{d\theta} \quad . \tag{2.46c}$$

The axial functions in Eq. 2.46 are given by

$$U_{i,mn} = \zeta_{i,mn}^{+} \hat{F} \exp\left(-ik_{mn}^{x+} x\right) + \zeta_{i,mn}^{-} \hat{G} \exp\left(-ik_{mn}^{x-} x\right) \tag{2.47}$$

with

$$\zeta_{x,mn}^{\pm} = \frac{k_{mn}^{x\pm}}{k - Mak_{mn}^{x\pm}} \tag{2.48a}$$

$$\zeta_{r,mn}^{\pm} = \zeta_{\theta,mn}^{\pm} = \frac{i}{k - Mak_{mn}^{x\pm}} \quad . \tag{2.48b}$$

Besides the perturbations of velocity and pressure, their relation to the fluctuating energy is of relevance for the development of the stability analysis procedure, particularly for the mean flow calculation procedure (Sec. 4.2.2). In the following, the description of acosutic energy is illustrated for the currently discussed duct flow configuration. Many approaches have been taken to describe the energy associated with the flow perturbations. A rather general form is given by Myers [17]. For isentropic fluctuations along with constant sound speed the acoustic energy becomes

$$E' = \frac{p'}{2\eta_s} + \frac{\bar{\rho}}{2} \boldsymbol{u}' \cdot \boldsymbol{u}' + \frac{p'}{c^2} \bar{\boldsymbol{u}} \cdot \boldsymbol{u}' \tag{2.49}$$

with the isentropic compressibility

$$\eta_s = \frac{1}{\rho c^2} \quad . \tag{2.50}$$

The acoustic energy (Eq. 2.49) obeys the equation

$$\frac{\partial E'}{\partial t} + \nabla \cdot \boldsymbol{W}' = D' \tag{2.51}$$

with the acoustic energy flux vector $\boldsymbol{W}'$ and the source term D'. For purely acoustic perturbations (cf. Sec. 2.3.3) in isentropic, inviscid flow of an ideal gas they read

$$\boldsymbol{W}' = \bar{\rho} \bar{\boldsymbol{u}} \cdot \boldsymbol{u}' \boldsymbol{u}' + + \bar{\boldsymbol{u}} \bar{\boldsymbol{u}} \cdot \boldsymbol{u}' \rho' + p' \boldsymbol{u}' + \frac{1}{\eta_s} \bar{\boldsymbol{u}} p'^2 \tag{2.52}$$

$$D' = 0 \quad . \tag{2.53}$$

2.4.3 Implications for Rocket Combustion Chamber Acoustics

In rocket engine combustion instabilities longitudinal modes are typically of minor importance [5, 18]. The high mass flow leaving the nozzle leads to significant damping effects due to the convective transport of oscillation energy despite the generation of perturbations by the accelerated flow in the nozzle. Radial and transverse modes pose a more serious danger for engine stability. Most commonly, transverse oscillations are the source for critical instabilities, including the test case which this work focuses on.

The frequencies of the transverse modes are strongly connected to the axial wave number via the so-called cut-on frequency ω_{co}: The axial wave numbers (Eq. 2.45a) become complex below an oscillation frequency

$$\omega_{mn,co} = s_{mn} c \frac{\sqrt{1 - Ma^2}}{R} \tag{2.54}$$

as the squareroot term in Eq. 2.45a becomes negative. According to Eq. 2.43a a imaginary wave number leads to a spatial decay of the amplitudes in the direction of wave propagation. To visualize the evanescence of amplitudes the case of a T_1 mode with a purely right running plane wave ($\hat{G}_{10} = 0$ in Eq. 2.43a) and a standing circumferential amplitude distribution ($A^{\theta-}_{mn} = A^{\theta+}_{mn}$ in Eq. 2.43c) is considered. For $k^r_{mn}/k_m n = 1.16$ and a flow Mach number of $Ma = 0.1$ the resulting normalized pressure amplitude distribution is shown in Fig. 2.4. Three influencing factors can be identified that determine the cut-on frequency: first, the mode order via the Bessel derivative roots, which are shown in Fig. 2.5. With increasing radial and tangential order, the values of the roots increase and thus the cut-on frequency for the respective modes becomes higher. Second, the sound speed, which is governed by the combustion process via the local temperature and flow composition. Its axial distribution obtained as area weighted average across the chamber cross-section is shown for the cylindrical region of an H_2/O_2 engine with length l_c in Fig. 2.6. The last factor in Eq. 2.54 is mainly linked to the chamber's geometry. However, in the front part of the chamber, the radius is constant and the influence of combustion on the sound speed determines the development of the cut-on frequency. The initial region of

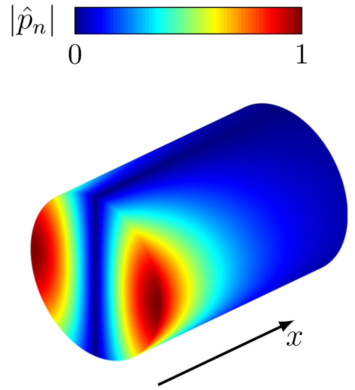

Figure 2.4: Cut-off T_1 mode

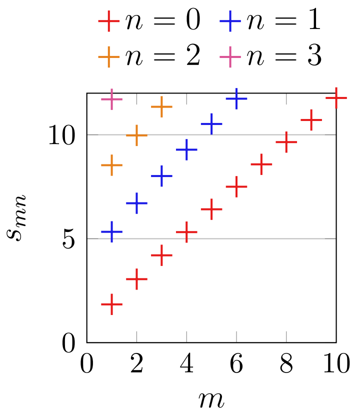

Figure 2.5: n^{th} root of dJ_m

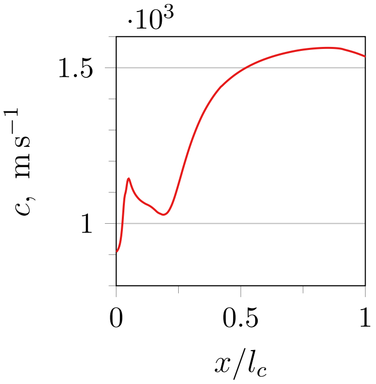

Figure 2.6: Sound speed profile

lower sound speed has been found to be decisive for the potentially unstable eigenmodes of the engine that is considered in the present work [12, 13]. The associated instability mechanisms are covered in Sec. 3.1.2. A T_1 mode can form at a frequency determined by the level of sound speed at this plateau but is cut-off further downstream, limiting the occurrence of high amplitudes to the region close to the faceplate [12, 13].

2.5 Flame Radiation Modeling

In the present work experimental radiation images are used to validate the single flame calculations. In this section, an overview over the fundamentals of radiation modeling from literature and previous works is given. The discussed principles and models are the basis on which a sound concept for the calculation of OH* radiation images for turbulent rocket engine flames is developed in Sec. 5.2, which is subsequently used for single flame validation in Sec. 5.3. Besides the OH* radiation around the center wavelength of $\lambda_c \approx 310\,\text{nm}$, the broadband blue radiation is characteristic for H_2/OT flames and of interest in the present work.

In the following, the basic concept of flame radiation modeling is introduced (Sec. 2.5.1). Submodels required for OH* emission (Sec. 2.5.2) and absorption (Sec. 2.5.3) calculations are outlined subsequently. Finally, blue radiation is covered in Sec. 2.5.4. A more detailed introduction to the topic of radiative transport and the absorption and emission mechanisms is given e.g. by Modest [19].

2.5.1 Radiation Description

The microscopic principle governing flame radiation is visualized in Fig. 2.7. For conciseness a simplified, quasi one-dimensional representation is chosen although the shown processes are in general isotropic. The radiation perceived by an observer is the result of emission and absorption along his line-of-sight. For the case of flame radiation, both processes are governed by different states of the fluid's molecules and the transition between these states. First, there is the ground state, which is the reference constitution of a species. In contrast, the excited state is energetically higher than the ground state. A molecule can be excited by different mechanisms, e.g. by the absorption of a photon or during a chemical reaction. When a molecule falls back from its excited to its ground state a photon is emitted at a wave number ν that is determined by the energy difference between both states. This mechanism is the source of flame radiation. Its modeling principles are discussed in Sec. 2.5.2 and Sec. 2.5.4. The reverse process, i.e. the excitation of a molecule due to absorption, reduces the perceived radiation (cf. Sec. 2.5.3). In general, multiple species contribute to emission and absorption. For the OH^* radiation calculations in the present work, however, it is sufficient to consider OH as emitting species. The blue radiation emission is addressed in Sec. 2.5.4. Concerning absorption, at most self-absorption

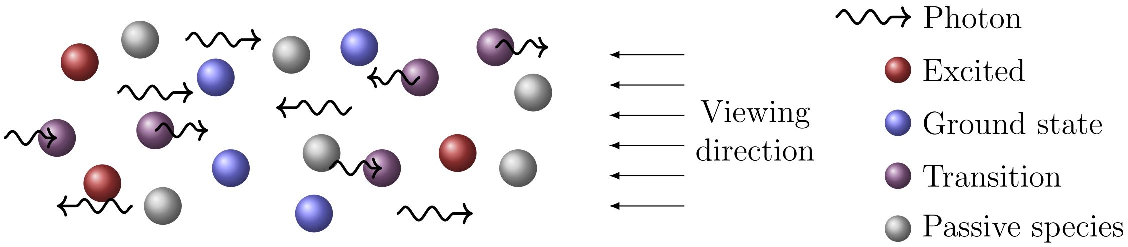

Figure 2.7: Radiation principle

is accounted for, which refers to absorption by the same species that is emitting radiation.

For the quantitative description of the radiation process, the spectral intensity I_s is used. It denotes the radiative energy flow per solid angle and unit area normal to the path as well as per a spectral variable s. Common choices for the spectral variable are the wavelength ($s = \lambda$) or the optical wave number ($s = \nu$). The experimental validation data used in the scope of the present work provide the integral value

$$I = \int_{\Delta s} I_s ds \tag{2.55}$$

with Δs the spectral range of interest. The conversion between wave length and wave number specific spectra can be obtained from the equality of the integral intensity of both descriptions (see App. B). The spatial development of the spectral intensity is described by the radiative transport equation. When considering a one-dimensional ray and a system that is steady with respect to radiative time scales ([20, 21]), this equation reads [19, 21]

$$\frac{\partial I_s}{\partial x} = -k_s I_s + e_s \quad . \tag{2.56}$$

Here k_s denotes the spectral absorption coefficient and e_s is referred to as spectral emission coefficient [19].

To evaluate Eq. 2.56 the absorption coefficient and the source term e_s need to be modeled. Approaches to calculate OH* emission are given in Sec. 2.5.2. Absorption is discussed in Sec. 2.5.3. The model derived by Fiala [21] for blue radiation is considerably simpler than that of OH* and is addressed separately in Sec. 2.5.4.

2.5.2 OH* Emission Modeling

The emission coefficient e_s constitutes the source term in the radiative transport equation, Eq. 2.56. There are several models available to calculate the local emission of OH* radiation. The classical model combines an emissivity with the black body radiation intensity to provide a quantitative estimation of the emission coefficient. A more basic approach is to assume proportionality of OH^* radiation to the OH^* concentration. Such a model provides a qualitative distribution without absolute intensity values. In this section, the classical approach is introduced, followed by an overview of different ways to obtain OH^* concentrations for the basic model. The relation between the different approaches will be discussed in Sec. 5.2.1.

2.5.2.1 Classical Gas Radiation Approach

The classical approach for gas radiation proposes [19]:

$$e_s = \varepsilon_s I_{b,s} \tag{2.57}$$

with the emissivity ε_s. $I_{b,s}$ is the spectral black body radiation intensity, which for the wave number as spectral variable ($s = \nu$) reads

$$I_{b,\nu} = \frac{2hc_l^2}{\nu^3}\left(\exp\left(\frac{hc_l\nu}{k_BT}\right) - 1\right)^{-1} \quad . \tag{2.58}$$

The index ν denotes that the radiation is given wave number specific. The term c_l refers to the speed of light, k_B is the Boltzmann constant and h the Planck constant. Under local thermodynamic equilibrium Kirchhoff's law is valid, stating

$$\varepsilon_s = k_s \quad , \tag{2.59}$$

i.e. the emissivity equals the absorption coefficient, which is discussed in Sec. 2.5.3.

2.5.2.2 OH* Concentration Approach

The second type of emission models assumes proportionality between OH^* concentration and emission. It only requires the calculation of spatial distribution of OH^*, which is discussed in the following.

Two effects lead to the emission of OH^*-radiation: thermal and chemical excitation. According to the summary given by Fiala [21, 22] the dominant chemical excitation mechanism is the combination of atomic hydrogen and oxygen during collision with a third body Q:

$$\mathrm{O} + \mathrm{H} + \mathrm{Q} \rightleftharpoons \mathrm{OH}^* + \mathrm{Q} \quad . \tag{2.60}$$

The second contribution to the OH* formation is the thermal excitation or, contrary, quenching of OH* by the collision with other molecules, which can be modeled as

$$\mathrm{OH} + \mathrm{Q} \rightleftharpoons \mathrm{OH}^* + \mathrm{Q} \quad . \tag{2.61}$$

Fiala [21] studied the importance of both mechanisms by comparing the reaction rates occurring in one-dimensional counterflow diffusion flames. At high temperatures thermal excitation rates clearly exceed the chemical ones. The cross-over temperature where thermal excitation becomes dominant lays between about 2500 K and 2900 K, depending on the used reaction mechanism. Basis of the used reaction description was the H_2/O_2 mechanism by Ó Conaire et al. [23], patched with the rate coefficients for chemical OH* formation (Eq. 2.60) by Kathrotia et al. [24] as well as the coefficients for thermal quenching (Eq. 2.61) provided by Tamura et al. [25]. However, as pointed out by Fiala the rate coefficients for the chemical formation of OH* are subject to high uncertainty. Likewise the set of thermal excitation or quenching reactions has been calibrated for lower temperatures only with no solid data available for the high temperature range.

The explicit calculation of the OH* concentration from a reaction mechanism using Eq. 2.60 or Eq. 2.61 has been termed the Detailed Chemistry Radiation Model by Fiala et al. [22]. While this is a rather detailed model to obtain the OH* distribution, several approaches have been proposed to simplify this procedure. In the most basic case, the OH* distribution is approximated by ground state OH [26]. A more elaborate approach is the Equilibrium Filtered Radiation Model (EFRM-A)[3] proposed by Fiala et al. [22]. It is based on chemical equilibrium

$$\frac{[\mathrm{OH}^*]}{[\mathrm{OH}]} = \exp\left(-\frac{\Delta^* \mu^0_{OH}}{R_m T}\right) \sim \exp\left(-\frac{h c_l}{k_B \lambda T}\right) \tag{2.62}$$

---

[3] Fiala used the term EFRM to referr to the emission model and EFRM-A for a combination of the EFRM with self-absorption. As in the present work only the case including self-absorption is of relevance, the term EFRM-A is used all over in favor of a concise nomenclature.

with $\Delta^* \mu^0_{OH}$ denoting the difference of standard state Gibbs free energy between excited and ground state OH. The proportionality relation in Eq. 2.62 has been introduced by Fiala [21, 22] based on the assumption of thermal excitation of a single state with the corresponding wave length λ. Practically, Eq. 2.62 is evaluated at the center wave length λ_c of the considered spectrum.

2.5.3 Absorption and Net Emission

The solution of the radiative transport Equation 2.56 as well as the evaluation of the classical gas phase emission coefficent (Eq. 2.57) requires knowledge of the absorption coefficient. An extensive number of absorption data is given in the HITRAN database [27]. The data are provided as spectral line intensities S_{ref} at reference conditions, from which the corresponding values S at the state of interest are calculated as described by Rothman et al. [28]. However, in a spectrum the absorption lines are not sharp but rather blurred around their peak wave number. Data for two mechanisms that contribute to the blurring, pressure broadening (described by a Lorentz profile) and Doppler-broadening (modeled as Gaussian curve), are provided in HITRAN. The superposition of both contributions is described via a Voigt profile $\mathcal{V}$ leading to

$$k_{mol} = \mathcal{V} S \quad . \tag{2.63}$$

The resulting quantity is a spectral absorption coefficient per molecule, k_{mol}, which can be converted to the spectral absorption coefficient via

$$k = k_{mol} N_A \left[OH^* \right] \tag{2.64}$$

with the Avogadro constant N_A and the molar OH* concentration $[OH^*]$.

The net emission from a volume of spatially constant absorption and emission coefficient can be evaluated analytically from Eq. 2.56 [21] yielding

$$I_s = \frac{e_s}{k} \left[1 - \exp\left(-k \left(x - x_0 \right) \right) \right] + I_{\nu,0} \exp\left(-k \left(x - x_0 \right) \right) \quad . \tag{2.65}$$

Here $I_{s,0}$ denotes the intensity of the radiation entering the domain (at coordinate x_0) and x the one-dimensional coordinate of the radiation path.

The net emission is given by the first term in Eq. 2.65 while the second term represents the radiation transmitted through the volume. For large distances $x - x_0$ the net emission approaches the value e_s/k and the transmitted emission becomes zero. For the classical gas phase radiation model Eq. 2.65 can be reformulated using Eq. 2.57 to give

$$I_s = I_{b,s} + (I_{s,0} - I_{b,s}) \exp\left(-k_s (x - x_0)\right) \quad , \tag{2.66}$$

i.e. in the long distance limit the spectrum exiting the uniform volume approaches that of a black body.

For the EFRM-A model Fiala proposed a combination of the wave-length independent emission described in the previous section and an absorption model, where a set of reduced absorption coefficient

$$k_r = \frac{k}{[\mathrm{OH}]} \tag{2.67}$$

is fitted to approximate the relation

$$\frac{dI}{I} = -k_{r,i}[\mathrm{OH}]x \quad . \tag{2.68}$$

2.5.4 Blue Radiation

While originating from chemiluminescence, the exact source of blue radiation is subject to some uncertainty. Fiala [21] refers to the works of Diederichsen et al. [29], Gaydon [30] and the later studies of Padley [31] and Vanpee et al. [32] to identify two potential reactions leading to the excited states emitting blue radiation:

$$\mathrm{OH} + \mathrm{H} \longrightarrow \mathrm{H_2O}^* \tag{2.69a}$$

$$\mathrm{OH} + \mathrm{OH} \longrightarrow \mathrm{H_2O_2}^* \quad . \tag{2.69b}$$

From spatially resolved radiation images, the reaction Eq. 2.69b is identified to better describe the flame structure [21]. For the qualitative emissions of blue radiation, the relation

$$e_{blue} \sim [\mathrm{OH}]^2 \tag{2.70}$$

is proposed. As the flame is optically thin with respect to the blue radiation, no absorption needs to be considered, yielding simple line of sight integration as appropriate for obtaining the flame image:

$$I_{blue} = \int_{x_0}^{x} e_{blue} d\check{x} \quad . \tag{2.71}$$

The blue radiation modeling according to Eq. 2.70 and Eq. 2.71 is used for the radiation based single flame validation in Sec. 5.3.4.

3 Test Cases

Three test cases are studied in the present thesis for various purposes. The combustion chamber D (BKD), an H_2/O_2 combustion chamber run at the German Aerospace Center (DLR), is the most important one. It is used for the validation of the stability assessment procedure in Chap. 6 to 8 as well as the evaluation and calibration of the single flame simulations in Sec. 5.3. In contrast, the virtual demonstrators TCD2 and TCD3 are thrust chamber concepts designed by ArianeGroup that feature key aspects of next generation main stage rocket engines. The TCDs will be used to evaluate the relevance of the nozzle correction for the acoustic predictions in Sec. 6.2. The numerical setup used for the simulation of the test cases is given in Sec. 5.1. In the present section, the specifications of the different configurations are introduced, starting with BKD (Sec. 3.1) and followed by the TCDs (Sec. 3.2).

3.1 BKD

The BKD, shown in Fig. 3.1, is the main test case in the present work, used for the development and validation of the stability assessment procedure. It is a multi-element H_2/O_2 rocket combustion chamber operated on a test bench at the DLR. Its performance parameters fall within the lower range of upper-stage engines [33]. Several load points have been tested, some of them thermoacoustically stable whereas others showed self-excited combustion instabilities. The geometry and operating conditions relevant for the present work are specified in Sec. 3.1.1. An overview of the various BKD studies dealing with combustion stability is given subsequently (Sec. 3.1.2).

3.1.1 Specifications

The BKD is composed of the injection system, a cylindrical chamber section and the nozzle (Fig. 3.1a). The main dimensions are listed in Tab. 3.1a. Due to the focus of the present work on the chamber acoustics, only the convergent part of the nozzle is considered. The primary instrumentation is contained in a measurement ring close to the faceplate.

The injection head (Fig. 3.1b) comprises 42 elements through which H_2 and O_2 are injected coaxially. The element geometry is specified in Fig. 3.1c and Tab. 3.1b, the oxidizer dome is shown in Fig. 3.1a with its dimensions given in Tab. 3.1c. The cylindrical volume at the center of the dome belongs to the ignition system.

Table 3.1: BKD specifications

(a) Combustion chamber

cylinder section		nozzle section		film cooling slot		
⌀	length	⌀ throat	length	r inner	r outer	sector angle
80	225.5	50	48.8	39.95	40.45	29°

† lengths given in mm

(b) Injectors

common		oxidizer							fuel	
no.	rec	⌀			length		taper angle	bevel	⌀	
		post	mouth	thr	post	thr			inner	outer
42	2	3.6	3.7	1.9	68	3.1	20°	0.3×45°	4	4.5

† lengths given in mm

(c) Oxidizer dome

height	⌀		
	base	upper	igniter
14.4	74.8	46	12

† lengths given in mm

(d) Instrumentation

dynamic pressure		static pressure			window	
x	angular offset	x			⌀	x
5.5	45°	5.5	80.5	125.5	18	8

† lengths given in mm

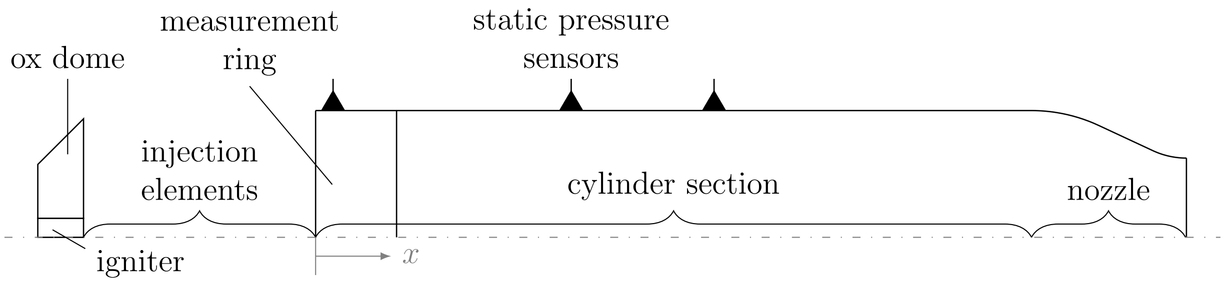

(a) Longitudinal sketch

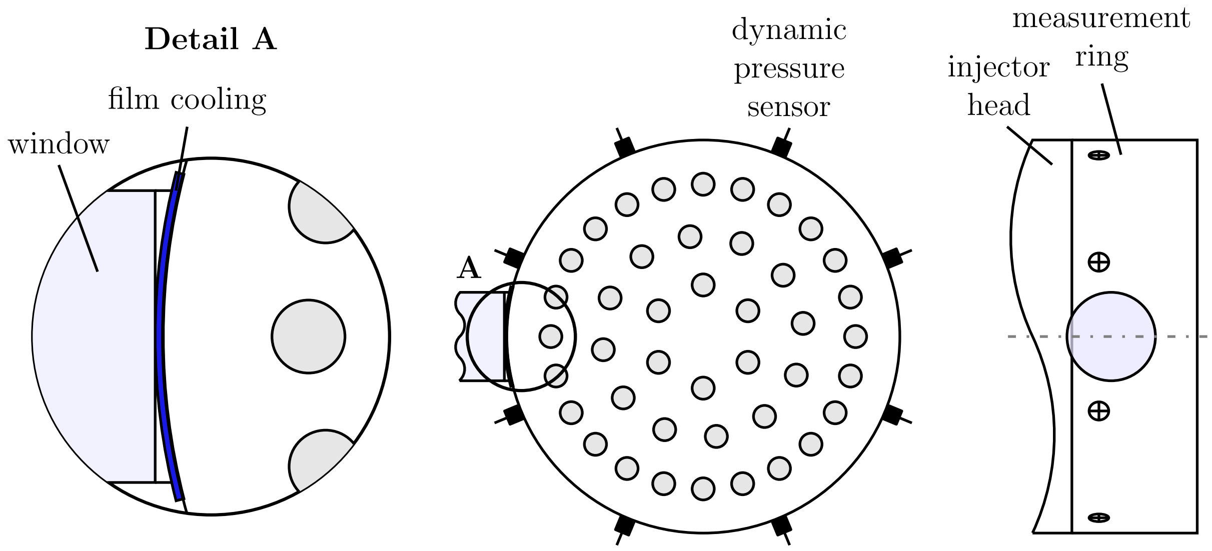

(b) Injection pattern and measurement ring

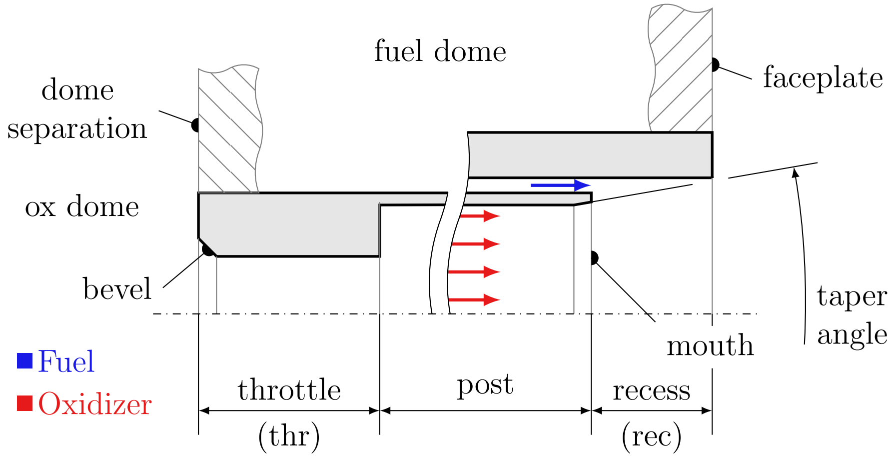

(c) Injector element

Figure 3.1: BKD combustion chamber geometry

Table 3.2: Operating points with optical window access

	stability	p_c, bar	$O/F^\dagger$	$\dot{m}$, $\mathrm{kg\,s^{-1}}$			T, K		
				O_2	$H_2^\dagger$	$film$	O_2	H_2	$film$
LP1	stable	51.39	5	3.4	0.68	0.043	114.4	102.4	290
LP2	unstable	81.35	4.92	5.37	1.09	0.043	112.7	103.4	292

†excluding film cooling

The measurement ring (Fig. 3.1b) comprises eight dynamic pressure sensors and fiber optical probes for measuring OH* radiation. In later experiments, an optical access window has been added to allow the recording of 2D flame radiation images. The window is film-cooled with hydrogen that is injected at the outer side of the injector head (cf. Fig. 3.1b and Tab. 3.1a). A notch in the chamber wall initially gives room to the coolant flow and starts bending towards the regular chamber diameter at an angle of about 1.8°, 18.8 mm downstream of the face plate. Three static pressure sensors are placed along the chamber wall. The instrumentation specifications that are relevant in the present work are summarized in Tab. 3.1d. Further information can be found in the publication of Armbruster et al. [6].

Numerous load points have been investigated for the BKD (cf. Sec. 3.1.2) with typical operating pressures lying between 50 bar and 80 bar. In this work, the operating points of a newer measurement campaign [6] are considered as these feature optical window access to the flame that allows for additional validation of the simulated flame structure. The specifications of these load points, a stable one at a chamber pressure of about 50 bar and an unstable one at about 80 bar, are given in Tab. 3.2[1]. To assess the state of the propellants at injection, their crtitical points are given in Tab. 3.3. As can be seen from Fig. 3.2 the injection conditions of H_2 are clearly supercritical whereas O_2 is injected in a transcritical state for LP2. For LP1 the O_2 injection temperature is subcritical, while the chamber pressure is only slightly higher than the critical pressure of O_2.

---

[1] Note that the load point IDs have been reused in different experimental studies [6, 33], which is why LP1 and LP2 covered here are not identical to those provided for previous test-runs although they share the same name.

Table 3.3: Propellant critical points

	O_2	H_2	CH_4
p_c, bar	50.4	13.0	46.1
T_c, K	154.6	33.2	190.6

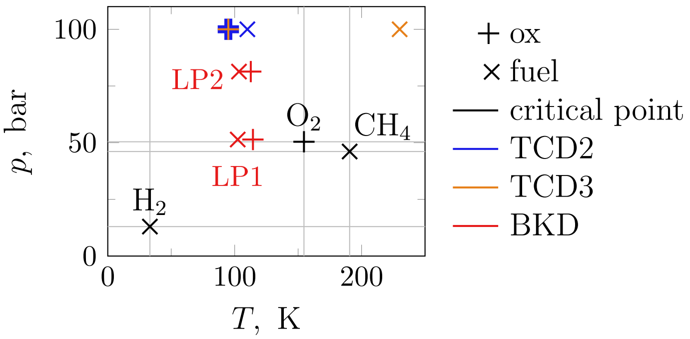

Figure 3.2: Injection conditions

3.1.2 Previous Studies

The thermoacoustic behavior of the BKD has been subject to both numerical and experimental studies. To provide the research context for the present work's results in terms of the BKD's acoustic behavior, an overview of the findings from previous studies is given in the present section, starting with the experiments and followed by the modeling approaches.

A characterization of the BKD stability behavior for several load points is conducted by Gröning et al. [34], focusing on different mixture ratios and chamber pressures. The study also contains an overview of several post-processing approaches that are used to extract information from the experimental BKD data. The T_1 mode is found to be dominant whenever an instability occurs. An analysis of the mode orientation shows a spinning behavior with a varying character of rotation, where unstable load points tend to show more standing behavior. In a subsequent study [35] the impact of the fuel temperature on the chamber stability is considered by varying the mixture ratio and chamber pressure for two different hydrogen temperatures. The impact of the chamber pressure on the eigenfrequencies is found to be minor compared to that of hydrogen temperature and mixture ratio. The reason is the different sensitivity of the sound speed in the combustion chamber to these parameters. Regarding the instability mechanism, a coupling with the oxygen injection system is brought up. Moreover, significant oscillations, termed x-modes, are found at frequencies that cannot be associated with certain cylinder modes. These eigenfrequencies show a different dependence on the operating conditions than the identified cylinder modes and are reckoned to possibly originate from the hydrogen manifold. Concerning the stability behavior no clear correlation with the hydrogen temperature is identified. However, the finding that unstable modes tend to become more standing is confirmed. A more extensive study on the role of hydrogen temperature [36,37] is conducted by means of an injection temperature ramping test. It is found that the impact of the hydrogen temperature on the sound speed distribution in the chamber is a dominant factor for the chamber eigenfrequencies. The possiblity of the x-modes originating from the hydrogen injector is ruled out [37]. The source of instabilities in the BKD is studied further [33]. By evaluating data obtained from the optical probes along with the dynamic pressure measurements, a mechanism deciding about (in)stability is determined: Resonances in the oxygen injectors lead to oscillations of the heat release in the flame. Consequently, the frequency of these oscillations depends on the injector length and the sound speed of the oxygen but is rather independent of the processes in the combustion chamber. If an eigenfrequency of the combustion chamber coincides with one of the heat release frequencies, pressure amplitudes in the chamber increase, indicating an unstable load point. This mechanism is pointed out to be consistent with the impact of the fuel temperature on the stability behavior since chamber eigenfrequencies, and thus the agreement between heat release and pressure fluctuation frequencies [36], depend on the hydrogen temperature. An analysis [38, 39] of the phase differences of the OH* and pressure signals for the T_1 mode confirms a frequency offset between both signals. When analyzing short time-windows the phase offset is found to cluster around zero for an unstable load point while a stable case shows a more even distribution of phase differences. The role of the injector dynamics is studied further by Armbruster et al. [6]. They install the optical access window and analyze 2D OH* and blue radiation flame images. A DMD analysis reveals longitudinal structures in the flame dynamics of an unstable load point, supporting the suggested role of the injectors in the destabilization of combustion. In this context, hydrodynamic instabilities at the throttle are found to excite the injector acoustics. However, in contrast to previous test runs the heat release fluctuations at the injector eigenfrequencies, which were discussed above, were not found for the stable load point considered in this study.

Besides the experimental studies, several numerical approaches have been undertaken to reproduce and explain the stability behavior of the BKD. This paragraph gives an overview of works based on Large Eddy Simulations (LES), findings obtained with hybrid methods are covered subsequently. A preliminary LES study of a single flame[2] as well as the full configuration on a coarse mesh have been conducted for an unstable load point by Urbano et al. [40, 41]. The results show a reasonable overall agreement despite a slight underestimation of the mean chamber pressure and an overestimation of the propellant domes' pressures. The T_1 mode is clearly visible at a frequency close to the experiment, however no instability occurrs for the in fact unstable load point. Even after exciting the domain, the acoustic fluctuation decay quickly. Nevertheless, acoustic coupling between the chamber T_1 and the oxygen injectors is found, particularly at the outer injection ring with the injector L_2. A finer mesh is used in a subsequent study [42], yet not reaching the target mesh size proposed in the previous studies. Two load points, a stable and an unstable one are considered. Both are predicted to be linearly stable by the LES. However, with sufficiently strong initial perturbation, a limit cycle is reached for an unstable load point with a pressure RMS of about 15 % of the chamber mean pressure. For both cases, the T_1 mode is predicted to be standing. Again, coupling between the chamber T_1 and the oxygen injectors occurs. A solution of the Helmholtz equation in the chamber agrees well with the mode shapes and frequencies extracted from the LES. An analysis of the individual flames reveals that the heat release fluctuations in flames located at the pressure anti-node are significantly stronger than those observed in the nodal region, indicating a correlation between the pressure and heat release fluctuations. However, the authors of the study point out that this does not necessarily imply that the pressure fluctuations themsevlves are driving the flame response. The mean contribution to the Rayleigh index of the chamber occurs in the initial flame region close to the face plate. Further analysis of the simulated

---

[2] In contrast to the present work (cf. Sec. 5.1.4), a downscaled version of the chamber nozzle has been included in the single flame domain.

limit cycle [43] addresses heat release fluctuations and Rayleigh indices of individual flames. It is found that, at equal fluctuation amplitudes relative to the respective mean velocity, the flame is more sensitive to velocity fluctuations at the hydrogen than at the oxygen injector mouth. The proposed instability mechanism is that the pressure fluctuations in the front region of the chamber give rise to velocity fluctuations at the hydrogen injector which drive a shear layer instability. An assessment of the role of the individual flames not only in terms of driving but also damping [44] shows that all flames are driving the instability with the strongest contributions coming from flames close to a pressure antinode. At the same time the flames from the inner two injector rings contribute to the damping in the chamber, predominantly those close to a pressure node. A comparison of the T_1 and R_1 mode showed that despite weaker driving, the R_1 amplitudes are similar to those of the T_1 due to different damping. Schmitt et al. [45] has studied another stable load point along with an unstable counterpart with higher hydrogen injection temperature. The LES shows a self-excited instability, however the experimentally stable load point is predicted to be unstable and vice versa.

A different approach has been followed by Kaess et al., who studied the BKD using the tool PIANO-SAT to solve the LEE in time domain for stable and unstable conditions on a quasi one-dimensional mean flow. The flame response is extracted as function of pressure oscillations from a single flame CFD simulation. While the oscillation frequencies are reasonable, the stability behavior is not captured correctly, with both load points being predicted to be stable.

3.2 Virtual Thrust Chamber Demonstrators

To study the impact of the flow acceleration in the nozzle on the mean flow and the associated chamber acoustics (cf. Sec. 6.2), several virtual Thrust Chamber Demonstrators (TCDs) are employed as test cases. The TCDs are three engine concepts specified by ArianeGroup to feature key technologies for next generation rocket engines. Regarding thermoacoustic stability, two of the configurations can be considered to be critical. TCD2 [46] is an H_2/O_2 engine designed with a lower than usual injection pressure loss. While this reduces the power requirements of the turbopumps, the potential for acoustic coupling between chamber and feed system increases. One central aspect of TCD3 [47] is its fuel flexibility. Besides H_2/O_2 it shall also be operational with the propellant combination CH_4/O_2. As CH_4 combustion is in general more susceptible to instabilities than H_2 flames, the methane load point of TCD3 is considered as second relevant demonstrator test case.

Both TCDs represent main stage engines with about 1000 kN of thrust and a gas generator engine cycle. The combustion chamber geometries and main dimensions are given in Fig. 3.3 and Tab. 3.4. The BKD is shown for comparison. The injection patterns are shown in Fig. 3.4a. Both cases are designed with a high number of 396 and 468 injection elements respectively, shown in Fig. 3.4b with the dimensions given in Tab. 3.5. Note that for the TCDs the bevel is at the opposite side of the throttle compared to the BKD (Fig. 3.1c). The higher number of injection elements for TCD3 fits into nearly the same chamber diameter as TCD2 due to the significantly smaller size of the slit for fuel injection, while the diameter of the oxygen mouth changes only weakly. The operating conditions are given in Tab. 3.6. The nominal chamber pressures are at 100 bar and oxygen is injected transcritical, the respective fuel at supercritical conditions (Tab. 3.3, Fig. 3.2).

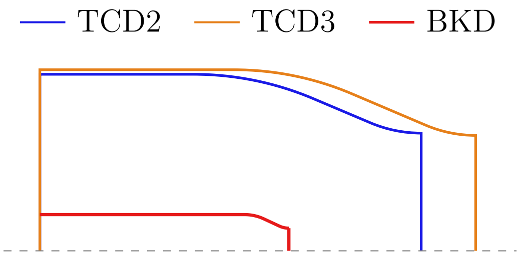

Figure 3.3: TCD chambers

Table 3.4: TCD chamber specifications

	cylinder section		nozzle section	
	⌀	length	⌀ throat	length
TCD2	390	169	260	251
TCD3	400	213.2	255	266.8

† lengths given in mm

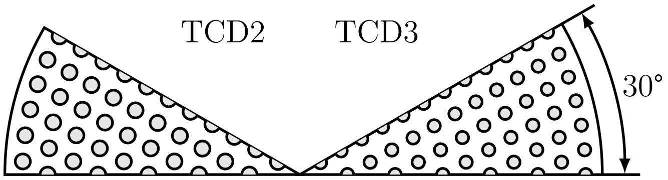

(a) Injection pattern

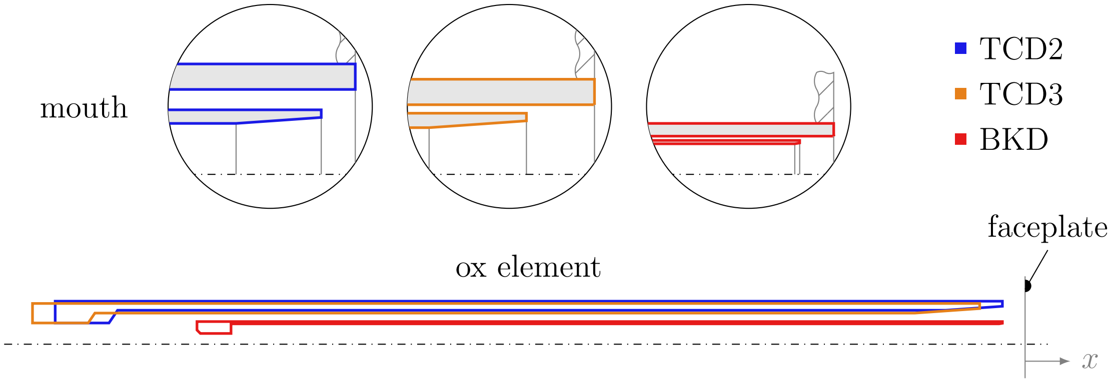

(b) Injection elements

Figure 3.4: TCD injection systems

Table 3.5: TCD injection system specifications (see also Fig. 3.1c)

	common		oxidizer							fuel	
			⌀			length		taper angle	bevel (aperture)	⌀	
	no.	rec	post	mouth	thr	post	thr			inner	outer
TCD2	396	2	6	6.7	3.75	78	5.5	8°	112°	7.6	10
TCD3	468	4	5.5	6.3	3.75‡	78‡	5.5‡	8°	112°	7.2	8.2

† lengths given in mm   ‡ not specified for TCD3; taken from TCD2

Table 3.6: TCD operating conditions

	propellants	p_c, bar	O/F	$\dot{m}$, kg s^{-1}		T, K	
				ox	*fuel*	*ox*	*fuel*
TCD2	H_2/O_2	100	6	194.3	32.4	95	110
TCD3	CH_4/O_2	100	3.4	218.55	64.28	95	230

4 Stability Assessment Procedure

In the present chapter the concept of the stability assessment procedure is outlined. The method is designed to determine the acoustic behavior of the type of configuration discussed in Sec. 2.1. It takes into account the characteristic acoustic behavior of a rocket combustion chamber as covered in Sec. 2.4.3. In the following, the overall structure of the procedure is outlined before its main components are discussed in more detail. The highly test case specific single flame simulations are covered separately in Sec. 5.1. This makes it easier to apply the methodology to a wider range of cases by selecting the flame simulation details to meet the requirements of the respective operating conditions and injector design. The analysis of the procedure by means of the test cases of the current work (Chap. 3) is conducted in Chap. 6 to 8.

The stability prediction is carried out as an eigenvalue analysis of the perturbed chamber flow where the imaginary part of the complex eigenfrequency characterizes the stability behavior. The computationally lean stability assessment relies on a hybrid methodology, i.e. mean state, flame response and finally perturbations are calculated separately from each other. This way the different simulations can be optimized in terms of computational domain, grid resolution and modeling complexity to cover only the sub-processes that characterize the respective model component. Calculating the acoustics of the chamber requires to include the whole chamber volume into the computational domain, whereas the combustion dynamics are characterized using a single flame. However, to obtain the flame response the local flow dynamics and mixing need to be accurately resolved, while the acoustic length scales are of the same order as the chamber dimensions and thus can be computed on a much coarser grid using a simplified mean flow.

An overview of the stability assessment procedure is given in Fig. 4.1. It is organized in four components:

- Mean flow
- Flame response
- External components
- Stability computation

The connecting part is the stability computation of the chamber by means of a perturbation analysis. This step requires the results from the other three components. The mean flow (Sec. 4.2) is the reference state for which the perturbation analysis is carried out. It is modeled as quasi one-dimensional and based on the radially averaged properties of a single flame simulation. The flame response (Sec. 4.3) characterizes the feedback of the flame when exposed to acoustic perturbations. It is obtained from an artificially excited single flame simulation that requires eigenfrequencies and pressure amplitude distributions from an acoustic analysis without flame feedback as input. Finally, external components can be coupled to the acoustic analysis. Absorbers or the injection system are modeled as impedance boundary conditions or scattering matrices to capture their impact on the oscillations in the numerically resolved chamber parts. In the following, the stability assessment procedure components are discussed in more detail, starting with the perturbation modeling for the acoustic analysis (Sec. 4.1), followed by the calculation of the mean flow (Sec. 4.2) and finally the flame response (Sec. 4.3). The present work focuses on these main components. Considering the open issues addressed in this thesis, dome coupling is of minor importance and not considered further in favor of a concise analysis (cf. Sec. 4.1.2.1). An analysis of the impact of absorbers on the chamber acoustics has been given elsewhere [48].

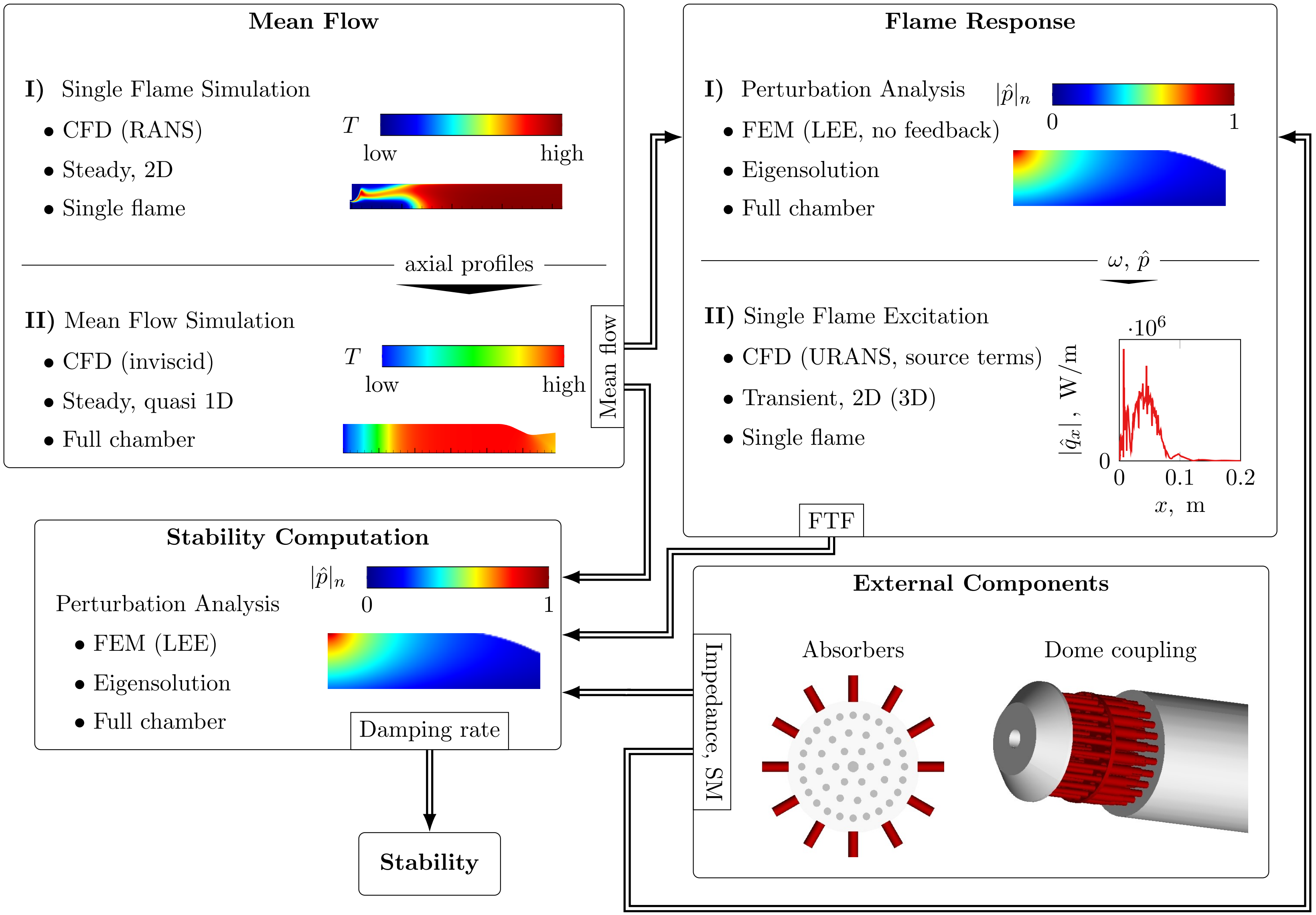

Figure 4.1: Schematic of stability assessment procedure

4.1 Perturbation Analysis

The stability assessment procedure contains two simulations of the chamber acoustics. One is the final step of the stability calculation, in which the modal damping rate is obtained. The other one provides mode shape and oscillation frequencies for the excitation simulations that are used to characterize the flame response (cf. Sec. 4.3). The acoustic simulations are actual perturbation analyses that solve the LEE (Eq. 2.30, 2.31 and 2.36) on a domain covering the whole chamber (cf. Sec. 4.1.2). In this section, the modal analysis that is used for the characterization of the chamber acoustics is introduced along with the Bloch ansatz, which allows to conduct the acoustic simulations in two-dimensions (Sec. 4.1.1). The numerical treatment and selection of boundary conditions are given in Sec. 4.1.2. The calculation of the mean flow is discussed in Sec. 4.2. Perturbation simulations are conducted for the passive acoustic characterization (Chap. 6) and the final stability assessment (Chap. 8).

4.1.1 Modal Analysis

The chamber's acoustics and stability behavior are obtained in form of a modal analysis. The analysis is conducted to either characterize the chamber's passive acoustics or to calculate the stability prediction including the flame response. The difference between both cases is the specification of the heat release fluctuations on the RHS of the pressure fluctuation equation 2.36. For the passive characterization the heat release fluctuations are set to zero. For the stability computation they need to be included. The direct representation of the heat release fluctuations using the linear enthalpy of formation fluctuations (Eq. 2.35) is not applicable. The main reason is that the acoustic analysis is carried out for a simplified mean flow (cf. Sec. 4.2). The flames are not resolved individually, so perturbations of the detailed flow patterns required for the evaluation of the enthalpy of formation balance equation 2.25 are not available. Instead, the flame response is modeled via a flame transfer function that is obtained based on single flame simulations as described in Sec. 4.3.

The perturbation calculations are carried out as eigensolution study in frequency space. Each eigensolution corresponds to a chamber mode with the eigenvector representing the complex perturbation amplitudes ($\hat{\phi}$) of the flow fields. The associated complex eigenfrequency consists of the real valued oscillation frequency ω and the damping rate α:

$$\Omega = \omega + i\alpha \quad . \tag{4.1}$$

The damping rate denotes the exponential decay of the oscillation amplitude in time and ultimately determines the modal stability behavior with $\alpha \geq 0$ indicating a stable mode and vice versa. Combining complex amplitude and frequency gives the fluctuations of a quantity ϕ as

$$\phi' = \hat{\phi} \exp(i\Omega t) \quad . \tag{4.2}$$

An eigenvector can be scaled by a non-zero constant and remains an eigenvector. Thus the obtained complex amplitude distributions describe the relative distribution of the fluctuations in the field but do not provide an absolute scale of the occurring oscillations.

The modal analysis requires a transformation of the time domain equations 2.30, 2.31 and 2.36 into frequency space, which is done via a Fourier-transform. In this process, the structure of the equations is retained with the perturbations quantities ϕ' being replaced by their complex amplitudes $\hat{\phi}$ and the time derivative $\partial/\partial t \phi'$ by the frequency space pendant $i\Omega\hat{\phi}$. The perturbation description can be further simplified by taking advantage of the circumferential structure of the acoustic solution in a cylindrical duct flow (cf. Sec. 2.4.2, Eq. 2.43c), following the Bloch approach [49]. Thereto, the complex amplitude is replaced by its two-dimensional distribution $\tilde{\phi}$ in a reference plane combined with an analytic ansatz for its azimuthal dependence:

$$\hat{\phi} = \tilde{\phi} \exp(im\theta) \tag{4.3}$$

with m the transverse order of the mode of interest. Experimentally, the circumferential distribution of the pressure fluctuations has been found to correspond well to the duct flow solution as well, so the analytic ansatz Eq.

4.3 is considered a reasonable approximation even for the non-isentropic and non-uniform case. Solving for $\tilde{\phi}$ instead of $\hat{\phi}$ allows to perform the perturbation calculations on a two-dimensional domain even for modes with transverse character.

The actual amplitude distributions can be reconstructed from the two dimensional solution during post-processing. Due to the positive sign of the exponent, the ansatz of Eq. 4.3 corresponds to a clockwise rotating mode (cf. Eq. 2.43c). However, the general circumferential distribution consists of clockwise and counter-clockwise rotating modes. As the mean flow is swirl-free, the only equation that contains derivatives in circumferential direction is the circumferential momentum equation:

$$i\Omega\hat{\boldsymbol{u}}_\theta + \bar{u}_r\frac{\partial \hat{u}_\theta}{\partial r} + \frac{\bar{u}_r}{r}\hat{u}_\theta + \bar{u}_z\frac{\partial \hat{u}_\theta}{\partial z} = -\frac{1}{\rho}\frac{\partial \hat{p}}{\partial \theta} \quad . \tag{4.4}$$

Noting that

$$\frac{\partial\Theta^-/\partial\theta}{\Theta^-} = -\frac{\partial\Theta^+/\partial\theta}{\Theta^+} = im \quad , \tag{4.5}$$

it can be concluded that for the left- and right-turning contributions the following is valid:

$$\hat{\phi}^+ = \begin{cases} \hat{\phi}^-, & \phi \neq \hat{u}_\theta \\ -\hat{\phi}^-, & \phi = \hat{u}_\theta \end{cases} \quad . \tag{4.6}$$

Thus the correct reconstruction of the circumferential velocity amplitude as superposition of left and right rotating mode is

$$\hat{u}_\theta = -\frac{i}{m}\tilde{u}_\theta\left(A^{\theta-}_{mn}\exp(im\theta) - A^{\theta+}_{mn}\exp(-im\theta)\right) \quad , \tag{4.7}$$

while it is

$$\hat{\phi} = -\frac{i}{m}\tilde{\phi}\left(A^{\theta-}_{mn}\exp(im\theta) + A^{\theta+}_{mn}\exp(-im\theta)\right) \tag{4.8}$$

for all other perturbation variables.

4.1.2 Numerical Setup

The perturbation analysis consists of an eigensolution study based on the LEE (Sec. 2.3). The equations 2.30, 2.31 and 2.36 are solved using the sta-

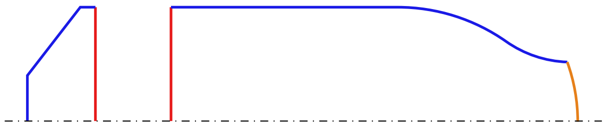

Figure 4.2: Domain for perturbation simulation

Table 4.1: Perturbation boundary conditions

color	type	specification
🟦	wall	$\hat{\boldsymbol{u}} \cdot \boldsymbol{n} = 0$
🟥	A) inlet	$\hat{\rho}\bar{\boldsymbol{u}} \cdot \boldsymbol{n} + \hat{\boldsymbol{u}}\bar{\rho} \cdot \boldsymbol{n} = 0$ $\hat{s} = 0$
	B) interface	scattering matrix
🟧	outlet	$\hat{p} = 0$

bilized finite element method with the software COMSOL Multiphysics®. The present section starts with the introduction of the computational domain and boundary conditions. Thereafter the aspect of flow stabilization is addressed.

4.1.2.1 Computational Domain and Boundary Conditions

The computations are carried out for the whole combustion chamber, represented as two-dimensional axis-symmetric domain (cf. Sec. 4.1). The associated geometry of a generic rocket thrust chamber is shown in Fig. 4.2 with the boundary conditions summarized in Tab. 4.1. Fig. 4.2 shows two separated regions, the combustion chamber and the oxidizer dome further upstream. In the present work, only the combustion chamber is considered. However, in the overall concept of the stability assessment procedure (Fig. 4.1) the dome can be coupled to the chamber via a scattering matrix, allowing to account for dome acoustics without the need to resolve the small-scale structures of the injection system. The wall boundaries are acoustically hard. The outlet is positioned in the slightly supersonic region of the nozzle. This way the growth of numeric instabilities in the supersonic nozzle part is avoided while the chamber acoustics are still decoupled from the environment by the sonic conditions at the throat. Consequently, the choice of the boundary conditions at the exit is of minor importance. A zero pressure fluctuation condition is found to be favorable for the numeric stability. The inlet of the chamber is considered acoustically neutral (zero mass flux fluctuations).

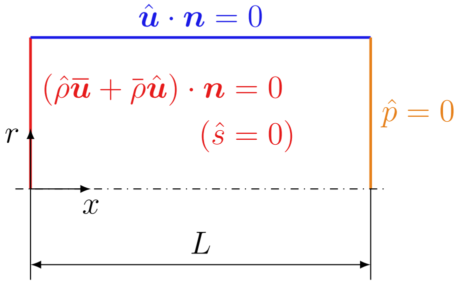

Field	Value
$\bar{u}_x$	$100\,\mathrm{m\,s^{-1}}$
$\bar{u}_r$	0
c	$347\,\mathrm{m\,s^{-1}}$
ρ	$1\,\mathrm{kg\,m^{-3}}$

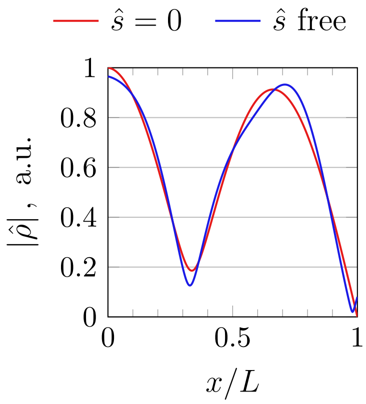

(a) Duct flow specification

(b) Density amplitude distribution

Figure 4.3: Role of entropy boundary condition

In contrast to previous work [12] a constraint for the entropy $\hat{s}$ is posed at the inlet in addition to the acoustic part of the boundary condition. It accounts for the usage of the non-isentropic set of equations. The necessity of this approach is demonstrated for the simple case of a longitudinal mode in the cylindrical duct shown in Fig. 4.3. A uniform flow of air at ambient conditions and a velocity of $100\,\mathrm{m\,s^{-1}}$ is specified along with an acoustically neutral upstream and a constant-pressure downstream boundary condition. The density amplitudes of the longitudinal three-quarter wave eigenmode are shown in Fig. 4.3 for two cases: one with a zero entropy fluctuation condition at the inlet and one with just the acoustic boundary conditions. For the zero entropy fluctuation setup, the resulting pressure and density fluctuations are related isentropically. For the case with the entropy unspecified, the pressure profile remains nearly identical but non-isentropic fluctuations lead to deviations in the density amplitudes (Fig. 4.3). So despite the principle absence of entropy sources within the just discussed setup, the calculated eigenmode may induce an entropy perturbation already at the inlet when only acoustic boundary conditions are used. For this reason, a zero entropy fluctuation boundaray conditions is used at the chamber inlet for the perturbation simulations throughout the present work.

4.1.2.2 Stabilization

The numerical discretization of a convective equation with finite elements has a side effect of acting like an artificial negative viscosity [50]. This may impact the results and numerically destabilize the solution. As countermeasure, an artificial stabilization term is added to the equations. The amount of stabilization impacts both eigenfrequencies and amplitude distributions of the modal solution. A comparison [51] of two common approaches, the Streamline Upwind Petrov-Galerkin and the Galerkin/Least-squares (GLS) method, for acoustic simulations showed no significant difference. Following previous works [12, 13] GLS stabilization is applied. For this approach, the stabilization term added to the weak form of the discretized equations reads for an individual element that covers the domain Ω^e [50]

$$\mathcal{T} = \int_{\Omega^e} \tau \mathcal{L}(\mathcal{W}) \mathcal{R} dV \tag{4.9}$$

with $\mathcal{R}$ the residual of the equation to be solved and $\mathcal{L}(\mathcal{W})$ the differential operator of the equation applied to the weighting function. The remaining parameter τ controls the distribution of stabilization in the domain. The parameter may depend on mesh size and further parameters of the equation. While for simple 1D problems an exact solution for τ, that gives the correct amount of dissipation to balance the numeric destabilization, is possible, a general solution for complex cases is not available. As in previous works, the formulation of Ullrich et al. [52] that is based on evaluating the formulation given of Le Beau et al. [53] for the LNSE is used:

$$\tau = \tau_s \max_{n_{dim}} \left(\frac{h_i}{|\bar{\boldsymbol{u}}_i| + c} \right) \tag{4.10}$$

with n_{dim} the number of dimensions, h_i the characteristic size of the cell in dimension i and τ_s a constant parameter controlling the amount of stabilization. While its impact on the oscillation frequency in the present application is usually small, α_τ may notably affect the damping rate. Schulze [12] calibrated the value of α_τ by minimizing the offset between the calculated eigenfrequencies of the two orthogonal eigensolutions that belong to each transverse mode and found a value of $\alpha_\tau = 0.1$. This approach, however,

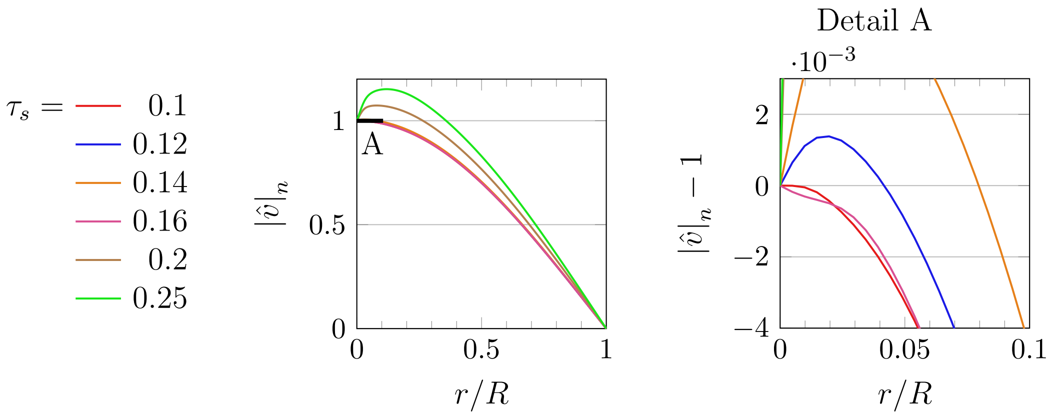

Figure 4.4: Influence of stabilization on radial velocity amplitudes

is not applicable to 2D calculations with the Bloch approach, as here only one transverse eigensolution is obtained. Instead, basic properties of the solution field are used for calibration. Thereto the radial profile of the radial velocity amplitude is evaluated at the chamber inlet. There, no significant entropy or vorticity fluctuations are expected and the amplitude distribution in the inlet cross-section can be assumed to result from the cylinder acoustics. For a T_1 mode this implies that the radial gradient of the radial velocity fluctuations becomes zero at the chamber axis. As can be seen from Fig. 4.4 the value of this gradient depends on the stabilization parameter. For the shown case an initial region with $\alpha_\tau \lesssim 0.1$ can be identified in which the zero-gradient condition is fulfilled by the solution. This agrees well with the value from the previous 3D studies. As the nozzle region is particularly prone to numeric instabilities, in some cases it has been found appropriate not to keep α_τ constant but to notably increase its value with the Mach number.

4.2 Mean Flow

The mean flow is the reference state for the calculation of the perturbations in the combustion chamber, as discussed in Sec. 4.1. The flow in the combustor is dominated by a high number of diffusion flames, whose detailed resolution requires a significantly higher grid density than that necessary to capture the large scale acoustic modes. Thus, during the development of the stability assessment procedure several approaches have been taken to get a simplified but still acoustically representative mean flow. In the following, an overview of the different strategies used in previous works is given (Sec. 4.2.1) and open issues are addressed. On this basis, a revised approach is developed in Sec. 4.2.2, leading to several consistent mean flow calculation procedures. They are evaluated and compared with each other in Chap. 6. To allow for the application of the mean flow approaches to thrust chamber configurations where the convergent nozzle section constitutes a significant portion of the chamber volume, a nozzle correction is proposed in Sec. 4.2.3. Its impact on the chamber acoustics is evaluated in Sec. 6.2. Finally, a strategy to systematically assess the impact of radial stratification in the mean flow on the perturbation solutions is developed (Sec. 4.2.4), which is the basis for the corresponding analysis in Sec. 6.3. The numerical setup for the mean flow calculations is summarized in Sec. 4.2.5.

4.2.1 Previous Works

In the context of the development of the stability assessment procedure acoustic simulations of rocket combustion chambers have been performed by Pieringer [10], Török [11] and Schulze [12]. Their approaches share the concept of a quasi one-dimensional, inviscid mean flow with no radial stratification in the cylindrical chamber section and two-dimensional flow-patterns occurring only due to the nozzle.

The mean flow used by Pieringer [10] is computed as two-dimensional CFD solution of a quasi uniform flow through chamber and nozzle. The flow is injected uniformly along the chamber faceplate at completely mixed and burned conditions. The injection composition and state of the fluid are calculated from chemical equilibrium with the CEA [15] code. After the cylindrical chamber section is passed rather uniformly, the usual nozzle flow structures are obtained further downstream. A comparison with experimental data has not been conducted. Török [11] uses the same principle approach. However, instead of relying on chemical equilibrium calculations, he extracts the flow properties at the outlet of a single flame simulation. Compared to an experiment, the T_1 eigenfrequency is overestimated by about 25 %. The step from a quasi uniform to a quasi one-dimensional mean flow has been taken by Schulze [12,13]. Like before, a two-dimensional simulation of the full domain is conducted. However, the flow composition is specified depending on the axial location along with a corresponding energy source term representing the process of combustion along the chamber. The species mass fractions and energy source term are obtained by radially averaging the flow field of a steady single flame simulation. To ensure that the axial sound speed distribution matches the single flame results, the density[1] of the mean flow is adapted in a post-processing step via

$$\bar{\rho} = \frac{\kappa \bar{p}}{c_{1D}^2} \quad . \tag{4.11}$$

The axial sound speed profile c_{1D} is extracted from the single flame simulation by area weighted radial averaging:

$$c_{1D} = \frac{1}{A} \int_0^R c 2\pi r dr \tag{4.12}$$

with A the local cross-sectional area and R the corresponding outer radius. A comparison to experimental oscillation frequencies has shown a significant improvement compared to the uniform approaches. This is explained by the T_1 mode being anchored at the faceplate where the unmixed (and thus unburned) flow possesses a lower sound speed, which leads to lower eigenfrequencies compared to the completely burned state.

The usage of the density calculation according to Eq. 4.11 ensures that the sound speed distribution is representative of the single flame results and thus the eigenfrequencies are captured correctly. However, due to the density scaling during post-processing the results no longer fulfill the Euler equations, which were solved in the mean flow CFD simulation. This has several drawbacks:

- If temperature is not adapted along with density, the LEE solutions

---

[1] As the LEE are formulated in terms of pressure and density rather than temperature (cf. Eq. 2.30, 2.31 and 2.36), density scaling can be used to modify the sound speed in the flow.

become sensitive towards a change of the state variables used to describe the mean flow in the governing equations. A form of the LEE (cf. Sec. 2.3.2) that is based on mean temperature and pressure will behave different than one that depends on mean pressure and density.

- The violation of the flow equations can be interpreted as inducing source terms of mass, momentum and energy in the mean flow. These may impact the acoustic results in an unknown way, questioning their validity.

A revised mean flow calculation procedure that does not have these issues is derived in the next section 4.2.2.

4.2.2 Revised Mean Flow Calculation

Considering the results of the studies discussed in Sec. 4.2.1, an axially non-uniform mean flow appears to be a necessary prerequisite to capture the essential acoustics of the chamber. While the small-scale flow structures are primarily associated with radial and circumferential gradients, the axial dimension of the diffusion flames is comparable to the geometric length of the chamber. Thus, the inclusion of axial gradients in the mean flow does not primarily interfere with the requirement of a computationally efficient procedure. Altogether, an approach is required to obtain a quasi one-dimensional flow solution in the whole chamber, which is consistent with the Euler Equations. At the same time it must reproduce the axial distributions of certain flow properties or fields (see below), which are obtained from single flame simulations. In this section, a general approach to fulfill above requirements is developed. Different choices for the axial profiles reproduced by the mean flow are discussed, leading to three different versions of the mean flow calculation procedure. These are tested in Sec. 6.1.

The basic structure of the mean flow calculation procedure is shown in Fig. 4.5. It consists of three steps:

1. Single flame simulation: A steady simulation of a single rocket-engine flame is calculated. Its solution is used in the next step to obtain the one-dimensional profiles for the simulation of the whole chamber. The setup for the single flame simulation depends on the test case under consideration. For the present work it is described in Sec. 5.1.

2. Extraction of axial profiles: From the single flame solution obtained in the previous step one-dimensional profiles are extracted based on radial averaging or the heat release extraction procedure discussed in Sec. 5.1.3.

3. Quasi one-dimensional simulation: In the final step to obtain the mean-flow a two-dimensional axis symmetric CFD simulation of the whole chamber is conducted. Several procedures are used at run-time and during post-processing to make sure that the profiles obtained in the previous step are met by the solution while complying with the governing equations.

In the following, the chamber simulation in step three is discussed. Focus

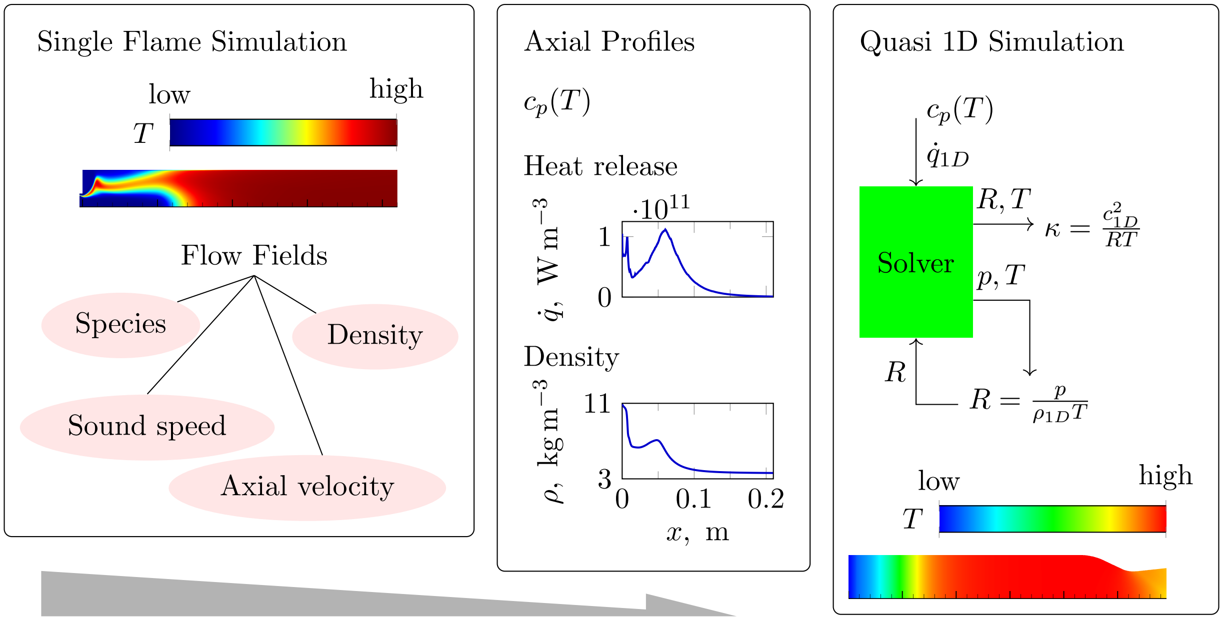

Figure 4.5: Procedure for the the two-parameter mean flow calculation

is placed on the way the solution is manipulated to reproduce the desired one-dimensional profiles in the cylindrical chamber section. The selection of the profiles that are reproduced and their calculation from the single-flame results are discussed thereafter. Finally, the treatment of the nozzle section is addressed.

In the final calculation of the chamber mean flow (third step in Fig. 4.5) the steady Euler Equations (inviscid form of Eq. 2.11, 2.12 and 2.18) are solved on a domain covering the whole combustion chamber. The flow is injected uniformly across the whole faceplate area at the average temperature of the single flame simulation after the recess. By design, the flow stays quasi one-dimensional, with its axial development based on several radially averaged fields of the single flame solution (see below). The radial averaging rises the lowest flow temperatures from the cryogenic injection temperatures to a level where an ideal gas EOS (cf. Sec. 2.2.2) can be applied. This is the justification for the usage of the ideal gas simplification in the derivation of the LEE (Sec. 2.3). The flow is considered to be composed of a pseudo-fluid. As discussed below, the properties of this fluid are chosen to ensure that certain flow characteristics of the single flame simulation are reproduced by the mean flow. Thus, the presence of different species and the associated heat release are not included in the model. To nevertheless account for the impact of combustion on the axial development of the flow temperature, an energy source is employed. It is extracted from the single flame results as described in Sec. 5.1.3. The specific heat capacity is modeled via 7-coefficient JANAF polynomials [15]. Their coefficients are given as axial distribution, computed from the radial mass flow weighted average

$$\phi_{1D} = \frac{1}{A\rho u_x} \int_0^R \rho u_x \phi 2\pi r dr \tag{4.13}$$

of species mass fractions in the single flame. The full setup for the chamber simulation is summarized in Sec. 4.2.5.

There are three stages where flow properties can be altered in a CFD solution: pre-processing, at simulation runtime and post-processing. The first stage is uncritical in terms of equation consistency. As the governing equations are solved during the simulation, any manipulation of properties or boundary conditions during pre-processing automatically becomes part of a solution that complies with said equations. Likewise, influencing the solution at run-time is unproblematic. As the solution is obtained iteratively, once convergence is achieved, the results comply with the governing equations as well as any sub-models employed. However, special attention is required when manipulating fields during post-processing. There, the alteration of e.g. a single thermodynamic state variable may cause incosistencies in the EOS or with the governing equations (cf. Sec. 4.2.1). While the alteration of multiple variables is possible in accordance with the EOS, incompatibilities e.g. of an altered density with the velocity field in terms of mass conservation (Eq. 2.11) are to be expected. However, manipulation of properties that enter the flow equations in an integral sense is possible. This refers to the specific isobaric or isochoric heat capacities c_p or c_v. They influence the flow solution by relating the sensible enthalpy or energy to the local flow temperature. This conversion takes the form of a temperature integral (Eq. 2.5b). Thus, the value of e.g. c_p at the flow temperature can be changed without inducing inconsistencies with the energy equation, as long as the integral value (cf. Eq. 2.5b)

$$\Delta\bar{h}_s = \int_{T_{ref}}^{\bar{T}} c_p d\check{T} \tag{4.14}$$

remains constant.

To ensure that the mean flow is consistent with the governing equations as well as the ideal gas EOS, the only option to influence the solution are the fluid properties. This can be interpreted as introducing a pseudo-fluid. It goes into the flow solution via its specific heat capacity and the specific gas constant. According to the previous discussion, the gas constant must be altered either during pre-processing or at simulation run-time as it directly relates thermodynamic state variables (Eq. 2.5a). In contrast, the value of the specific heat capacity at the solution temperature may be changed during post-processing. According to Eq. 2.7 a change of the specific heat capacity at a given specific gas constant corresponds to a modification of the isentropic coefficient κ. So the isentropic coefficient can be directly adapted during post processing. The corresponding specific heat capacity is then

Table 4.2: Summary of mean flow calculation procedures

Methodology	single flame	pre-processing	run-time	post-processing
density scaling [12]	c_{1D}	-	-	$\bar{\rho} = \kappa \bar{p} / c_{1D}^2$
c-i	c_{1D}, $\eta_{c,1D}$	$\bar{\rho}_{1D} = \left(\eta_{c,1D} c_{1D}\right)^{-1}$	$R = \frac{\bar{p}}{\bar{\rho}_{1D} \bar{T}}$	$\kappa = \frac{c_{1D}^2}{R \bar{T}}$, $c_p = R \frac{\kappa}{\kappa - 1}$
c-s	c_{1D}, $\eta_{s,1D}$	$\bar{\rho}_{1D} = \left(\eta_{s,1D} c_{1D}^2\right)^{-1}$		
c-κ	c_{1D}, κ_{1D}	-	$R = \frac{c_{1D}^2}{\kappa_{1D} \bar{T}}$	$\kappa = \kappa_{1D}$, $c_p = R \frac{\kappa}{\kappa - 1}$

obtained from Eq. 2.7. In summary, there are two variables that can be altered to obtain specific flow profiles, the isentropic coefficient and the specific gas constant. In general, this allows to reproduce axial profiles of two flow fields or properties, leaving several options to calculate the mean flow. Possible choices are discussed in the following.

To fully specify the mean-flow calculation procedure, the axial profiles that are reproduced by the solution need to be selected. Three choices are discussed, corresponding to three different calculation procedures. They are summarized along with the previous 'density scaling' approach by Schulze [12] (cf. Sec. 4.2.1) in Tab. 4.2. The most important axial profile to be reproduced by the mean flow is the sound speed, which determines the real part of the eigenfrequency. The sound speed can be adapted in two ways: by changing the isentropic coefficient as

$$\kappa = c_{1D}^2 \frac{\bar{\rho}}{\bar{p}} \tag{4.15}$$

or the gas constant according to

$$R = \frac{c^2}{\kappa \bar{T}} \quad . \tag{4.16}$$

Note that the second option (Eq. 4.16) requires that the final distribution of the isentropic coefficient is already known at run-time since the specific gas constant cannot be changed during post-processing.

After accounting for the desired sound-speed distribution via Eq. 4.15 or Eq. 4.16, one more axial profile is to be selected in order to specify the mean flow. First, the usage of Eq. 4.15 is considered, i.e. the specific gas constant is the remaining parameter to be specified. To this end, two characteristic acoustic properties are considered as second profile to be reproduced by the mean flow. The field impedance

$$\eta_i = \frac{1}{\bar{\rho} c} \tag{4.17}$$

relates the acoustic velocity to the pressure fluctuations, as can be easily seen by comparing Eq. 2.43a with Eq. 2.47. The isentropic compressibility plays a significant role in the relation between pressure fluctuations and fluctuation energy (cf. Eq. 2.49). According to their definitions either of the field impedance (Eq. 4.17) or the isentropic compressibility (Eq. 2.50) can be reproduced at a given sound speed by adapting the density. To this end, the specific gas constant is calculated from the local flow temperature, pressure and a target density ρ_{1D} as

$$R = \frac{\bar{p}}{\bar{\bar{T}} \rho_{1D}} \quad . \tag{4.18}$$

The target density profile is obtained during pre-processing. From the field impedance it is calculated as

$$\rho_{1D} = \frac{1}{\eta_{i,1D} c_{1D}} \tag{4.19}$$

with the profiles of field impedance and sound-speed obtained according to Eq. 4.13. The approach to reproduce sound speed (Eq. 4.15) and field-impedance (Eq. 4.18 and 4.19) with the mean flow is referred to as *c-i* method. If instead sound speed (Eq. 4.15)and isentropic compressibility are to be reproduced (*c-s* approach), the target density profile for the evaluation of Eq. 4.18 is obtained according to

$$\rho_{1D} = \frac{1}{\eta_{s,1D} c_{1D}^2} \quad . \tag{4.20}$$

Alternatively to adapting the sound speed distribution via the isentropic coefficient (Eq. 4.15) there is the option to correct the sound-speed via the gas-constant (Eq. 4.16). This approach leaves the isentropic coefficient to be specified. According to the pressure fluctuation equation 2.36 κ has a strong impact on the influence the flame feedback has on the perturbations. This leads to the third revised approach, which, besides the sound speed, reproduces the averaged (Eq. 4.13) isentropic coefficient[2] κ_{1D}. The mean flow calculation based on the profiles of sound speed and isentropic coefficient is termed $c-\kappa$ approach.

While the concepts just outlined are the core part of the mean flow calculation, their applicability is restricted to the cylindrical part of the chamber. As the single flame simulations do not capture the flow patterns in the nozzle section, the profiles of sound speed, isentropic compressibility and field impedance do not account for the increasing flow velocity and thus decreasing temperatures in this region. If the combustion process is sufficiently complete at the end of the cylindrical section, the flow properties may be treated as frozen. The chamber domain is split into two parts at the location of the nozzle entrance x_0. In the front part, $x \leq x_0$, where the flow can be considered to be incompressible, the previously described approach is followed. From that point onward ($x > x_0$) the isentropic coefficient and the gas constant are kept constant with their qualitative radial distribution being conserved:

$$\begin{array}{l} \kappa|_{x,r_n} = \kappa|_{x_0,r_n} \\ R|_{x,r_n} = R|_{x_0,r_n} \end{array} , \quad r_n = r/R \tag{4.21}$$

with R the local outer radius of the chamber. For the *c-i* and *c-s* approaches the isentropic coefficient is gradually adapted along the nozzle during post-processing, to match the value from the chamber simulation at the nozzle throat [3]. That way it is ensured that the sound speed at the nozzle throat matches that from the CFD solution. The location of the sonic line is retained and the correct acoustic boundary condition is set for the chamber. For cases where there is still significant heat release in the nozzle, a correction of the heat release profile from the single flame simulations is proposed in the next section 4.2.3 to account for the flow acceleration in the nozzle.

---

[2] Note that the role of κ in the flame feedback term might suggest alternate extraction procedures, e.g. by basing κ_{1D} on the regions of highest heat release fluctuation. However, that level of detail is not to be considered yet as will be seen in Chap. 8.

[3] Such an adaption is not necessary for the *c*-κ method as $\kappa = \kappa_{1D}$ already matches the single flame results.

4.2.3 Nozzle Correction

The basic treatment of the nozzle flow according to Eq. 4.21 is based on the assumption that no significant reaction occurs in the nozzle and the relevant heat release has already been completed in the cylindrical chamber section. However, depending on the chamber design (cf. Fig. 3.3 in Sec. 3.2) the convergent nozzle section may cover a significant part of the chamber length. To modify the heat release distribution obtained from the single flame simulation in order to account for the flow acceleration in the nozzle, a non-iterative procedure has been proposed by Chemnitz et al. [54]. Later an improved, iterative procedure based on one-dimensional flow equations [55] has been used. This version of the nozzle correction is outlined in the following.

The process of the nozzle correction is visualized in Fig. 4.6 for a representative flow through the nozzle with the contour shown in Fig. 4.6a. To correct the heat release for the flow acceleration (Fig. 4.6b), a Lagrangian point of view is taken: As a fluid element passes through the single flame domain, mixing dominated combustion leads to heat release. Assuming that mixing and thus combustion proceeds at the same rate irrespective of the absolute velocity, the volumetric heat release in a region of axial dimension Δx that the fluid needs the time $\Delta t = \Delta x / u_x$ to pass through leads to the heat release correction

$$q = q_{ref} \frac{u_{x,ref}}{u_x} \approx q_{ref} \frac{u_{x,0}}{u_x} \quad . \tag{4.22}$$

Here $_{ref}$ denotes a reference value that is interpolated from the single flame simulation as described below. The associated flow velocity in the single flame simulation can be approximated by its value at the nozzle entrance (index $_0$) as combustion in the nozzle is rather advanced and the impact on the overall density is minor compared to the compressibility related density changes. This simplification is justified by a simple estimate: Along the nozzle, the flow velocity increases by a factor of about four. To lead to a comparable acceleration, density would have to decrease by a factor of four

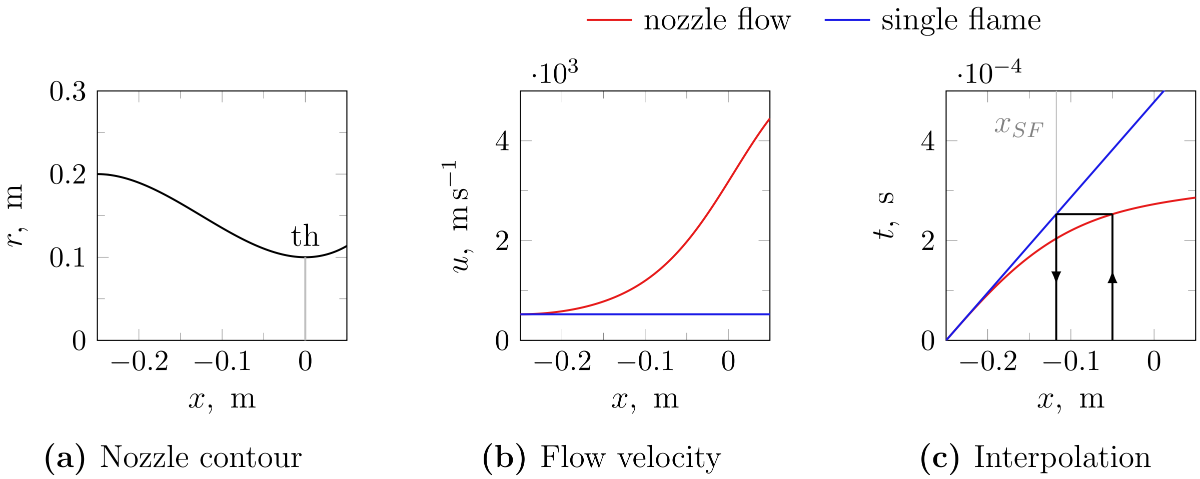

(a) Nozzle contour **(b)** Flow velocity **(c)** Interpolation

Figure 4.6: Interpolation principle for nozzle correction

since

$$(\rho u_x)_{1D} = \frac{1}{A}\int_A \rho u_x dA = const. \tag{4.23}$$

within each nozzle cross-section. As the single flame simulation can be considered as rather isobaric in terms of mean pressure, the density decrease again corresponds to an increase of the temperature by a factor of four (Eq. 2.5a), given rather small changes of the molar mass and thus the specific gas constant. The equilibrium temperature of the chamber flow is below 3500 K. Thus, for combustion related density changes to cause the same flow acceleration as the nozzle, the flow temperature at the nozzle inlet must not exceed a value of 800 . . . 900 K. So there is a considerable range of nozzle inlet temperatures where the temperature is high enough to allow for combustion related density changes to be neglected ($T >> 800\,\mathrm{K}$) despite heat release still going on ($T < 3500\,\mathrm{K}$).

To evaluate Eq. 4.22, the heat release rate q_{ref} needs to be interpolated from the single flame domain. The interpolation principle is shown in Fig. 4.6. As the heat release correction (Eq. 4.22) corresponds to a modified axial distribution of the mixing process, which dominates combustion, a direct geometrical interpolation is not appropriate. Instead, combustion is parametrized in terms of its progress, i.e. the heat release is treated as function of the heat released upstream, leading to the interpolation rule

$$q_{ref}\big|_{x} = q_{SF}\big|_{x_{SF}} \quad , \int_{x_0}^{x,SF} q_{SF} A d\check{x} = \int_{x_0}^{x} q A d\check{x} \tag{4.24}$$

with x the axial position in the chamber simulation and x_{SF} the corresponding interpolation location in the single flame simulation. Eq. 4.24 can be interpreted as an interpolation via the time that a fluid element has passed since entering the nozzle rather than the axial distance from the nozzle entrance (cf. Fig. 4.6c).

Equation 4.22 in combination with Eq. 4.24 constitutes a procedure to obtain the heat release distribution in presence of a nozzle from a single flame simulation. In its initial form [54] this procedure has been applied not-iteratively by performing a CFD nozzle flow simulation without heat release, extracting the axial velocity distribution, evaluating the correction equations and then performing another nozzle flow simulation including the corrected heat release rate. However, the heat released in the nozzle is expected to change the axial velocity distribution, which is not accounted for in the non-iterative approach. Moreover, the need for an additional CFD simulation is unfavorable. Thus, the equations for one-dimensional, frictionless flow with heat addition and area change are solved instead. As the heat source contribution to these equations causes a singularity at sonic conditions, the nozzle domain is split into three parts: A shortened convergent section that ends slightly before the nozzle throat ($Ma \leq 0.99$), a divergent section that starts in the slightly supersonic regime ($Ma =\geq 1.01$) and a transsonic region that links both. In the sub- and supersonic regions, the full equations are solved, while in the transsonic section the flow is considered isentropic. As the heat release is already low at the throat location, this approximation is acceptable. In the given context, the Mach number in the transsonic region is determined by the ratio of the local cross-sectional area to the throat area alone. Thus, the subsonic part of the transsonic section poses a Mach number boundary condition at the end of the convergent section. Together with the mass flow and total temperature at the nozzle inlet a boundary value problem is obtained. The governing equations are introduced in the following.

The flow equations for the nozzle correction are based on steady, one-dimensional, frictionless flow of and ideal gas with constant isentropic coefficient and specific heat. For a constant cross-section, this setup corresponds to a Rayleigh flow, with the only source of entropy being the heat release. For isentropic conditions a relation between Mach number and cross section is available. The total differential of the Mach number can be constructed as superposition of these two contributions:

$$dMa = \left.\frac{\partial Ma}{\partial s}\right|_{A=const} ds + \left.\frac{\partial Ma}{\partial A}\right|_{s=const} dA \quad . \tag{4.25}$$

The partial differentials in Eq. 4.25 are given by Truckenbrodt [56], leading to the relation

$$\frac{dMa}{Ma} = \underbrace{\frac{1+\kappa Ma^2}{2\left(1-Ma^2\right)}\frac{d\mathfrak{q}}{c_pT}}_{\left.\frac{dMa}{Ma}\right|_A} \underbrace{-\frac{2+\left(\kappa-1\right)Ma^2}{2\left(1-Ma^2\right)}\frac{dA}{A}}_{\left.\frac{dMa}{Ma}\right|_s} \quad . \tag{4.26}$$

The heat source $d\mathfrak{q}$ in Eq. 4.26 is mass specific and related to the volumetric heat release q cf. Eq. 2.24 via

$$d\mathfrak{q} = \frac{q}{\rho u_x}dx = \frac{qA}{\dot{m}}dx \quad . \tag{4.27}$$

Furthermore, closure of Eq. 4.26 requires the temperature distribution, which is obtained via the differential of the isentropic relationship between static and stagnation (index $_t$) temperature:

$$\frac{dT}{T} = \frac{1-\kappa}{1+\frac{\kappa-1}{2}Ma^2}Ma\ dMa + \frac{1}{1+\frac{\kappa-1}{2}Ma^2}dT_t \quad . \tag{4.28}$$

Again this differential consists of two contributions, the isentropic expansion in the first term and the change of stagnation temperature due to heat addition in the second term. The latter can be replaced via

$$dT_t = \frac{d\mathfrak{q}}{c_p} \quad . \tag{4.29}$$

Inserting Eq. 4.29 into Eq. 4.28 and eliminating the term $d\mathfrak{q}/(c_pT)$ via Eq. 4.26 a temperature differential in dependence of Mach number and area change is obtained:

$$\frac{dT}{T} = 2\frac{1-\kappa Ma^2}{1+\kappa Ma^2}\frac{dMa}{Ma} + \frac{2}{1+\kappa Ma^2}\frac{dA}{A} \quad . \tag{4.30}$$

Eq. 4.30 together with Eq. 4.26 and the heat release correction Eq. 4.22 and 4.24 are a closed set of equations describing the nozzle flow in the chamber in the presence of heat release. Their solution yields the velocity distribution in the nozzle and thus via Eq. 4.22 and 4.24 the corrected heat release profile. With this profile, the mean flow is calculated as described in Sec. 4.2.2. However, now the source term distribution that represents the heat release does not only cover the cylindrical part of the chamber but includes the nozzle section as well. The impact of the nozzle correction on chamber acoustics is studied in Sec. 6.2.

4.2.4 Radially Stratified Mean Flow

The efficiency of the stability assessment procedure partly relies on neglecting radial and circumferential gradients in the mean flow. This has been reasoned [12] by the compactness of the flow-normal small scale structures as compared to the acoustic length scales. At the same time, a significant amount of field-damping, a stabilizing mechanism arising from the axial gradients in the mean flow, has been found. Nevertheless, the consequences that neglecting radial gradients has for the stability predictions have not been studied explicitly. To better assess the soundness of the mean flow concept (Sec. 4.2.2), the impact of radial gradients on the chamber acoustics is considered in Sec. 6.3 of the present work. For this purpose, several mean flow solutions are calculated, which are equal in terms of their underlying axial profiles (cf. Sec. 4.2.2) but differ in terms of radial stratification. A first approach to this topic has been given in a previous study [57] by imposing radial gradients of varying intensity on a mean flow while retaining the averaged one-dimensional profiles. This analysis is extended in Sec. 6.3 of the present work. The partly revised underlying calculation procedure for the stratified mean flow is described in the following.

The basic idea of flow stratification relies on the mean flow calculation approach outlined in Sec. 4.2.2. However, instead of one dimensional axial profiles ($_{1D}$), a two-dimensional target distribution ($_{2D}$) is used in Eq. 4.15 and 4.18, respectively:

$$\kappa = c_{2D}^2 \frac{\bar{\rho}}{\bar{p}} \tag{4.31}$$

$$R = \frac{\bar{p}}{\bar{T}\rho_{2D}} \quad . \tag{4.32}$$

The reference distributions are obtained by applying analytical radial stratification functions ψ_ϕ to the one-dimensional profiles of sound speed ($\phi = c$) and density ($\phi = \rho$):

$$\phi_{2D} = \phi_{1D}\psi_\phi \quad . \tag{4.33}$$

They are designed in a way that on radial averaging according to Eq. 4.13 the one dimensional profiles are retained, i.e.

$$(\phi_{2D})_{1D} = \phi_{1D} \ , \phi = c \quad , \ \rho \quad . \tag{4.34}$$

Analogously, the heat release is stratified via a stratification function ψ_q. In the following, the radial structure of a single flame is discussed. On this basis, the radial stratification functions for the different fields are developed.

The principal radial structure of a single BKD flame, calculated with the setup described in Sec. 5.1, is shown in Fig. 4.7. The temperature (Fig. 4.7b) possesses a clear peak in the mixing layer along a wide portion of the chamber. In contrast, already a short distance downstream of the faceplate the sound speed profile (Fig. 4.7c) is characterized by a high value region close to the wall and a trough at the core of the flow. Depending on the axial location, the transition between both regions varies in shape. The difference between temperature and sound speed arises from the different flow properties: While the inner region of the flame is oxygen rich, the outer part has a higher fraction of hydrogen, which has a low molecular weight, leading to a higher sound speed. In the downstream region of the chamber both profiles have homogenized. The density (Fig. 4.7d) shows the strongest relative change along the chamber radius. The cryogenic injection of oxygen leads to a density of $\mathcal{O}10^3\,\mathrm{kg\,m^{-3}}$. In contrast, densities that are three orders of magnitude smaller occur in the combustion products.

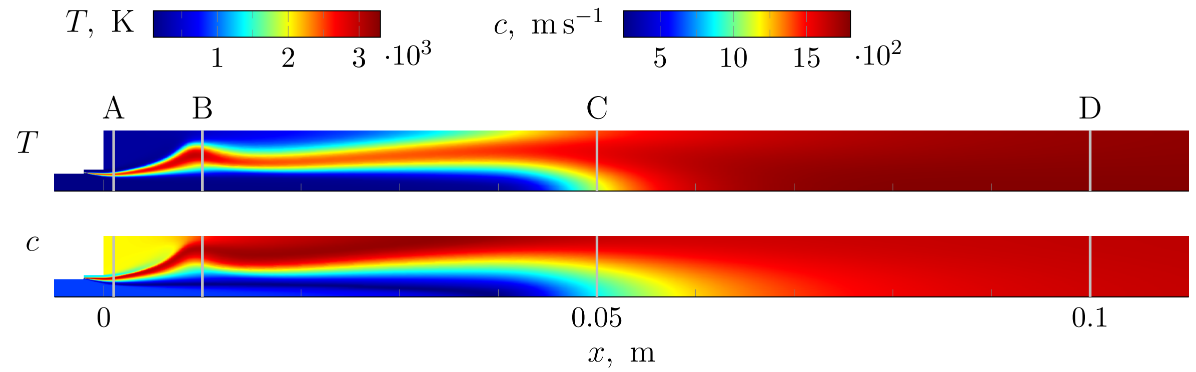

(a) Flow fields

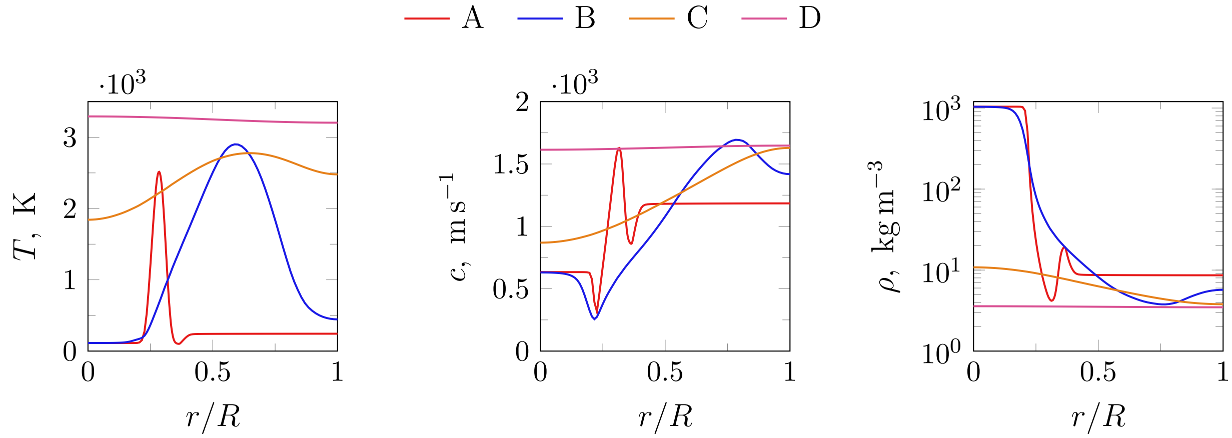

(b) Temperature profile **(c)** Sound speed profile **(d)** Density profile

Figure 4.7: Flow stratification from a single flame simulation

Based on the above discussion of radial stratification along a single flame, the stratification functions ψ_ϕ are developed. In general, all flow fields are subject to the stratification arising from the diffusion flame structure. However, in favor of a concise analysis, stratification is not applied to all mean flow fields at once. The flow properties, represented in the perturbation equations by the isentropic coefficient and the specific gas constant, mostly influence the impact of the flame response on the acoustics (Eq. 2.36). As the stratification analysis in Sec. 6.3 is conducted for a passive flame, i.e. no feedback is considered, these flow properties are kept approximately constant in radial direction[4]. The most important flow property for the real

---

[4] These properties are not exactly constant due to the approximative character of the stratified en-

valued eigenfrequency is the sound speed. Consequently, its stratification function forms the basis, from which the other fields' stratification is derived.

Starting point for deriving the mean flow's stratification functions is the sound speed:

$$c_{2D} = c_{1D}\psi_c \quad . \tag{4.35}$$

To ensure that the differently stratified mean flows possess the same axial sound speed profile with respect to the averaging procedure Eq. 4.13, it is required that

$$\frac{1}{A}\int_0^R \psi_c dA = 1 \quad . \tag{4.36}$$

At the same time the reduction of stratification along the chamber must be explicitly modeled, mimicking the effect of turbulent mixing on the flow. To conveniently account for these two aspects, the following approach is taken for the stratification function:

$$\psi_c = 1 + A_\psi \psi_x \psi_r \quad . \tag{4.37}$$

The second term in Eq. 4.37 describes the local relative deviation from the mean profile. It contains a stratification amplitude A_ψ that governs the maximum deviation from the mean. The radial stratification function ψ_r defines the shape of the variable's variation in radial direction. It takes values between $\psi_r = -1$ and $\psi_r = 1$ and fulfills Eq. 4.36. Finally the axial stratification function ψ_x is used to represent the mixing process by decreasing from a value of $\psi_x = 1$ at the beginning of the stratified region to $\psi_x = 0$ at its end. Recalling the previous discussion of the structure of the sound speed field, the radial stratification function is chosen as a cosine connecting a minimum value at the flame axis to the maximum value at the outer boundary:

$$\psi_r = \cos(2\pi n_{fl}\frac{r}{R}) \quad . \tag{4.38}$$

---

ergy source derivation discussed below. Imperfections in the resulting radial temperature distribution are reflected in the gas constant as the target density is reproduced exactly by design of the mean flow calculation (cf. Sec. 4.2.2.). The stratification of the corrected isentropic coefficient, which is calculated during post-processing, can be considered to be minor as it only needs to compensate for radial pressure variations which are low compared to the mean pressure.

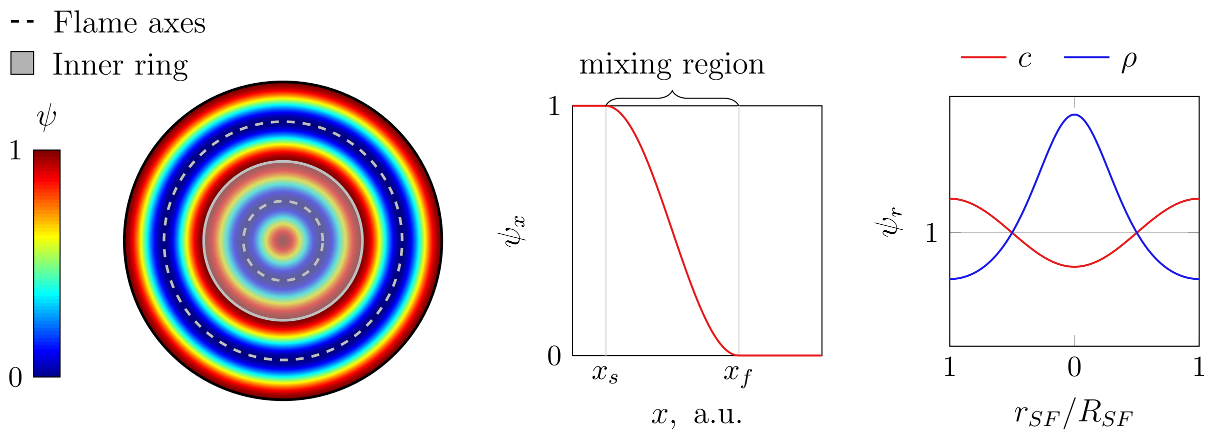

(a) Radial flame structure **(b)** Axial stratification function **(c)** Radial stratification function

Figure 4.8: Mean flow stratification

The parameter n_{fl} defines the number of flame structures placed along the chamber radius. The shape of the radial sound speed stratification for a single flame is shown in Fig. 4.8c. As the flow is still considered two-dimensional, which is necessary to sufficiently resolve the gradients on the computational grid, each flame structure takes the form of a flame ring as shown in Fig. 4.8a. The axial decay of stratification is parametrized by two variables: the starting location x_s separates the initial, rather unmixed region from the zone where mixing occurs. The mixing process is completed at $x = x_f$, downstream of which the flow is homogeneous. The complete axial stratification function reads

$$\psi_x = \begin{cases} 1, & x \leq x_s \\ 0.5\left(1 + \cos\left(\frac{x - x_s}{x_f - x_s}\right)\right), & x_s < x < x_f \\ 0, & x \geq x_f \end{cases} \tag{4.39}$$

and is visualized in Fig. 4.8b.

With the unstratified isentropic coefficient and gas constant the appropriate stratification function for the temperature can be derived using the ideal gas sound speed as

$$\psi_T = \psi_c^2 \quad . \tag{4.40}$$

Since the temperature distribution is governed by the heat release, Eq. 4.40

needs to be converted into a stratified heat source distribution. Assuming uniform mass flux and neglecting kinetic energy, the appropriate relation reads

$$\begin{aligned} q &= \frac{\dot{m}c_p}{A}\frac{\partial T}{\partial x} \\ &= \frac{\dot{m}c_p}{A}\left(\frac{dT_{1D}}{dx}\psi_c^2 + T_{1D}\psi\frac{\partial \psi_c}{\partial x}\right) \quad . \end{aligned} \tag{4.41}$$

So the stratified heat release distribution is composed of two contributions, one describing the rise of the overall sensible enthalpy level in axial direction and one equalizing part that represents the mixing process. The first contribution can be represented by an axial reference temperature distribution T_{1D}. It must be set properly to ensure that the total heat release at each axial position in the chamber is matched:

$$\frac{1}{A}\int_0^R q dA = q_{1D} \quad . \tag{4.42}$$

To calculate the one-dimensional reference temperature distribution, Eq. 4.41 is inserted along with the definition of the stratification function (Eq. 4.37 to Eq. 4.39) into Eq. 4.42. After evaluation of the area weighted radial average an inhomogeneous ordinary differential equation of first order is obtained:

$$\begin{gathered} \frac{dT_{1D}}{dx} + c_{x3}T_{1D} = \frac{A}{\dot{m}c_p}\frac{q_{1D}}{c_{x1}}, \quad \text{with} \\ c_{x1} = 1 + \frac{A_\psi^2\psi_x^2}{2}, \quad c_{x2} = A_\psi^2\psi_x\frac{d\psi_x}{dx}, \quad c_{x3} = \frac{c_{x2}}{c_{x1}} \quad . \end{gathered} \tag{4.43}$$

The initial value problem defined by this ODE and the inlet temperature

$$T_{1D}\big|_{x=0} = \frac{1}{c_{x1}A}\int_0^R T dA\bigg|_{x=0} \tag{4.44}$$

can be readily solved to give

$$T_{1D} = \left[\frac{\overline{T}_{1D}\big|_{x=0}}{c_{x1}} + \frac{A}{\dot{m}c_p}\int_0^x \frac{q_{1D}}{c_{x1}}\exp\left(\int_0^x c_{x3}d\check{\check{x}}\right)d\check{x}\right]\exp\left(-\int_0^x c_{x3}d\check{x}\right) \tag{4.45}$$

with the derivative

$$\frac{dT_{1D}}{dx} = \frac{A}{\dot{m}c_p}\left(\frac{q_{1D}}{c_{x1}} - c_{x3}T_{1D}\right) \quad . \tag{4.46}$$

The result can be interpreted as follows: The gradient, Eq. 4.46, goes into the first addend of Eq. 4.41. The term c_{x1} corresponds to the radial average

$$c_{x1} = \frac{1}{A}\int_0^R \psi^2 dA \tag{4.47}$$

and thus the normalization of the first term in Eq. 4.46 compensates for the non-unity radial area average of the squared stratification function that is applied to the reference heat release profile. The second term arises from the equalizing contribution in Eq. 4.41 not averaging to zero.

Finally, the stratification function for the density is required. As the pressure is rather constant within each cross-section the temperature stratification function combined with radially constant flow properties suggests

$$\psi_\rho = \frac{1}{\psi^2} \quad , \tag{4.48}$$

see Fig. 4.8c for a comparison of stratification functions. This choice is consistent with the observed flow patterns as the regions of high density are located in the core of the flame. Recalling Fig. 4.7d, it stands out that the density stratification that has been derived from the sound speed distribution is weaker than that encountered in a BKD flame, which is a result of the real gas modeling in the latter. More important, the stratification functions Eq. 4.35 and 4.48 match the *c*-*s* as well as the *c*-*i* methodologies (cf. Tab. 4.2). On radial average, both the isentropic compressibility (*c*-*s* approach)

$$\frac{1}{A}\int_0^R \left(\frac{1}{\rho c^2}\right) dA = \frac{1}{A}\int_0^R \left(\frac{1}{\rho_{1D}c_{1D}^2}\right) dA = \frac{1}{\rho_{1D}c_{1D}^2} \tag{4.49}$$

and the field impedance (c-κ approach)

$$\frac{1}{A}\int_0^R \left(\frac{1}{\rho c}\right) dA = \frac{1}{\rho_{1D}c_{1D}}\frac{1}{A}\int_0^R \psi dA = \frac{1}{\rho_{1D}c_{1D}} \tag{4.50}$$

correspond to their one-dimensional profiles. As moreover the isentropic coefficient is constant for both approaches, they are also compatible with the c-κ mean flow calculation procedure.

Analogously to the equalizing heat source used to represent turbulent and diffusive energy transport (cf. Eq. 4.41), a momentum source term is defined, which relaxes the flow to a uniform distribution of axial momentum, using local flow velocity and the length of the mixing zone as characteristic parameters:

$$\mathcal{S}_{ux} = c_u \left(\frac{\dot{m}}{A} - \rho u_x \right) u_x \tag{4.51}$$

with c_u a constant controlling the strength of the equalizing momentum source.

Combining the mean flow calculation procedure outlined in Sec. 4.2.2 with two-dimensional reference profiles (Eq. 4.33) based on analytic stratification functions (Eq. 4.37) provides a methodology to obtain mean flow fields with controlled radial stratification. The approach is completed by the stratification functions for sound speed (Eq. 4.35), heat release (Eq. 4.41) and density (Eq. 4.48). The stratification is controlled by two parameters, the stratification amplitude and the number of flame structures along the chamber radius. The functions' design ensures that the calculated mean flows are equivalent in terms of the averaging procedures that are used to obtain the quasi one-dimensional mean flow in Sec. 4.2.2. On this basis, the impact of radial stratification on the chamber acoustics is studied in Sec. 6.3.

4.2.5 Numerical Setup

In the present section the domain geometry and boundary conditions for the previously outlined mean flow calculation (Sec. 4.2.2 and 4.2.4) are summarized. The solution domain covers the whole chamber, as shown in Fig. 4.9. Since the flow is quasi one-dimensional, a rather coarse computational grid can be applied. The boundary conditions are given in Tab. 4.3. In accordance with the employed Euler Equations, which neglect viscous transport (cf. Sec. 2.3), the wall is modeled as adiabatic free slip wall. The

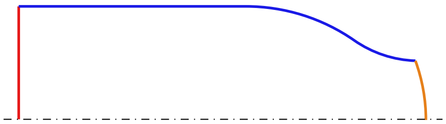

Figure 4.9: Domain for mean flow simulation

Table 4.3: Mean flow boundary conditions

color	type	specification
🟦	wall	$\boldsymbol{u} \cdot \boldsymbol{n} = 0$
🟥	inlet	$\dot{m}$, T
🟧	outlet	supersonic

mass flow is injected uniformly across the chamber cross-section at a temperature calculated as area weighted cross-sectional average of the single flame temperature at the axial position of the faceplate. At the outlet, the flow is supersonic, so no explicit boundary conditions are specified there.

4.3 Flame Feedback

Flame feedback is the potential driver of combustion instabilities. Within the stability analysis it appears as source term in the LEE pressure equation 2.36 as discussed in Sec. 4.1. This source is modeled based on a Flame Transfer Function (FTF), which relates the heat release fluctuations to the perturbation variables. Since the dynamics of mixing and combustion that govern the heat release in the chamber may include non-linear processes, the FTF is obtained from a solution of the Navier Stokes Equations together with the energy conservation equation (Eq. 2.11, 2.12 and Eq. 2.21). In line with the target of a computationally efficient procedure, the flame response is extracted from a single flame simulation (cf. Sec. 5.1). Previous studies [3, 58] have identified two principle coupling mechanisms between acoustics and combustion: Pressure coupling refers to heat release perturbations corresponding pressure fluctuations. It occurs in pure form at pressure antinodes. Velocity coupling describes the response of the single flame to transverse velocity fluctuations, which can be extracted at a velocity anti-node. At all other locations the flame response can be considered as superposition of these two contributions. In a previous BKD study [12], the pressure coupling mechanism has been found to have a considerably stronger impact on the chamber stability than velocity coupling.

In the following, the process to retrieve the flame response for both coupling types are discussed. Focus is placed on the calculation of the heat release perturbations arising from pressure and velocity oscillations. The way the results are converted to FTFs is discussed in Sec. 7.2. In the present section, for each coupling mechanism (Sec. 4.3.1 for pressure and Sec. 4.3.2 for velocity coupling) an overview of the previous results and modeling approaches is given. Deficiencies of theses methods are addressed and a revised form of the FTF extraction procedure is presented. Velocity coupling is used in the context of single flame simulation validation in Sec. 5.3.3, the pressure response is studied in Chap. 7 and applied in the stability analysis in Chap. 8.

4.3.1 Pressure Coupling

Pressure coupling describes the flame response to acoustic pressure fluctuations in the chamber. The corresponding heat release fluctuations are modeled via an FTF, following the generic approach:

$$\hat{q} = F\hat{T}F_p \hat{p}_{ref} \frac{\bar{q}_{ref}}{\bar{p}_{ref}} \quad . \tag{4.52}$$

Here $\bar{q}_{ref}$ and $\bar{p}_{ref}$ are reference mean values and $\hat{p}_{ref}$ refers to a reference pressure amplitude. The choice of these quantities is not unambiguous and will be discussed in Sec. 7.2. The flame transfer function for pressure coupling is calculated from the heat release and pressure fluctuations of a single flame located at a pressure anti-node. Thus the key component to characterize the flame response is to impose the relevant flow perturbations that a flame in the pressure anti-node of a transverse chamber mode is exposed to on a single flame simulation. Previous works on this topic are summarized in Sec. 4.3.1.1. The deficiencies of the developed excitation procedures are analyzed, taking into account the mechanisms that lead to heat release fluctuations in transverse modes in Sec. 4.3.1.1. On this basis a revised approach to obtain heat release fluctuations associated with transverse modes from single-flame simulations is proposed in Sec. 4.3.1.3. It is studied for

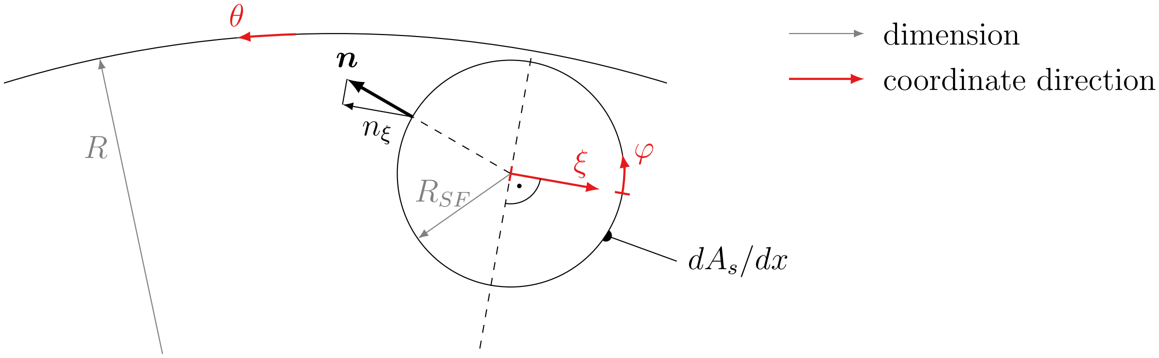

Figure 4.10: Nomenclature for the single flame excitation geometry

a BKD load point (cf. Sec. 3.1) in Sec. 7.1 and employed for the stability analysis in Chap. 8.

4.3.1.1 Previous Development

The common idea for the pressure FTF calculation in previous work is to consider the flame as acoustically compact in cross-stream direction and to stimulate pressure fluctuations whose axial distribution corresponds to those obtained from an acoustic simulation (cf. Sec. 4.1) of the complete chamber. This approach is also referred to as pressure excitation. The relation between chamber and excitation simulation domain is shown in Fig. 4.10 (see also Sec. 5.1.4). The single flame domain (outer radius R_{SF}) is located within the combustion chamber (outer radius R). The different coordinates are introduced in the following upon use.

Schmid and Sattelmayer [58] use source terms to mimic the effect of transverse chamber acoustics on a single flame. The pressure fluctuations at the pressure anti-node of a transverse mode are induced by the local addition and subtraction of mass due to the mass flux arising from acoustic fluctuations (cf. Fig. 4.11, point A). Consequently, to study the impact of pressure fluctuations on the flame dynamics, mass is harmonically injected and extracted at the lateral boundaries of the single flame domain.

The mass source for the above excitation method is calculated based on a

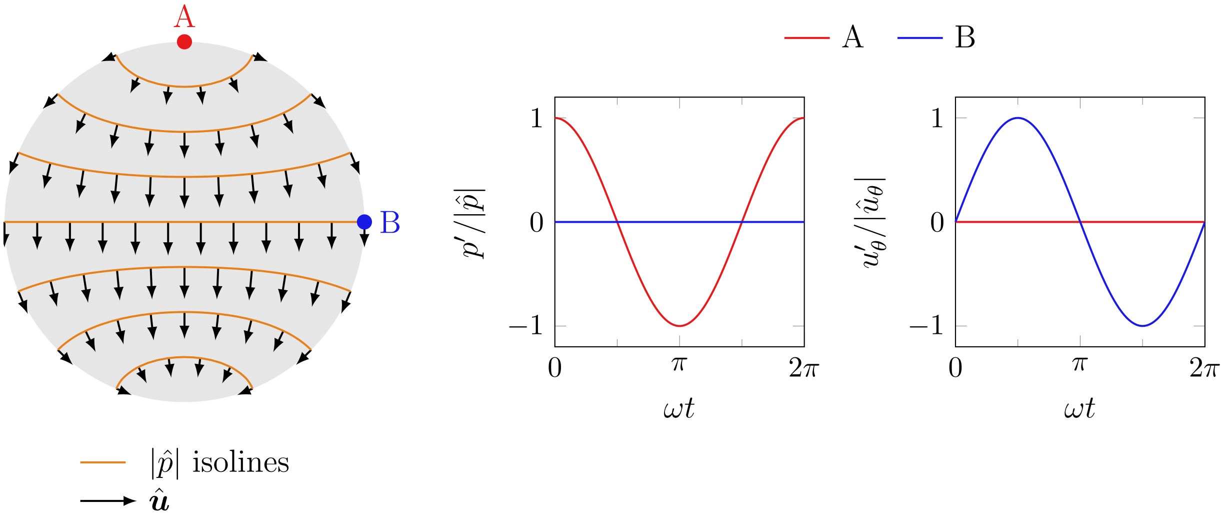

Figure 4.11: T_1 mode acoustic flow structure; A: Pressure antinode, B: velocity antinode

target (subscript $_t$) pressure fluctuation given as[5]

$$p'_t = \hat{p}_t \exp(i\omega t) cos(k\xi) \quad , \tag{4.53}$$

which represents the pressure fluctuations that shall be imposed on the flame. In Eq. 4.53 ω is the oscillation frequency of the mode under consideration, $k = \omega/c$ is the wave number (cf. Eq. 2.44) and ξ is the circumferential coordinate, linearized at the location of the flame under consideration as shown in Fig. 4.10. So this approach replaces the analytical circumferential solution for a curved geometry, $\Theta_{mn} = cos(m\theta)$ (cf. Eq. 2.42 and 2.43), with a local cartesian approximation, $\Theta_{mn} = cos(k\xi)$. As already stated by Schmid and Sattelmayer [58] the value of the wave number k does not match the actual radial wave number of a transverse mode (Eq. 2.45b in Sec. 2.4). The phase of the pressure amplitude is set constant across the domain in this initial approach. To obtain the velocity fluctuations at the boundary of the single flame domain that correspond to the target pressure fluctuation Eq. 4.53 is inserted into the ξ-wise (cf. Fig. 4.10) linearized momentum equation. Mean flow gradients are neglected. The mass to be

---

[5] The complex exponential form of the harmonic oscillations is used here for consistency with the other derivation in this work. The original derivation has been performed for a sinusoidal target pressure perturbation.

injected into the single flame domain is approximated by multiplying the calculated velocity fluctuations with the mean density, giving

$$\frac{d\dot{m}_r'}{A_s} = u_\xi' \bar{\rho} = i\frac{\hat{p}_t}{c} \left|\sin\left(-k\xi\right) n_\xi\right| \exp(i\omega t) \tag{4.54}$$

with $\boldsymbol{n}$ the outward facing normal vector of the single flame domain boundary and A_s its shell surface, see Fig. 4.10. Schmid [3] extends the approach by using an axially dependent value of the target pressure amplitude with a distribution based on the analytical duct-flow acoustics solution (Eq. 2.42 and 2.43). Along with the mass source, momentum and energy source terms are derived to account for the mass addition in the respective conservation laws.

A validation of the approach has been conducted by comparing the target pressure amplitude distribution (Eq. 4.53) to the pressure oscillations that are actually obtained in the pressure excitation simulation [3]. For homogeneous flow excellent agreement has been found. However, once flow inhomogeneties were included in the calculations, severe differences between the target pressure profile and the resulting amplitude distribution were observed. Two reasons were identified: First, the sound speed used for the evaluation of Eq. 4.54 has not been adapted based on the local flow. Second, inconsistencies between the unsteady pressure profile imposed at the outlet of the single flame domain and the pressure fluctuations arise from the occurrence of axial acoustic waves in the simulation.

The pressure excitation procedure that the present work starts from is a modification of the above approach by Schmid and Sattelmayer, which has been introduced by Schulze [12]. He replaced the analytical axial distribution of the pressure amplitude by the amplitude profile obtained from a perturbation simulation of the studied configuration. Likewise, the sound speed is taken as the one-dimensional profile used in the mean-flow calculations (cf. Eq. 4.12). However, this approach still has the deficiency that the pressure fluctuations that occur in the excited single flame simulation do not match the target pressure fluctuations used to derive the source term (Eq. 4.54). A study by Chemnitz and Sattelmayer [54] showed that this deviation between target and actual pressure fluctuations can have a tremendous impact on the stability prediction. Depending on whether the target or the actually occurring pressure fluctuations are used for the FTF-calculation, the calculated stability behavior changed from stable to unstable. This topic is addressed further in Sec. 8.1.

An alternative approach to those described above has been taken by Török [11]. A periodically moving wall that follows the velocity u'_ξ is placed at a lateral domain boundary. The wall velocity is set uniform along the whole domain. A second approach that he proposed is the usage of a modified pressure and an isentropically adapted temperature and density as input for the chemical kinetic calculations. Both excitation methods result in significantly different pressure amplitude and phase distributions across the chamber. Neither approach matches the target pressure amplitude. The results have not been validated or used further.

4.3.1.2 Single Flame Domain Acoustics and Pressure Coupling Mechanisms

As outlined in the previous section 4.3.1.1 the main issue of the mass-source based single flame excitation is that the target pressure fluctuations which are meant to be imposed on the flow differ from those that are actually obtained in the simulation. The practical consequences that this deviation has for the stability predictions will be discussed in Sec. 8.1. In the present section the mechanisms leading to the observed pressure fluctuation mismatch are discussed. To understand the way these mechanisms reflect in the heat release fluctuations, an analysis of the processes that characterize the response of a single flame to a transverse chamber mode is conducted. The discussion is the basis for the subsequent development of a revised pressure response calculation procedure in Sec. 4.3.1.3.

The fundamental problem that causes a deviation between the pressure fluctuations obtained in the simulation and the target profile is the different acoustic behavior of the full chamber and the single flame domain at the excitation frequency. As discussed in Sec. 2.4.2 the stability-relevant transverse chamber modes are cut-on only close to the face plate. Further downstream, their amplitudes decline in axial direction. The radius of the single flame domain is considerably smaller than that of the whole chamber (cf. Sec. 5.1.4). Thus, it has a higher cut-off frequency than the chamber (cf. Eq. 2.54) and the chamber T_1 frequency corresponds to longitudinal fluctuations in the single flame domain. The periodic injection and extraction of mass according to Eq. 4.54 models the acoustic mass-flow that the single flame in a pressure anti-node of the chamber T_1 would be exposed to. However, in addition to the pressure fluctuations that are expected from the mass sources inside the single flame domain, the domain's own, longitudinal acoustics are excited. Thus in the single flame simulation longitudinal pressure fluctuations are superimposed on those corresponding to the mass source terms. This explanation will be confirmed by BKD single flame results in Sec. 7.1. To understand the impact that acoustic perturbations have on the heat release, the mechanisms governing its fluctuations are analyzed in the following.

The combustion in the chamber occurs in diffusion flames developing between the coaxially injected propellants (cf. Sec. 2.1). In such configurations, heat release is governed by the injection conditions, cross-streamwise mixing and finally chemical reaction. In the following, the impact that acoustic pressure fluctuations have on any of these processes is discussed. Regarding the injection conditions the primary response mechanism to be expected is a change of the propellants' mass flows due to a change of the injector's counter pressure in the chamber. In principle, the temperature and density changes that accompany the pressure fluctuations at the chamber inlet affect the injection conditions as well. However, for these changes to have a significant impact on the flow in the chamber, very high acoustic amplitudes are required. So this mechanism is not relevant for linear stability analyses. In the chamber, heat release is strongly affected by cross-streamwise mixing. It is only weakly dependent on the absolute pressure level but is governed by turbulence and hydrodynamic shear-layer instabilities. In contrast, reaction kinetics are in general subject to pressure influences. However, in the present study this sensitivity can be neglected. To demonstrate this aspect, the maximum temperature as well as the temperature profile as function of mixture fraction (cf. Sec. 5.1.3) are shown in Fig. 4.12 for the two propellant combinations H_2/O_2 and CH_4/O_2. The profiles are calculated from

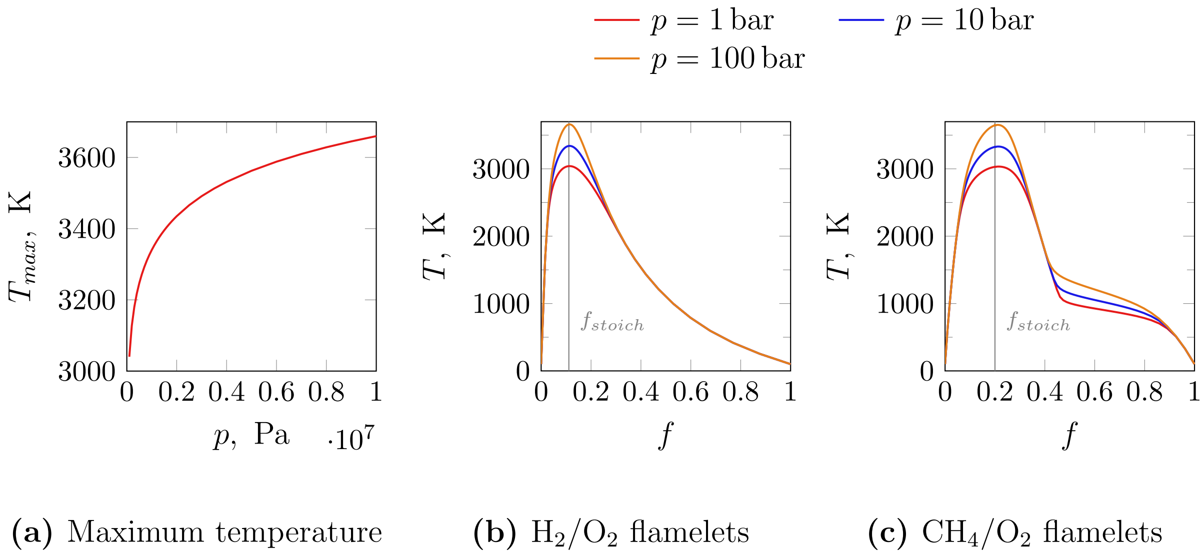

(a) Maximum temperature **(b)** H_2/O_2 flamelets **(c)** CH_4/O_2 flamelets

Figure 4.12: Pressure sensitivity of equilibrium temperatures

local chemical equilibrium (cf. Sec. 5.1.3), which is justified as combustion in the chamber is mixing-dominated. The qualitative shape of the temperature profiles in Fig. 4.12b and Fig. 4.12c is pressure independent but the maximum temperature changes. The development of the temperature maximum via pressure is given in Fig. 4.12a. The curves for the considered propellant combinations do not show significant differences. Particularly in the high pressure range, the sensitivity of the maximum temperature to pressure is low. The ratio of relative fluctuations is rather constant along the whole pressure range:

$$\frac{\partial T_{max}}{\partial p}\frac{p}{T_{max}} \approx 0.04 \quad , \tag{4.55}$$

i.e. the relative amplitude of temperature fluctuations to be expected by direct pressure effects on chemistry is only 4 % of the imposed relative pressure amplitude.

Following the previous explanations, the actual pressure value is of minor importance for the heat release fluctuations. However, the pressure fluctuations of a transverse mode come along with a mass flow that periodically enters and leaves the domain normal to the flame axis. This cross-stream mass flow directly influences the mixing of the radially stratified flow. The effect of longitudinal modes on the flow significantly differs from that associated with a transverse oscillation. Instead of impacting radial mixing, they induce axial velocity fluctuations, leading to a periodic axial displacement of the flow. In conclusion the actual pressure fluctuations occurring in the chamber are of secondary importance for the flame response. Instead, for transverse modes the associated cross-stream mass flow oscillations are the dominant mechanism impacting the heat release. The pressure amplitudes observed in the single flame simulation are a superposition of the source term related fluctuations and longitudinal acoustics. In this case the relation between pressure and heat release fluctuations obtained in the single flame simulations does not correctly reflect the flame dynamics associated with a transverse mode.

4.3.1.3 Revised Pressure Excitation

The previous approaches to characterize the pressure coupling mechanism were directed at reproducing a certain pressure rise in a compressible flow by mass injection or manipulating the domain geometry. As pointed out in Sec. 4.3.1.2 the key issue in this undertaking is the change of the domain's acoustic behavior when considering a single flame volume instead of the whole chamber. However, the actual pressure fluctuations in the chamber can be considered to be of minor importance for the heat release fluctuations. Instead, the acoustic-induced mass flow has the dominating impact on the flame response (cf. Sec. 4.3.1.2). Based on this concept, a revised version of the pressure excitation is developed in the present section. The basic idea is to avoid influences of the single flame domain's eigenacoustics by modeling the flow as incompressible[6] (cf. Sec. 2.2.2). The impact of the transverse acoustics on the mode is brought into the simulation by modeling the transport processes associated with the acoustic mass fluxes. They are represented by volumetric source terms, which are derived in Sec. 4.3.1.3.1. The presence of source terms in incompressible flow induces additional, non-acoustic flow oscillations. This aspect is discussed in Sec. 4.3.1.3.2. There, also a dynamic modification of the local density is proposed to reduce the

---

[6] Several approaches to suppress longitudinal dynamics, like the usage of non-reflecting outlet boundary conditions or inserting a region of high viscosity at the chamber end, remained unsuccessful.

Table 4.4: Source terms for pressure excitation

Flow				Combustion & Turbulence		
conservation Eq.		source	ϕ	variable	source	ϕ
mass (Eq. 2.11)		Eq. 4.59	–	turb. kinetic energy	Eq. 4.68	k
momentum (Eq. 2.12)	x	Eq. 4.70, 4.68	u_x	turb. dissipation rate	Eq. 4.68	ϵ
	r	Eq. 4.68	u_r	mean mixture fraction	Eq. 4.68	f
enthalpy (Eq. 2.21)		Eq. 4.68	H	mixture fraction variance	Eq. 4.68	f'^2

negative side effects from incompressible flow modeling in the single flame computations. The flame response obtained from the approach derived in the present section is evaluated for the BKD in Sec. 7.1 and applied in the stability analysis in Chap. 8.

4.3.1.3.1 Excitation Source Terms The mass fluxes induced by acoustic fluctuations (cf. Sec. 4.3.1.3) cause additional convective transport. To model the effect that this convection has on the single flame solution, source terms for the equations describing flow (Eq. 2.11, 2.12 and 2.21, cf. Sec. 5.1), combustion (cf. Sec. 5.1.3) and turbulence (cf. Sec. 5.1.1) are derived in the following. Starting point is the mass source term for the continuity equation. Based on the result, source terms for the other equations are derived. Finally, an additional, pressure-related momentum source is proposed to account for the axially non-constant excitation pressure amplitudes. The resulting source terms are summarized in Tab. 4.4.

The acoustically induced mass flows are the result of transverse velocity fluctuations. For a flame located at a pressure antinode, these fluctuations are small but not zero due to the finite cross-section of the single flame domain. The associated flow pattern is not axissymmetric, i.e. the induced velocity fluctuations have a radial as well as circumferential component. In the present work, like in the previous one [12], the pressure-response calculations are based on two-dimensional simulations (cf. Sec. 5.1) for computational efficiency. So any cross-stream mixing modulation is purely radial. The injection at the domain boundary (cf. Sec. 4.3.1.1) is replaced by a volumetric source term distribution. This way no representative sound speed profile for the calculation of the mass sources according to Eq. 4.54 needs to be determined. Moreover, the time delay between the injection of the excitation mass flow at the boundary and the injected mass reaching the center of the single flame domain is eliminated. The findings of Chemnitz and Sattelmayer [57] showed that the presence of radial flow gradients in the mean flow does not significantly alter the pressure mode shape of the chamber T_1 mode. In contrast, the radial velocity perturbations were clearly influenced by radial stratification of the sound speed distribution. Thus it seems appropriate to assume a constant pressure amplitude within each flame cross-section for the derivation of the source term. In this case, the target amplitude distribution (Eq. 4.53) becomes

$$p'_t = \hat{p}_t \exp(i\omega t) \quad . \tag{4.56}$$

The pressure-related isentropic density change is calculated as (cf. Eq. 2.37),

$$\frac{\partial \rho}{\partial t} = \frac{1}{c^2}\frac{\partial p}{\partial t} \quad . \tag{4.57}$$

The mass source $\mathcal{S}_m$ shall represent the convection due to radial acoustic mass flux fluctuations. It is obtained from the linearized continuity equation 2.30. Since the single flame is considered axis-symmetric, circumferential gradients vanish, giving

$$\mathcal{S}'_m \equiv -\frac{1}{r}\frac{\partial}{\partial r}\left(r\rho u_r\right)' \overset{Eq.2.30}{=} \frac{\partial \rho'}{\partial t} + \bar{u}_x\frac{\partial \rho'}{\partial x} + \frac{\partial \bar{u}_x}{\partial x}\rho' + \bar{\rho}\frac{\partial u'_x}{\partial x} + \frac{\partial \bar{\rho}}{\partial x}u'_x \quad . \tag{4.58}$$

Due to the long flame and the primarily radial stratification of the flow the term depending on the axial gradient of the mean-flow velocity is neglected. The last two terms in Eq. 4.58 contain the axial velocity fluctuations and their gradient, respectively. Due to the transverse nature of the mode, axial velocity fluctuations are predominantly induced by secondary mechanisms. The evanescence of the pressure amplitudes due to the change of the cut-on frequency along the chamber length (cf. Sec. 2.4) causes fluctuations of the axial pressure gradient, which in turn lead to axial velocity fluctuations (cf. Eq. 2.31). Likewise, axial mean flow gradients may induce axial velocity perturbations according to Eq. 2.31. Neglecting the corresponding terms and combining Eq. 4.57 and 4.58 leads to the source term formulation

$$\boxed{\begin{aligned} \mathcal{S}'_m &= \frac{1}{c^2}\left(\frac{\partial p'_t}{\partial t} + \bar{u}\frac{\partial p'_t}{\partial x}\right) \\ &\approx \frac{1}{c^2}\left(\frac{\partial p'_t}{\partial t} + u\frac{\partial p'_t}{\partial x}\right) \end{aligned}} \quad . \tag{4.59}$$

To obtain Eq. 4.59 temporal and axial gradients of the sound speed have been assumed to be small. The approximation in Eq. 4.59 adds the second order convection term $1/c^2 u' \frac{\partial p'}{\partial x}$ to the RHS. This adaption is advantageous for the implementation of the source term calculation in the single flame simulations. The consistency of the mass source according to Eq. 4.59 with the mass flow excitation of Schmid et al. (Eq. 4.54) is shown in the following. Thereto, the radial excitation mass flow per axial distance is calculated from both equations and the results are compared.

First, the additional assumptions used in the derivation of Eq. 4.54 are applied to Eq. 4.59, namely a purely axial density and sound speed profile as well as negligible convection. Integrating Eq. 4.59 within one cross section and using the harmonic ansatz for p' gives for the total radial mass flow per axial distance

$$\frac{d\dot{m}'_r}{dx} = \int_{A_{sf}} \mathcal{S}'_m d\breve{A} = i\pi R_{sf}^2 \frac{\omega}{c^2} \hat{p}_t \exp(i\omega t) \tag{4.60}$$

with A_{sf} the cross-sectional area of the single flame domain. For the approach of Schmidt et al. (Eq. 4.54) the linearized circumferential coordinate and the corresponding normal vector component are expressed as

$$\xi = R_{sf} cos(\phi) \ , \quad n_\xi = cos(\phi) \tag{4.61}$$

with ϕ the angular coordinate of the single flame domain (cf. Fig. 4.10). An order of magnitude estimation of the sine argument in Eq. 4.54 for a T_1 mode gives

$$\mathcal{O}\frac{\omega}{c}\xi = \frac{10^4}{10^3} 10^{-2} = 10^{-1} \quad , \tag{4.62}$$

so the small-angle approximation $sin(\omega/c\xi) \approx \omega/c\xi$ can be used. Inserting the small-angle approximation along with Eq. 4.61 into Eq. 4.54 and integrating along the perimeter of the domain cross-section gives

$$\begin{aligned}\left.\frac{\partial \dot{m}'_r}{\partial x}\right|_{r=R_{sf}} &= \int_0^{2\pi} \frac{d\dot{m}'}{dA_s} R_{sf} d\varphi \\ &= i\int_0^{2\pi} \cos^2(\varphi) d\varphi R_{sf}^2 \frac{\omega}{c^2} \hat{p}_t \exp(i\omega t) \\ &= i\pi R_{sf}^2 \frac{\omega}{c^2} \hat{p}_t \exp(i\omega t)\end{aligned} \tag{4.63}$$

with A_s the single flame domain surface area (cf. Fig. 4.10). This result is identical to Eq. 4.60, which has been obtained from Eq. 4.59. So the acoustic mass flows within each cross-section match for both approaches.

Based on the the mass source (Eq. 4.59) now the source terms for the other transport equations are derived. The mass source represents the net mass added at a certain location in the chamber due to acoustic-induced mass flow. The associated radial mass flux at position r in the single flame domain is obtained as

$$\frac{\partial \dot{m}'_r}{\partial x} = \int_0^r \mathcal{S}'_{m,p'} 2\pi \check{r} d\check{r} \quad . \tag{4.64}$$

This mass flux impacts any flow field whose transport equation contains a convective term (cf. Tab. 4.4). However, the mass source term (Eq. 4.59) only models the redistribution of mass within the domain cross-section. The velocities associated with the mass flux according to Eq. 4.64 are not induced. Consequently, the acoustics-related radial convective transport of other variables needs to be explicitly modeled via source terms as well. The temporal fluctuations of a variable ϕ due to convection (subscript $_{conv}$) read

$$\left.\frac{\partial(\rho\phi)}{\partial t}\right|_{conv} = -\nabla \cdot (\rho \boldsymbol{u} \phi)' \tag{4.65}$$

or, when considering the radial component,

$$\left.\frac{\partial(\rho\phi)}{\partial t}\right|_{conv,r} = -\frac{1}{r}\frac{\partial}{\partial r}\left(r\rho u_r \phi\right) \tag{4.66}$$

$$= -\frac{1}{r}\frac{\partial}{\partial r}\left(r\overline{\rho u}_r \phi\right) - \frac{1}{r}\frac{\partial}{\partial r}\left(\frac{1}{2\pi}\frac{\partial \dot{m}'_r}{\partial x}\phi\right) \quad . \tag{4.67}$$

The first term on the RHS of Eq. 4.67 is part of the solution of the excitation simulation and thus does not need to be modeled explicitly. The effect of the acoustic mass flow fluctuations on the flow is contained in the second term of Eq. 4.67. The source term S_ϕ to model the acoustically induced convective transport of a variable ϕ reads:

$$\boxed{\mathcal{S}'_\phi = -\frac{1}{r}\frac{\partial}{\partial r}\left(r\frac{\dot{m}'_r}{A}\phi\right)} \tag{4.68}$$

with $\dot{m}'_r$ according to Eq. 4.64. The source term Eq. 4.68 occurs in all flow equations except for the continuity equation (see Tab. 4.4). Since this way only the net-transport due to acoustic induced mass flow is modeled without inducing the associated acoustic velocity fluctuations, the pressure excitation is separated from the velocity excitation (Sec. 4.3.2) even more clearly than in the case of radial mass injection at the domain boundaries (Eq. 4.54).

The principle behind the convective source term also reflects in the way Eq. 4.68 is implemented in the solver, visualized in Fig. 4.13. For each computational cell i the radial mass flux $\dot{m}'_{r,j}$ at its face A_j is calculated from Eq. 4.64. Following Stokes' theorem, the source is then obtained as

$$\mathcal{S}'_{\phi,i} = -1/V_i \sum_{j=\{r^\pm,z^\pm\}} \dot{m}'_{r,j}\phi_k A_j n_{r,j} \tag{4.69}$$

with k the index of the cell upstream of face A_j according to $\dot{m}'_r$. V_i is the volume of cell i and $n_{r,ij}$ is the radial component of the face's outward pointing normal vector.

The mass source term Eq. 4.58 has been developed under the assumption that the acoustic pressure fluctuations are constant within each chamber section. However, the pressure amplitudes change along the chamber axis. The resulting axial pressure gradient fluctuations cause axial velocity fluctuations (cf. Eq. 2.31). While their impact on the radial mass flux fluctuations has been neglected in the derivation of Eq. 4.59, they can be readily accounted for in the excited single flame simulation. Due to the incompressible flow modeling, no acoustic pressure fluctuations occur in the single flame

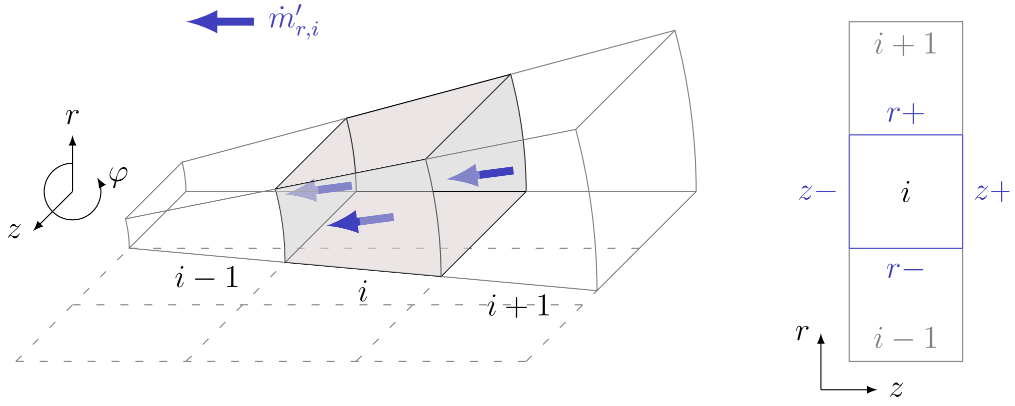

Figure 4.13: Volume source term principle

simulation and thus the aforementioned pressure gradient fluctuations are not captured. To nevertheless account for the acoustic pressure gradient fluctuations an additional source term is applied to the axial momentum equation, reading

$$\boxed{\mathcal{S}'_{u,\nabla p'} = -\frac{\partial p'_t}{\partial x}} \quad , \tag{4.70}$$

based on the target pressure fluctuation Eq. 4.56. With Eq. 4.70 all source terms used for the single flame pressure excitation in this work have been introduced (cf. Tab. 4.4). Their application has some side-effects on incompressible flow, requiring a dynamic adaption of the local density. The incompressible flow dynamics and the development of said density correction are discussed in the next section 4.3.1.3.2.

4.3.1.3.2 Density Modulation Due to the decoupling of density from pressure, the propagation of acoustic waves is not captured correctly in incompressible flows. An acoustic pressure disturbance immediately affects the whole domain, allowing only processes whose time scales are much longer than those of acoustic propagation to be described correctly. While this behavior prevents the occurrence of acoustic modes related to the domain's eigenfrequencies, incompressible flows still show a dynamic response when exposed to unsteady source terms. To study these dynamics, an analytical solution for an incompressible, one-dimensional duct flow with harmonic mass addition is derived and analyzed. First, the case of constant density is considered in order to gain basic understanding of the processes occurring in excited, incompressible flow. This constant density case is found to potentially cause high velocity oscillations. To suppress these fluctuations, a second case with harmonically varying density is developed. This approach can be interpreted as a correction that introduces the compressible density response associated with a certain acoustic mode into the flow. The flame responses obtained with the different approaches are compared to each other in Sec. 7.1.

To study the incompressible flow dynamics a one-dimensional duct is considered. The domain stretches from $x = 0$ to $x = L$ and has a constant cross-sectional area A. The sound speed is constant and the flow is isentropic, i.e. Eq. 4.59 is applicable. Like for the single flame simulations, a constant mass flow boundary is set at the inlet, $\dot{m}|_{x=0} = \dot{m}_0$, while at the outlet the pressure is fixed, $p|_{x=L} = p_{out}$. The harmonic target pressure fluctuation is given as

$$p'_t = A_{ex} \psi_x \sin(\omega t) \tag{4.71}$$

with A_{ex} the target pressure amplitude at $x = 0$ and ψ_x the spatial shape function of the target pressure amplitude with $\psi_x|_{x=0} = 1$. For consistency with the constant outlet pressure $\psi_x|_{x=L} = 0$ is required. Since the flow is constant in cross-stream direction, the convective axial momentum source term Eq. 4.68 reads

$$\mathcal{S}'_u = \mathcal{S}'_m u_x \quad . \tag{4.72}$$

The pressure fluctuation gradient term Eq. 4.70 is neglected.

First, the case of temporally and spatially constant density is considered:

$$\frac{\partial \rho}{\partial t} = 0 \ , \ \nabla \rho = \mathbf{0} \quad . \tag{4.73}$$

Based on the continuity and inviscid momentum equations (cf. Eq. 2.11 and 2.12) an analytic solution for the flow velocity and pressure can be derived (cf. App. C.1), yielding

$$u_x = \frac{1}{\rho}\left(\frac{\dot{m}_0}{A} + \int_0^x \mathcal{S}'_m d\check{x}\right) \tag{4.74a}$$

$$p = p_{out} + \int_x^L \int_0^{\check{\check{x}}} \frac{\partial \mathcal{S}'_m}{\partial t} d\check{x} d\check{\check{x}} \quad . \tag{4.74b}$$

For further evaluation of the dynamic velocity and pressure, a target pressure amplitude distribution (cf. Eq. 4.71) is specified, loosely based on the shape of the axial amplitude distribution of a cut-off T_1 mode:

$$\psi_x = \cos\left(\frac{x}{L}\frac{\pi}{2}\right) \quad . \tag{4.75}$$

The mass source is calculated from Eq. 4.59 while neglecting the convective contribution[7]. For this case evaluating Eq. 4.74a and Eq. 4.74b gives

$$u_x = \frac{\dot{m}_0}{\rho A} + A_{ex}\frac{\omega}{\rho c^2}\cos(\omega t)\sin\left(\frac{x}{L}\frac{\pi}{2}\right)\frac{2L}{\pi} \tag{4.77a}$$

$$p = p_{out} - A_{ex}\frac{\omega^2}{c^2}\ \sin(\omega t)\ \cos\left(\frac{x}{L}\frac{\pi}{2}\right)\left(\frac{2L}{\pi}\right)^2 \quad . \tag{4.77b}$$

Eq. 4.77 can be interpreted as follows: Since the density is constant, any mass injected by the source terms must be transported convectively in order to fulfill the continuity equation 2.11. This leads to the velocity fluctuations (Eq. 4.77a). The acceleration associated with these velocity fluctuations corresponds to an unsteady pressure gradient. Along with the constant pressure

---

[7] This simplification eases the analytical solution. To confirm its justification the ration between the convective and the transient contribution in Eq. 4.59 for the shape function Eq. 4.75 is considered:

$$\frac{u_x \partial p'_t/\partial x}{\partial p'_t/\partial x} = \underbrace{\frac{u_x \pi/(2L)}{\omega}\tan\left(x\frac{\pi}{2L}\right)}_{amplitude\ ratio}\tan(\omega t) \quad . \tag{4.76}$$

For the T_1 mode of a representative rocket engine configuration (cf. Tab. 4.5) *amplitude ratio* $<<1$ holds for the most part of the duct. It only fails close to the outlet, where pressure amplitudes are small anyhow. The same logic applies to the temporal oscillations of Eq. 4.76, which are described by a tangent. The time range where the convective contribution to the source term Eq. 4.59 becomes equal or exceeds the transient part in magnitude is considerably small. The convective part in this time range is still significantly lower than the transient contribution at other time instances. Thus the convection related term in Eq. 4.59 can indeed be considered secondary compared to the transient part.

outlet this causes the pressure fluctuations (Eq. 4.77b). Taking the ratio of actual (from Eq. 4.77b) and target pressure amplitudes (Eq. 4.71) gives[8]

$$\frac{p'}{p'_t} = -\frac{\omega^2}{c^2}\left(\frac{2L}{\pi}\right)^2 \quad . \tag{4.78}$$

So the incompressible pressure fluctuations resulting from the source term excitation are in opposite phase to the pressure fluctuations used for the calculation of the source term. For a quantitative assessment of the dynamics under realistic conditions, a set of specifications based on the T_1 mode of the BKD test cases is considered. The values of the variables required for the evaluation of Eq. 4.77a and 4.77b for a single flame are given in Tab. 4.5. The pressure fluctuations at the domain inlet are shown for a relative excitation amplitude of $|\hat{p}|_{t,rel} \equiv A_{ex}/p_{out} = 0.01$ (cf. Eq. 4.71) in comparison with the target pressure fluctuations in Fig. 4.14. It is clearly visible that both curves are in opposite phase to each other (cf. Eq. 4.78). However, as discussed in Sec. 4.3.1.2 the direct impact of the pressure fluctuations on the heat release is small. Instead, the mass flow oscillations associated with the velocity fluctuations (Eq. 4.77a) are of interest, which are discussed below.

As density and volume of the domain are constant over time, the total mass inside the domain does not change. However, under excitation conditions a variable part of the mass stored in the domain no longer originates from the inlet mass flow but has been injected via the excitation source term. The total mass that has been injected from the source term is obtained

Table 4.5: Model flow specifications based on BKD T_1 mode

$f = \frac{\omega}{2\pi}$	$\dot{m}_0$	p_{out}	$r = \sqrt{\frac{A}{\pi}}$	L	c	ρ
10 kHz	$0.15\,\mathrm{kg\,s^{-1}}$	80 bar	6 mm	0.2 m	$1500\,\mathrm{m\,s^{-1}}$	$20\,\mathrm{kg\,m^{-3}}$

---

[8] The identical shape of the target pressure fluctuations and those occurring in the flow results from the ansatz chosen for the spatial distribution in Eq. 4.75 and is not general. E.g. for a linear ansatz $p'_t = A_{ex}\left(1 - \frac{x}{L}\right)\sin(\omega t)$ the resulting pressure fluctuations according to Eq. 4.74b is

$$p' = A_{ex}\frac{\omega^2}{c^2}\sin(\omega t)\left(\frac{x^2}{2} - \frac{x^3}{6L} - \frac{L^2}{3}\right) \quad .$$

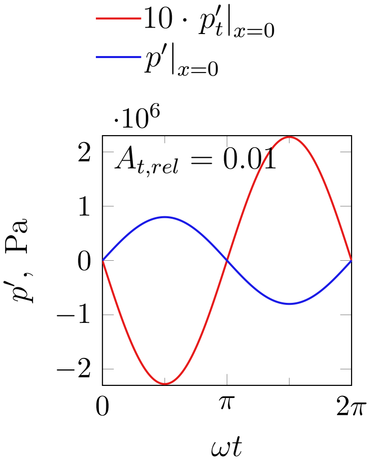

Figure 4.14: Pressure

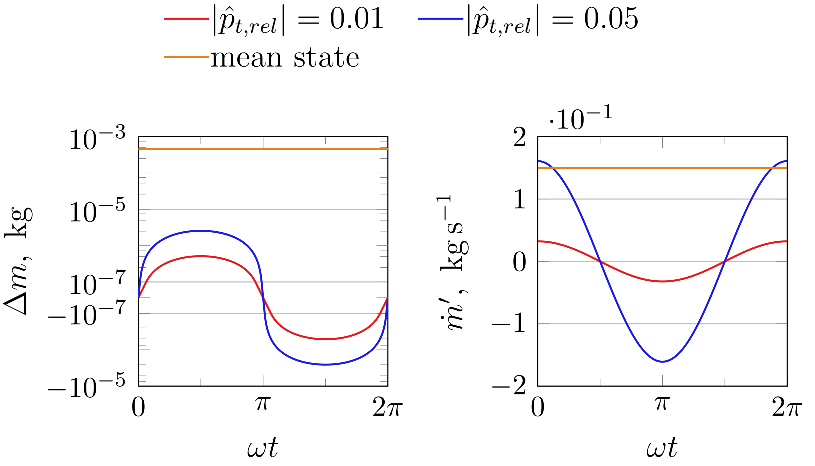

(a) Mass

(b) Mass flow

Figure 4.15: Contribution of mass source to flow

by integrating the mass source (Eq. 4.59) over time and space[9]. It can be considered as upper boundary for the mass in the domain originating from the excitation. The temporal development of this quantity via one excitation cycle is shown in Fig. 4.15a. For both excitation amplitudes, the amount of mass added by the source terms is at least two orders of magnitude lower than the total mass in the domain. However, this does not apply to the source term induced mass flow, shown in Fig. 4.15b. While for $|\hat{p}_{t,rel}| = 0.01$ the excitation mass flow peaks at around 20 % of the mean value, for $|\hat{p}_{t,rel}| = 0.05$ it temporarily even exceeds the inlet mass flow. This temporarily leads to a reversed flow at the domain outlet. For a more complex setup like that of a single flame simulation such a flow reversal might lead to a breakdown of the characteristic flow structures.

As just discussed, the application of source terms to an incompressible, constant density flow leads to velocity fluctuations. These arise from the convective transport of the mass brought into or extracted from the flow by the source terms. The additional convection is necessary in order to fulfill the continuity equation 2.11 since the isentropic density fluctuations, which

---

[9] Note that this integral only balances the mass that has been brought into or extracted from the domain by the mass source term. It does not account for the outflow of mass originating from the source terms through the outlet.

are usually associated with the acoustic propagation of disturbances, are not captured. To suppress the source-term related velocity fluctuations, a harmonic density variation is introduced, that accounts for the compressible density changes corresponding to the target pressure fluctuations:

$$\rho = \bar{\rho} + \frac{1}{c^2} p'_t \quad . \tag{4.79}$$

The mass source term is calculated according to Eq. 4.59 with the target pressure fluctuations from Eq. 4.71. Under these conditions the analytic flow solution becomes (cf. App. C.2):

$$u_x = \frac{\dot{m}_0}{A\, \rho|_{x=0}} \tag{4.80a}$$

$$p = p_{out} + \frac{u_x}{c^2} \left.\frac{\partial p'_t}{\partial x}\right|_{x=0} \left(\frac{1}{\rho|_{x=0}} \int_x^L \rho d\check{x} + \int_L^x \psi d\check{x} \right) + \frac{u_x^2}{c^2} p'_t \quad . \tag{4.80b}$$

At each time instant the velocity is constant across the whole domain and determined by the inlet mass flux along with the density at $x = 0$. Since $|\hat{\rho}| << \bar{\rho}$, the velocity fluctuations can be considered as reasonably small. For the conditions from Tab. 4.5 they are shown in Fig. 4.16. The pressure fluctuations (Eq. 4.80b) obtained with the target pressure amplitude distribution according to Eq. 4.71 and Eq. 4.75 are shown for $A_{t,rel} = 0.01$ in Fig. 4.16a. The fluctuations are considerably lower compared to the constant density case (Fig. 4.14). The temporal development of the flow velocity (Eq. 4.80a) is shown in Fig. 4.16b. The occurring amplitudes are small compared to the mean velocity.

In summary, the harmonic density modulation (Eq. 4.79) is a viable approach to suppress the incompressible flow velocity dynamics arising from the source terms Eq. 4.59 and Eq. 4.68. Its usage in the context of an actual flame response calculation is studied further in Sec. 7.1.

4.3.2 Velocity Coupling

Velocity coupling is the second flame response mechanism besides the pressure coupling discussed in Sec. 4.3.1. It refers to the response of the flame

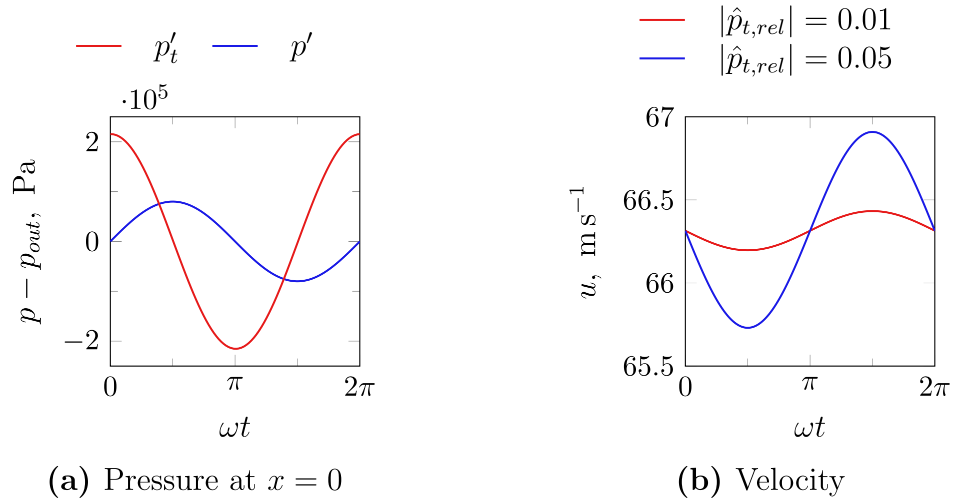

(a) Pressure at $x = 0$ **(b)** Velocity

Figure 4.16: Incompressible flow with harmonic density fluctuations

to transverse velocity fluctuations. Unlike the pressure response, which depends on the mass added to or substracted from the single flame by acoustic mass flows, the velocity coupling represents a unidirectional acceleration without significant net mass flow across the domain borders. The impact of the velocity response on the chamber stability has been found to be minor [12] compared to the pressure coupling. However, several studies [12,45] have found a notable influence on the flow field in the form of flame shortening. Thus, the flame's velocity response will be considered for the radiation based validation in Sec. 5.3.3. Thereto, the velocity fluctuations that a single flame is exposed to in the presence of a chamber T_1 are induced in a single flame simulation. The corresponding procedure is covered in the present section. First, an overview of the previous development of this velocity excitation approach is given (Sec. 4.3.2.1), followed by the revised procedure that is developed in the present work (Sec. 4.3.2.2).

4.3.2.1 Previous Development

Analogously to the pressure response calculation discussed in Sec. 4.3.1 the effect of transverse velocity fluctuations on a single flame is modeled via source terms. The method is based on the work of Schmid and Sattelmayer [58]. A flame in a velocity anti-node of the chamber is considered since there pure acoustic velocity fluctuations without superimposed pressure oscillations occur (point B in Fig. 4.11). Due to the asymmetry of the acoustic velocity at the pressure nodal line three-dimensional simulations need to be carried out (cf. Sec. 5.1.4). As the flame is insensitive to the direction of the velocity fluctuations, the heat release fluctuates at double the excitation frequency [3]. The impact of the chamber's transverse acoustics on the single flame are represented by a cross-stream momentum source term (see Fig. 4.10 for coordinate definitions)

$$\mathcal{S}'_{u,\xi} = \bar{\rho}\frac{\partial u'_\xi}{\partial t} \quad . \tag{4.81}$$

Initially, Schmid and Sattelmayer [58] propose to use a global reference density, which in combination with a constant velocity amplitude leads to a constant source term. Later Schmid calculates the excitation velocity amplitude $\hat{u}_\xi$ based on an equivalent excitation pressure [3] as

$$\bar{\rho}\hat{u}_\xi = \frac{|\hat{p}_t|}{cs_{mn}} \quad . \tag{4.82}$$

Schulze [12] applies the same coordinate linearization as in the derivation of the pressure excitation (cf. Sec. 4.3.1.1, Eq. 4.53), leading to the source term

$$\mathcal{S}_{u,r} = kcos(k\xi)\hat{p}_t exp(i\omega t) \quad . \tag{4.83}$$

The analysis of the BKD flame response with the excitation procedure [12] showed that, despite having a small impact on the stability behavior, the transverse velocity fluctuations lead to a notable flame shortening. This has been confirmed by LES-studies of the BKD [45].

4.3.2.2 Revised Velocity Excitation

In the present work, velocity excitation is used in the context of OH* radiation-image based validation (cf. Sec. 5.3.3). Thereto, a single flame in the outer injector row is considered, requiring an excitation approach that takes into account the velocity fluctuations of a specific flame. While the approach of Schmid (Eq. 4.82) accounts for the mode order via the

Bessel derivative root s_{mn} (cf. Eq. 2.45b), it does not include the dependence of the velocity fluctuations on the radial position in the chamber. Furthermore, the later introduction of the circumferential pressure distribution's cartesian approximation (cf. Eq. 4.53, Sec. 4.3.1.1) into the velocity excitation equations (Eq. 4.83) changes the wave number used in the source term calculation. In the following, a revised source term is derived that is based on the full analytical solution for cylindrical duct flow acoustics (cf. Sec. 2.4). It takes into account results of a previous study regarding the influence of radial stratification on transverse eigenmodes [57].

The derivation of the revised excitation procedure consists of three steps. First, a relation between the target pressure amplitude distribution and the velocity amplitudes at the pressure nodal line is retrieved, based on the acoustic solution of a uniform duct-flow (cf. Sec. 2.4). From these velocity amplitudes a momentum source term is derived. Finally, the source term is corrected for the fact, that the flow is non-uniform across the single flame's cross-section. Starting point for the derivations is the circumferential linear momentum equation (cf. Eq. 2.31). The chamber mean flow is considered swirl free and there is no radial velocity component. Likewise at the pressure nodal line there are no radial velocity fluctuations for a transverse mode. Moreover, in agreement with the original derivation of the source term, axial convection effects are neglected. The result is the equation

$$\frac{\partial u'_\theta}{\partial t} = -\frac{1}{r\bar{\rho}}\frac{\partial p'}{\partial \theta} \quad , \tag{4.84}$$

which is evaluated at the pressure nodal line for a standing transverse mode of order m. The target pressure amplitude Eq. 4.56 represents a pressure anti-node, which is located at the chamber wall. To obtain the cross-sectional distribution of the target pressure amplitude, it is combined with the radial and circumferential shape functions from the analytic duct acoustics solution (Eq. 2.43b and 2.43c):

$$\hat{p} = \hat{p}_t \frac{R_{mn}}{R_m n|_{r=R}} \Theta_{mn} \quad . \tag{4.85}$$

The radii r and R here refer to the coordinate frame of the whole chamber and not the single flame domain. After inserting Eq. 4.85 into Eq. 4.84 the target velocity amplitude at the pressure-nodal line is obtained as

$$\hat{u}_{\theta,t} = i\hat{p}_t \frac{m}{\omega r \bar{\rho}} \frac{J_m\left(s_{mn} r/R\right)}{J_m\left(s_{mn}\right)} \quad . \tag{4.86}$$

To evaluate the source term required for the flame excitation the circumferential momentum equation, this time including axial convection, is rearranged. As we consider pure velocity excitation and the mean flow on which the fluctuations are imposed is rather isobaric, the pressure term vanishes resulting in

$$\mathcal{S}_\theta = \bar{\rho}\left(\frac{\partial u'_\theta}{\partial t} + u_x \frac{\partial u'\theta}{\partial x}\right) \quad . \tag{4.87}$$

The density from the mean flow can be used here as we consider a pressure node, i.e. no acoustic density fluctuations occur. A previous study of the impact of radial stratification on the acoustics [57] showed that while the pressure amplitudes are nearly unaffected by radial flow gradients, the velocity amplitude distribution follows the sound speed stratification. To represent this result in the excitation procedure, the momentum source is varied based on the local sound speed:

$$\mathcal{S}_\theta = \bar{\rho}\left(\frac{\partial u'_{\theta,t}}{\partial t} + u_x \rho \frac{\partial u'_{\theta,t}}{\partial x}\right) \frac{c}{c_{1D}} \quad . \tag{4.88}$$

Eq. 4.88 is the source term used for the velocity fluctuations. It is used within transient single flame simulation following the setup described in Sec. 5.1. The velocity excitation results are used for the radiation based single flame validation in Sec. 5.3.3.

5 Single Flame Simulation

The stability assessment procedure outlined in Chap. 4 relies heavily on simulations of single rocket flames. To provide a sound basis for the evaluation and assessment of the procedure and its components in Chap. 6 and 7, in the present chapter the calculation approach for the single flame simulations is developed and validated. The chapter is divided in three parts. In Sec. 5.1 the numerical setup for the single flame simulations is discussed. In the subsequent section 5.2 an approach is developed to obtain OH^* radiation images from the numerical results. These are used together with further experimental data for the validation of the single flame calculations (Sec. 5.3). The validated setup is the basis for the mean flow and flame response calculations used in Chap. 6 and Chap. 7, respectively.

5.1 Numerical Setup

In the present section, the modeling for the single flame simulations is introduced. To ensure the appropriateness of the model choices and the numerical setup, a validation of the single flame results is carried out using experimental data in Sec. 5.3. Different variants of the single flame simulation setup are used. To extract the axial profiles for the mean-flow simulations, steady, two-dimensional calculations are performed. In contrast, the characterization of the flame dynamics requires transient simulations, either in two or three spatial dimensions, depending on the type of flame response under consideration (cf. Sec. 4.3). While pressure excitation is applied in two-dimensional simulations, velocity excitation calculations need to be conducted three-dimensional. The aspects of domain selection and dimension are addressed further in Sec. 5.1.4 of the present chapter.

The calculations are carried out with ANSYS® Fluent [59]. This tool offers real gas modeling capabilities along with customization options [60] that allow to implement the specific sub-models required for the stability assessment procedure (Chap. 4). The simulations are conducted using Fluent's coupled solver, a pressure based algorithm that solves the momentum and continuity equations simultaneously. This choice along with a strong underrelaxation of density are necessary to achieve convergence. In the following, the modeling of turbulence (Sec. 5.1.1), combustion (Sec. 5.1.3) and the used equation of state (Sec. 5.1.2) are addressed. Finally, domain selection along with discretization aspects (Sec. 5.1.4) and boundary conditions are discussed (Sec. 4.1.2.1).

5.1.1 Turbulence Modeling

The single flame results are obtained from Reynolds Averaged Navier Stokes (RANS/URANS) simulations. This is done with respect to the requirement of a computationally lean stability assessment procedure[1]. Turbulence closure of the RANS equations is achieved using the k-ϵ model. This choice is based on a study by Chemnitz et al. [61] that compares numerical results obtained with different solvers, combustion and turbulence models for a single CH_4/O_2 rocket engine flame with experimental validation data. From the two most common models, the k-ϵ and the k-ω-sst model, the k-ϵ model has been found to provide significantly better agreement with the experimental data, particularly in combination with a flamelet combustion model. The turbulent transport of species and energy is modeled as gradient based flux with the respective diffusivities obtained via turbulent Schmidt (Sc_t) and Prandtl (Pr_t) numbers. For the BKD these are calibrated using experimental data in Sec. 5.3. For the TCDs their values are selected based on a previous study covering a single-flame rocket combustor fueled with either H_2/O_2 or CH_4/O_2 [62]. Their values are $Sc_t = 1.1$ for TCD2 and $Sc_t = 0.7$ for TCD3.

---

[1] For comparison, the LES of a single BKD load point required a mesh with 10 M cells [40]. The authors of a full BKD LES study [43] note that, while LES is suitable to help the understanding of instability phenomena, its cost becomes unreasonable for systematical design studies.

For the k-ϵ model specific wall treatment needs to be applied when regions close to solid boundaries (here at the faceplate and in the injection system) are resolved. For this purpose, several models are available in Fluent, three of them seem appropriate for the current application:

- Scalable Wall Functions (SWF)
- Enhanced Wall Treatment (EWT)
- Menter Lechner near wall treatment (ML)

These three approaches have in common that they allow for a flexible wall resolution, i.e. cells may be placed even within the viscous sublayer, giving more flexibility in terms of grid generation. In the following, the treatment of the turbulent quantities for the different wall models is briefly outlined. Detailed information, also on the treatment of energy and momentum equations, are given in the Fluent Theory Guide [63]. The Scalable Wall Functions make use of the classical wall function approach, referring to Launder and Spalding [64]. However, to avoid deterioration for low values of the dimensionless wall distance[2] y^* the argument of the wall functions is replaced by $\widetilde{y^*} = \max\left(y^*, 11.225\right)$, i.e. the wall nearest cell is treated as having a sufficient distance to the wall to lie within the log-law region of the boundary layer. For the enhanced wall treatment the flow is divided into a viscosity affected near-wall and a fully turbulent region based on a turbulent Reynolds number that takes the wall distance as length scale. In the inner region a low-Reynolds one-equation model [65] is solved and the calculated turbulent viscosity is smoothly blended with the solution in the outer flow. The Menter Lechner near wall treatment uses an additional source term in the k transport equation that accounts for the impact of near wall effects on turbulence. However, details on the formulation of the source term are withheld by ANSYS.

As the present work deals with the acoustic stability on system level, local effects of turbulence modeling on the solution are of minor importance.

---

[2] In Fluent, the dimensionless wall distance y^* is used. In contrast to the more common y^+, the reference velocity is based on the turbulent kinetic energy rather than the wall shear stress. However, for equilibrium turbulent boundary layers both definitions give close results [64].

However, a potential impact of the wall treatment on the large scale flow properties needs to be considered in the model selection. The wall pressure profiles obtained from a steady, two-dimensional simulation of BKD load point LP2 (cf. Sec. 3.1.1) with different wall models are shown in Fig. 5.1a and are almost identical. More distinct differences are found when evaluating the flame structure and combustion development in terms of the axial heat release distribution (Fig. 5.1b) and the contour of stoichiometric mixture fraction (Fig. 5.1c). While the Enhanced Wall Treatment and the Scalable Wall Functions produce nearly identical results, the Menter Lechner approach predicts a slightly shorter flame. In the heat release distribution this leads to slightly increased values in the front part of the chamber but an earlier decay. The same behavior is found for LP1 (calculated with the constant Z approach, see section 5.1.2). So regarding the relevant flow profiles the Fluent-specific Menter Lechner approach deviates from the more established models and no data are available for the test case that allow for a detailed experimental validation. Therefore the Menter Lechner near wall treatment is discarded in this work. Since the other two models produce equivalent results, the Scalable Wall Functions are selected, as they improve convergence compared to the Enhanced Wall Treatment.

5.1.2 Equation of State

The injection conditions of the different test cases lie in the trans- or slightly supercritical regime (cf. Fig. 3.2). The adequate modeling of the flow at this state requires a real gas description. A comparison of the thermal EOS of several common real gas approaches against data from the NIST database for BKD conditions [12] showed that the Soave Redlich Kwong (SRK) model [66] provided the best agreement, with a good prediction of densities, although notable deviations occurred in the sound speed. The SRK EOS is a cubic EOS, possessing the structure of Eq. 2.9. While there are additional advanced equations of state, that provide further improvements, these cannot be implemented in the used solver at reasonable cost.

For the BKD load point LP1 a slightly different approach needs to be taken.

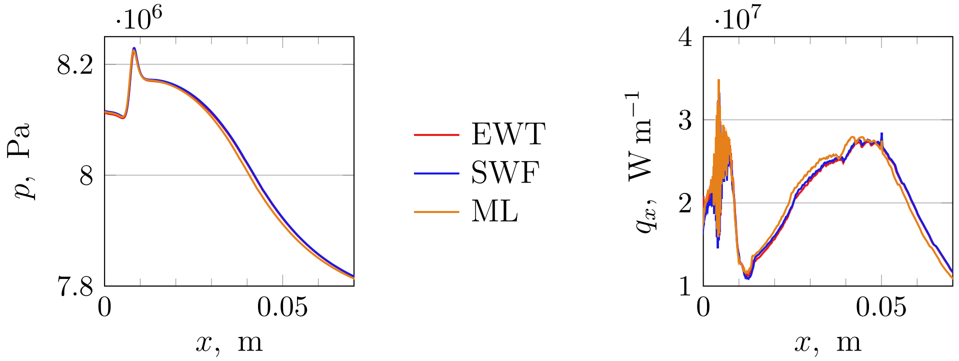

(a) Wall pressure **(b)** Heat release

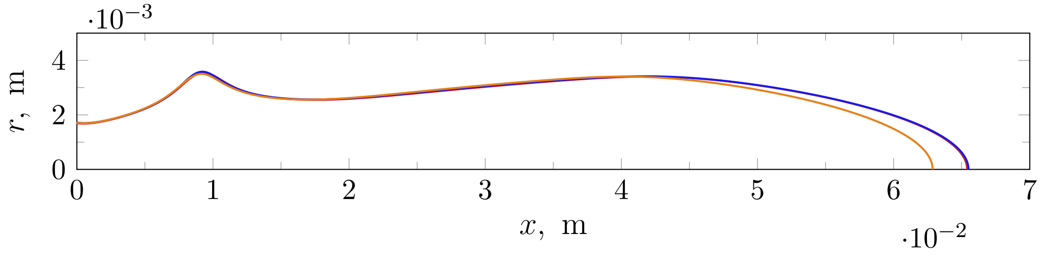

(c) Flame contour

Figure 5.1: Influence of turbulence wall modeling on single flame results for BKD LP2

The nominal chamber pressure of this case, which is measured at the measurement ring in the front region of the chamber (cf. Tab. 3.1d and Fig. 3.1), is only slightly above the critical pressure of oxygen. As the pressure decreases further downstream (cf. Fig. 5.1a) the flow regime becomes subcritical, leading to convergence problems. Two approaches to overcome this issue without devoting unreasonably large resources to the CFD simulations are considered in the following: a fully incompressible simulation and an ideal gas description combined with a spatially non-constant but pressure-independent real gas factor. As the pressure change across the chamber is small (about 6 % of the nominal value for LP1) and density and temperature gradients mainly arise from the combustion, an incompressible simulation can be considered appropriate. Thereto, the density is calculated using the thermodynamic SRK EOS at the nominal chamber pressure for the local flow composition and temperature. The alternative is to evaluate the real gas factor according to Eq. 2.8 at a reference pressure p_{ref} that is set to the

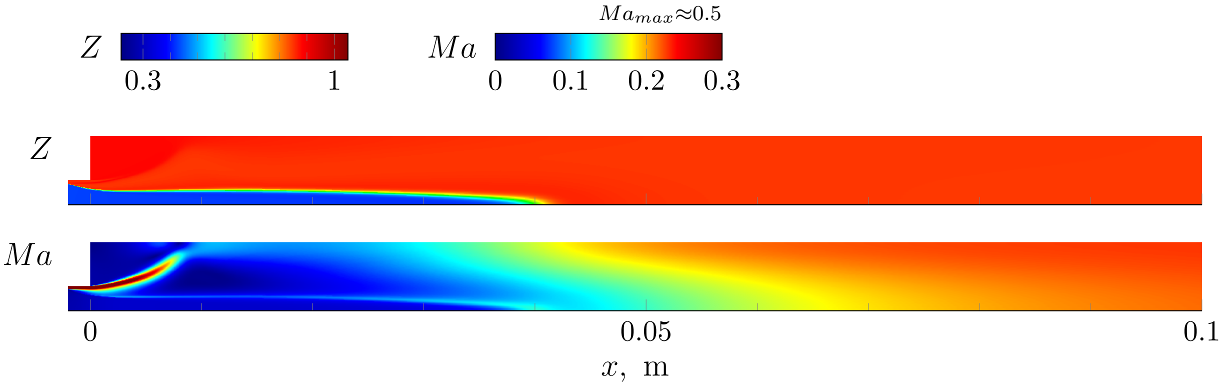

Figure 5.2: Mach number and real gas factor for BKD LP2

nominal chamber pressure, which is supercritical for all BKD load points considered in this work (cf. Sec. 3.1.1). This method is referred to as 'Z_{ref}'-approach in the following. It bases on the incompressible density as well but corrects it for pressure changes like an ideal gas as

$$\rho = \rho_{SRK,p_{ref}} \frac{p}{p_{ref}} \tag{5.1}$$

with ρ_{SRK} the density calculated at the local flow composition and temperature for the reference pressure p_{ref}.

With both approaches no real gas effects are considered in the caloric equation of state. Since the impermeable domain boundaries are modeled as adiabatic, total energy redistribution within the flow is of minor importance. Moreover, the Mach number predominantly lies in the incompressible regime, reaching high values up to $Ma = 0.5$ only in the hydrogen rich region (Fig. 5.2, bottom). In contrast, deviations of the real gas factor from $Z = 1$ predominantly occur within the dense oxidizer core (Fig. 5.2, top) and the error introduced by the calorically ideal gas model is considered acceptable.

To further analyze the impact of the selected EOS on the single flame solution, LP2 is considered. As its operating conditions are well within the supercritical regime, a reference solution using the SRK-EOS can be calculated along with the just introduced Z_{ref} and the incompressible approach.

The results are obtained from a steady, two-dimensional calculation with $Sc_t = 0.7$. The heat release for the three models is shown in Fig. 5.3a. The results with the incompressible and Z_{ref} approach are close to each other. They mainly deviate from the SRK real gas approach in the region between $0.02\,\mathrm{m} \lessapprox x \lessapprox 0.06\,\mathrm{m}$. There the simplified approaches underestimate the heat release obtained with the SRK EOS. The incompressible solution obtained with a different turbulent Schmidt number ($Sc_t = 0.9$ instead of $Sc_t = 0.7$) is included in Fig. 5.3a as well. By comparison, the impact of the turbulent Schmidt number on the heat release profile is found higher than that of the selected EOS modeling approach. For the wall pressure distribution the incompressible results predict a smaller but earlier pressure drop compared to the SRK EOS (Fig. 5.3b). The Z_{ref} model shows good agreement with the SRK results close to the faceplate and approaches the incompressible solution further downstream. Overall, the wall pressure dis-

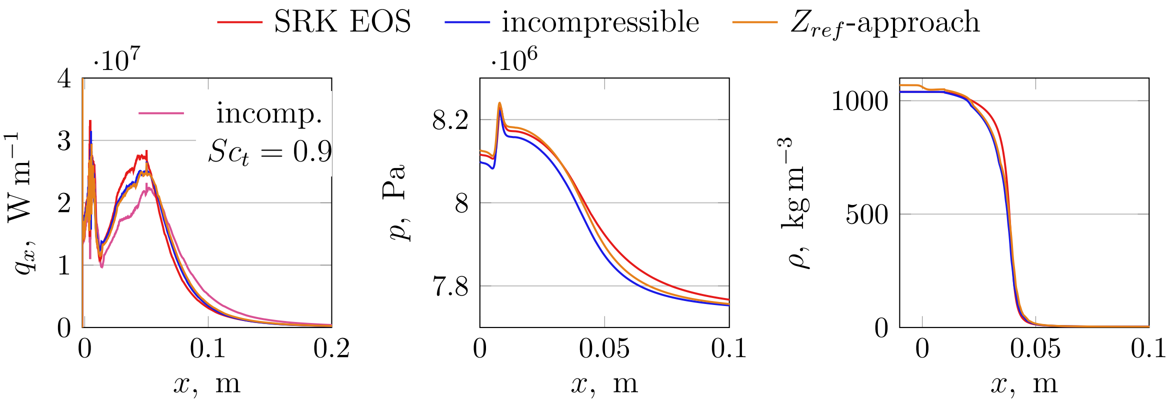

(a) Heat release **(b)** Wall pressure **(c)** Density at axis

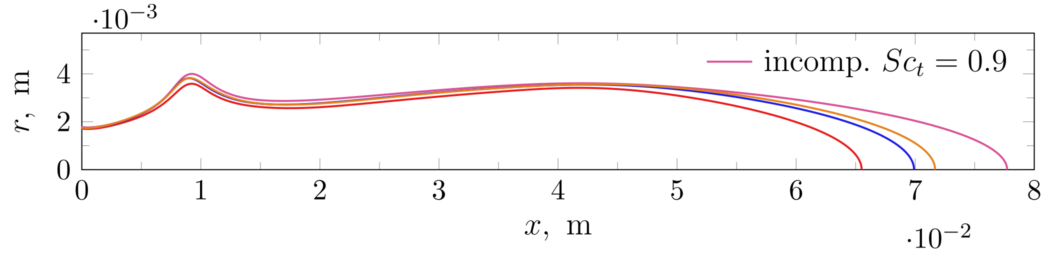

(d) Flame contour

Figure 5.3: Influence of the compressibility model on single flame results for BKD LP2

Table 5.1: EOS and compressibility in the single flame simulations

Simulation Type	BKD		TCDs
	LP1	LP2	
steady	incompressible	SRK	SRK
excitation (pressure)	incompressbile/Z_{ref}	incompressible/SRK	–
excitation (velocity)	–	incompressible	–

tributions obtained with the three models are quite similar to each other. Most directly, the impact of the compressibility model is seen in the density profile at the chamber axis (Fig. 5.3c). There the Z_{ref} approach overestimates the density in the oxidizer core as the high value of $\partial p/\partial \rho$ in the vicinity of the critical point is not captured. However, the location of the density drop shows that the oxidizer core has a similar length for all approaches. The two-dimensional flame contour is shown in Fig. 5.3d. The general agreement between the flame shapes obtained with the different EOS is good. The results obtained with the SRK EOS predict a slightly shorter and thinner flame compared to the ideal gas and Z_{ref} simulations. For reference, again results from an incompressible calculation at a different turbulent Schmidt number are included in Fig. 5.3d. Like for the heat release profile (Fig. 5.3a) the impact of the turbulent Schmidt number on the flame length is higher than that of the EOS choice. Given the uncertainty that remains in terms of the calibration of this number (cf. Sec. 5.3) as well as of the simplification of the computational domain (Sec. 5.1.4 and 5.3.1), the deviation induced by the adaption of the EOS seems acceptable. An overview which EOS or compressiblity approach is applied in the different simulations is given in Tab. 5.1. Due to its near-critical operating conditions, the incompressible approach is used for LP1 if applicable. To study the impact of compressbility on the excitation results (cf. Sec. 7.1) the Z_{ref} approach is used. As the operating conditions of LP2 and the TCDs are supercritical and considerably far from the respective propellants' critical points (cf. Fig. 3.2), the SRK EOS can be used in these cases.

Beside the EOS, viscosity and thermal conductivity are required to solve the flow equations. As turbulent processes are dominant in momentum, mass and energy transport, those properties are set constant across the whole chamber. Since the impact of molecular diffusion on the flow fields is expected to be strongest in the injection system, the values are based on oxygen at representative injection conditions: $\mu = 1 \cdot 10^{-4}\,\mathrm{Pa\,s}$, $\lambda = 0.13\,\mathrm{W\,m^{-1}\,K^{-1}}$.

5.1.3 Combustion Model and Heat Release

To model combustion in the single flame simulations, a non-premixed flamelet model is used. This choice offers two advantages: solving transport and kinetics of individual species and reactions is avoided and the turbulence closure of the mean reaction rates can be accounted for by an efficient statistical approach (see below). The first aspect is of particular relevance to ensure fuel flexibility of the setup. While there are compact reaction mechanisms that give reasonable results for H_2/O_2 combustion, hydrocarbon fuels like methane require a rather high number of species and reactions, quickly increasing the computational effort. In the following, the main characteristics of the flamelet combustion model in the form implemented in Fluent [63] are outlined and a procedure to extract axially resolved heat-release distributions from the results is introduced.

The basic idea of the flamelet approach is depicted in Fig. 5.4. Combustion in the flow is considered as an ensemble of small flame structures (flamelets), here counterflow diffusion flames. The normalized temperature distribution of such a flamelet is shown in Fig. 5.4b. Besides additional non-equilibrium or turbulence related parameters (see below), temperature and species composition of each flamelet depend on the local mixture ratio between fuel and oxidizer. This ratio is quantified by the mixture fraction f that varies between 0 and 1 and corresponds to the local cumulative mass fraction of all atoms that originate from the fuel stream. The Reynolds averaged distribution of the mixture fraction in the simulatiom domain is obtained from a transport equation that replaces those of the individual species. The resulting field structure for a single rocket engine flame is sketched in Fig. 5.4a with the mixing between the oxidizer core flow and the fuel rich outer

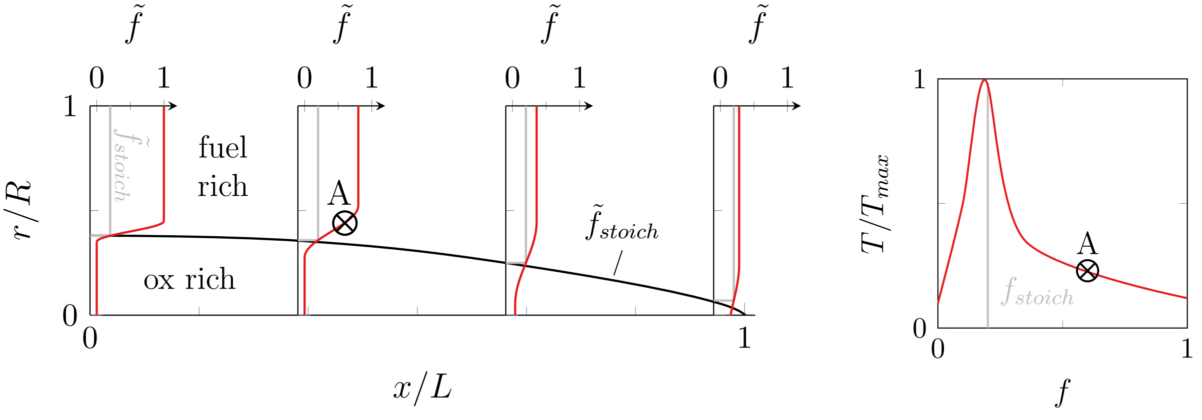

(a) Structure of mixture fraction field **(b)** Flamelet

Figure 5.4: Flamelet model principle

flow creating a co-flow diffusion flame (see also Sec. 2.1). Given the mixture fraction field, the temperature and composition of the flow are interpolated from the flamelet.

The mixture-fraction based approach outlined above allows to apply an efficient statistical model for turbulence-chemistry interaction (TCI). The TCI-model accounts for the non-linear effect of non-resolved turbulent variations of the local mixing on mean temperature and flow composition. The mixture fraction fluctuations are assumed to follow a β-probability density function (PDF, $\mathcal{P}$). To fully specify this PDF, the mixture fraction variance is required in addition to the mean mixture fraction. It is obtained from the solution of an additional transport equation.

Chemical non-equilibrium is represented via the scalar dissipation, which is directly related to the strain rate of a counter-flow diffusion flamelet. In the flow, the scalar dissipation is estimated based on local turbulence and mixture fraction variance. For zero scalar dissipation, the flamelet is in local chemical equilibrium, i.e. the flow composition does not depend on reaction kinetics but is governed by the mixing behavior of fuel and oxidizer.

Besides the just discussed model specific flamelet parameters, the local enthalpy and pressure potentially impact the flow composition and temperature. However, changes in pressure can be neglected for the flamelet generation as discussed in Sec. 4.3.1.2 but are accounted for in the calculation of the flow density if applicable (cf. Sec. 5.1.2). The enthalpy distribution in the flow is obtained from Eq. 2.21. Consistent with the isobaric treatment of the flamelets, the temporal pressure derivative in the enthalpy equation is neglected (cf. Sec. 2.2). In general, the parametrization of the chemistry in the flame by means of mixture fraction statistics and scalar dissipation can be carried out at different enthalpy levels. However, Fluent poses some restrictions to limit the number of interpolation dimensions. When considering chemical non-equilibrium via the scalar dissipation, only a semi-diabatic treatment of the flow is available: While density and temperature calculations take into account the local flow enthalpy, the species mole fractions are obtained at a fixed reference enthalpy. In contrast, if only equilibrium flamelets are considered, the enthalpy goes into the local flow composition as well but strain is neglected. The flamelet tables generated with Fluent show negligible sensitivity to scalar dissipation, which is why the diabatic equilibrium model is used in this work. Real gas effects are not included in the flamelet generation and the real gas density is calculated from flow composition, temperature and pressure.

Several steps of the stability assessment procedure require the axial heat release rate distribution. Its mean value goes into the mean flow calculation (Sec. 4.2) and the flame response is modeled based on the heat release fluctuations (Sec. 4.3). However, the heat release rate is not directly available from the flamelet model. A tabulation based on the flamelet coordinates is not applicable as well, as the flow composition is parametrized and not its temporal derivative. Thus, the heat release is obtained from the transport equation of the enthalpy of formation (Eq. 2.25). Since only the axial profile is required, the evaluation can be simplified via radial integration:

$$q_x = -\int_0^R \mathcal{S}_{h_f^0} dA = -\int_0^R \left[\rho \frac{\partial h_f^0}{\partial t} + \rho \boldsymbol{u}_x \frac{\partial h_f^0}{\partial x} - \frac{\partial}{\partial x} \left(\frac{\mu_t}{Sc_t} \frac{\partial h_f^0}{\partial x} \right) \right] dA - \mathfrak{A}_{h_f^0} \tag{5.2a}$$

with

$$\mathfrak{A}_{h_f^0} = 2\pi R \left(h_f^0 \rho \boldsymbol{u} \cdot \boldsymbol{n}_{r,u} \right)_{r=R} \tag{5.2b}$$

accounting for any enthalpy of formation passing in radial direction across the domain boundaries, e.g. during the excitation simulations. The term $\boldsymbol{n}_{r,u}$ denotes the radial unit vector pointing outwards of the domain with $\boldsymbol{n}_{r,u} = \mathbf{0}$ for a purely axially oriented surface. The diffusion term in Eq. 5.2a neglects molecular transport as turbulent mixing is dominant.

5.1.4 Computational Domain and Discretization

Single flame simulations are carried out in two and three dimensions. Three-dimensional simulations are used with and without velocity excitation in the context of radiation based single-flame validation (cf. Sec. 5.3). All other simulations in this work, including any TCD calculations, are two-dimensional. In the following, the selection of the computational domain for the single flame simulations in 2D/3D is discussed and an overview of the respective computational grids is given. Finally, the discretization schemes are addressed shortly. Even though the content of this section is centered around the BKD test case, the mesh structure and resolution for the TCD-simulations are analogous.

A generic domain for the single flame simulations is shown in Fig. 5.5. It comprises a part of the combustion chamber as well as the downstream region of the injector (cf. Fig. 3.1c). As the fuel is injected in axial direction, the fuel inlet is modeled directly as planar boundary condition at the back of the recess. Due to the conical shape of the oxygen injector's downstream part, a portion of the oxygen post is resolved, up to a short distance upstream of the taper[3]. In the excited simulations, not resolving the full injector ensures that the comparison between compressible and incompressible results is not affected by the acoustic response of the injection system (cf. Chap. 7). The cross-sectional area in the chamber part is $1/n_{inj}$ of the whole chamber cross-section with n_{inj} the number of injection elements. That way, if the total mass flow is evenly distributed to the injection elements, representative values of the flow velocity can be expected.

---

[3] For some steady cases the injection system including part of the dome volume has been included as well. However, the impact on the solution in the chamber is negligible.

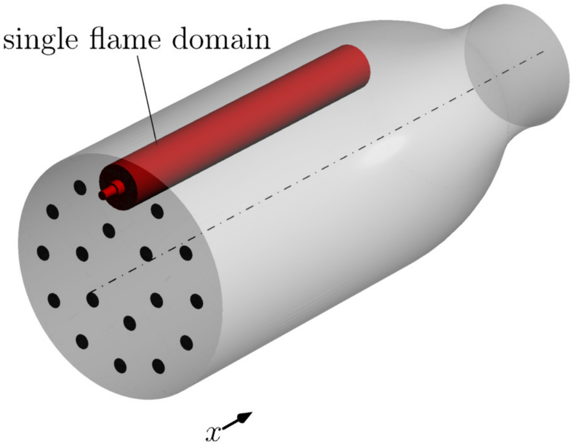

Figure 5.5: Single flame domain

For the two-dimensional simulations the domain radius is fully specified by this condition. However, in the three-dimensional cases the selection of the single flame domain cross-section's shape is not unambiguous. Fig. 5.6 shows a segment of the injection pattern of the BKD (cf. Fig. 3.1b), partitioned according to the above criterion regarding the single flame domain's cross-sectional area. For comparison, a circular domain is included as well, which represents the axis-symmetric two-dimensional domain and is similar to the hexagonal shape used in previous works's 3D simulations [3, 12]. The shape of the single flame domain's cross-section depends on the injector row under consideration. The outer row deviates significantly from the axis-symmetric case, which in turn is more similar to the middle row. As the three-dimensional simulations are used for validation purposes (cf. Sec. 5.3.3) and experimental radiation images are dominated by the wall-nearest flames, the domain shape corresponding to the outer injection row is selected. The impact of the domain selection on the single flame results is discussed further in the context of the single flame validation in Sec. 5.3.1.

To discretize the single flame domains, a block structured grid is used. The radial grid lines are kept strictly orthogonal to the injector axis. This is done to allow for the explicit evaluation of the excitation source terms as described in Sec. 4.3.1.3 (Eq. 4.59 and 4.68) as well as the efficient extraction of the axial heat release distribution (cf. Sec. 5.1.3). For the two-dimensional BKD cases the grid is shown in Fig. 5.7. The high axial resolution is due to

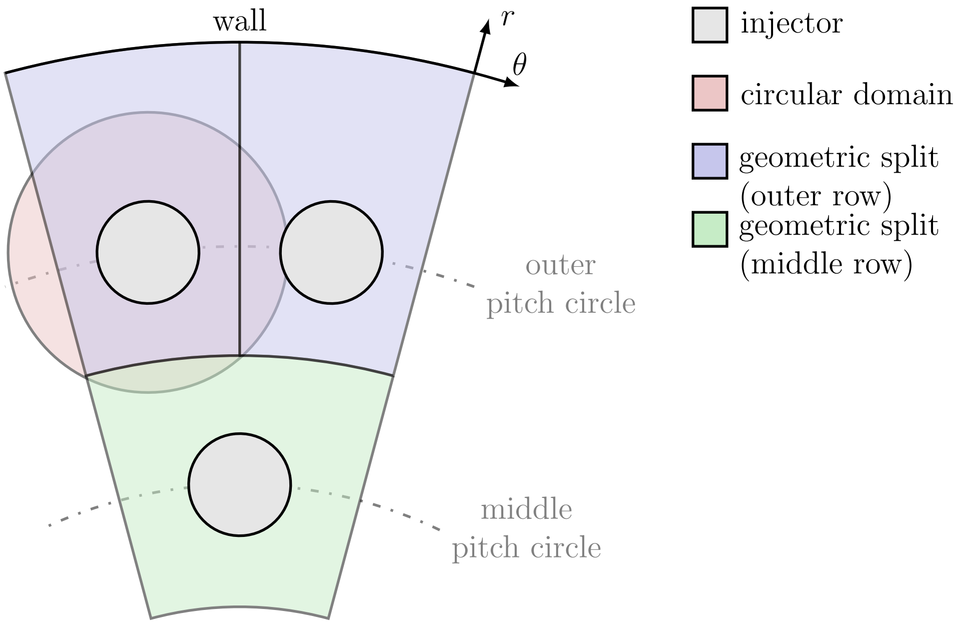

Figure 5.6: Injection pattern segment of the BKD

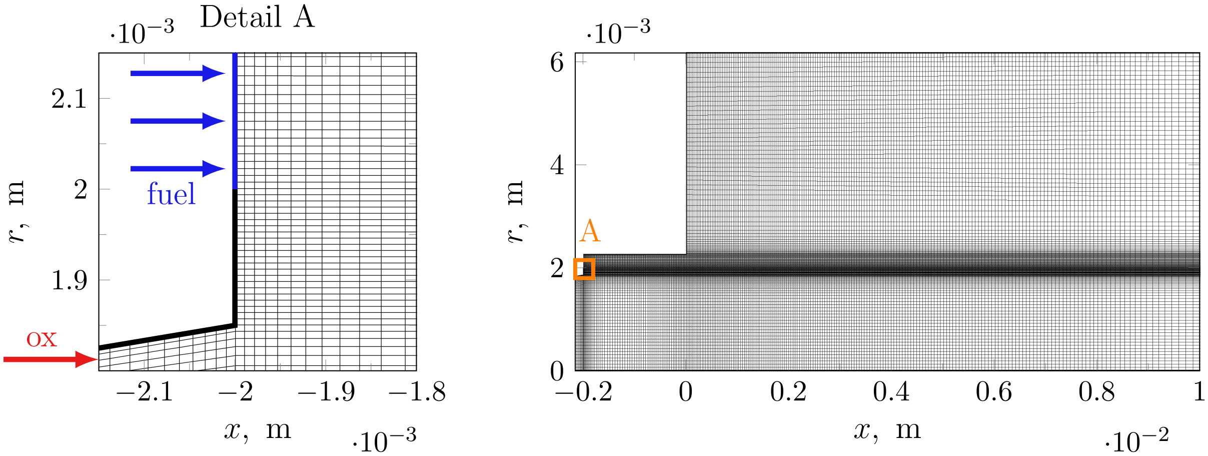

Figure 5.7: Computational grid in front region of the BKD

the necessity to resolve axial gradients for the extraction of the heat release (cf. Sec. 5.1.3). The real gas conditions induce high density gradients at the edge of the oxidizer core, requiring sufficient radial resolution. A grid study for BKD LP2 has been conducted, employing a refined and a coarsened version of the final grid. The cell numbers (n_{cells}) are shown along with results for global flow structures in Fig. 5.8. The flame length is shown in

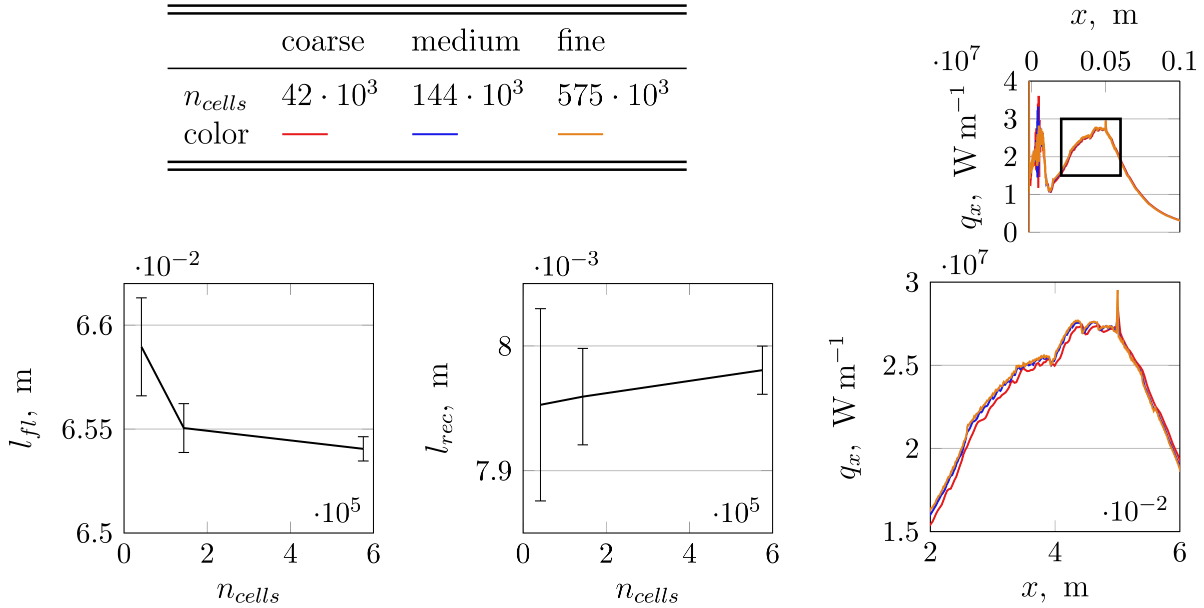

	coarse	medium	fine
n_{cells}	$42 \cdot 10^3$	$144 \cdot 10^3$	$575 \cdot 10^3$
color	🟥	🟦	🟧

(a) Flame length **(b)** Corner recirculation zone length **(c)** Heat release

Figure 5.8: Grid study for BKD LP2

Fig. 5.8a. It is calculated as the distance of the position where the contour of stoichiometric mixture fraction closes at the axis from the faceplate (cf. Sec. 2.1 and Fig. 5.3d). The error bars indicate the size of the cell within which stoichiometry is reached. The flame length shows clear convergence with increasing resolution and changes are already small between the coarse and the medium mesh. A flattening is observed in the development of the corner recirculation zone length as well (Fig. 5.8b), not as distinct as for the flame length but with even smaller relative changes between the grids. The heat release rate (Fig. 5.8c) shows the same trend and the solution can be considered to be well grid converged.

The grid for the three dimensional simulations of a single injector domain in the outer flame row, including the cooling film, is shown in Fig. 5.9. To keep the computational effort acceptable, the domain is restricted to the region $x < 0.075\,\mathrm{m}$ and a coarser grid than in the two-dimensional simulations is used. Nevertheless, the grid comprises more than 1.2 M cells with about 300 cells along the injection axis.

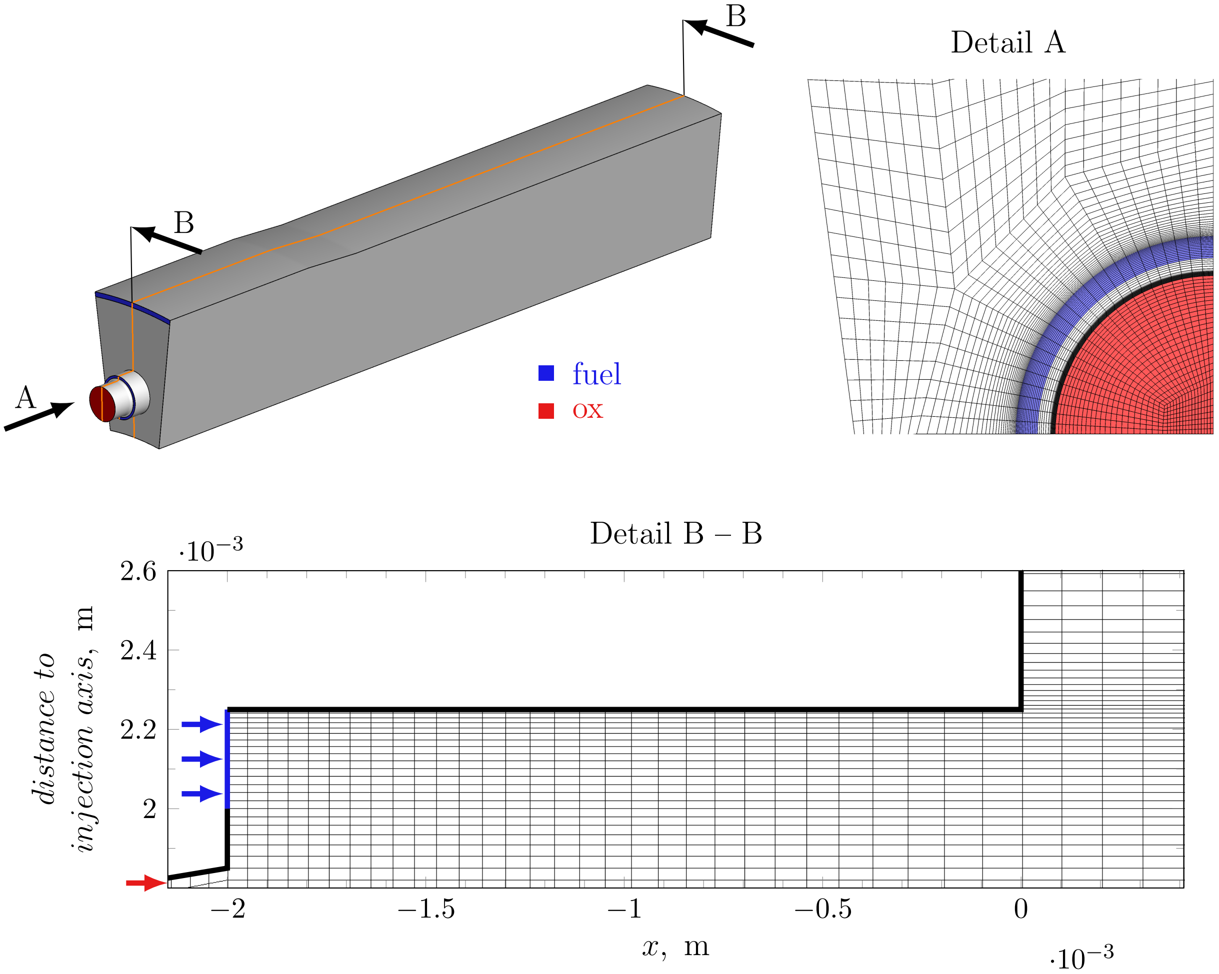

Figure 5.9: Computational grid for 3D simulation

The numerical discretization schemes are of second order in space. In time, bounded second order implicit discretization [63] is used.

5.1.5 Boundary Conditions

The boundary conditions for the two-dimensional single flame simulations are specified in Fig. 5.10 along with Tab. 5.2. At the inlets, mass flow and temperature are specified according to the test case descriptions in Chap. 3 (Tab. 3.2 and 3.6). Regarding turbulence, a medium turbulent intensity [59]

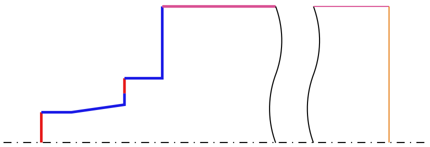

Figure 5.10: Single flame domain

Table 5.2: Single flame boundary conditions

color	type	specification	
		general	turbulence
🟦	wall	$\boldsymbol{n} \cdot \nabla T = 0$ $\boldsymbol{u} = \boldsymbol{0}$	SWF
🟥	inlet	T, $\dot{m}$	$I = 0.05$, D_H
🟧	outlet	p	
🟪	symmetry		

of

$$I = \frac{\sqrt{2/3k}}{|\boldsymbol{u}|} = 0.05 \tag{5.3}$$

with k the turbulent kinetic energy, is specified. The turbulent dissipation rate is estimated using the turbulent length scale l_t, which again is calculated from the hydraulic diameter D_H of the respective inlet [59]:

$$\epsilon = \frac{k^{3/2}}{l_t}, \quad l_t = 0.07 D_H C_\mu^{-3/4} \tag{5.4}$$

with the model constant C_μ.

The walls are treated as adiabatic no-slip walls with scalable wall functions for turbulence treatment, as discussed in Sec. 5.1.1. At the outlet, the pressure is fixed. For the simulations with excitation a constant outlet pressure is justified, as the modes of interest are of transverse type and cut-off in the rear part of the chamber, i.e. pressure amplitudes at the outlet are low (cf. Sec. 2.4.3). A symmetry condition is used to describe the boundary of the single injector domain towards the chamber volume. This boundary type is preferred to a free-slip wall as it does not invoke any wall specific turbulence treatment. For the three-dimensional cases the boundary conditions are mainly identical to those of the two-dimensional setup. However, as a flame of the outer injector row is considered, the chamber wall is one of the domain's lateral boundaries. The film cooling injection is modeled as additional inlet with mass flow and temperature according to Tab. 3.2.

5.2 Calculation of OH* Radiation Images

The validation of the BKD single flame computations in Sec. 5.3 requires a sound calculation procedure to obtain OH* radiation images from the numerical results. In the experiment, the recorded radiation is determined by emission and absorption along line-of-sights through the flame. This circumstance needs to be accounted for when calculating the numerical flame images in order to ensure comparability to the experimental data. The principle approach is shown in Fig. 5.11a. Each point in the OH* image corresponds to the radiation intensity at the end of a line-of-sight. All lines-of-sight are assumed to be parallel. Where a line-of-sight intersects the single flame domain, the radiation intensity is altered due to emission and absorption in the reacting flow. When evaluating the radiation intensity along a line-of-sight, two-dimensional flow results need to be virtually rotated around the domain axis to obtain the correct distribution of radiative properties (cf. Fig. 5.11). As the resulting flame radiation image is symmetric with respect to the location of the flame axis, it is sufficient to calculate only its top half. For three-dimensional cases (cf. Sec. 5.1.4), the intersections of the lines-of-sight with the flame region need to be calculated based on the domain geometry, as shown in Fig. 5.11b.

The fundamentals of radiation modeling have been introduced in Sec. 2.5. Along each line-of-sight, the radiative transport equation 2.56 is solved to obtain the detected radiation intensity. Three points need to be considered:

- The selection of the emission model.
- The evaluation of the radiative transport equation in turbulent flow.
- The computationally efficient approximation of the radiation's spectral dependence.

In the following, the impact of these aspects on the calculated radiation images are successively analyzed for a rocket flame. For this purpose an adiabatic, incompressible solution for a BKD-like single flame at 80 bar is used. The flow is considered to be in local chemical equilibrium, i.e. its local

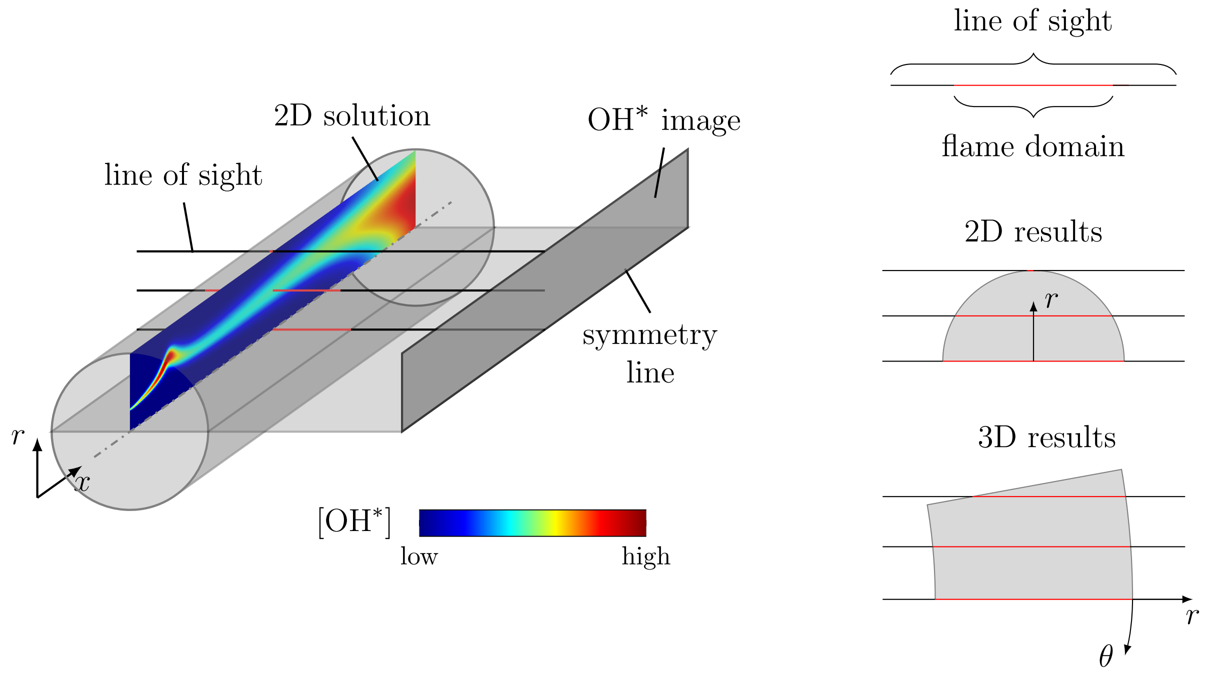

(a) Principle sketch for 2D results **(b)** Cross-sectional view

Figure 5.11: Calculation principle for numerical OH* images

composition depends only on the mixing between fuel and oxidizer (cf. Sec. 5.1.3). For this configuration, due to the flamelet combustion model, the fields of mean mixture fraction and mixture fraction variance (Fig. 5.12) along with the PDF-table fully determine the local composition, temperature and density of the solution. Thus any of the used radiation models can be implemented in the frame of a compact post-processing calculation. Following the discussion of the modeling aspects, the numerical implementation of the OH* image calculation procedure is addressed. Finally, a summary of the main conclusion from the present chapter is given.

5.2.1 Radiation Model Selection

For the calculation of the OH* radiation image, the radiative transport equation 2.56 is solved along multiple lines-of-sight (cf. Fig. 5.11). Thereto the spatial distribution of radiation emission and absorption needs to be modeled. An overview of the different approaches to calculate these terms

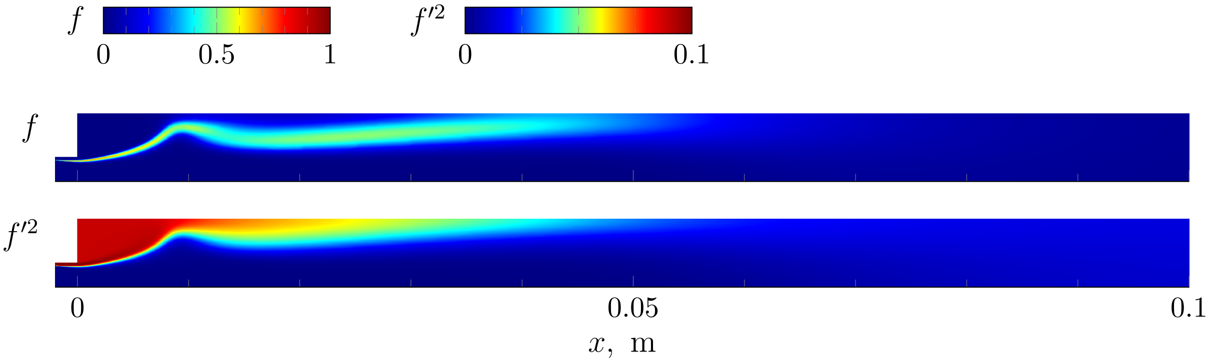

Figure 5.12: Single flame solution for OH* modeling study

has been given in Sec. 2.5.2 and Sec. 2.5.3 respectively. The modeling options for the absorption term basically differ in the way the radiation's spectral dependence is approximated, which is discussed comprehensively in Sec. 5.2.3. The models available for the emissivity appear to have more fundamental differences. Of the emission models presented in Sec. 2.5.2, the two more elaborate ones are considered further: the EFRM-A model that has been designed to combine computational affordability with reasonable accuracy and the classical radiation model that also provides a quantitative prediction of the radiation intensity. In the following, the discretized form of the radiative transport equation is introduced, providing the background to subsequently discuss the emission models.

The radiative transport equation 2.56 forms the basis for calculating the development of radiation intensity across the flame. The equation is recast in accordance with the numerical representation of the flow as shown in Fig. 5.13. The ray is considered to pass through a sequence of volumes with constant properties. The intersection length between ray and a volume is termed Δx. Following Eq. 2.65 the discretized form of the transport equations reads:

$$I_s^+ = \underbrace{e_{(s)}\left[1 - \exp\left(-k_s \Delta x\right)\right]}_{\mathcal{E}_{s,net}} + \underbrace{I_s^- \exp\left(-k_s \Delta x\right)}_{\mathcal{T}_s} \tag{5.5}$$

with the spectral net emission $\mathcal{E}_{s,net}$ and the spectral transmission $\mathcal{T}_s$. The superscripts $^-$ and $^+$ denote radiation entering and leaving a constant property volume respectively.

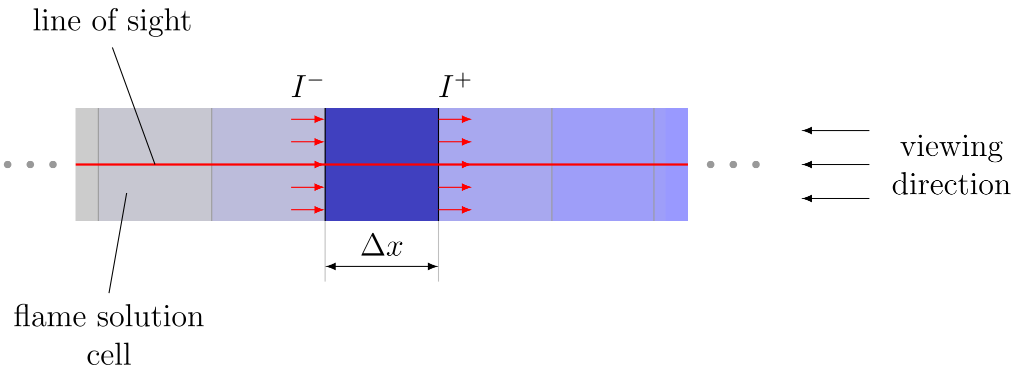

Figure 5.13: Discretized line-of-sight

The structure of Eq. 5.5 allows to directly apply the EFRM-A model in the form provided in several publications [21, 22, 26]. The model combines the integral emission according to Eq. 2.62, which is evaluated at the center wave length λ_c of the spectral range of interest, with spectrally dependent absorption:[4]

$$e \sim [\mathrm{OH}^*] \tag{5.6}$$

$$\mathcal{E}_{s,net} \sim [1 - \exp(-k_s[\mathrm{OH}^*])] \quad . \tag{5.7}$$

Combining these two equations shows a difference compared to the classical net emission, Eq. 2.65, where the inverse spectral absorption coefficient appears as pre-factor. The emission term for both models reads

$$e_{(s)} = \begin{cases} \frac{e_s}{k_s} = I_{b,s} & \textit{classical model} \\ \sim [\mathrm{OH}^*] & \textit{EFRM-A} \end{cases} \quad . \tag{5.8}$$

Inserting Eq. 2.58 and Eq. 2.62 yields

$$e_{(s)} = \begin{cases} \frac{2hc_l^2}{\nu^3}\left(\exp\left(\frac{hc_l\nu}{k_B T}\right) - 1\right)^{-1} & \textit{classical model} \\ [\mathrm{OH}]\left(\exp\left(\frac{hc_l\nu}{k_B T}\right)\right)^{-1} & \textit{EFRM-A} \end{cases} \quad . \tag{5.9}$$

As the EFRM-A provides only a qualitative distribution of the OH* radiation, globally constant factors can be dropped for a comparison of the two

---

[4] This model always has been applied along with a spectral simplification based on pseudo absorption coefficients [21, 22, 26]. The approach is used in a fully spectrally resolved form here. That way, the pure model comparison is separated from the aspect of spectral approximation. This aspect will be addressed in Sec. 5.2.3.

models. Furthermore, the window width of the filter is small compared to the center wave number[5] ν_c; for the BKD measurements: $\frac{\Delta\nu}{\nu_c} \approx 0.03$ and $\frac{\Delta\nu^3}{\nu_c^3} \approx 0.09$. Thus the wave number in the classical model can be replaced by the center wave number as well. These simplifications lead to:

$$e_{(s)} \sim \begin{cases} \left(\exp\left(\frac{hc_l\nu_c}{k_BT}\right) - 1\right)^{-1} & \textit{classical model} \\ [OH]\left(\exp\left(\frac{hc_l\nu_c}{k_BT}\right)\right)^{-1} & \textit{EFRM-A} \end{cases} . \tag{5.10}$$

The exponent in Eq. 5.10 contains the second radiation constant $c_2 = \frac{hc_l}{k_B} \approx 0.0144\,\mathrm{m\,K}$. Together with the filter center wave number of $\nu_c = \frac{1}{310\,\mathrm{nm}}$ and an upper temperature limit of $T_{max} \approx 3500\,\mathrm{K}$ the exponent takes a minimum value of $\frac{hc_l}{k_B}\frac{\nu_{center}}{T_{max}} \approx 13.26$. Thus, the exponential term is clearly dominant in Eq. 5.10, which can be approximated as

$$e_{(s)} \sim \begin{cases} \exp\left(-\frac{hc_l\nu_c}{k_BT}\right) & \textit{classical model} \\ [OH]\exp\left(-\frac{hc_l\nu_c}{k_BT}\right) & \textit{EFRM-A} \end{cases} . \tag{5.11}$$

So the only significant difference between the emission terms of both models is the multiplication with the OH concentration for the EFRM-A.

To study the relevance of the deviation between both emission terms in Eq. 5.11, an H_2/O_2 equilibrium flamelet is considered. Its temperature and [OH] profiles are shown in Fig. 5.14a. The value of the corresponding exponential term from Eq. 5.11 is given in Fig. 5.14b. Compared to the temperature distribution, its peak is considerably narrower. The comparison between both complete emission terms from Eq. 5.11 (Fig. 5.14c) reveals only small differences. The peak is governed by the exponential term and including the OH concentration as pre-factor just leads to a slightly earlier decline at its super-stoichiometric side. However, the overall profiles are almost identical. The impact of the radiation model on a complete flame image is shown in Fig. 5.15. The image has been calculated for a turbulent flame as introduced in Sec. 5.2.2, where also a more detailed discussion on the image structure

---

[5] For consistency with previous publications using the wave-length based equations, $\nu_c = \frac{1}{\lambda_c}$ is used here instead of calculating the center wave number based on the wave number range of the spectral analysis window.

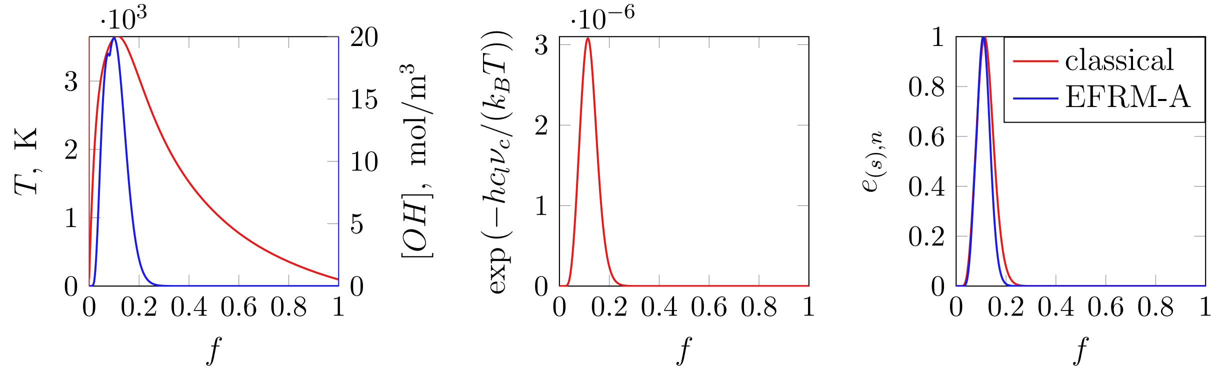

(a) Flame profile **(b)** Exponential term **(c)** Emission profiles

Figure 5.14: Emission distribution across an 80 bar equilibrium flamelet

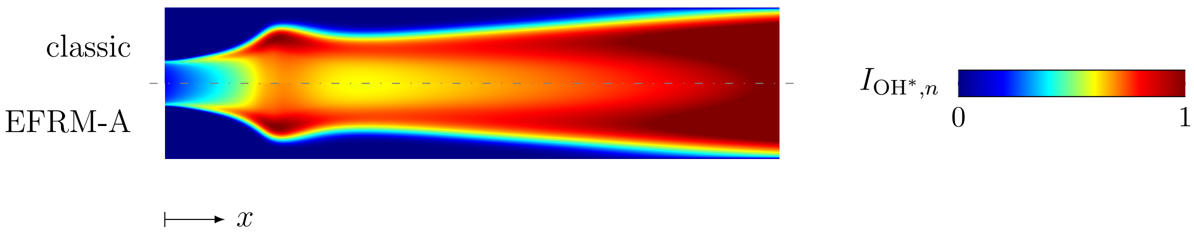

Figure 5.15: OH* radiation image calculated with the classic and the EFRM-A approach

is given. As expected from the previous analysis, no significant differences between the results of the classical and the EFRM-A approach are visible.

As the classical model has the principle advantage of providing a quantitative estimation of the radiation intensity without significant drawbacks in terms of implementation, it is used in the remainder of this work. Regarding the calculation of the OH* concentration, the flamelet profile in Fig. 5.14a confirms the validity of the equilibrium assumption (cf. Sec. 2.5.2.2) as in the regions of notable OH concentrations the temperature lies fairly above the crossover value of $T \approx 2700\,\mathrm{K}$ given by Fiala [21].

5.2.2 Turbulence Impact on Radiation Images

The radiation models discussed in the previous section 5.2.1 are designed to model the radiation properties for a given set of instantaneous temperature and [OH] data. However, the flow in rocket combustion chambers is highly turbulent and the flow fields obtained from the RANS simulations represent average data instead of instantaneous fields. While the RANS equations are based on ensemble or Favre-averaged values of the mean flow fields (cf. Sec. 2.2.1), the numerical modeling of combustion used in the present work provides additional information on the unresolved turbulent fluctuations of the mixture fraction (Sec. 5.1.3). Via the presumed β-PDF-model for the mixture fraction statistics, a way to include turbulent influences on quantitities depending non-linearly on the flamelet variables is available. As the previously outlined radiation descriptions are highly non-linear in terms of temperature, this has the potential to significantly affect the computed radiation images. The role of turbulence in the calculation of the mean OH* concentration field from ground state OH and temperature (Eq. 2.62) has been pointed out by Fiala et al. [21, 22]. In the context of rocket engine flames, this aspect has been approached by Schulze et al. [26]. However, the influence of turbulence in these studies was restricted to the emission term of the EFRM-A model (Eq. 5.8).

In the following, an approach is developed to evaluate the radiative transport equation in a way that takes into account turbulence to the extent that is possible and consistent with the single flame CFD. This concerns the evaluation of the emission and transmission terms in Eq. 5.5 in the presence of turbulence in general, independent of the actually chosen emission model (Sec. 5.2.1) or spectral approximation (Sec. 5.2.3). Starting from this reference case, two simplified variants of the radiation calculation in turbulent flow are introduced and evaluated. They show the relation of the consistent approach to the methods used in previous works [21, 26] and require a lower implementation effort. Following the findings in Sec. 5.2.1 the discussion is carried out for the classical emission model (Eq. 2.5.2.1). To provide additional insight into the mechanisms leading to the differences between the radiation images obtained with the different turbulence treatments, the development of radiation intensity along a representative line-of-sight is analyzed.

First, the approach, which fully accounts for the effect of turbulence on the radiation calculations is developed. As basis for the derivation the assumptions used in the evaluation of the radiative transport equation or implied by the overall simulation setup are recalled:

1. The statistically resolved influence of turbulence is limited to oscillations of the mixture fraction. This is the basic assumption that underlies the overall setup for the flow simulations.[6]
2. The cells are statistically independent from each other, i.e. the PDFs of different cells can be evaluated separately.
3. Each cell is perfectly mixed at all times and the radiation time scale is small compared to any transient time scales of the flow or turbulence.
4. The flow is approximately isobaric.

With the first and second prerequisites, the turbulent fluctuations manifest in the Favre-averaged value (cf. Sec. 2.2.1) of a variable ϕ that follows the PDF $\mathcal{P}$ as

$$\tilde{\phi} = \int_0^1 \phi_{fl} \mathcal{P} df \quad . \tag{5.12}$$

The index $_{fl}$ denotes the flamelet profile of the variable.

The third assumption allows to use Eq. 5.5 for the evaluation of the radiation intensity. The RHS terms of this equation depend on temperature, pressure, OH concentration, a spectral variable and the distance Δx. As the pressure varies only weakly across the flame, its impact on the results is neglected (simplification four), leaving four independent parameters. The net emission and transmission term in Eq. 5.5 can be evaluated separately. Under full

---

[6] In the flow equations turbulent transport of momentum, species and enthalpy is included as well. However, this enters the radiation calculations only indirectly via the fields of mixture fraction and its variance.

inclusion of non-linearity into the PDF-integration, the net-emission term reads

$$\tilde{\mathcal{E}}_{s,net} = \int_0^1 I_{b,s,fl} \left[1 - \exp\left(-k_s \Delta x\right) \Delta x\right] \mathcal{P} df \tag{5.13a}$$

and the transmission becomes

$$\tilde{\mathcal{T}} = I_s^- \int_0^1 \exp\left(-k_s \Delta x\right) \mathcal{P} df = I_s^- \tilde{\alpha}_s \quad . \tag{5.13b}$$

The term α_s is a transmission factor denoting which fraction of the incident radiation I_s^- leaves the volume. In Eq. 5.13b I_s^- remains outside of the PDF-integration due to the statistical independence of different cells (assumption 2). Regarding the evaluation of Eq. 5.13, a tabulation of the PDF-integrated terms is necessary to keep calculations computationally affordable. The number of table dimensions is determined by the number of independent parameters in the respective integrand. Aside from the mixture fraction statistics, the two terms that need to be evaluated in each cell when applying Eq. 5.13 depend on three coordinates: wave number, temperature and spatial distance. This makes the table structure rather complex. Previous works [26] only accounted for the non-linearity of the averaged OH* concentration (Eq. 5.6) with respect to temperature and ground-state OH. Otherwise the average of the fluctuating flow field variables were used to calculate the radiation terms instead of averaging the fluctuating radiation terms. While such an approach is easier to implement, it does not agree with the turbulent radiation terms (Eq. 5.13). In the following, two successively simplified versions of Eq. 5.13 are constructed and evaluated. This way, the potential for model simplifications is accessed and the relation of the current results to those of the previous studies is shown.

In the first step of simplification the black body emissivity and the exponential term in the net-emission are treated as statistically independent. Under this assumption, their PDF-integration can be carried out separately, leading to the net-emission term

$$\tilde{\mathcal{E}}_{s,net} \approx \int_0^1 I_{b,s,fl} \mathcal{P} df \, [1 - \underbrace{\int_0^1 \exp\left(-k_{s,fl} \Delta x\right) \mathcal{P} df}_{\tilde{\alpha}_s} \,] \quad , \tag{5.14a}$$

while the transmission term remains identical to Eq. 5.13b:

$$\tilde{\mathcal{T}} = I_s^- \int_0^1 \exp\left(-k_s \Delta x\right) \mathcal{P} df = I_s^- \tilde{\alpha}_s \quad . \tag{5.14b}$$

In Eq. 5.14 the exponential term $\tilde{\alpha}_s$ occurs in both, net-emission and transmission. As the black-body radiation depends only on temperature and wave number, now one two-parameter term and the three-parameter absorption factor need to be evaluated.

In the second simplification step the calculation of the exponential α_s is drawn out of the PDF-integration. Instead a PDF-integrated absorption coefficient

$$\tilde{k}_s = \int_0^1 k_{s,fl} \mathcal{P} df \tag{5.15}$$

is used, leading to the net-emission

$$\tilde{\mathcal{E}}_{s,net} \approx \int_0^1 I_{b,s,fl} \mathcal{P} df \left[1 - \exp\left(-\tilde{k}_s \Delta x\right)\right] \tag{5.16a}$$

and the transmission

$$\tilde{\mathcal{T}} = I_s^- \exp\left(-\tilde{k}_s \Delta x\right) \quad . \tag{5.16b}$$

With this simplification, the dependence of α_s on the spatial distance can be evaluated explicitly, without needing to be considered in the PDF-integration. So the absorption term $\tilde{\alpha}_s$ now depends on only two additional parameters.

The second simplification comes close to the approach used in previous studies [21,22,26], where in addition OH concentration is excluded from the absorption coefficient by using a reduced absorption coefficient $k_{s,r}$:

$$\tilde{k}_s \approx \underbrace{k_{mol}|_{\tilde{T}}\, N_A}_{\tilde{k}_{s,r}} \overline{[\mathrm{OH}]} \quad , \tag{5.17}$$

see also Eq. 2.64. Considering the temperature dependence of the line intensity of the OH* bands in the wave length range $305\,\mathrm{nm} \leq \lambda \leq 315\,\mathrm{nm}$

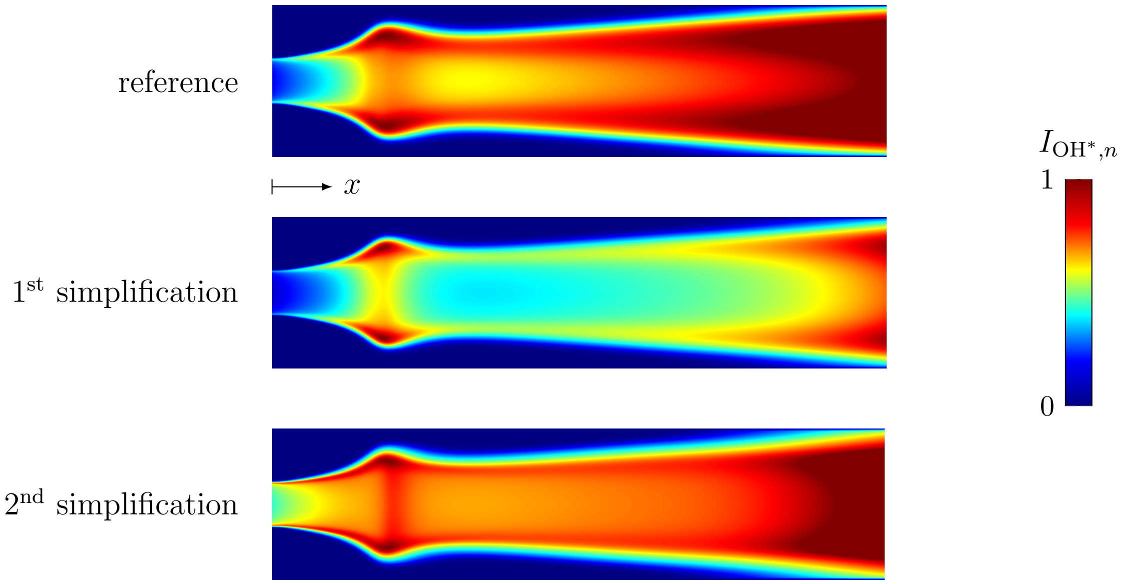

Figure 5.16: Impact of the turbulence modeling variant on the OH* image

an impact of this simplification can be expected. However, in light of the results presented below, this will not be considered in detail.

The ‘reference approach’ (Eq. 5.13), the ‘1st’ (Eq. 5.14) and the ‘2nd simplification’ (Eq. 5.16) are evaluated for the classical radiation model. The resulting OH* images are shown in Fig. 5.16. The structure is governed by an increasing intensity along the shear layer, culminating in a distinct maximum at the outer region of the flame bulge. Further downstream, a core of lower intensity is surrounded by a high intensity region whose inner boundary bends towards and finally reaches the flame axis. The impact of the model variant on the images is severe. Comparing the 1st simplification to the reference approach shows first of all a notable drop of the core flow radiation intensity. At the same time, the tip of the core region becomes less sharp. Only small changes occur in the region upstream of the flame bulge. Going from the 1st to the 2nd simplification, the normalized intensity in the core region rises again. This partial reversal of the impact that the 1st simplification has on the radiation image can be explained by comparing the variants’ equations. When introducing the 1st simplification (Eq. 5.13 to Eq. 5.14), only the net-emission changes, while the transmission term remains identical, with the just shown consequences for the radiation intensity.

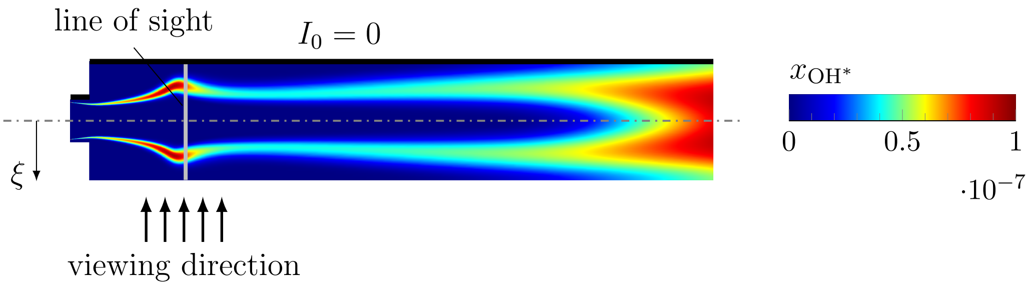

Figure 5.17: Line-of-sight for spectral approximation study

However, from the 1st to the 2nd simplification (Eq. 5.14 to Eq. 5.16) both, net-emission and transmission are changed similarly. If now the absorption factor (see Eq. 5.14) decreases due to this modification, net emission as well as transmission increase. As the outer regions of the radiation image are less affected by absorption due to the flame's cross-sectional geometry (cf. Fig. 5.11b), increased transmission raises the relative core region intensity. However, even though the relative intensity level in the core region is close to the reference approach for the 2nd simplification, notable differences remain. The flame tip retains the blunt shape from the 1st simplification, and upstream of the flame bulge the intensity fairly increases above the level of the reference approach.

To obtain insight into the development of the radiation intensity as a ray passes through the flame and to relate the results of the present study to previous works by the author [57], a representative line-of-sight through the flame is considered as shown in Fig. 5.17. The background radiation is set to $I_0 = 0\,\mathrm{W\,m^{-2}}$ and the position along the line-of-sight is described in terms of the normalized coordinate ξ, ranging from $\xi = -1$ at the backside of the flame to $\xi = 1$ at the boundary facing the observer.

Along this line, the radiation intensity is calculated for the case with fully consistent turbulence treatment of the radiation terms (Eq. 5.13) and a simplistic model where emission and absorption in Eq. 5.5 are evaluated directly from the averaged flow-fields. The latter corresponds to the approach employed in the previous study [57]. The spatial development of the spectrally resolved radiation intensity is shown in Fig. 5.18. Accounting for turbulence

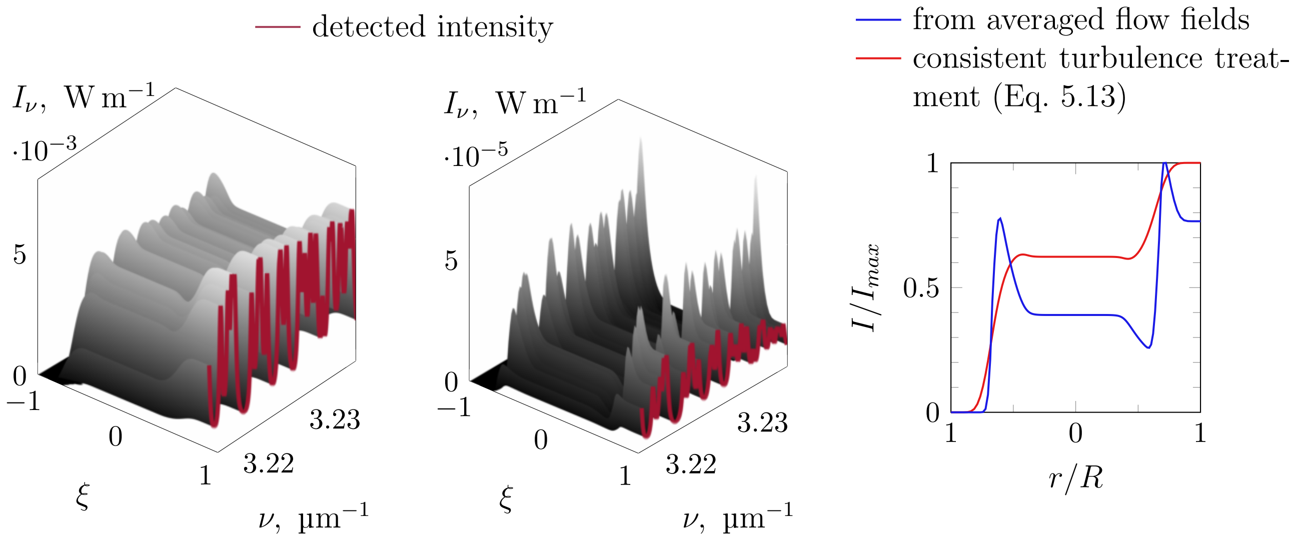

(a) Consistent turbulence treatment **(b)** From averaged flow fields **(c)** Integral

Figure 5.18: Radiation intensity reference solution

has a notable impact on the spectral radiation profile with the spectrum becoming more equally distributed. Moreover, the spatial development of the intensity along the line-of-sight changes as well. This can be seen well from the integral intensity profiles shown in Fig. 5.18c. For the case of radiation calculation from averaged flow fields, the intensity decreases considerably after the peak caused by the first reaction zone and the final intensity is governed by the emission in the shear layer closest to the observer (cf. [57]). In the turbulent case, however, the decrease in radiation intensity between the reaction zones is almost negligible. The significant difference originates from the strong temperature non-linearity of the black body emissivity (Fig. 5.19a, see also Fig. 5.14b). The temperature and integral emissivity profile for a flamelet are given in Fig. 5.19c with the peak of the emission being significantly narrower than that of the temperature. The shape of the PDF at the location of highest emission along the line-of-sight is included in Fig. 5.19c. It is clearly visible that the turbulent fluctuations reach into the region of strongest non-linearity, leading to the observed emissivity increase of about one order of magnitude. In comparison to the emissivity, the effect of turbulence on absorption is rather small, as can be seen from the spectrally averaged absorption coefficient in Fig. 5.19b.

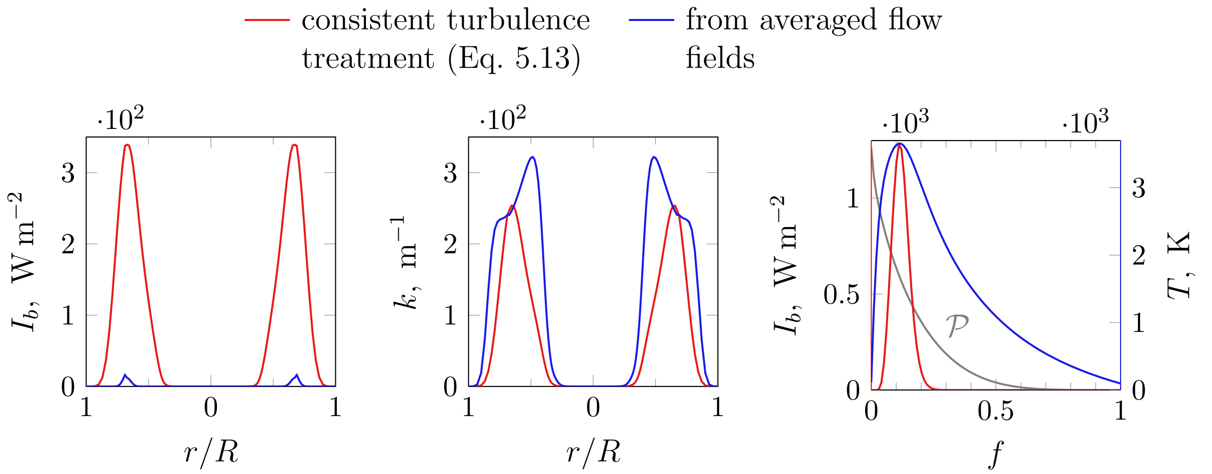

(a) Black body emission **(b)** ν-averaged absorption coefficient **(c)** Black body emissivity and PDF at emission peak

Figure 5.19: Radiation properties

In summary, each of the discussed simplifications for the calculation of radiative transport in turbulent flow has a notable, non-trivial impact on the predicted radiation image. Thus, the fully consistent approach (Eq. 5.13), which includes the most detailed representation of turbulence effects on radiation, is used for the OH* radiation based single flame validation in Sec. 5.3.3.

5.2.3 Spectral Approximation

The discussion in Sec. 5.2.1 and 5.2.2 treated the development of radiation intensity along the lines-of-sight in a spectrally resolved way. The integral intensity at the observer's location has been calculated from the spectrum afterwards. However, for practical applications this approach is computationally not affordable due to the high spectral resolution required to capture the detailed structures of emission and absorption. Several approaches have been undertaken to remedy this issue, see eg. [19]. For the EFRM-A model [21,22] the calibration of several pseudo absorption coefficients to approximate the integral radiation intensity while accounting for the overall effects of spectral dependence has been proposed. Regarding the classical model, a systematic analysis of the simplification of the spectral description for rocket engine flames has been conducted by Chemnitz et al. [67]. In that study, the radiation transport along a representative line-of-sight (Fig. 5.17) through a rocket engine flame were calculated for the $\lambda = 310\,\mathrm{nm} \pm 1\,\mathrm{nm}$ range. The radiation terms in Eq. 5.5 were evaluated from the averaged flow fields without explicitly considering turbulence (cf. Fig. 5.18b). Different degrees of spectral simplification were applied by partitioning the spectrum into several bands using various methods, as discussed below. Finally, the rates of convergence of the band approximations towards the fully spectrally resolved results were compared. In the following, this analysis is extended to turbulent radiation modeling. First, the principle of band approximation is introduced. Based on this prerequisite, the spatial development of radiation intensity is analyzed. Starting point is the spectrally resolved reference solution with consistent modeling of turbulence effects on radiation, which has been discussed in Sec. 5.2.2 (Fig. 5.18a). The convergence of the integral intensity obtained with the band approximations to this reference solution is then used to assess the performance of the approximations with the different partitioning methods.

5.2.3.1 Band Approximation

The principle of the band approximation method is to group regions Δs_i of the spectral range of interest Δ_s together into so-called bands. Instead of solving the radiative transport equation 5.5 for the detailed spectrum, the spectral ranges within each band are treated integrally. The number of bands n_{bd} needs to be sufficiently high to ensure that the total radiation intensity is fairly approximated:

$$\sum_{i=1}^{n_{bd}} I_{\Delta s_i} \approx \int_{\Delta s} I_s ds \quad . \tag{5.18}$$

Together, the bands cover the whole considered spectral range and must not overlap. However, each single Δs_i is not necessarily a connected space.

The band approximated form of the discretized radiative transport equation

5.5 reads

$$I^{+}_{\Delta s_i} = \mathcal{E}_{\Delta s_i,net} + I^{-}_{\Delta s_i}\alpha_{\Delta s_i} \tag{5.19}$$

with

$$I_{\Delta s_i} = \int_{\Delta s_i} I_s ds \tag{5.20}$$

$$\mathcal{E}_{\Delta s_i,net} = \int_{\Delta s_i} \mathcal{E}_{s,net} ds \tag{5.21}$$

$$\alpha_{\Delta s_i} = \frac{1}{\Delta s_i}\int_{\Delta s_i} \alpha_s ds \quad . \tag{5.22}$$

To fully define the band approximation, a method is required to partition the spectral range into the different bands. Two partitioning methods are considered, which are introduced in the following: The *value-based* method, which has been found to provide the best approximation quality at given computational effort in the previous study [67], and the *sequential* partitioning for reference. These partitioning strategies can be considered as simple forms of the k-distribution and narrow-band approaches [19], respectively. They are visualized for an OH absorption coefficient at representative conditions in Fig. 5.20. The alternating colors indicate the different bands, i.e. the spectrum is split in vertical direction for the sequential and horizontally for the value based partitioning. The straightforward partitioning approach is a segmentation of the wave number[7] range of interest in bands of equal width (Fig. 5.20a). This method is referred to as sequential partitioning. Far better convergence however was reached in the pre-study [67] by dividing the spectrum based on the value of the absorption coefficient (value based partitioning, Fig. 5.20b). Thereto the overall range of absorption coefficients is divided into n_{bd} sections and the spectral ranges falling within each section are grouped together. This partitioning method requires a reference profile of the OH absorption coefficient, which is computed at the chamber pressure and a temperature of $T = 3000$ K (Fig. 5.20).

---

[7] The wave number is the spectral variable used in the present work. However, the procedure can be analogously applied to a wave length based description.

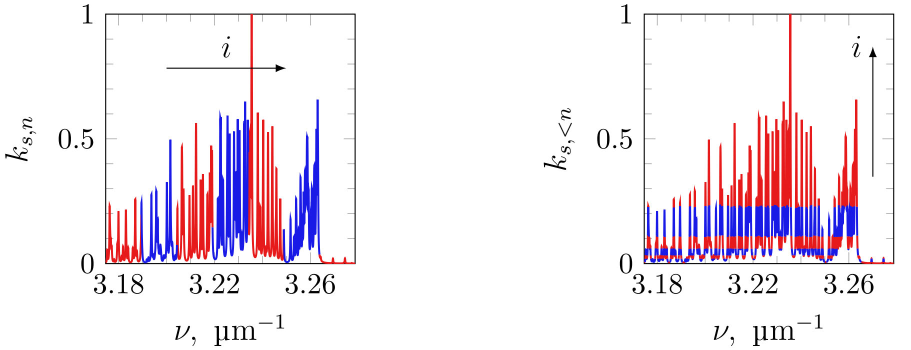

(a) Sequential partitioning **(b)** Value based partitioning

Figure 5.20: Partitioning approaches ($n_{bd} = 7$)

5.2.3.2 Approximation Quality

With the discussed spectrally resolved reference profiles, the band-approximation quality of the considered partitioning approaches is evaluated. The relative error $\mathfrak{E}_I$ of the integral intensity at the location of the observer, obtained with the band approximation (Eq. 5.18) is given in Fig. 5.21. The computations have been performed using consistent turbulence treatment (Eq. 5.13) and cover the full spectral range from the BKD experiment ($\lambda_c \pm 5\,\text{nm}$ with the center wave length $\lambda_c = 310\,\text{nm}$). In addition, results for the reduced wave number range ($\lambda_c \pm 1\,\text{nm}$) that has been used in the previous study [57] are included for reference. For both spectral ranges the relative error of the value based partitioning decreases significantly faster with increasing band number than that of the sequential approach. Good results are obtained with less than $n_{bd} = 10^1$ bands. At the same time, the value based approach is only weakly sensitive towards the width of the spectral range. In contrast, the sequential approach requires about $n_{bd} = 10^2$ or $n_{bd} = 10^3$ bands for satisfactory results. The better convergence of the value based partitioning is consistent with previous findings for the simple approach [57]. In the remainder of the present work, value based grouping with $n_{bd} = 5$ bands is used to approximate the spectral dependence of the OH* radiation.

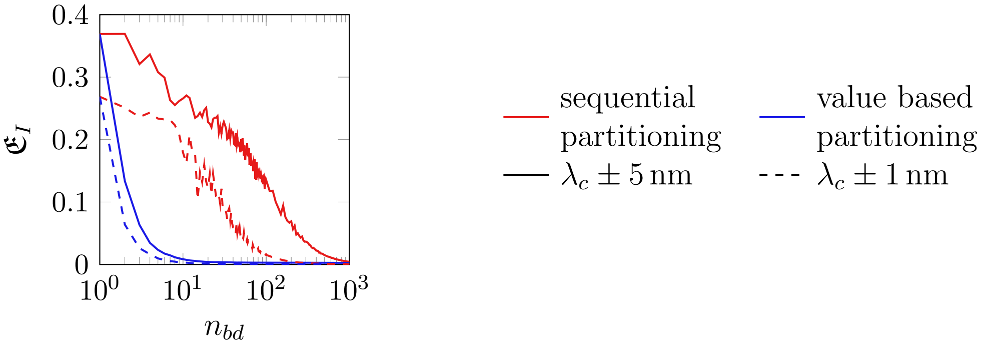

Figure 5.21: Relative band approximation error

5.2.4 Numerical Implementation

Following the previous findings, the classical radiation model with full turbulence interaction (Eq. 5.13) is used, combined with the spectral band approximation (Eq. 5.18) using value based grouping (Fig. 5.20b). The implementation of the band-approach requires an efficient evaluation of the associated absorption and emission properties. Therefore, analogous to the flamelet tabulation, for each band the terms in Eq. 5.5 as given in Eq. 5.13a and 5.13b are tabulated as function of mixture fraction, its variance and enthalpy. As these three parameters determine temperature and OH* concentration the last free variable is the distance Δx. To avoid adding another dimension to the already three-dimensional table, the emission is approximated by

$$\mathcal{E}_{\Delta s,net} = \int_{\Delta\nu} I_{b,\nu}\left(1 - \exp\left(-k_\nu \Delta x\right)\right) \tag{5.23}$$

$$\approx c_{e,0}\left(1 - \exp\left(-c_{e,1}\Delta x\right)\right) \quad , \tag{5.24}$$

while the absorption term

$$\alpha_{\Delta s} = \frac{1}{\Delta\nu}\int_{\Delta\nu} \exp\left(-k_\nu \Delta x\right) \tag{5.25}$$

is modeled as

$$\alpha_{\Delta s} \approx 1 + c_{a,0}\left(\exp\left(-c_{a,1}\Delta x\right) - 1\right) \quad . \tag{5.26}$$

The coefficients $c_{e,0}$, $c_{e,1}$, $c_{a,0}$ and $c_{a,1}$ are obtained from curve-fitting. As the fitting functions for emission and absorption are non-linear in terms of

$c_{e,1}$ and $c_{a,1}$, respectively, these two coefficients are not tabulated directly. Instead, in addition to $c_{e,0}$ and $c_{a,0}$ a reference value of $\mathcal{E}_{\Delta s}$ and $\alpha_{\Delta s}$ at a fixed distance Δx_{ref} is tabulated. Interpolation is then carried out for this reference value and $c_{e,1}$ and $c_{a,1}$ are calculated from the result.

At each enthalpy level the equations 5.24 and 5.24 are evaluated for a laminar flamelet and extended to the mixture fraction variance dimension via PDF-integration. With the absorption properties for each cell known, Eq. 5.5 can be evaluated. For the three-dimensional cases this is done using explicit ray-tracing (cf. Fig. 5.11b). For the two-dimensional cases, an efficient semi-recursive procedure has been developed. Its schematic is given in Fig. 5.22. Fig. 5.22a shows a cross-sectional view of Fig. 5.11a. In radial direction, the computational grid consists of n cells. For each cell, the radiation intensity detected at the end of the corresponding line-of-sight through the flame is calculated. The line-of-sight of a cell i_{ref} intersects twice with each cell from i_{ref} to the outer boundary of the domain, $i = n$. For the calculation of the radiation intensity, the line-of-sight is split in two. Starting from cell i_{ref}, the development of radiation intensity between $\xi = -1$ to $\xi = 0$ is evaluated recursively using the function $\mathcal{I}^+$ that takes the cell index i as argument and returns the radiation intensity I^+ of the cell, see Fig. 5.22b with Eq. 5.5 and Fig. 5.13 for nomenclature. From there on, the right side between $\xi = 0$ and $\xi = 1$ is evaluated explicitly via Eq. 5.5. The final results is the detected radiation intensity at cell i_{ref}.

5.2.5 Summary of Findings

The necessary modeling detail to calculate OH* radiation images from numerical results that are suitable for comparison with the experiment has been studied. A comparison of emission models showed that the classical radiation model and the EFRM-A yield nearly identical results with the classical model having the principle advantage of providing quantitative estimations of the radiation intensity. An approach to capture the impact of turbulence on the radiation images in a way that is consistent with the CFD simulation setup (Sec. 5.1) has been developed. Any simplification of

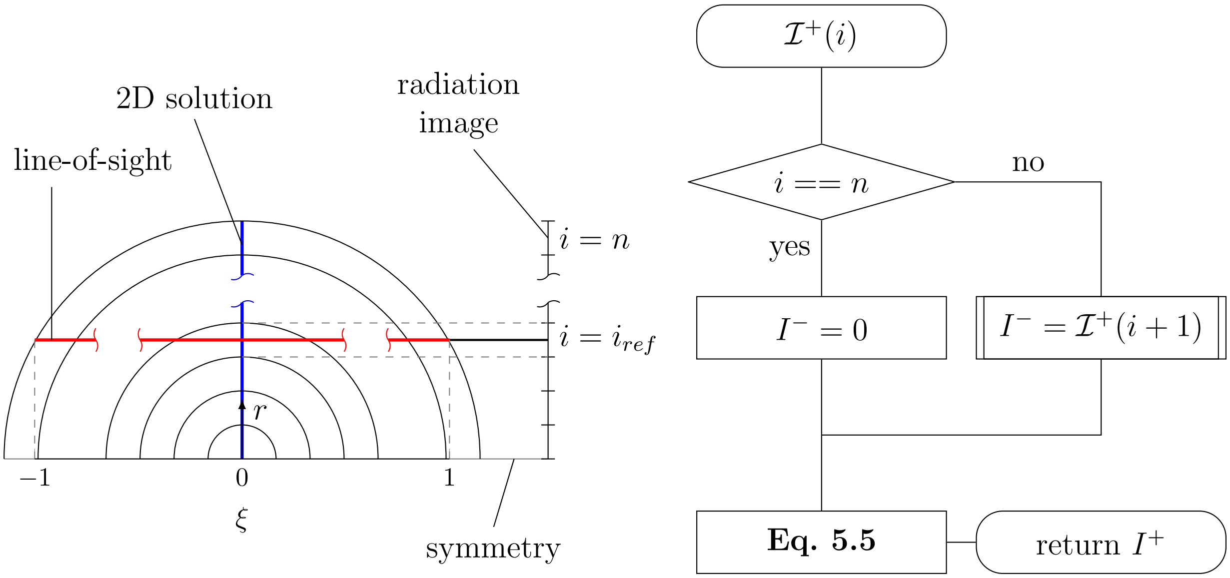

(a) Grid structure schematic **(b)** Recursive intensity calculation

Figure 5.22: Implementation scheme for OH* radiation image calculation

this approach resulted in notable differences between the obtained radiation images. The spectral approximation of radiation modeling has been studied for this consistent turbulence treatment. It has been found that a band approximation using value based spectral partitioning converged well to the results based on spectrally resolved calculations. Consequently, the OH* image calculation for the single flame validation in Sec. 5.3.3 will be based on the classical emission model combined with fully consistent turbulence treatment and a band approximation of the spectral range.

5.3 Single Flame Validation

The stability assessment procedure (Chap. 4) relies on the numerical flow fields computed for single flames (cf. Sec. 5.1). In the present section, the numerical single flame results are validated with experimental data. This is done to ensure that the discussion of the results from the different parts of the stability assessment procedure (Chap. 6 to 8) relies on reasonable flow predictions and that no deficiencies of the CFD-modeling are attributed to the methodology. For the BKD, three sets of data are available that can be used for validation purposes: radiation images of blue and OH^* radiation and static pressure measurements along the chamber wall (cf. Sec. 3.1). In the following, the experimental data are used to calibrate the turbulent Schmidt number of the simulations and evaluate the soundness of the single flame results in terms of flame structure and combustion process. First, an overview of the flow and flame structure is given (Sec. 5.3.1) with focus on their connection to the validation data. Starting point for the actual validation are the wall pressure distributions (Sec. 5.3.2). Then, OH^* radiation images are covered in Sec. 5.3.3, followed by blue radiation (Sec. 5.3.4). Finally, the conclusions of the section are summarized in Sec. 5.3.5.

5.3.1 Flow Structure and Validation Data

The flow structure of a single rocket engine flame has been introduced in Sec. 2.1. In the present section, a more detailed look at the flow in a BKD single flame is taken. The impact of the simulation domain (cf. Sec. 5.1.4) on the solution structure is studied and the relation between the validation data and the characteristic flow features is addressed.

The combustion occurs in the diffusion flame forming between the oxidizer and fuel streams. The underlying mixing process governs the reaction process (cf. Sec. 5.1.3) and thus the axial distribution of the heat release rate, shown in Fig. 5.23a for a two-dimensional case. It has two peaks: one at the end of the recirculation zone and a second one around the location where the stoichiometric line reaches the axis. The second maximum belongs to a considerably larger region of high heat release that extends notably beyond the length of the cold oxygen core before rapidly decreasing to zero. Both types of validation data, wall pressure and radiation images, are linked to the combustion process. With an increasing amount of heat released the average density drops, leading to a decrease of static pressure due to accel-

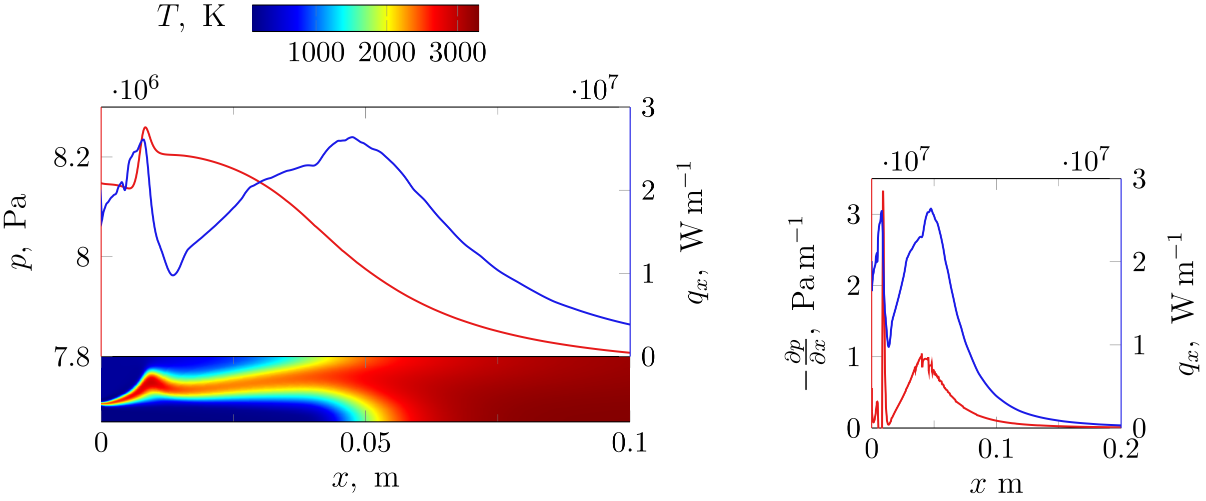

(a) Wall pressure, heat release and temperature field

(b) Wall pressure gradient and heat release

Figure 5.23: Relation between flow solution and validation variables

eration effects. At the same time, combustion leads to a total pressure drop, as known from a Rayleigh flow. The correlation between local heat release and wall pressure gradient is demonstrated in Fig. 5.23b where the structure of the main heat release peak is clearly visible in the pressure gradient distribution. Close to the faceplate however, the recirculation zone governs the wall pressure profile (Fig. 5.23a) forming a short low-pressure region. The validation based on the pressure data is conducted in Sec. 5.3.2.

As can be seen from the discussion of OH* radiation modeling in Sec. 2.5 and 5.2 the OH* images are governed by the temperature and OH distribution across the flame. As the combustion occurs in the form of a diffusion flame, i.e. reactions and heat release are mixing dominated (cf. Sec. 5.1.3), the flame radiation is directly linked to the flow structure. If the mixing process is not captured correctly, the flame shape observed in the radiation images cannot be met. Conclusively, the flame radiation images provide access to the spatial structure of the flow. Nevertheless, they are a two-dimensional representation of three-dimensional flow fields (cf. Sec. 5.2). The procedure for the numerical calculation of the flame-radiation images has been designed for a single flame. Technically, the procedure could be adapted to cover the whole flame cluster of the BKD, however the computational expense would be unreasonable. At the same time, the comparison between numerical results and experiment based on one flame is justified by the experimental findings. These show a distinct structure of the flame that the window is centered at. There is no significant distortion from other flames. Possible explanations are the superposition of the other flames to a rather homogeneous background radiation and, for OH^*-radiation, self-absorption that reduces the radiation of background flames. The radiation-based validation is conducted in Sec. 5.3.3 and 5.3.4.

While the general flow characteristics discussed above hold for all single-flame simulations considered in the present work, the detailed flow structures are subject to the cross-sectional shape of the selected domain (cf. Sec. 5.1.4). The two-dimensional simulations correspond to a circular cross-section, which can be considered a reasonable approximation for the middle injector row. In contrast, the outer domains are rather longish with a clearly excentric position of the injector (cf. Fig. 5.6). To give an idea of the underlying flow structures, in the following the flame shape obtained from three-dimensional calculations of a single flame in the outer injector row is compared to a two-dimensional axis symmetric case in Fig. 5.24. By design, for the two-dimensional case, the flame possesses a circular cross-sectional shape at each axial position. For the three-dimensional results, this is only the case in the upstream part of the chamber. There, the shape of the diffusion flame is determined by the circular injection of the propellants. As the flow moves downstream, the impact of the domain geometry on the flame becomes visible and the flow adapts to the angular cross-section. The flame becomes flatter in radial direction and is shifted towards the wall. This comes along with a more complex, three-dimensional structure of the recirculation zone, compared to the two-dimensional case. In about the second half of the flame, the stoichiometric contour reaches the lateral boundaries. Neighboring flames are no longer clearly separated but form a continuous flame sheet along the chamber circumference.

Due to the dominant role that mixing has on the flame, the flow fields are sensitive to turbulent species diffusion. The associated modeling parameter is the turbulent Schmidt number Sc_t with an increase of Sc_t decreasing tur-

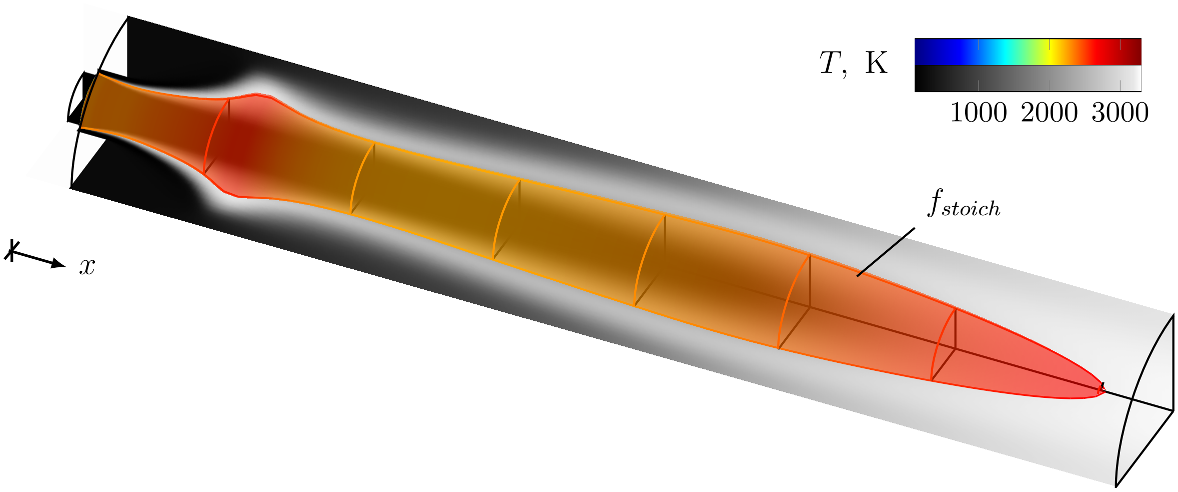

(a) 2D axis-symmetric

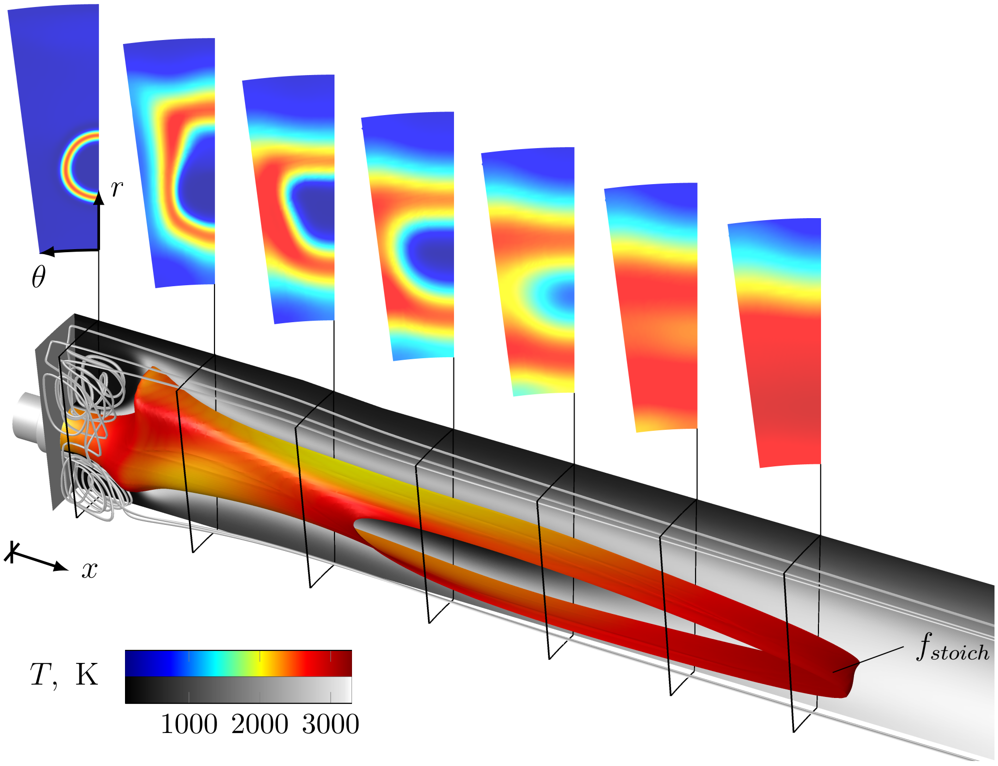

(b) 3D

Figure 5.24: Outer injector row solution

bulent diffusivity and vice versa. In the following two sections (Sec. 5.3.2 and 5.3.3) the experimental results will be used to calibrate the turbulent Schmidt number. For the unstable LP2 this calibration maps some instability effects into the steady solution. Transverse velocity fluctuations reduce the flame length [12,45]. This flame shortening also occurs in the flow underlying the experimental data of LP2. As the steady single flame simulations do not resolve instability related flame shortening, this phenomenon instead results in a lower calibrated turbulent Schmidt number. To explicitly study the impact of flame shortening on the radiation images, a transient simulation with velocity excitation is included for LP2 in Sec. 5.3.3. During the validation of the associated images, the rotation of the T_1 mode in the experiment needs to be kept in mind. Even though the mode tends to become more standing for unstable cases, the mode orientation changes over time and data on its position relative to the observation window are currently not available. Thus the experimental radiation image represents a superposition of several mode orientations, whereas the excitation in the simulations is harmonic with a fixed amplitude distribution. Nevertheless, the effect of the instability on the flame image can be assessed qualitatively (Sec. 5.3.3).

5.3.2 Wall Pressure Distribution

The wall pressure distribution and its relation to the flow structures has been discussed in the previous section 5.3.1. On this basis, the wall-pressure based validation is carried out in the following. A comparison of the numerically calculated profiles from two-dimensional single flame simulations with experimental data is shown in Fig. 5.25 for different turbulent Schmidt numbers. The data are normalized by the value of the last sensor position. This normalization eliminates small differences of the absolute pressure level from the comparison. This is beneficial for the validation as the axial development of the wall pressure is more important than the absolute pressure value (cf. Sec. 5.3.5), which is strongly influenced by the specification of the outlet boundary condition (Sec. 5.1.5). The last sensor is selected as reference since it is located in the region of lowest axial pressure gradients. In the front and rear region of the chamber the wall pressure is nearly unaffected

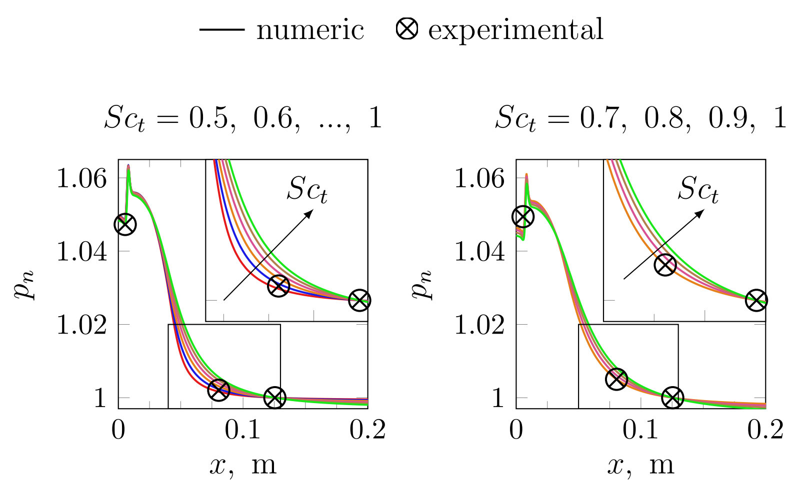

(a) LP1 **(b)** LP2

Figure 5.25: Normalized wall pressure distribution from 2D simulations

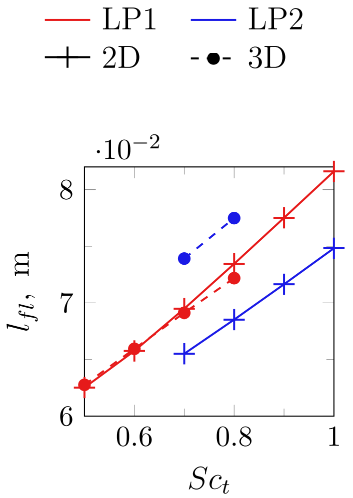

Figure 5.26: Flame length

by the turbulent Schmidt number, indicating that neither the size of the recirculation zone nor the final degree of mixing reached at the domain outlet are sensitive to this parameter. However, the magnitude of the axial wall pressure gradient increases with decreasing turbulent Schmidt number due to faster mixing and combustion (cf. also [61]). As the first sensor position is close to the re-attachment point of the recirculation zone and thus lies in a region of high axial wall pressure gradients, its value is considered to be less important for the validation than that of the second sensor. The comparison of experimental and numerical data shows that for LP1 a value of $Sc_t = 0.5$ or $Sc_t = 0.6$ is appropriate. Since those values lie at the lower range of typical turbulent Schmidt numbers, $Sc_t = 0.6$ is selected. For LP2 the Schmidt number is slightly higher with $Sc_t = 0.7$ giving the best approximation of the experimental data. The selection of the turbulent Schmidt number will be considered further in the OH* radiation based validation (Sec. 5.3.3).

The changes in the wall pressure distribution are associated with a change of the flame length. Fig. 5.26 shows the axial distance between the downstream tip of the stoichiometric contour (cf. Sec. 2.1 and 5.3.5) and the faceplate in dependence of the turbulent Schmidt number. The flame lengths of both load points lie within the same range. The dependence of the flame length on the turbulent Schmidt number is nearly linear with a slightly lower slope for LP2 than for LP1. The selection of the computational domain does not significantly impact the flame length. Indeed, at constant turbulent Schmidt number, the three-dimensional results of LP2 give a higher flame length than the two-dimensional ones. However, as the turbulent Schmidt number is calibrated individually for each case, the flame length is adjusted to follow the experimental data, and the observed differences are compensated for by a different value of the turbulent Schmidt number. The observed impact of the domain geometry can be explained as follows: In the two-dimensional case, flow and flame can expand uniformly across the domain cross-section. In contrast, in the three-dimensional domain lateral expansion is limited by the narrower circumferential shape of the domain (cf. Sec. 5.1.4). Even though there is more volume available towards the chamber wall, the reacting flow does not fully occupy this volume, as can be seen from Fig. 5.24. Instead, the deflection of the flame towards the outer regions of the domain leads to a further contraction in lateral direction. So effectively, in the three-dimensional simulations the flame occupies a smaller cross-sectional area than in the two-dimensional cases, explaining the higher flame length. Compared to LP2, LP1 has an about 60 % lower total mass flow (cf. Sec. 3.1). Thus the impact of the computational domain's cross-sectional shape on the flame length is lower. At the same time other effects like the deflection of the flame towards the chamber wall have a stronger relative impact on the development of the flow. Moreover, the different mass-flows of LP1 and LP2 lead to differences in turbulence and thus mixing, which affects the flame length as well.

The impact of the turbulent Schmidt number on the heat release (Fig. 5.27a) is consistent with the wall pressure distribution. The increase of the pressure gradient's magnitude with lower values of Sc_t corresponds to an increase of the main peak of the heat release distribution. As this means increased mixing and combustion in the upstream part of the chamber, the heat release decreases in the downstream section. The dominant consequence of the domain selection is a notable increase of the maximum value of the narrow first peak (cf. Fig. 5.27b, 5.27c). This can be probably attributed to the changed structure of the recirculation zone. Further downstream the

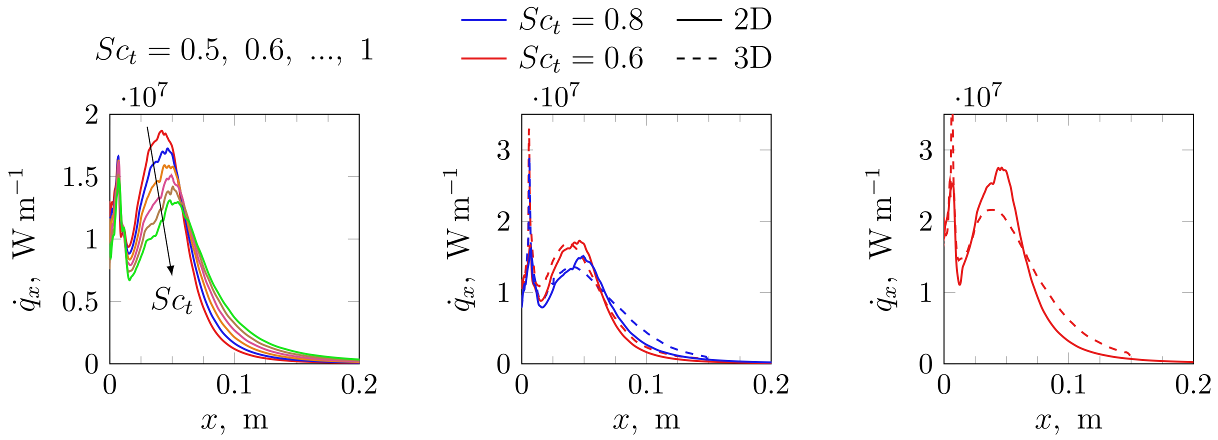

(a) LP1, 2D **(b)** LP1, 2D/3D **(c)** LP2, 2D/3D

Figure 5.27: Axial heat release distribution

differences between the two and three-dimensional results are minor.

5.3.3 OH* Radiation Images

In addition to the one-dimensional validation via the wall pressure, the prediction quality of the two- or three-dimensional flow structure can be assessed via flame radiation images. The process to obtain images from the numerical results that are comparable to the experimental ones has been discussed in Sec. 5.2. On this basis, the radiation based validation is carried out in the following. Thereto, three types of simulation are considered. As reference cases, three dimensional simulations are used. They are conducted on a domain that represents a flame in the outer injector row (cf. Sec. 5.1.4), which corresponds to the flame visible in the experiment (cf. Sec. 3.1). In three dimensions both steady and for the unstable LP2 unsteady simulations with velocity excitation (cf. Sec. 4.3.2) are conducted. The excited simulations are used to study the effect of acoustic-induced flame shortening on the images. The third simulation type to be considered is the basic two-dimensional setup (Sec. 5.1) that corresponds to the single flame simulations used for the evaluation of the stability assessment procedure in the remainder of this work (Chap. 6 to 8).

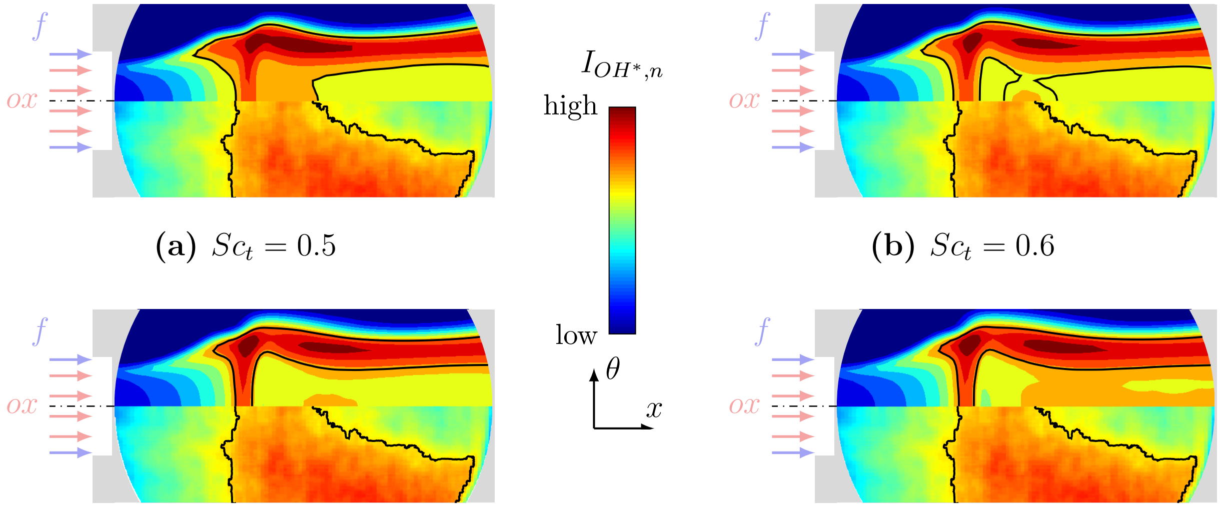

(a) $Sc_t = 0.5$ **(b)** $Sc_t = 0.6$

(c) $Sc_t = 0.7$ **(d)** $Sc_t = 0.8$

Figure 5.28: Experimental (bottom) and numerical (top) OH* radiation for LP1 from three-dimensional simulations

OH* radiation images from steady three-dimensional simulations of LP1 for different turbulent Schmidt numbers are shown along with the experimental ones in Fig. 5.28. In the experiment, intensity initially increases until at about one quarter of the window a region of high intensity forms, marked by the black iso-line in Fig. 5.28. Further downstream, this zone bends around a low-intensity core. Inside the high intensity area, a peak region of highest intensities can be identified. The overall structure of the numerical radiation image agrees with the experimental one. Radiation intensity grows from low values at the inlet, forms a high intensity peak region and develops a low-intensity core further downstream. However, two deviations are found that can be attributed to the missing background radiation in the numeric images: Close to the faceplate the numerical results show that radiation intensity increases along the shear layer in the plane of observation, but lower intensities are predicted in the core and the outer region. In contrast, the experiment shows a more uniform intensity distribution across the image height. The same applies further downstream, where the high intensity region around the core is surrounded by a zero-intensity outer region in the numeric results. In contrast the experiment shows high intensities up to the outer edge of the image. These deviations can be explained by the distribution of the hot combustion products in the visible part of the flame: In the region close to the faceplate, they are concentrated in a thin shear layer and even further downstream they do not reach the domain boundary. Thus the background radiation from the other flames determines the radiation intensity in these regions. The shape of the low-intensity core strongly depends on the turbulent Schmidt number. For $Sc_t = 0.5$ (fig. 5.28a) the shape of the core flow region, marked by a black intensity iso-line, agrees well with the experiment. The high intensity region is reasonably met by the simulation. Only the location of the maximum intensities appears to be slightly further upstream in the numerical solution. However, the associated structure is weak in the experiment and thus to be taken into account with care. For higher turbulent Schmidt numbers (Fig. 5.28a, 5.28b and 5.28d) the structure and position of the core region changes, leading to considerable differences in the observed radiation pattern.

For LP2 the radiation images from three-dimensional simulations, with and without velocity excitation, are shown in Fig. 5.29. The pricniple structure of the image is the same as just discussed for LP1. However, two significant deviations between numerical results and experiment are visible, which do not change qualitatively for different turbulent Schmidt numbers. First, the core region is considerably less intense and wider in the experiment. Second, an offset between the axial location of the high intensity regions occurs. This might be explained by the fact that LP2 is unstable. Previous BKD studies with LES [42] and excited RANS [12] simulations showed that instabilities and particular the transverse velocity fluctuations shorten the flame. To test this hypothesis, a transverse velocity excitation simulation as described in Sec. 4.3.2 is conducted. A pressure amplitude of 1 bar is used for the excitation. This choice has been made due to the uncertainty of the mode orientation (cf. Sec. 5.3.1). On the one hand the value lies considerably below the maximum amplitudes observed in the experiment (2.3 bar or 4.5 bar peak to peak [6]), but on the other hand can be expected to already have a notable impact on the solution with $|\hat{p}|/\bar{p}_c > 1\,\%$. The resulting image, averaged over one oscillation period, is shown in Fig. 5.29c. A slight improvement of the structures on the upstream side of the high intensity region is visible (bottom). However, the intensity difference between the peak

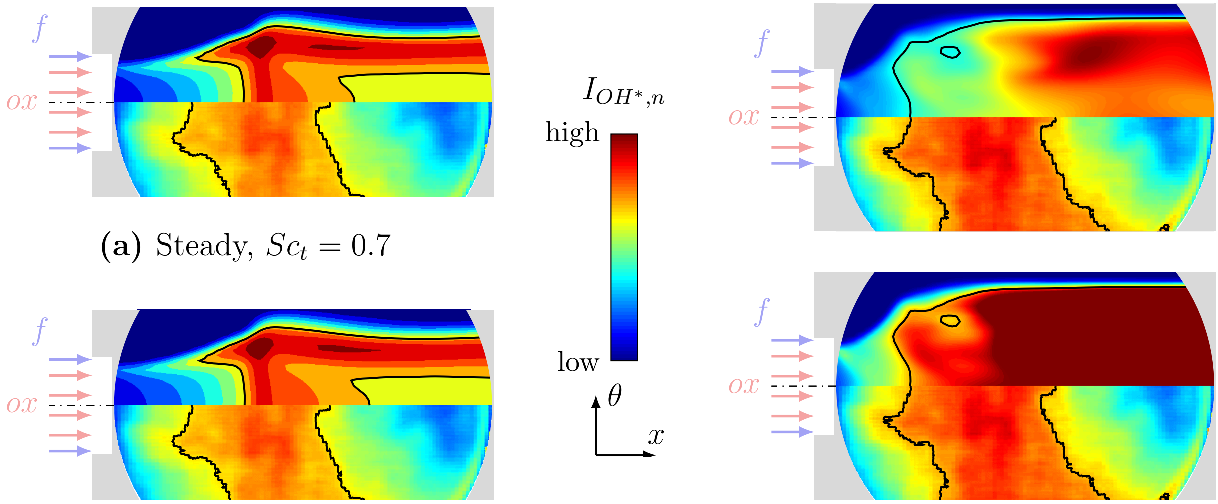

(a) Steady, $Sc_t = 0.7$

(b) Steady, $Sc_t = 0.8$

(c) Velocity excitation, $Sc_t = 0.7$, different color ranges

Figure 5.29: Experimental (bottom) and numerical (top) OH* radiation for LP2 from three-dimensional simulations

and the core region is even more reduced, increasing the deviation from the experiment (Fig. 5.29c, top).

While the three-dimensional simulations are more accurate at representing the single flame domain than two-dimensional ones, their computational cost is too high for the stability assessment procedure. For this reason, the impact of the reduction to two dimensions is further investigated in the following with the focus on the comparison of the numerical results with the experimental data including the effect of the choice of the turbulent Schmidt number (Sec. 5.3.2).

Thus, the results of the two-dimensional, axis symmetric simulations are used in the actual stability assessment procedure. They are considered in the following. Besides the general comparison of numerical results and experiment, an extension of the calibration of the turbulent Schmidt number in Sec. 5.3.2 is of interest.

The impact of the turbulent Schmidt number on the radiation images for LP1 can be seen from the OH* radiation intensity distribution shown in Fig.

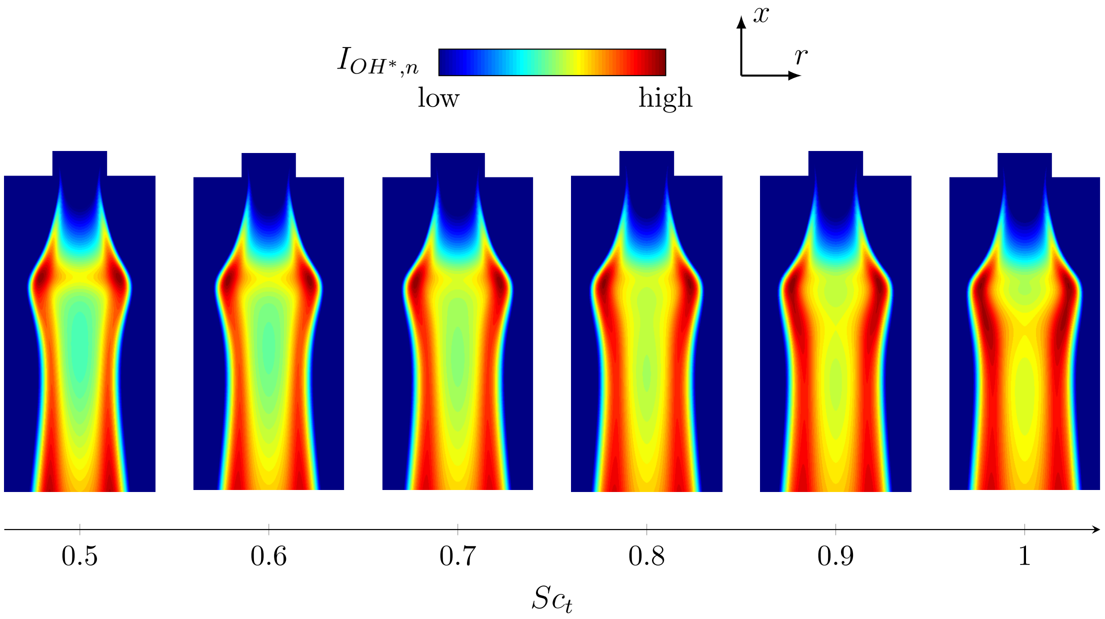

Figure 5.30: Impact of turbulent Schmidt number on OH* radiation image of LP1

5.30. The images are normalized with the local intensity maximum in the flame bulge. In the following, focus is placed on the impact of the turbulent Schmidt number on the radiation image structure. At low turbulent Schmidt numbers a thin region of increased intensity connects the peak zones in the bulge region. Downstream, the intensity decreases towards the low-intensity core. With increasing turbulent Schmidt number the core intensity becomes higher, causing the aforementioned pattern to vanish. Beyond $Sc_t = 0.9$ the region of maximum intensity in the flame bulge becomes longer and the core region is divided into two zones by an additional streak of slightly increased intensity. The numerical results for turbulent Schmidt numbers below $Sc_t = 0.9$ agree with the structures observed in the experimental images (cf. Fig. 5.28). The characteristic high-intensity region at the upstream boundary of the core is reproduced better as the turbulent Schmidt number gets lower. This agrees with the findings of the wall pressure based validation for LP1 (Sec. 5.3.2) which showed good agreement between numerical results and experiment at low turbulent Schmidt numbers.

A direct comparison between numerical results and experiment is shown

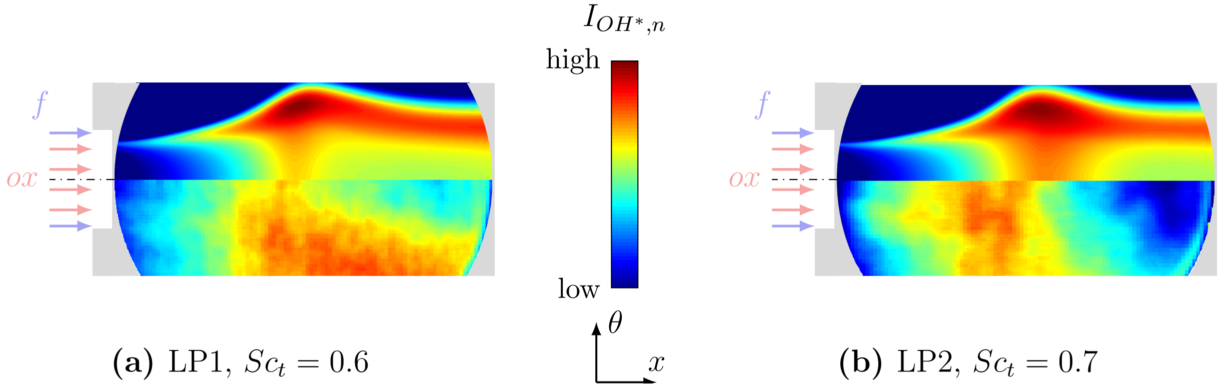

(a) LP1, $Sc_t = 0.6$

(b) LP2, $Sc_t = 0.7$

Figure 5.31: Experimental and 2D numerical OH* radiation

in Fig. 5.31a. For the two-dimensional case, the location of the intensity maximum is even slightly better reproduced than for the three-dimensional results (cf. Fig. 5.31). In the upstream region of the image, the numerical results predict a stronger radial intensity gradient than the experiment while the intensity difference between peak and core region is slightly underestimated. However, the overall structures of the numerical images agree well with the experiment.

For LP2 a comparison of the two-dimensional OH* images from the simulation (Fig. 5.31b) with the experiment shows the same trend as the three-dimensional cases (Fig. 5.29). In the simulations the high intensity region is located further downstream than in the experiment. However, at the same time the impact of the turbulent Schmidt number (Fig. 5.32a) is considerably weaker than for LP1 and only small changes of the core zone are visible. Thus, an additional verification of the turbulent Schmidt number calibration from Sec. 5.3.2 cannot be conducted based on the shape of the core zone. Nevertheless, the position of the low intensity core depends slightly on the turbulent Schmidt number. This is illustrated by the position of the initial intensity peak on the flame axis, which constitutes the upstream boundary of the core region, shown in Fig. 5.32b. A linear dependence of this location on the turbulent Schmidt number is observed, consistent with the flame length trend discussed in Sec. 5.3.2.

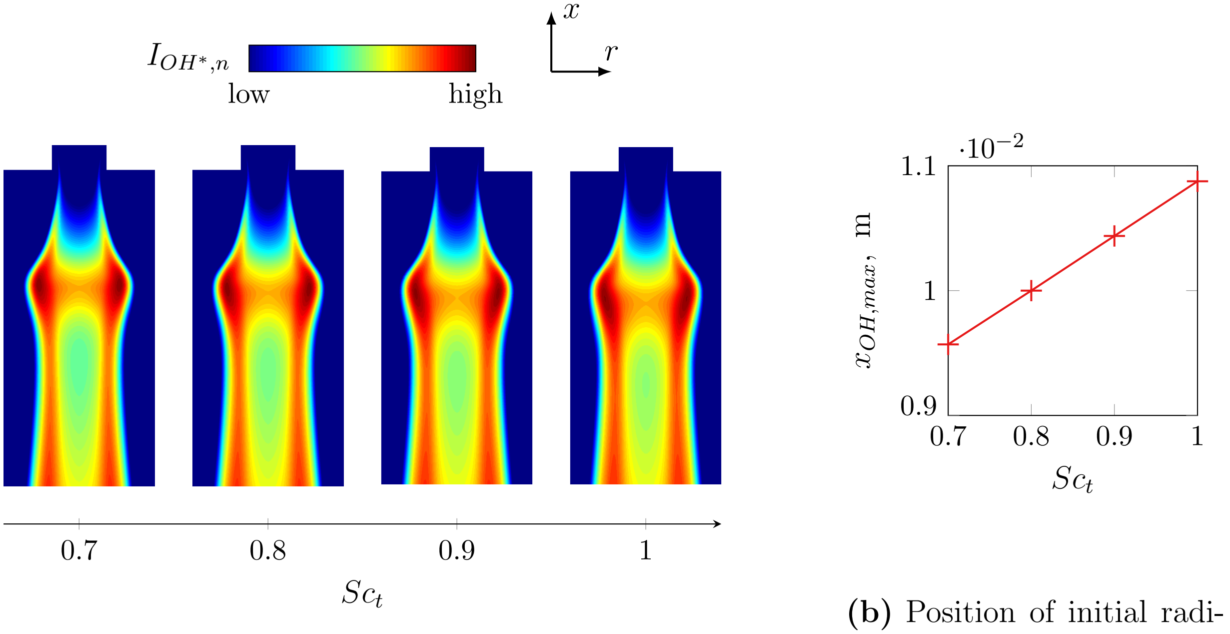

(a) OH* image

(b) Position of initial radiation maximum at axis

Figure 5.32: Impact of turbulent Schmidt number on OH* radiation image of LP2

5.3.4 Blue Radiation

Besides the OH* radiation, blue radiation images are available for the BKD. As discussed in Sec. 2.5.4 previous studies came to the conclusion that self-absorption is negligible and the flames can be considered optically thin regarding blue radiation. Thus the corresponding images can be obtained from the numerical solutions by simple line-of-sight integration of the blue radiation emissions, which are obtained from Eq. 2.70. The resulting images from the three-dimensional simulations of LP1 are shown for different turbulent Schmidt numbers in Fig. 5.33. The numerically calculated structures differ notably from the experimentally observed ones. The calculated images possess a structure similar to the OH* images, which originates from the approximation of emission via the squared OH concentration (Eq. 2.70). In contrast, the experiment shows a rather continuous increase of the radiation intensity in downstream direction. Close to the flame axis, intensities are lower. These deviations cannot be explained by the negligence of

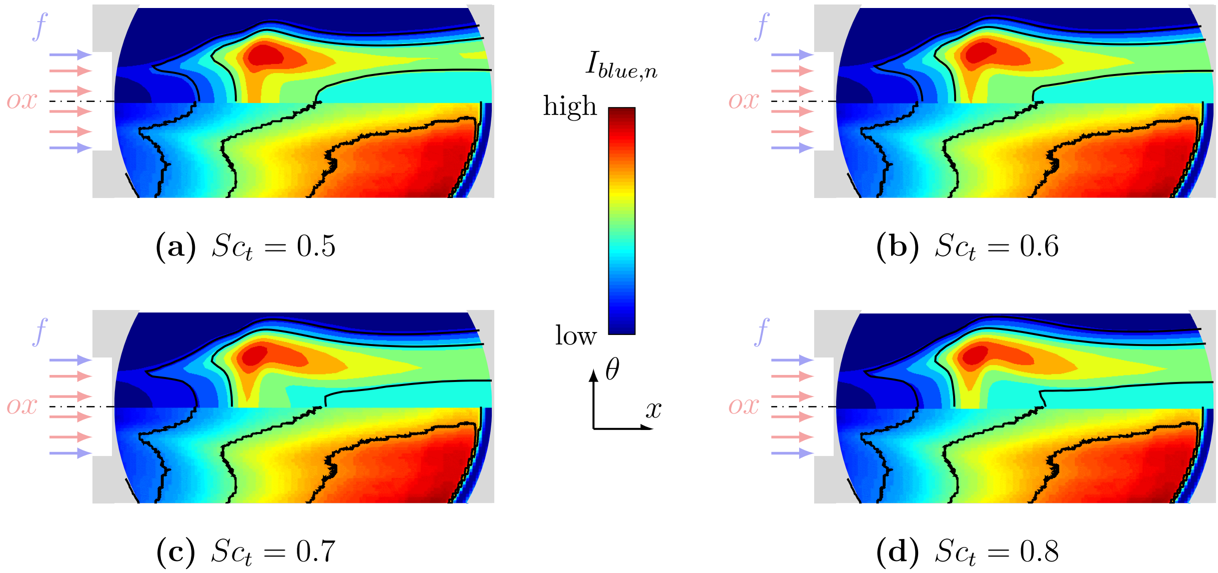

(a) $Sc_t = 0.5$ **(b)** $Sc_t = 0.6$

(c) $Sc_t = 0.7$ **(d)** $Sc_t = 0.8$

Figure 5.33: Experimental (bottom) and numerical (top) blue radiation for LP2

back-ground radiation from other flames in the chamber. As all flames are anchored at the injector, they are located at equal axial positions. Thus any superposition of several flames can lead to blurring of the image structures in radial direction but not to the different axial intensity development visible in Fig. 5.33. As these major deviations between simulation and experiment occur only for the blue radiation, whereas pressure profiles (Sec. 5.3.2) and OH^* images (Sec. 5.3.3) agree well, it is concluded that there is a deficiency in the calculation procedure for the blue radiation images. However, further investigation of blue radiation modeling approaches is beyond the scope of this work and the validation is thus based on the other available data.

5.3.5 Summary of Findings

To provide a sound basis for the application of the stability assessment procedure (Chap. 4) the single flame calculations for the BKD load points LP1 and LP2 have been validated using experimental data. The turbulent Schmidt numbers that give the best agreement between simulation results and experiment have been determined for later use in this work. A relation between the axial static pressure profiles and the mean heat release in the chamber has been shown and by appropriate selection of the turbulent Schmidt number good agreement between the experimental static pressure measurements and the two-dimensional numerical results has been achieved. The flame structure has been assessed via OH^* radiation images. The subsequent comparison to experimental data showed good agreement for LP1 in both, the two- and three-dimensional case. For LP2 the overall flame structure has been met reasonably well, however the high intensity regions are shifted downstream in the simulation compared to the experiment. Evaluating the effect of acoustic velocity fluctuations on the images revealed an improvement of the predicted flame structure on the upstream side of the high intensity zone, however in the rear part of the measurement window deviations increased. Regarding blue radiation, severe differences between numerically obtained and experimental flame images have been found. Those can be attributed to deficiencies in the available blue radiation model. Nevertheless, the good agreement in terms of the wall pressure distribution along with the overall comparable flame structures indicates that the results obtained with the simulation setup from Sec. 5.1 adequately represent the flames in the combustion chamber.

6 Passive Chamber Acoustics

Using the test cases outlined in Chap. 3 the stability assessment procedure described in Chap. 4 is evaluated based on the validated single flame simulation setup from Chap. 5. The evaluation is divided in several steps. In the present chapter, the acoustics of a flow without flame feedback (passive acoustics) are considered. This type of simulation provides the oscillation frequency and target pressure amplitude distribution for the flame response calculation (cf. Sec. 4.3). While the flame response significantly impacts the outcome of the stability predictions via the damping rate, the oscillation frequencies and mode shapes are affected rather weakly. Thus the basic acoustic characteristics of the chamber can be assessed from the perturbation solutions for a passive configuration, which is conducted in the present chapter. Based on the results of the passive acoustic analysis, the flame response calculations are carried out in Chap. 7. The final stability assessment is addressed in Chap. 8.

Besides the perturbation simulation approach (Sec. 4.1) the simulation of the passive chamber acoustics requires the mean flow, whose calculation procedure has been developed in Sec. 4.2. This allows to study the impact that the various mean flow calculation approaches (c-s, c-i and c-κ, cf. Tab. 4.2) have on the predicted basic acoustics of the chamber. In the present chapter a validation of the predicted oscillation frequencies is conducted (Sec. 6.1) considering the different mean flow variants given in Sec. 4.2.2. The sensitivity of the acoustics towards the single flame simulations is evaluated and the experimentally observed modes are identified. Thereupon, in Sec. 6.2 the nozzle correction developed in Sec. 4.2.3 is tested for the TCDs (cf. Sec. 3.2). Finally, the impact of radial stratification on the chamber acoustics is addressed in Sec. 6.3. The findings are summarized in Sec. 6.4.

6.1 Validation of Quasi 1D Approaches

The basic idea of the mean flow calculation procedure is to reproduce characteristic acoustic properties of the chamber flow with a quasi one-dimensional flow. In Sec. 4.2.2 three different variants have been introduced, each reproducing the axial sound speed distributions and either isentropic compressibility (c-s), field impedance (c-i) or isentropic coefficient (c-κ) profiles. In the present section these approaches are evaluated for the BKD (cf. Sec. 3.1). In a first step, the resulting mean flow fields are compared directly (Sec. 6.1.1).Then, a characterization of the chamber's T_1 mode is conducted (Sec. 6.1.2) with the different mean flow variants and the computed eigenfrequencies are compared to measured PSDs. To study the impact of the single flame modeling on the computed chamber acoustics, the sensitivity of the complex eigenfrequencies to the flame length is included in the discussion.

6.1.1 Mean Flow Fields

The quasi one-dimensional mean flows obtained with the three calculation variants c-s, c-i and c-κ (cf. Tab. 4.2) are discussed in the following for the BKD. The Focus of the present subsection lies on the results for LP1, the mean flow for LP2 is addressed along with its acoustic characterization in Sec. 6.1.2.

The quasi one-dimensional mean flow results are characterized by the axial flow profiles. Three profiles are most relevant for the acoustic calculations: The sound speed governs the real valued eigenfrequency. The density is the main distinctive feature between the c-s and the c-i approaches as both differ in the pre-processed target density distribution (Eq. 4.19 and 4.20). The isentropic coefficient has a major influence on the impact of the flame response on the acoustics, which is discussed in Sec. 8.2. For LP1, the respective profiles are shown in Fig. 6.1[1]. By design the sound speed (Fig. 6.1a) is identical to the one-dimensional profile in the cylindrical chamber

---

[1] Note that to achieve convergence for the c-κ approach the inlet temperature had to be slightly changed for both LP1 and LP2. However, the offset is insignificant.

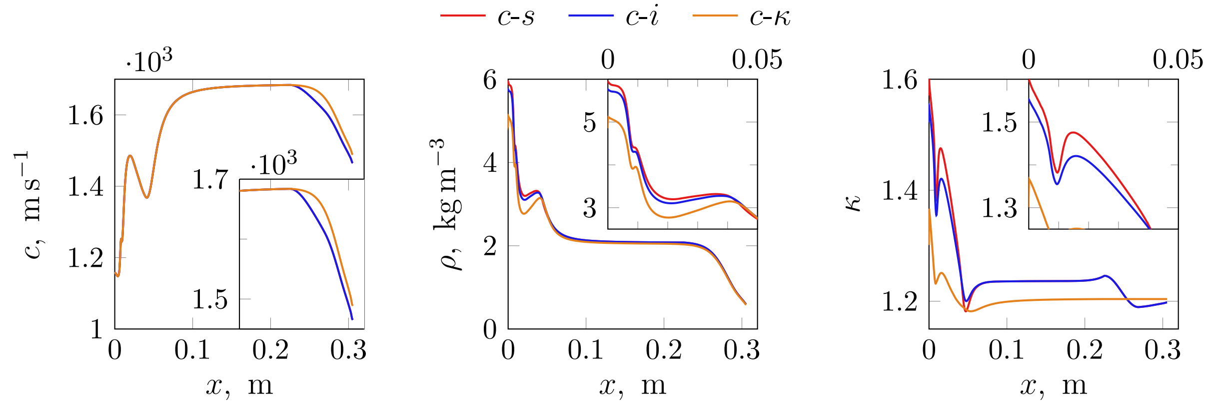

(a) Sound speed **(b)** Density **(c)** Isentropic coefficient

Figure 6.1: Axial mean flow profiles for BKD LP1

section for all three approaches. Deviations however occur in the nozzle part. There the profiles of the c-s and c-i approaches are still very similar, but the c-κ model behaves different. This is explained by the adaption of the mean flow in the nozzle region during post-processing (cf. Sec. 4.2.2). For the c-s and c-i approaches, the isentropic coefficient is gradually changed across the nozzle to the value obtained in the CFD simulation at the throat. For the c-κ flow no such adaption is required as the κ-distribution is not changed during post-processing.

The density distribution is quite similar for all three mean flow variants. Particularly for the c-i and c-s approaches, the profiles are nearly identical. Conclusively, there is no significant difference between the result of the radial density averaging based on isentropic compressibility and on field impedance. The density profiles resulting from the c-κ model, while similar in shape, possesses lower values in the front region of the chamber. Further downstream, however, all profiles are nearly identical. The most significant difference is found in the distribution of the isentropic coefficient (Fig. 6.1c): The c-i and c-s approaches show higher values than the c-κ method along the whole cylindrical section. The difference is strongest close to the faceplate. Due to the aforementioned adaption of the isentropic coefficient in the nozzle to ensure correct sonic conditions, the isentropic coefficient of the c-s and c-i models matches that of the c-κ approach at the nozzle throat.

6.1.2 Eigensolutions

In the following, the impact of the mean flow variants discussed in Sec. 6.1.1 on the T_1 mode in the chamber is addressed for LP1 and then for LP2.

The T_1 frequencies and damping rates obtained with the different mean flow variants for LP1 are shown in Fig. 6.2a along with the frequency of the peak value from the measured PSD. Consistent with the findings for the mean flow, the *c*-*s* and *c*-*i* approaches are almost identical in terms of damping rate as well as oscillation frequency. The *c*-κ approach however predicts an about 150 Hz lower eigenfrequency. The sound speed distribution (Fig. 6.1a) suggests that this might result from the rear part of the chamber. The T_1 mode, which is dominant close to the faceplate, exhibits certain pressure amplitude in the nozzle region as well, see also Sec. 2.4. Thus, the lower sound speed in the nozzle part of the chamber can have an influence on the associated eigenmode even if it is predominantly anchored at the faceplate. However, considering that the deviation of the eigenfrequencies computed with the different mean flow models is in the percent range it can be concluded that the contribution of the rear chamber amplitudes to the overall T_1 mode is low. The explanation is backed up by the distribution of

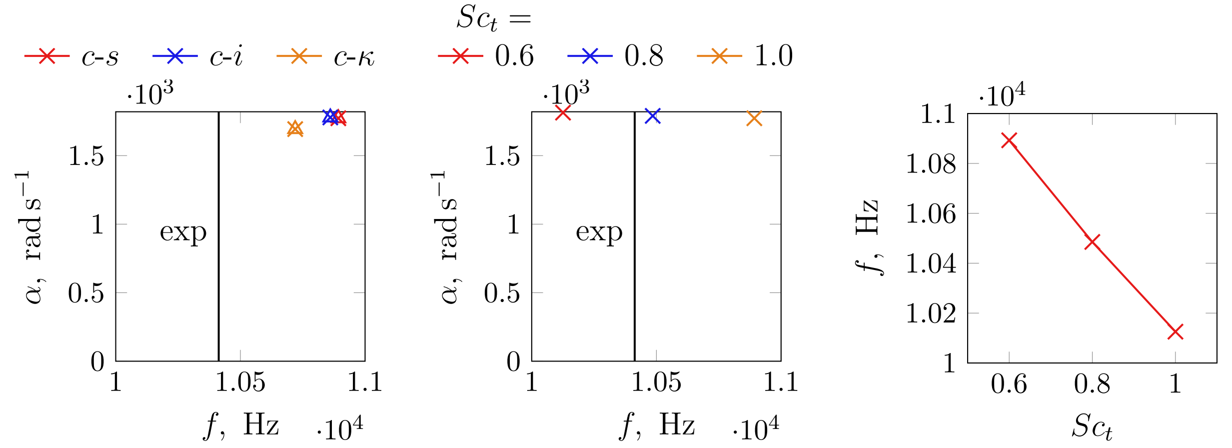

(a) Mean flow model **(b)** Turbulent Schmidt number **(c)** Frequency vs. turbulent Schmidt number

Figure 6.2: Sensitivity of the complex eigenfrequency to mean flow modeling for LP1

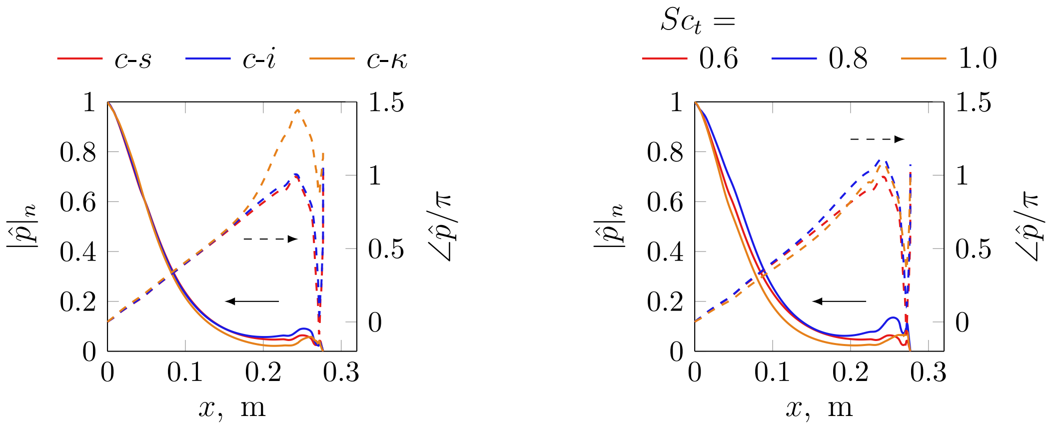

(a) Quasi 1D models **(b)** Turbulent Schmidt number (c-s model)

Figure 6.3: Sensitivity of axial pressure amplitude distribution to mean flow modeling for LP1

the pressure amplitude shown in Fig. 6.3a as well, where the main difference between the c-κ and the c-s or c-i approaches is the phase distribution in the nozzle region of the chamber. The relative impact of the model choice on the damping rate is slightly higher, amounting to about 5 % between c-i or c-s and c-κ approach respectively. Regarding the experiment, all three models overpredict the oscillation frequency by up to about 500 Hz. The agreement is slightly better for the c-κ than the other two models, however a notable offset remains. This discrepancy gives reason to consider the impact of further modeling parameters on the acoustic predictions.

Recalling the single flame validation in Sec. 5.3 it has been found that, while reasonable agreement between numerical and experimental flow structures has been achieved, the calibration of the turbulent Schmidt number is still subject to some uncertainty. For the c-s approach, the complex eigenfrequency obtained with several values of this parameter is shown in Fig. 6.2b. With increasing turbulent Schmidt number the oscillation frequency decreases. Within the common range of turbulent Schmidt numbers, $0.6 \leq Sc_t \leq 1$, the change of the osciallation frequency is about 800 Hz and thus considerably stronger than between the different mean flow models. The relation between turbulent Schmidt number and oscillation frequency is approximately linear as can be seen from Fig. 6.2c. Recalling the flame

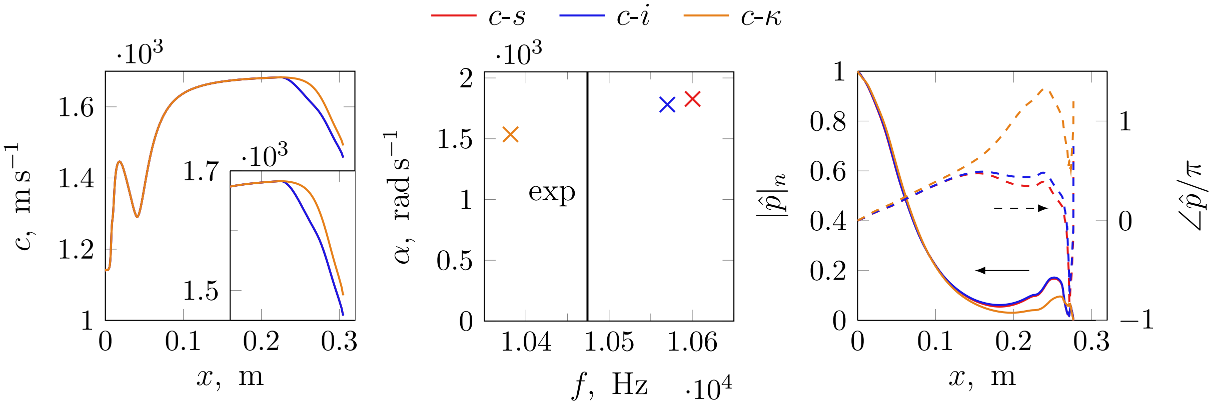

(a) Sound speed **(b)** T_1 eigenfrequency **(c)** T_1 pressure amplitude

Figure 6.4: Mean flow model impact on passive acoustics for LP2

length study (Fig. 5.26) this implies that a linear relation between flame length and eigenfrequency exists with an increase in flame length corresponding to a decrease of oscillation frequency. The impact of the turbulent Schmidt number on the oscillation frequency can be explained by the sound speed profile (cf. Fig. 6.1a). A decrease of the turbulent Schmidt number leads to faster mixing and combustion in the chamber and thus to a higher first peak of the sound speed, while the peak location is nearly unaffected. The T_1 mode frequency follows the increase of the sound speed in the upstream part of the chamber (cf. Sec. 2.4.3), whereas the change of the sound speed gradient has only a minor impact on the acoustics. This indicates that the T_1 mode frequency is governed by the level of the sound speed whereas the size of the region that is decisive for the frequency is less sensitive to the sound speed distribution: This interpretation is backed by the axial pressure amplitude distribution shown in Fig. 6.3b where only slight differences are visible for the different turbulent Schmidt numbers. Likewise, the damping rate (cf. Fig. 6.2b) is nearly independent of the choice of the turbulent Schmidt number. For LP2 the impact of the mean flow model on the results is analogous to that for LP1 as can be seen from the summary given in Fig. 6.4. However, in contrast to LP1, for LP2 using the turbulent Schmidt number chosen based on the single flame calculations in Sec. 5.3 gives very good agreement between experimental and numerically calculated eigenfrequencies.

The previous discussion has focused on the T_1 mode. A broader assessment of the overall system characteristics is obtained when considering a wider frequency range of the PSD covering different mode types. Based on the findings regarding the turbulent Schmidt number, $Sc_t = 0.8$ is used here for the analysis of LP1. For the mean flow calculation the *c*-*s* model is employed. This selection is somewhat arbitrary as the oscillation frequencies are considerably more sensitive to the turbulent Schmidt number than the mean flow model selection.

The measured PSD along with the numerically obtained oscillation frequencies is shown in Fig. 6.5a. In the lower frequency range only longitudinal modes are present. The dominant peak in this region is located between 2 kHz and 3 kHz and met with reasonably accuracy by the numerical results. At higher frequencies of up to 10 kHz the peaks in the PSD are less distinct than in the lower frequency range. Nevertheless the calculated eigenfrequencies seem to deviate stronger from the apparent PSD peaks. The outlet boundary condition has been considered as possible factor impacting the level of agreement in this region. Unlike the lower transverse or radial modes the longitudinal modes in general possess non-zero amplitudes in the rear part of the chamber. Despite the theoretical decoupling of chamber acoustics from the outlet boundary condition by the choked nozzle flow, the type of the outlet boundary condition might numerically impact the results. Therefore, the longitudinal modes have been reevaluated for an acoustically non-reflecting boundary condition at the outlet. The change of the boundary condition leads to a slight increase of the eigenfrequencies but the agreement of the numerical results with the experiment does not change notably. So the decoupling of the chamber acoustics from the outlet boundary condition is adequately captured by the numerical setup and the deviations between numerical results and experiment are caused by the modeling approach.

The transverse, radial and combined modes are clearly visible in the PSD. Starting with the T_1 mode the PSD peaks can be identified with good accuracy. Aside from the pure transverse or radial modes also combined modes appear, like the T_1L_1 or R_1L_1 mode. In general, the higher the frequency the more ambiguous the mode identification becomes. For example the T_2L_2

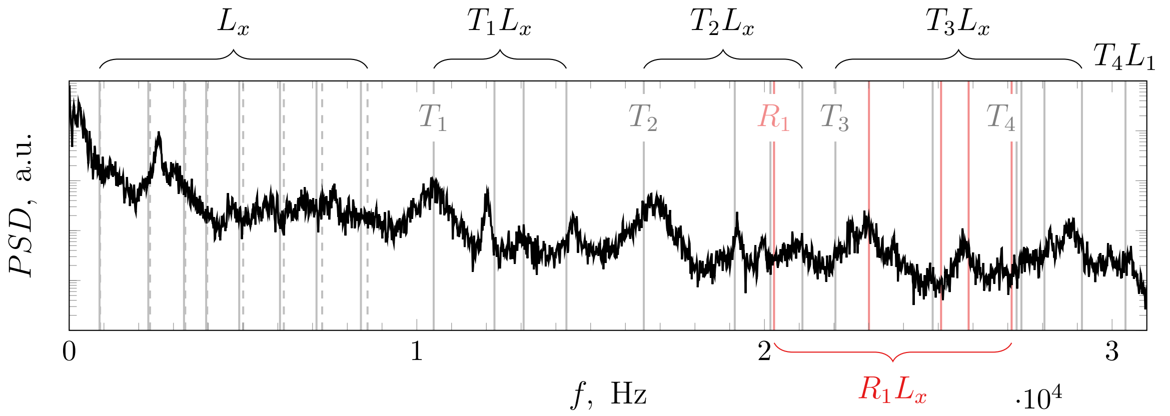

(a) LP1

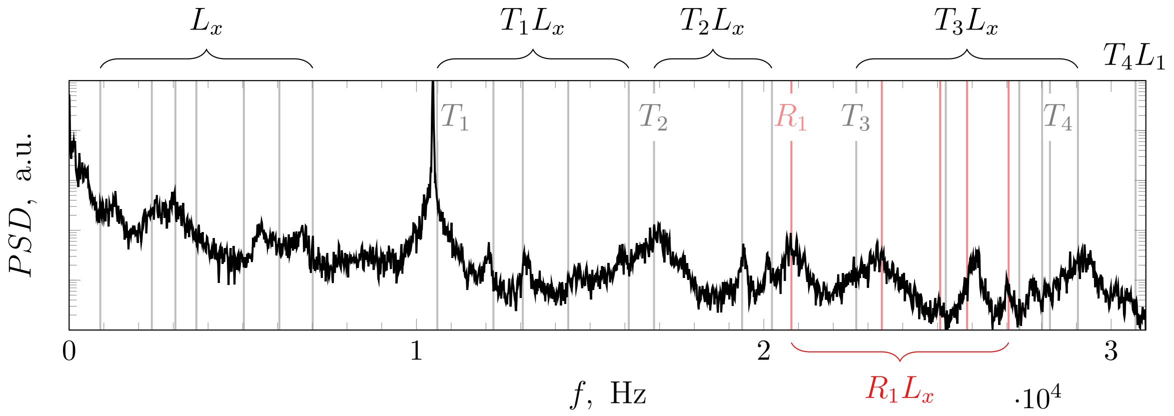

(b) LP2

Figure 6.5: Measured PSD and numerically computed eigenfrequencies

mode frequency is nearly identical with that of the R_1 mode and there are plenty additional longitudinal and combined modes in the upper frequency range of the plot that are not shown here.

For LP2 the measured PSD is shown in Fig. 6.5b. The unstable T_1 mode is clearly visible. Its frequency is met very well by the numerical analysis. This also applies to the other higher modes where the agreement is even better than for LP1.

Altogether, the frequency distribution is met well for both load points.

6.2 Nozzle Correction

Due to the long cylindrical section of the BKD, combustion is nearly completed when the flow enters the nozzle. Thus, no heat release in the nozzle region has been accounted for in the previous analysis (Sec. 6.1). However, combustion chambers like those of the TCDs are designed more compact, potentially leading to part of the combustion occurring in the convergent nozzle section. In Sec. 4.2.3 an approach has been introduced to account for heat release in the nozzle by modfiying the results of the constant cross-section single flame simulations (cf. Sec. 5.1). In the following, the impact of this procedure on the mean flow and the subsequent acoustic simulation are addressed for TCD2 and TCD3. A more general discussion on the acoustic properties of the TCDs has been given elsewhere [54, 55].

To obtain the necessary data on the reacting flow in the rear section of the nozzle, the length of the single flame domain is extended down to the position of the nozzle throat. The resulting temperature field is shown along with the chamber contour in Fig. 6.6. For both cases, the cold oxidizer core ends upstream of the onset of the convergent nozzle part. However, the sound speed distribution in Fig. 6.7 shows that there is still some, yet weak, reaction in progress in the rear part of the single flame domain. The

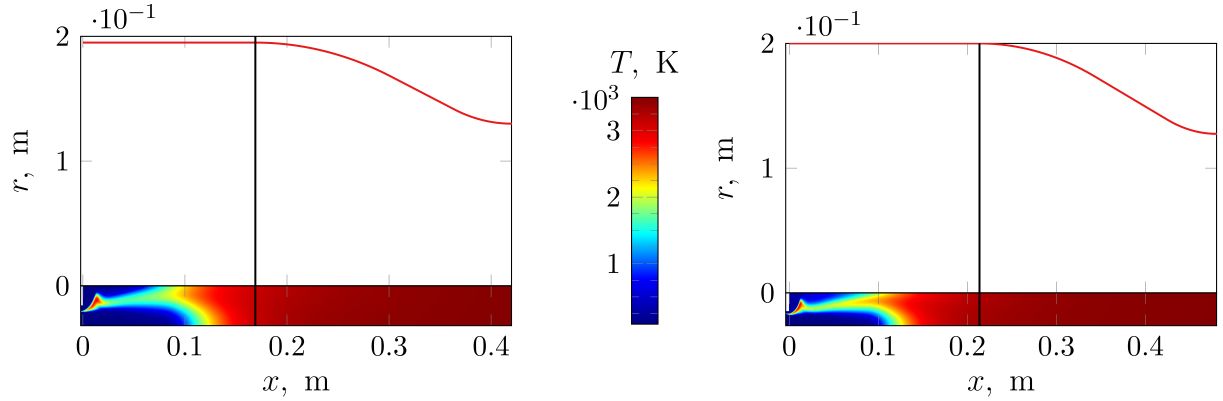

(a) TCD2 **(b)** TCD3

Figure 6.6: Single flame temperature field and chamber contour (single flame field scaled by a factor of 4 in radial dimension)

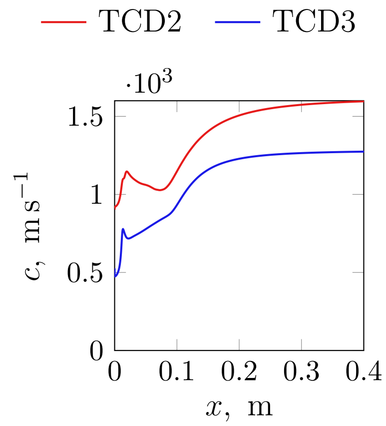

Figure 6.7: Sound speed

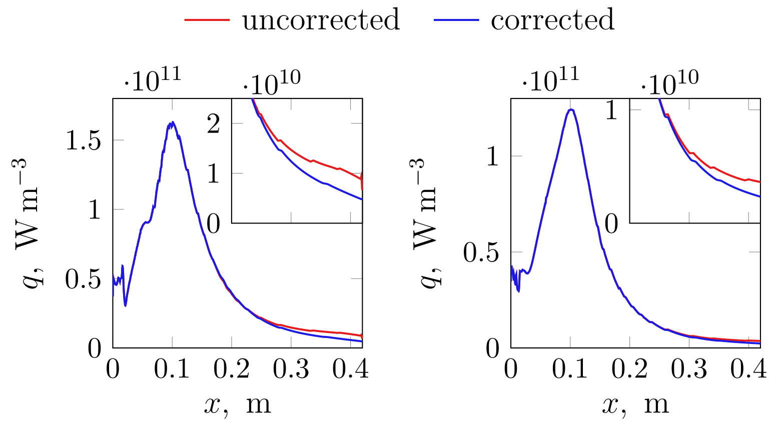

(a) TCD2

(b) TCD3

Figure 6.8: Heat release correction

flow properties required for the evaluation of the one-dimensional nozzle equations 4.26 and 4.28 are obtained at the domain outlet. The corrected and uncorrected heat release is shown in Fig. 6.8. The acceleration of the flow in the nozzle leads to a slight reduction of the volumetric heat release compared to the uncorrected case. However, considering the overall heat release distribution, the deviation is rather insignificant. The reasons is that for both TCDs the nozzle correction takes effect in a region downstream of the main heat release zone, which falls within the cylindrical part of the chamber.

To assess the impact of the nozzle correction on the chamber acoustics, the lowest longitudinal and transverse eigenmodes are calculated. For TCD2 there are two close-by T_1 modes, one ($T_{1,nz}$) in the nozzle section and the classical T_1 that is determined by the region of lower temperature near the faceplate (cf. Fig. 6.9). The complex eigenfrequencies of these modes are shown in Fig. 6.10a. As expected from the mean flow results, the impact of the nozzle correction on the eigenfrequencies is marginal in terms of both oscillation frequency and damping rate. The same applies to TCD3 (Fig. 6.10b).

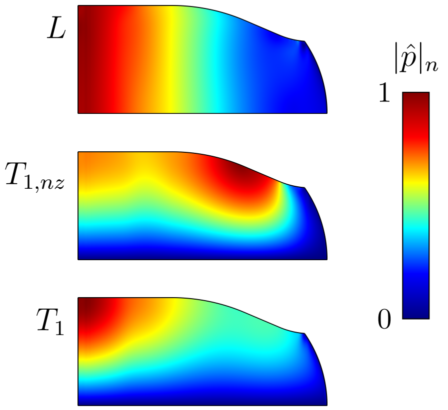

Figure 6.9: TCD2 pressure amplitude distribution

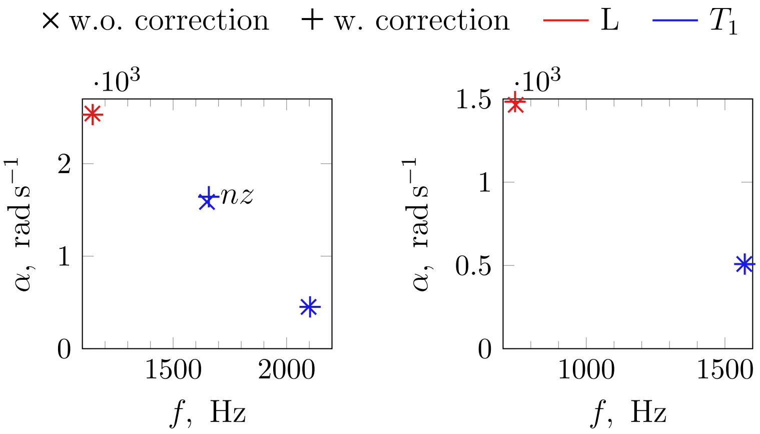

(a) TCD2

(b) TCD3

Figure 6.10: Complex eigenfrequencies

6.3 Effect of Stratification on Acoustics

The mean flow calculation procedures evaluated in Sec. 6.1 are all based on a quasi one-dimensional flow pattern that reproduces certain radially averaged properties from a single flame simulation. The underlying assumption is that the radial and circumferential stratification due to the diffusion flame structures in the chamber do not significantly impact the acoustics. In the present section the validity of this simplification is investigated. In Sec. 4.2.4 a model has been introduced to impose a controlled stratification on the mean flow while retaining identical results in terms of the averaging procedures underlying the quasi one-dimensional approaches (Sec. 4.2.2). This stratification approach is applied now to a combustion chamber whose geometry and axial mean flow profiles (Fig. 6.11) are based on the BKD. The parameters for the axial stratification function Eq. 4.39 are given in Tab. 6.1. The two remaining parameters, stratification amplitude A_ψ and number of flame structures n_{fl} are varied systematically in the following. Due to the design of the stratification functions a maximum amplitude of $A_\psi = 0.4$ is used as otherwise the local temperature minima drop to unreasonably low levels.

The derivation of the heat source (Eq. 4.41, 4.45 and 4.46) of the stratifi-

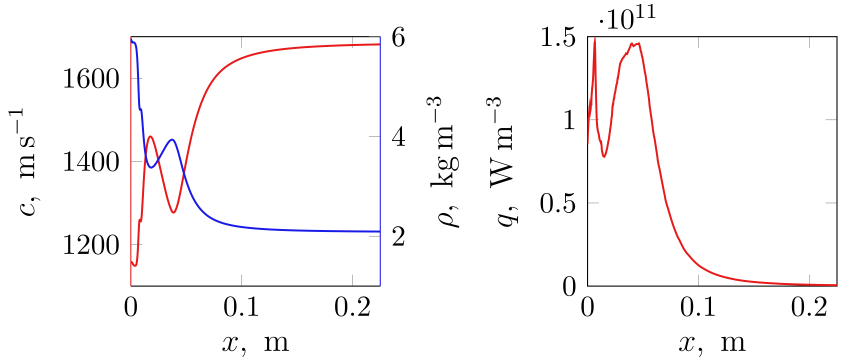

(a) Sound speed and density **(b)** Heat release rate

Figure 6.11: Axial profiles for stratified mean flow

Table 6.1: Parameters in Eq. 4.39 and 4.51

Parameter	Value
l_1	0.015 m
l_2	0.1 m
c_u	5

cation model is based on the assumption of a radially uniform mass flux. To assess the validity of this assumption, the axial distribution of the mass flux standard deviation $\sigma_{\rho u_x}$ normalized by the mean mass flux $\overline{\rho u}_x$ within each chamber cross-section is shown in Fig. 6.12 for $n_{fl} = 3$. The higher the stratification amplitude is the stronger the deviation from a radially uniform flow gets. After the initial deviations in the flame region the standard deviation approaches zero as the flow homogenizes towards the end of the cylindrical section. Thereafter the two-dimensional flow effects associated with the nozzle region set in. However, these are of no concern for the stratification model, which is applied only in the cylindrical chamber section. The maximum relative standard deviation has a value of about 0.1, which is acceptable.

The oscillation frequencies of the studied configuration for a continuous variation of the stratification amplitude are shown in Fig. 6.13a. Despite all shown results having the same averaged (Eq. 4.12) sound speed distribution, the eigenfrequencies change with the number of flames as well as the stratification amplitude. This is explained as follows. The basic interpretation of the chamber acoustics is based on the analytic duct flow solution (cf. Sec. 2.4). However, this solution is only valid for one-dimensional flow. The area weighted averaging of the sound speed has proven to be a rather robust ap-

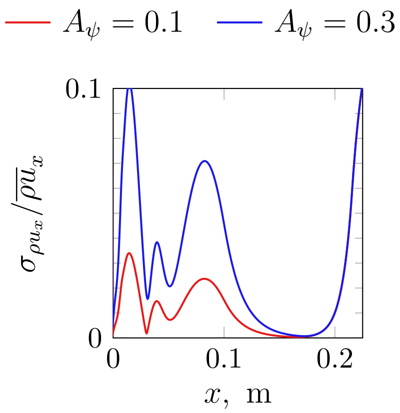

Figure 6.12: Stratified mass flux

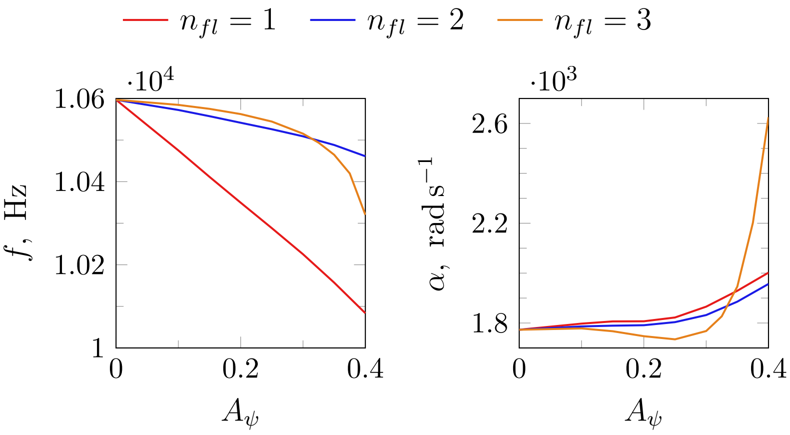

(a) Oscillation frequency

(b) Damping rate

Figure 6.13: Stratified flow complex eigenfrequencies

proximation, providing a good estimation of the actual eigenfrequencies (cf. Sec. 6.1.2 and [12]). However, it is not derived from an explicit description of stratified duct flow acoustics but rather heuristic in nature. Thus the observed deviations in eigenfrequency occur, but they remain smaller than 5 %. For all considered numbers of flame structures the eigenfrequency decreases with increasing stratification. This is in agreement with a previous study [57] with a slightly different stratification approach. The magnitude of the frequency gradient $\partial f/\partial A_\psi$ increases with increasing stratification amplitude, while showing a notable sensitivity to the number of flame structures. As n_{fl} increases, the frequency gradient at $A_\psi = 0$ becomes weaker, whereas its magnitude at high stratification amplitudes increases. A possible explanation for this behavior lies in two different stratification related mechanisms that impact the eigenacoustics. For the case with a single flame structure the flow varies radially at a length scale similar to that of the T_1 mode. So an immediate impact of stratification on the acoustics can be expected. In contrast, with increasing flame numbers the radial dimension of a single flame structure gets smaller (cf. Eq. 4.37) and the single flame becomes more compact compared to the wave length of the T_1 mode. This length scale difference accounts for the initially weaker frequency gradients with respect to the stratification amplitude at lower flame numbers. However, according to Eq. 4.37 the radial sound speed gradient in the flow is proportional to $n_{fl} A_\psi$, i.e. with increasing flame number the radial gradients get stronger. Strong radial gradients notably affect the perturbation solution as shown previously [57]. So, the higher sensitivity of the eigenfrequency to the stratification amplitude around $A_\psi = 0$ for low flame numbers is caused by the similar length scales of radial flow structures and acoustics. With increasing stratification the impact of gradient induced perturbations on the eigensolutions (cf. [57]) becomes stronger and finally exceeds the previous mechanism.

The damping rates for the stratified mean flow are shown in Fig. 6.13b. The curves exhibit a small initial incline of the damping rate with stratification amplitude, followed by a region of lower increase or even decline. At higher stratification amplitudes damping becomes stronger again with the damping rate gradient increasing continuously. With an increasing number of flame structures the initial incline of the damping rate becomes weaker but the damping rate gradient at high stratification amplitudes increases. This behavior is analogous to that of the oscillation frequencies, which has been discussed previously. The increase of damping with stratification deviates from the behavior observed in the previous study [57]. There, $n_{fl} = 2$ flame structures and a stratification amplitude up to $A_\psi = 0.3$ were considered. While the relative absolute change of the damping rate as well as the shape of the curve were comparable to those of the corresponding case in the present study, the previous work showed a decrease of the damping rate with increasing stratification amplitude. This shows that the impact of stratification on the damping rate strongly depends on the specification and setup of the specific case. Unlike the real valued eigenfrequency that primarily depends on the sound speed distribution, the damping rate is additionally linked to other fields like density and temperature. For an unstratified flow $A_\psi = 0$ the dominant damping mechanism is the so-called field damping [12], which is related to axial flow gradients. When radial stratification is increased ($A_\psi > 0$) axial gradients are affected as well. This comes from the axial dependence of the stratification function according to Eq. 4.39, which thus directly influences the field damping. This modification of the damping behavior due to changed axial gradients superimposes with pure radial-gradient related mechanisms like vortex-shedding. From the complex eigenfrequencies only the net-effect on damping is visible. Compared to the unstratified case with only axial gradients, damping increases by up to 50 %. Thus stratification is concluded to potentially exert a tremendous impact on the stability predictions.

6.4 Summary of Findings

The impact of the mean flow modeling on the passive chamber acoustics has been analyzed. The selection of a specific mean flow model (c-s, c-i, c-κ, cf. Sec. 4.2.2) has only a minor influence on the complex eigenfrequency. While the c-s and c-i results are very similar, the c-κ model predicts both lower oscillation frequencies and damping rates. However, the difference is small compared to the impact of the choice of the turbulent Schmidt number in the single flame simulations on the oscillation frequencies. In contrast, the turbulent Schmidt number does not impact the damping rate. If optimized turbulent Schmidt numbers are employed in the single flame simulations, the overall chamber acoustics observed in the experiment are well represented by the computed eigensolutions in terms of oscillation frequencies. The nozzle correction, introduced to account for flow acceleration in the rear part of compact combustion chambers (Sec. 4.2.3), has negligible effect on the complex eigenfrequencies. Radial flow gradients have been found to severely impact the eigensolutions. While the relative change of the oscillation frequency is small in the considered parameter range, the damping rate varies by up to 50 %. The consequences of these findings for the overall stability assessment will be further discussed in Sec. 8.3.

7 Flame Transfer Functions

After the discussion of the mean flow calculation and associated passive chamber acoustics in Chap. 6, the present section covers the dynamic flame response in terms of pressure coupling. It is the second prerequisite for the application of the stability assessment procedure (cf. Fig. 4.1, Chap. 4). The approaches used in the present chapter have been developed in Sec. 4.3. The flame response simulations employ the source terms derived in Sec. 4.3.1.3 and follow the setup described in Sec. 5.1. The necessary excitation frequencies and target pressure amplitude distributions are obtained from the passive acoustic analysis (cf. Sec. 6.1). The present chapter covers pressure coupling alone, which has been identified to govern potential driving of high frequency instabilities in the BKD [12, 42, 43]. Velocity coupling (cf. Sec. 4.3.2.2), which has been studied in the context of the radiation-based single flame validation in Sec. 5.3.3, is not investigated further because this mechanism does not lead to any response at the excitation frequency [3]. The findings of the present chapter are used further during the stability analysis in Chap. 8.

Flame Transfer Functions represent the dynamic flame response in the perturbation simulations (cf. Sec. 4.1). Their calculation consists of two parts.

- First, the dynamic response of a single rocket engine flame located at a pressure antinode to the chamber acoustics is simulated. The chamber acoustics lead to the target pressure fluctuation distribution, from which excitation source terms are calculated. The corresponding procedures from previous works (Sec. 4.3.1.1) as well as a revised approach, (Sec. 4.3.1.3) that is tested in the following, have been introduced previously.
- From the flame response results an FTF is extracted, which is used to

model the heat release fluctuations in Eq. 2.36.

The above steps are addressed sequentially for the BKD in Sec. 7.1 and Sec. 7.2, respectively. For the sake of comparability between compressible and incompressible results, the injector is not fully resolved in the corresponding simulations (cf. Sec. 5.1.4). The findings of the present chapter are summarized in Sec. 7.3.

7.1 Flame Response

The calculation of the FTF is based on the one-dimensional heat release fluctuations. These fluctuations are represented by their complex amplitude distribution along the single flame domain, obtained from an excitation simulation (cf. Sec. 4.3.1). In the present section, flame response results for the BKD are studied to provide a basis for the discussion of the FTF extraction procedure in Sec. 7.2. By comparing results from the revised, incompressible approach (Sec. 4.3.1.3) with compressible simulations, the impact of the longitudinal acoustics on the flame is evaluated. To avoid additional influences of the injector dynamics in the compressible cases, the injector is not resolved. The following discussion covers the results for LP1. The findings for LP2 are similar and shortly addressed at the end of the present section.

The heat release fluctuations are extracted from the flamelet based flow solution as described in Sec. 5.1.3. Since this procedure relies on gradient calculations and thus is prone to oscillations, spatial filtering is applied. The amplitude distributions of pressure and heat release are obtained by fitting a complex exponential (Eq. 4.2) to the phase averaged results with Ω set to the excitation frequency. Based on the passive acoustic calculations (cf. Chap. 6) LP1 is excited at a frequency of $f = 10.6\,\mathrm{kHz}$ with the excitation amplitude distribution shown in Fig. 7.1.

The complex heat release amplitude distributions of LP1 are shown for the compressible and incompressible case in Fig. 7.2. The axial distribution of

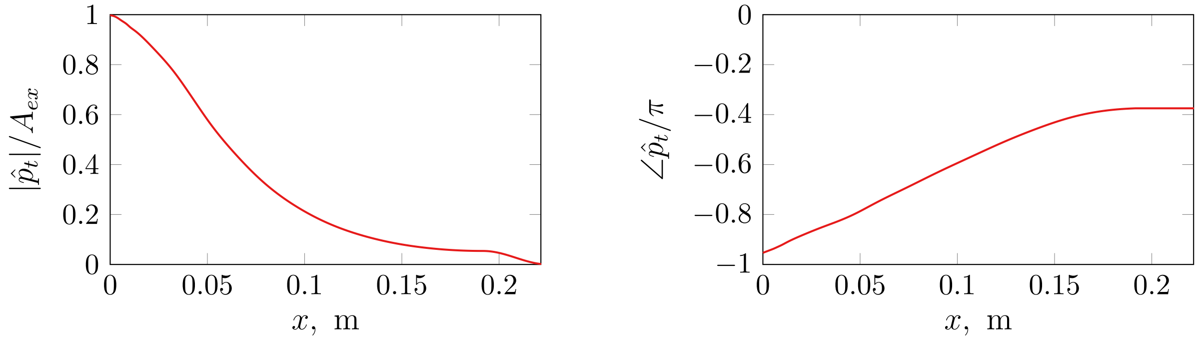

(a) Amplitude **(b)** Phase

Figure 7.1: Excitation pressure profile for BKD LP1

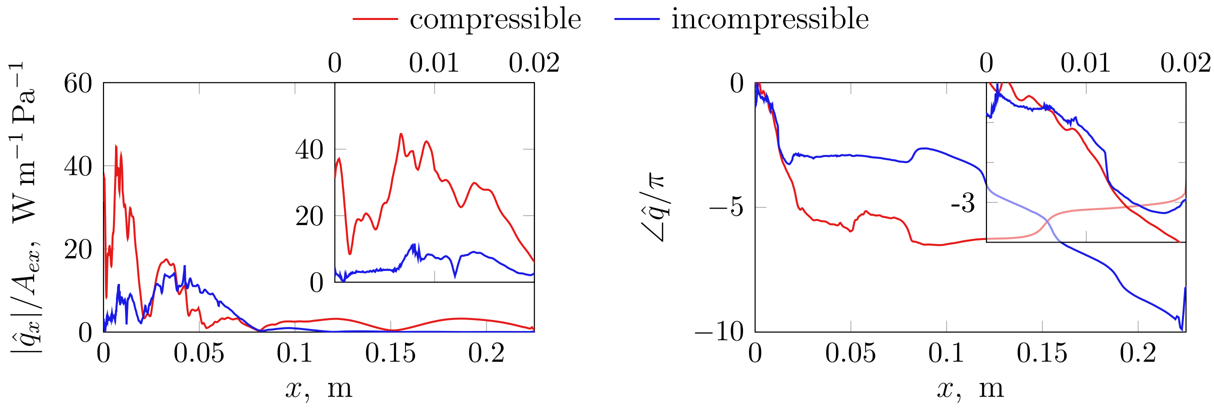

(a) Amplitude **(b)** Phase

Figure 7.2: Heat release amplitude distribution for BKD LP1

the heat release fluctuations is governed by two peaks. The first one belongs to a region ranging from the faceplate to $x \approx 0.02\,\mathrm{m}$, irrespective of the compressibility approach. The magnitude of the heat release amplitudes is considerably larger for the compressible than for the incompressible case. In the incompressible case a local minimum with a close to zero heat release amplitude occurs at $x \approx 0.012\,\mathrm{m}$ that is associated with a phase jump of $\Delta\angle\hat{q} \approx -\pi$. Aside from that, the phase is roughly continuously decreasing along the region of the first amplitude peak, covering a range of $\Delta\angle\hat{q} \approx 3\pi$. The second dominant peak stretches to $x \approx 0.08\,\mathrm{m}$. Its magnitude is about equal for both compressibility approaches. However, in the region between

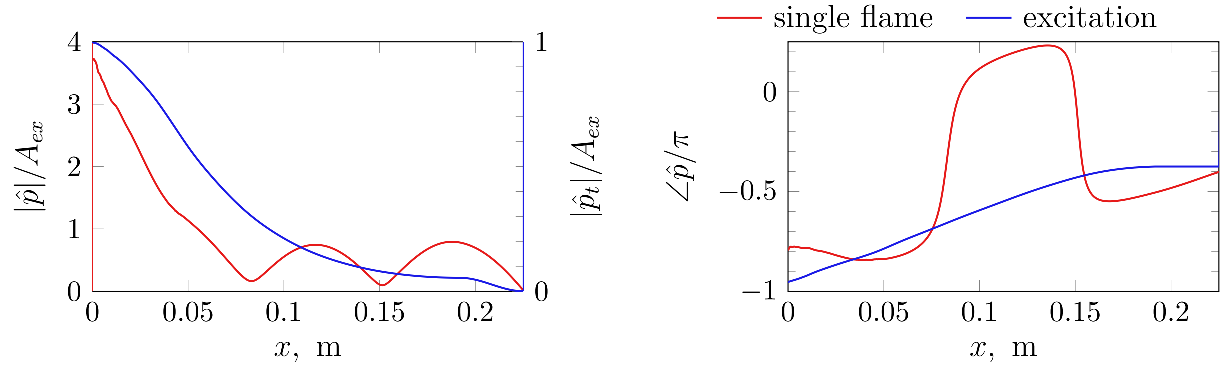

(a) Amplitude **(b)** Phase

Figure 7.3: Compressible pressure amplitude distribution for BKD LP1

$x \approx 0.045\,\mathrm{m}$ and $x \approx 0.07\,\mathrm{m}$ the compressible case shows a significant drop in the heat release amplitudes. In the downstream part of the chamber ($x > 0.07\,\mathrm{m}$), the compressible results possess two additional heat release peaks, whereas the incompressible heat release fluctuations are nearly zero.

To explain the occurrence of the two additional peaks in the downstream region of the chamber in the compressible case as well as the local drop of heat release amplitudes in the second main peak, the pressure amplitude distribution obtained from the single flame simulation is evaluated. As discussed in Sec. 4.3.1.2, this distribution in general does not match the target or excitation pressure distribution, which is obtained from the chamber's acoustic analysis and used to evaluate the source terms (cf. Tab. 4.4 and Sec. 4.3.1.1). Both distributions are shown for the compressible LP1 results in Fig. 7.3. The mismatch of both curves can be ascribed to longitudinal acoustics of the single flame domain, which is confirmed by the absolute amplitude values in Fig. 7.3a. The shape of the initial decline of the pressure amplitudes is reasonably met, even though the rate of decrease in the simulation results is higher than that of the excitation profile. The most significant difference, however, is the presence of pressure amplitude peaks in the downstream part of the chamber in the simulation. In contrast the excitation pressure shows a continuous decline of amplitudes in axial direction. The shape of the additional peaks clearly indicates the presence of a standing longitudinal wave. The constant-pressure outlet (cf. Sec. 5.1.5) imposes a node at the domain end. The wave length associated to the structures in the rear chamber region is $\lambda \approx 0.14 \ldots 0.15\,\mathrm{m}$ which agrees well with the wave length of $\lambda = 0.14\,\mathrm{m}$ that is obtained for a sound speed of $c = 1500\,\mathrm{m\,s^{-1}}$ at the excitation frequency. The phase jump of $\Delta\angle\hat{p} \approx -\pi$ between both amplitude peaks supports the conclusion that the pressure fluctuations in the downstream chamber part are of longitudinal nature. The longitudinal oscillations stretch into the high amplitude region close to the faceplate and impact the amplitude profile and phase (Fig. 7.3b) from $x \approx 0.05\,\mathrm{m}$ onward. Further upstream, the excitation mass flow dominates the domain acoustics. In conclusion, the additional heat release fluctuation peaks downstream in the chamber as well as the small drop at $x \approx 0.05\,\mathrm{m}$, which occur in the compressible simulation, can be attributed to longitudinal eigenacoustics.

Comparing the pressure phase distributions obtained in the single flame simulations to those of the target pressure fluctuations (Fig. 7.3b) shows that the trend observed in the simulation opposes the excitation profile in the first quarter of the chamber: While the phase of the calculated pressure fluctuations stagnates or even decreases in axial direction, the excitation profile's phase increases. Further downstream, the longitudinal domain acoustics cause a notable difference between the target and the obtained pressure phase distribution.

The pressure amplitude distributions for the incompressible case are shown in Fig. 7.4. After a short plateau close to the faceplate, the amplitudes decline nearly linearly down to zero at the constant pressure outlet. The phase is nearly constant along the whole domain. A comparison to the excitation profile is not appropriate as the mechanisms leading to pressure fluctuations differ significantly (cf. Sec. 4.3.1.3.2). However, the impact of the density modulation can be evaluated. A comparison to the case without density correction shows that the amplitudes are reduced by a factor of about two. This indicates that the incompressible flow dynamics are indeed partly suppressed by this approach. However, there are still significant pressure fluctuations remaining. These can be ascribed to the higher complexity of the single flame compared to the model flow used for the derivation of the

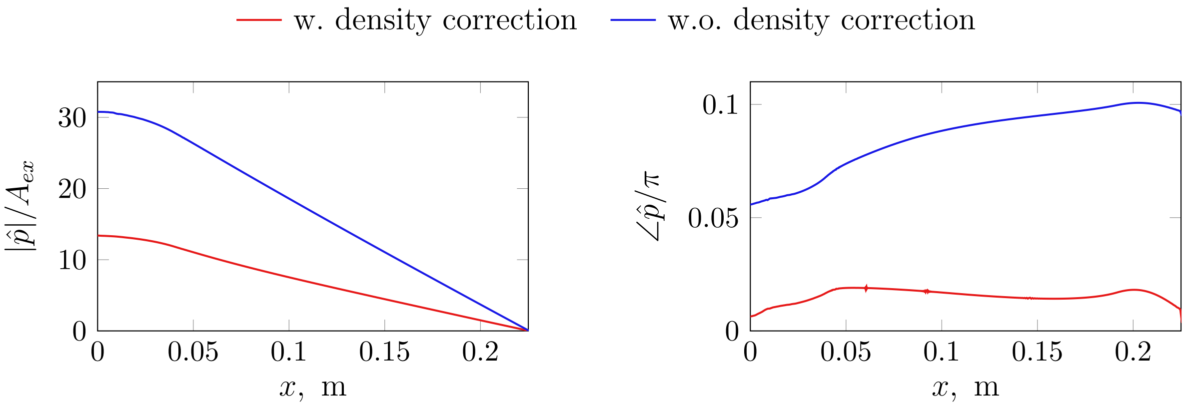

(a) Amplitude **(b)** Phase

Figure 7.4: Pressure amplitude from incompressible excitation simulation of BKD LP1

density correction in Sec. 4.3.1.3.2, which is based on the isentropic change of the local density in a uniform mean flow. However, the actual flow in the single flame domain is stratified and the source terms do not only add to and subtract mass from the domain but the local mixture ratio is changed as well, leading to combustion related density changes. These processes cannot be accounted for in a general way as they highly depend on the detailed flow solution. As the actual pressure value has only a weak impact on the heat release rate (cf. Sec. 4.3.1.2), the presence of the pressure fluctuations themselves does not pose a problem for the incompressible approach. At most, the flow processes leading to the fluctuations potentially affect the solution. A comparison of the compressible and incompressible results allows for some implications regarding the validity of the compressible case. For a discussion of the validation possibilities for the flame response calculations see Chap. 9. The first heat release peak (Fig. 7.2) is about four times stronger for the compressible than for the incompressible simulation, which corresponds to the compressible pressure amplitude at the faceplate, exceeding the target pressure amplitude by a factor of four (Fig. 7.3a). This indicates that the incompressible simulation captures the impact of the pressure fluctuations on the flow correctly.

The previous discussion bases on results obtained at a single excitation pres-

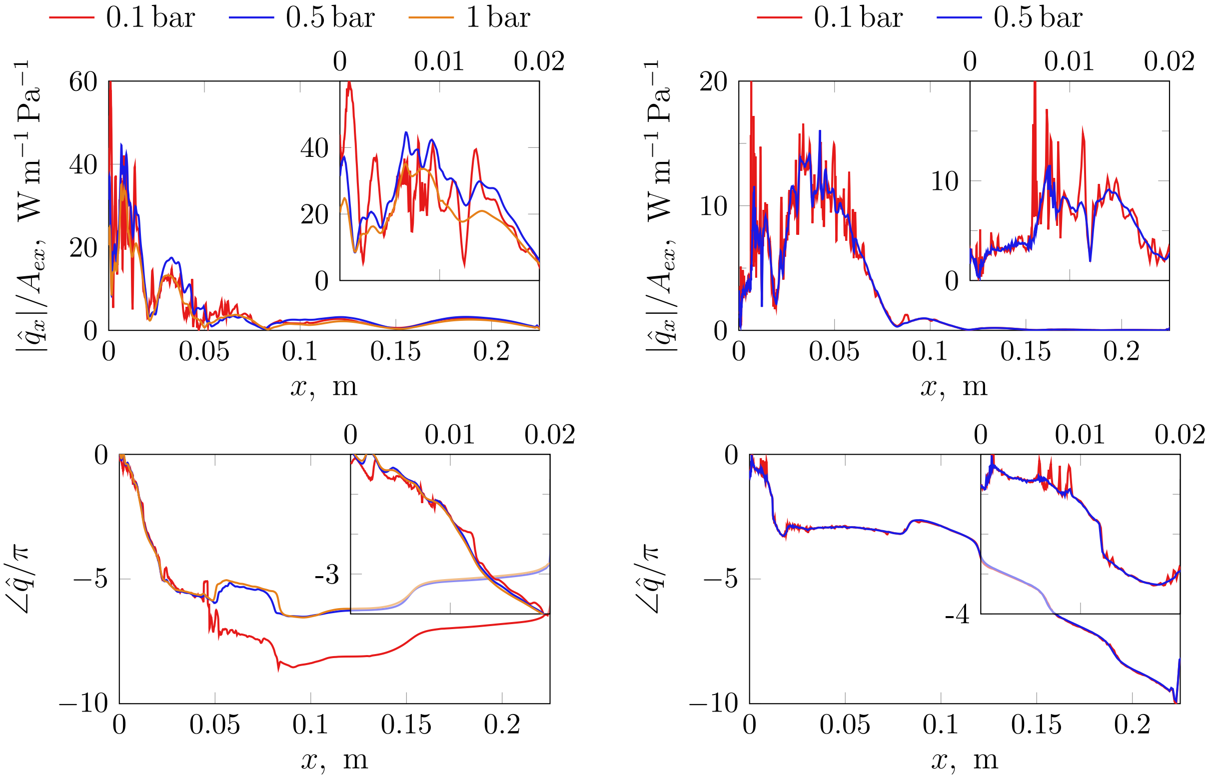

(a) Compressible (b) Incompressible

Figure 7.5: Impact of the excitation amplitude on the flame response of BKD LP1; amplitude (top) and phase (bottom)

sure amplitude. To verify the linearity of the calculated flame response, simulations at amplitudes ranging from 0.1 bar to 1 bar have been conducted. The corresponding heat release amplitude distributions are shown in Fig. 7.5, normalized by the excitation pressure at the face plate. The normalization allows to assess the linearity of the calculated flame response as for perfectly linear behavior the curves match. This is accomplished to a satisfactory degree. A notable impact of the excitation strength on the noise arising from the heat release rate extraction procedure (cf. Sec. 5.1.3) is observed: Higher excitation amplitudes lead to a smoother axial distribution. This indicates that noise from the gradient evaluation in Eq. 5.2a increases less with increasing excitation amplitude than the heat release fluctuations.

At higher excitation amplitudes the heat release fluctuations change more fundamentally. For the compressible case, this can be clearly seen for the

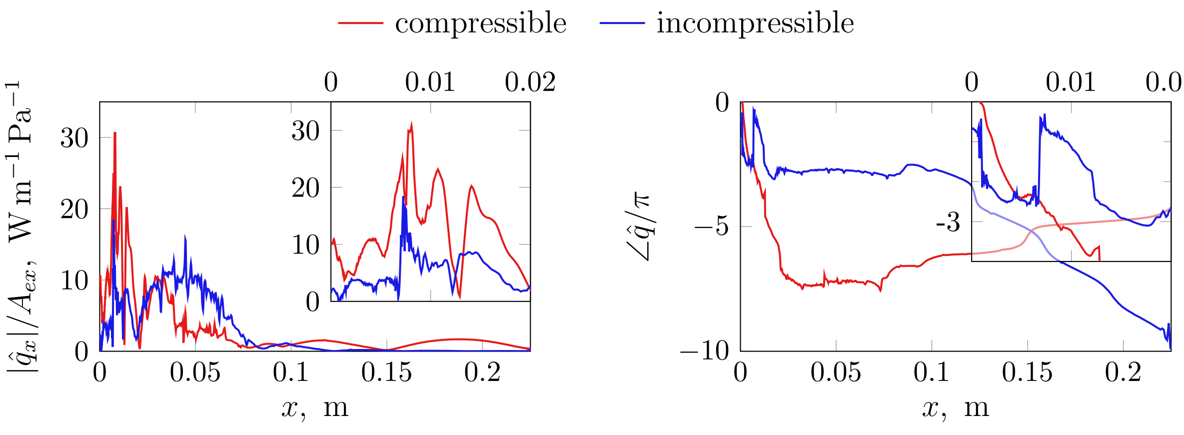

(a) Amplitude **(b)** Phase

Figure 7.6: Normalized heat release amplitude distributions for BKD LP2

first peak (Fig. 7.5a). While the normalized amplitude level is constant for an increase of the excitation amplitude from 0.1 bar to 0.5 bar, it decreases at an excitation amplitude of 1 bar, indicating non-linear saturation. The calculated pressure amplitudes saturate as well, showing an analogous decrease in magnitude.

For LP2 similar tendencies are observed as for LP1, although the overall level of heat release fluctuations is lower. The associated amplitudes are shown in Fig. 7.6, the pressure in Fig. 7.7. For the compressible simulations of LP2 the SRK EOS is used in contrast to the Z_{ref} model for LP1 (cf. Sec. 5.1.2, Tab. 5.1). So the compressibility model has no qualitative impact on the previously discussed behavior.

7.2 FTF Modeling

In the perturbation simulations the impact of the flame feedback on the acoustic stability is represented by the heat release fluctuation term on the RHS of Eq. 2.36. For the evaluation of this term, an FTF is required as described by Eq. 4.52 for the pressure response. In the present section, two approaches to model this FTF based on the flame response calculations

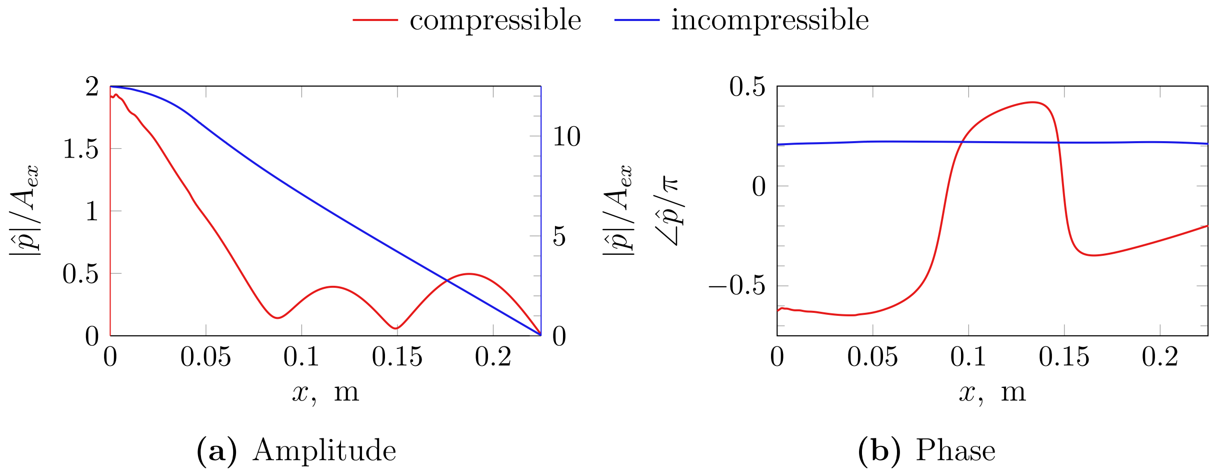

(a) Amplitude **(b)** Phase

Figure 7.7: Normalized pressure amplitude distributions for BKD LP2

(Sec. 7.1) are discussed:

- The zonal integration model of Zahn [68] has been used in previous BKD stability analyses [12, 13]. It proposes a simple relation between heat release and pressure fluctuations, which is extracted from the calculated flame response, aiming at a compensation for the impact of undesired flow dynamics on the simulation results.
- The modeling of the flame response based on the spatial distribution of the heat release fluctuations, which becomes viable as the incompressible single flame simulations aim for the calculation of the flame's response to the excitation pressure fluctuations while avoiding interference from the simulation domain's eigenacoustics.

Modeling, advantages and disadvantages of the two approaches are addressed in the following sections 7.2.1 and 7.2.2, respectively. The FTF models are applied during the stability analysis in Chap. 8.

7.2.1 Zonal Integration

The zonal integration model relates the integral heat release in individual flame segments to the pressure fluctuations at reference locations, one per segment. In the following, the general form of the model is introduced and its advantages and drawbacks are discussed (Sec. 7.2.1.1). Thereafter, the selection of the reference pressure variable is addressed (Sec. 7.2.1.2), before the specification of the model parameters for the BKD (Sec. 7.2.1.3).

7.2.1.1 Model Description

For the zonal integration FTF model the flame is axially divided into n segments, with segment i covering the space Δx_i. Within each segment, the heat release fluctuations are integrated and normalized by the respective mean heat release. By relating these normalized heat release fluctuations to the normalized pressure oscillations, the FTF is calculated as

$$\hat{FTF}_{p,i} = \underbrace{\frac{\int_{\Delta x_i} \hat{q} A dx}{\int_{\Delta x_i} \bar{q} A dx}}_{\dot{q}_{\Delta x,rel,i}} \frac{\bar{p}_{ref}}{\hat{p}_{ref,i}} \quad . \tag{7.1}$$

The reference pressure fluctuations $\hat{p}_{ref,i}$ are the pressure fluctuations that the flame responds to, evaluated at the reference location of segment i. The evaluation of the reference pressure fluctuations is discussed below. The mean reference pressure $\bar{p}_{ref}$ is used to make the FTF dimensionless. Its selection is rather arbitrary, as it is compensated for during the redimensionalization of the heat release fluctuations in Eq. 4.52. A common choice is the nominal chamber pressure (cf. Tab. 3.2). In the following, the term reference pressure is used to refer to the reference pressure fluctuations rather than the mean reference pressure.

The main advantages of the zonal integration model are:

- Due to the usage of multiple zones the model might partly compensate for the impact of the domain's eigenacoustics on the flame response. As a spatially resolved relation between heat release and pressure fluctuations is extracted from the flame response, the FTF is basically able to model the flame feedback for a pressure amplitude distribution that differs from the one of the excited single flame simulation. However, for this compensation to work, the governing mechanisms coupling the heat release to the pressure fluctuations must not be changed by the domain's eigenacoustics, which cannot be assumed in general (cf. Sec. 4.3.1.2).

- If the zone boundaries are determined ahead of the simulation, the amount of data that needs to be stored is reduced.
- For the flamelet combustion modeling the noise resulting from the heat release rate calculation based on the enthalpy of formation (cf. Sec. 5.1.3) is reduced due to the spatial integration.

However, in terms of modeling accuracy there are several drawbacks:

- The model is based on a rather simple relation between heat release and pressure fluctuations. First of all, there is no possibility to distinguish between the contributions to the heat release fluctuations that arise from longitudinal and transverse acoustics, respectively. This simplicity limits the approach's ability to adapt the flame response to certain pressure amplitude distributions.
- The piecewise integral treatment of the flame response reduces the spatial resolution of the heat release fluctuations in the perturbation simulations. The resolution cannot arbitrarily be increased by using more segments as with an increasing number of segments the dependence of the local heat release fluctuations on the upstream perturbations is not captured. For high segment numbers Eq. 7.1 describes a direct coupling between the local heat release and pressure fluctuations, which does not represent the actual flame response mechanisms (cf. Sec. 4.3.1.2).
- A detailed, case-specific analysis of the mechanisms governing the flame response is required in order to adequately select the segments' boundaries and the reference pressure locations.

7.2.1.2 Reference Pressure Fluctuations

The reference pressure fluctuations $\hat{p}_{ref,i}$ (cf. Eq. 7.1) couple the heat release fluctuations obtained from the flame response calculations to the pressure oscillations in the perturbation simulations. Besides the specification of the respective segments' reference locations, which are addressed in Sec. 7.2.1.3 for the BKD, there is a second aspect to be considered in the case of compressible simulations: As discussed in Sec. 7.1 there are two different pressure fluctuation distributions, the target pressure fluctuations used for the calculation of the source terms and the ones actually obtained as solution of the excited single flame simulation. The choice of the amplitude distribution that the reference pressure fluctuations are evaluated from can have tremendous consequences for the stability analysis, which will be addressed in Sec. 8.1. In the following, a general discussion of the reference pressure selection is given.

The pressure fluctuations obtained from the single flame simulation have been used as reference variables in previous studies [12, 13]. The usage of these fluctuations is necessary if the flame response's distortion by the simulation domain's eigenacoustics shall be compensated for. However, the potential of such a correction is limited as a superposition of heat release fluctuations from transverse and longitudinal acoustics is related to a superposition of transverse and longitudinal pressure fluctuations, i.e. the different mechanisms contributing to the flame response cannot be separated.

A major drawback of using the single flame pressure fluctuations as reference for the FTF caclulation results from the different level of detail in the perturbation and the flame response simulations. Dynamic flame radiation images measured at the BKD [6] showed longitudinal structures arising from the L_2 mode of the LOX-post and propagating into the chamber [6]. If a single flame simulation captures this phenomenon, it impacts the calculated pressure amplitudes. However, in the perturbation simulations for the chamber's stability predictions (cf. Sec. 4.1) the detailed injection geometry is not included and the impact of injector-related longitudinal structures on the pressure fluctuations is not accounted for. In this case the pressure fluctuations obtained from single flame simulations are not suitable to couple the associated heat release fluctuations to the pressure fluctuations in the perturbation simulations.

Taking the target pressure amplitudes used for the source term calculations as reference for the FTF calculation ensures consistency between the FTF and the perturbation simulation. However, this choice does not allow to potentially correct the flame response for distortions resulting from the single flame simulation concept. Thus, it requires that the excited single flame simulations adequately represent the flame's response to the target pressure fluctuations, without significant distortions.

In summary, the target pressure fluctuations are the preferable variable to describe pressure coupling, due to its consistency with the perturbation simulations. The only reason for considering the pressure fluctuations from the single flame simulations as reference variable is the attempt to compensate for the impact of simulation domain's eigenacoustics on the flame response calculations.

7.2.1.3 Parameter Specifications for the BKD

The application of the zonal model (Eq. 7.1) in the BKD stability analysis (Sec. 8.1) requires the specification of segment numbers, boundaries and reference pressure locations. In the present work, these parameters are selected based on the findings of Zahn [68], which has been employed for the FTF modeling in previous BKD Studies [12, 13].

Based on a study of the spatial distribution of the heat release fluctuations in a single flame simulation using Dynamic Mode Decomposition, Zahn [68] split the flame into two regions: The near-field ranges from the faceplate up to the boundary coordinate $x_{bd} = 0.015\,\mathrm{m}$[1] and the far-field covers the downstream part of the flame. In previous studies [12, 13] the middle of the near field has been selected as location for the reference pressure fluctua-

---

[1] Schulze [12] reported a boundary value of $x_{bd} = 0.013\,\mathrm{m}$. However, the center point was still given as $0.5x_{bd} = 0.0075\,\mathrm{m}$ and his calculations also suggest that the original boundary coordinate given by Zahn [68] has been used.

tions. In the far field, the fluctuations of turbulent kinetic energy has been proposed as coupling mechanism [68] since the reaction rate of the combustion model used in the simulations is governed by this variable. Thus, the location of the maximum turbulent kinetic energy fluctuations has been selected as the far field reference location [12, 13].

In the present work, the zone boundary is set to $x_{bd} = 0.02\,\mathrm{m}$, corresponding to the boundary between the two heat release fluctuation peaks of the flame response (cf. Fig. 7.2, Sec. 7.1). The reference pressure location of the near field is adapted accordingly to $x_{bd}/2$.

7.2.2 Spatially Resolved Heat Release Fluctuations

The zonal integration model (Sec. 7.2.1) provides an FTF that decribes the generalized spatial relation between the heat release and the reference pressure fluctuations. This spatial descripton is obtained at the cost of a rather low axial resolution of the flame feedback. However, previous works [12] showed that including flame feedback in the perturbation simulations only has a weak effect on the calculated mode shape. As the occurrence of acoustic modes is avoided in the incompressible single flame simulations, there is no need to correct the flame response for this kind of disturbance either. So for the incompressible case the spatial distribution of the heat release amplitudes is directly used to represent the flame response in the perturbation simulations. This approach implies that the incompressible flow dynamics that remain despite the density correction (cf. Sec. 7.1) do not significantly impact the flame response results, an assumption, which currently cannot be validated definitely due to the lack of detailed reference data. The FTF takes the form

$$F\hat{T}F = \frac{\hat{q}}{\hat{p}_{ref}} \frac{\bar{p}_{ref}}{\bar{q}_{ref}} = \frac{\hat{q}_x}{\hat{p}_{ref}} \frac{\bar{p}_{ref}}{\bar{q}_{x,ref}} \quad . \tag{7.2}$$

The reference mean pressure $\bar{p}_{ref}$ and the reference mean heat release $\bar{q}_{ref}$ are used for the normalization of the heat release and need to be compensated for when evaluating the heat release fluctuations according to Eq. 4.52. They may be chosen arbitrarily.

Since the pressure fluctuations obtained in the incompressible single flame simulations do not result from the propagation of acoustic waves at sound speed, they are not comparable to those of the perturbation simulations. Thus, the only reasonable choice for the evaluation of the reference pressure fluctuation in Eq. 7.2 is the target pressure amplitude distribution. Since the impact of the flame feedback on the mode shapes calculated in the acoustic simulations is small, the selection of the location for the reference pressure fluctuations becomes arbitrary, as long as the associated pressure amplitude is non-zero.

7.3 Summary of Findings

The flame response of the BKD has been evaluated based on the procedure introduced in Sec. 4.3.1. A comparison between results from compressible and incompressible simulation has been conducted to assess the role of the domain's eigendynamics in the flame response calculations. The compressible pressure fluctuations showed clear longitudinal acoustic structures in the downstream part of the chamber that also affect the high amplitude region close to the faceplate. These structures are successfully avoided by using an incompressible flow model. For this type of simulation the proposed density modulation (Sec. 4.3.1.3.2) considerably reduced the incompressible flow dynamics resulting from the application of the source terms. However, due to the complex nature of the reacting flow, notable pressure fluctuations were remaining. A comparison of the amplitude ratio obtained in compressible and incompressible simulations indicated that the incompressible approach adequately reproduces the flame response associated with the target pressure fluctuations. However, as there are no sufficiently detailed flame response data available, a final conclusion regarding the prediction quality of the incompressible approach cannot be drawn. The aspect of further validation possibilities is addressed in Chap. 9.

Two options to model FTFs based on flame response calculations have been discussed. The zonal integration approach offers some, though severely limited, capabilities to compensate for disturbances in the flame response calculations. Its drawbacks concern the spatial flame response resolution and the necessity to use the single flame pressure simulations for the aforementioned correction approach to work. Indeed, the usage of the target pressure fluctuations is clearly preferable for coupling the heat release to the pressure fluctuations via an FTF but requires the flame response results to represent the impact of the target pressure fluctuations on the flame without significant deviations. For such flame response data, the axial distribution of the heat release fluctuations can be directly used in the stability analysis, without creating a generalized spatial FTF model. When possible, this approach is to be preferred as it offers a detailed spatial distribution of the flame response and does not rely on an a-posteriori correction of the flame response calculations. The impact of the different FTF modeling approaches on the stability predictions is studied in Sec. 8.1.

8 Stability Analysis

To obtain the stability predictions, perturbation simulations are conducted that include the flame feedback, combining the mean flow discussed in Sec. 6.1 with the flame response modeling from Chap. 7. The impact that these two components and the associated modeling choices have on the stability prediction is discussed in the present chapter. First, the effect of the FTF-model on the complex eigenfrequencies is addressed (Sec. 8.1), followed by a discussion of the role of the mean flow modeling (Sec. 8.2). The findings are summarized in Sec. 8.3.

8.1 Role of the FTF Model

The flame transfer function represents the flame dynamics in the perturbation analysis (cf. Sec. 4.3.1). In Chap. 7 different approaches to obtain the flame response based on single flame simulations as well as to model the FTF based on this flame response have been discussed. In the present section the impact of different FTF modeling approaches on the stability predictions is studied. An overview of the used FTFs is given in Tab. 8.1. The FTF based on the heat release fluctuation distributions from incompressible single flame simulations as well as the target pressure distribution ($\hat{q}$-t-inc.) is the preferred concept (cf. Sec. 7.3). To assess the effect that the domain eigenacoustics in the single flame simulations have on the stability prediction, the $\hat{q}$-t-cmp. approach is included in the anlaysis, which differs from the $\hat{q}$-t-inc. model only in terms of compressibility modeling in the flame response calculation. When it comes to the zonal model, the z-sf-cmp. approach, which has been used in previous works, is the equivalent to the $\hat{q}$-t-inc. approach as it includes a correction for the single flame domain eigenacoustics. Again, the impact of this correction on the stability predic-

Table 8.1: Flame response modeling for the stability analysis

ID	Single Flame Simulation	FTF Model	Reference Pressure
$\hat{q}$-t-inc.	$\hat{q}$-distribution	target	incompressible
$\hat{q}$-t-cmp.			compressible
z-t-cmp.	zonal	target	compressible
z-sf-cmp.		single flame	compressible

tion can be assessed, by studying the results obtained with the z-t-cmp. approach, which is based on the target pressure fluctuation.

The results in the present section have been obtained with the *c*-*s* mean flow model (cf. Sec. 4.2.2 and 6.1). The impact of the mean flow calculation approach on the prediction is analyzed in Sec. 8.2.

The complex eigenfrequencies of the T_1 mode obtained with the different FTF models from Tab. 8.1 are shown in Fig. 8.1 along with the results from the passive acoustic analysis (cf. Sec. 6.1). First, the $\hat{q}$-t-inc. approach is considered, which relates the spatial distribution of the heat release amplitudes to the target pressure fluctuations. Compared to the case without flame feedback, the oscillation frequencies are shifted to lower values when including the FTF in the simulation. However, the changes of oscillation frequencies are minor compared to the incompressible FTFs' impact on the damping rates, which results in the prediction of severe linear instabilities for both LPs. To assess the impact of the longitudinal domain acoustics of the flame response calculations on the stability prediction, results obtained with the compressible $\hat{q}$-t-cmp. FTF modeling approach are considered. Again, the calculated oscillation frequencies become lower for both LPs, but the decrease is stronger than for the $\hat{q}$-t-inc. approach. The impact on the damping rates, however, is opposed to the one observed for the compressible flame response, with the $\hat{q}$-t-cmp. results showing even a slight stabilization of the acoustics. So apparently the outcome of the stability prediction is governed by the choice of the flame response calculations' compressibility model rather than the load point. While the change of damping rates observed with the compressible approach is considerably lower than that of the incompressible one, this does not apply to the mag-

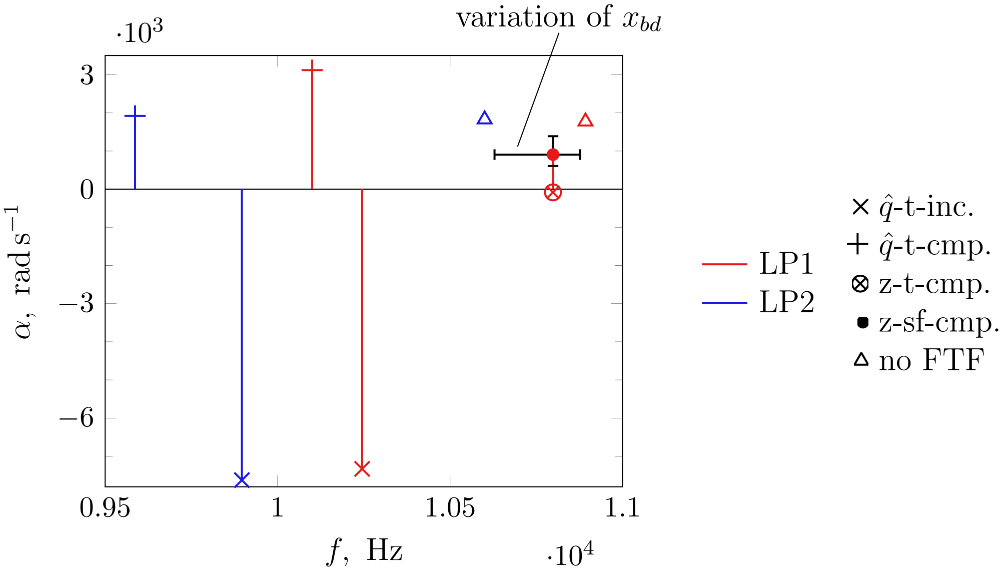

Figure 8.1: BKD stability predictions for FTFs based on the target pressure distribution

nitude of the respective heat release fluctuations (cf. Sec. 7.1, Fig. 7.2). Since for LP1 the maximum heat release amplitudes are about four times higher for the compressible than the incompressible simulations (cf. Fig. 7.2), it can be concluded that the different strengths of the FTFs' effects on the stability predictions are caused by the phase distributions of the heat release fluctuations, which is plausible according to the Rayleigh criterion (Eq. 1.1).

Besides the calculations using the spatial heat release amplitude distributions for flame response modeling, stability calculations with FTFs based on the zonal approach (z-t-cmp., z-sf-cmp.) have been performed for LP1. The zonal pendant to the $\hat{q}$-t-inc. model is the z-sf-cmp. approach, as it includes a correction for the side-effects of a compressibile flame response calculation. Like with the $\hat{q}$-t-inc. approach, both oscillation frequency and damping rate are reduced, even though the frequency shift as well as the destabilization are considerably weaker for the zonal model. The compressibility correction is removed from the zonal model by using the z-t-cmp. approach. For this FTF, the calculated oscillation frequency is nearly identical to the one obtained with compressibility correction. However, the damping rate is significantly reduced, resulting in the prediction of slightly unstable behavior. This is in agreement with the results of a previous study that found the stability prediction to depend on the selected reference pressure variable [55]. Compared to the results obtained with the approaches based on the spatial heat release amplitude distributions ($\hat{q}$-t-inc., $\hat{q}$-t-cmp.) the impact of the compressibility correction on the stability prediction is different. While for the heat release amplitudes using the incompressible flame response results leads to a considerable reduction of the damping rate, the opposite holds for the zonal approaches. So it can be concluded, that both models that correct the FTF for the single flame domain's eigenacoustics have a destabilizing effect on the calculated acoustics. However, the impacts of the different approaches to account for the effect of the single flame domain's eigenacoustics on the flame response are contrary to each other.

Finally, the sensitivity of the results obtained with the zonal model to the selection of the boundary is addressed. For a variation between $0\,\mathrm{mm} \leq x_{bd} \leq 50\,\mathrm{mm}$ the range of oscillation frequencies and damping rates is shown in Fig. 8.1. The oscillation frequency is found to vary rather moderately by about 300 Hz, whereas the damping rate covers a range of about 80 % of its mid-range value. Nevertheless, the previous findings from the present section still hold.

8.2 Role of the Mean Flow Model

Different approaches to calculate the mean flow that are consistent with the Euler Equations and at the same time reproduce certain axial profiles extracted from single flame simulations have been developed in Sec. 4.2.2 and evaluated in Sec. 6.1. Three different mean flow variants have been introduced (cf. Tab. 4.2), which are based on the axial distributions of sound speed and isentropic compressibility (c-s), sound speed and field impedance (c-i) or sound speed and isentropic coefficient (c-κ), respectively. In the following, the impact of the mean flow model selection on the stability predictions is studied. To model the flame response, the spatial distribution of the heat release fluctuations is coupled to the acoustic pressure via the target pressure fluctuation ($\hat{p}$-t-inc. and $\hat{p}$-t-cmp., cf. Tab. 8.1). As found in Sec. 8.1, these approaches exhibit a stronger impact on the stability predictions than the zonal model and thus is expected to show the role of the mean flow model more clearly than the other ones.

The mean flow solutions obtained with the different calculation procedures and the associated passive chamber acoustics have been evaluated in Sec. 6.1. It has been found that the c-s and c-i approaches provide quite similar results. The main difference compared to the c-κ approach is the isentropic coefficient (cf. Fig. 6.1c). While the impact this difference has on the damping rate is low in the case without flame response, the same is not expected for active flames with feedback. As can be seen from Eq. 2.36 the isentropic coefficient affects the coupling between heat release and pressure fluctuations:

$$i\omega\hat{p} + ... = (\kappa - 1)\,\hat{q} \quad . \tag{8.1}$$

As κ usually takes values between 1.2 and 1.6 the subtraction of 1 increases the sensitivity of the effect that the flame feedback has on the acoustics significantly.

For both load points the complex eigenfrequencies of the T_1 mode, obtained with the different mean flow models are shown in Fig. 8.2 for the different FTFs as well as the passive acoustics. Qualitatively, for all mean flow models including the flame response leads to the same behavior that has been discussed in Sec. 8.1: The oscillation frequency decreases, an FTF based on compressible flame response results has a stabilizing effect on the acoustics and an FTF extracted from incompressible calculations leads to negative damping rates.

For both LPs it stands out that with the $\hat{q}$-t-inc. flame response model the damping rates obtained for the c-κ mean flow are higher than those for the c-s and c-i approaches. The weaker impact of the flame feedback on the acoustic stability for the c-κ mean flow is in agreement with the lower values of κ obtained for this approach (cf. Fig. 6.1 and Eq. 8.1). When the compressible $\hat{q}$-t-inc. FTF is used, nearly identical damping rates are predicted with all mean flow models. A possible reason for this different behavior is the spatial distribution of both, κ (Fig. 6.1c) and the heat release fluctu-

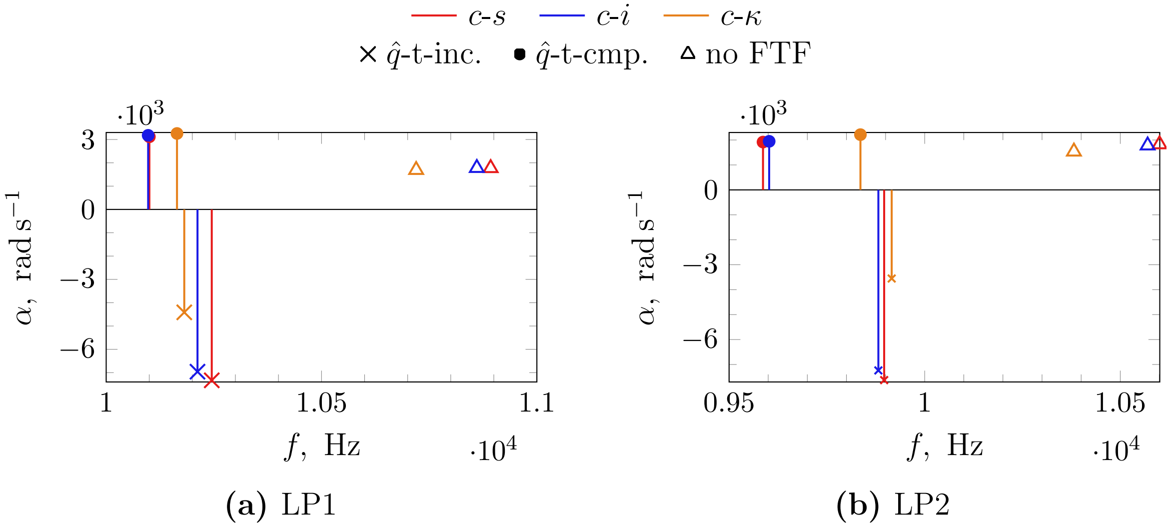

(a) LP1 **(b)** LP2

Figure 8.2: Impact of mean flow modeling on complex BKD eigenfrequencies

ations (Fig. 7.2). Given the different phase distributions of compressible and incompressible heat release fluctuations, the main contribution to the change of the damping rates may arise from different regions of the chamber, depending on the compressibility model used for the flame response calculations. As the isentropic coefficient varies across the chamber length as well (cf. Fig. 8.1), these regions may be affected differently by a change of the mean flow calculation procedure.

Besides the damping rates, the flame feedback affects the oscillation frequencies. Again, the effect of the mean flow modeling on the frequency depends on the flame response modeling. The oscillation frequencies obtained with the incompressible flame feedback modeling ($\hat{q}$-t-inc.) show similar offsets between the different mean flow models for both load points. For the compressible flame response ($\hat{q}$-t-inc.) the frequencies predicted with the c-κ approach show a considerable offset to those obtained with the other mean flow models, like already observed for the passive acoustics.

8.3 Summary of Findings

The impact of the flame response and mean flow modeling on the stability assessment has been studied.

The flame response modeling clearly governs the stability prediction. When using incompressible flame response calculations combined with the axial heat release amplitude distribution and target pressure fluctuations for FTF modeling ($\hat{q}$-t-inc.) as proposed in Sec. 7.2.2, a severely unstable T_1 mode is predicted. In contrast, FTFs based on compressible flame response computations ($\hat{q}$-t-cmp.) have a stabilizing effect on the calculated chamber acoustics. These different results are caused by the phase distributions of the heat release fluctuations obtained with the respective compressibility approaches. The FTFs following the zonal approach (z-t-inc., z-sf-inc.) both reduced the predicted damping rates, however considerably weaker than the $\hat{q}$-t-inc. approach. Depending on whether the target pressure fluctuations or those obtained from the flame response simulations are used for the FTF extraction, the T_1 mode is predicted to be unstable or stable respectively. So all three modeling choices, zonal/amplitude distribution, target/calculated pressure fluctuations as reference and incompressible/compressible flame response calculations can change the stability prediction from stable to unstable.

The impact of the different one-dimensional mean flow models on the stability prediction is rather small. The c-κ approach shows some differences in damping rates and oscillation frequencies in comparison with the c-s and c-i models. However, the changes are not nearly as significant as for the different flame response modeling approaches. However, this conclusion applies only to the comparison between the different one-dimensional mean flows, not for the impact of radial stratification (Sec. 6.3) on the stability prediction.

9 Conclusions

The present work contributes to the development of a computationally efficient procedure to predict the thermoacoustic stability of rocket engines. The reliability of the methodology's main components has been assessed, accounting for their sensitivity to modeling uncertainties. Revised modeling approaches have been proposed to address deficiencies of the procedure and their impact on the stability predictions has been studied. In the present chapter the conclusions regarding the procedure's components as well as its overall capabilities are given. Starting point are the mean flow modeling and the related acoustics, followed by the flame response and the stability calculations. Finally, capabilities and prospects of the procedure are addressed.

To ensure a sound basis for the analyses, a validation of single rocket engine flame simulations has been conducted. In this context several findings regarding the calculation of flame radiation images have been obtained, which have been summarized in Sec. 5.2.5 and 5.3.5.

Mean Flow A mean flow calculation procedure that is consistent with the Euler Equations while reproducing axial profiles obtained from radially averaged single flame results has been developed. Three different variants have been specified, which reproduce the sound speed combined with either the isentropic compressiblity (c-s), the field impedance (c-i) or the isentropic coefficient (c-κ). An acoustic analysis of the chamber showed that:

- The c-s and the c-i approaches provide nearly identical results in terms of mean flow and associated complex eigenfrequencies. The oscillation frequencies of the c-κ results are slightly lower but still similar to those obtained with the other models.
- The impact of the turbulent Schmidt number used in the single flame

simulations on the oscillation frequency is higher than that of the mean flow model choice, whereas the damping rate is nearly unaffected.

- The effect of the accelerated nozzle flow on the heat release distribution is negligible in terms of the passive chamber acoustics, even for compact chamber designs.

A study of the consequences that radial mean flow stratification has for the calculated chamber acoustics found that:

- The oscillation frequency is preserved well by the mean flow calculation procedure, changing less than about 5 % due to the stratification.
- Neglecting radial gradients can have a tremendous impact on the predicted damping rates, which change by up to 50 % within the studied parameter range.

So the most important development at issue for the mean flow modeling is to account for the effects of radial stratification on the damping in the combustion chamber.

Flame Transfer Functions A revised excitation approach based on incompressible flow modeling has been developed to avoid an impact of the simulation domain's eigenacoustics on the calculated flame response. The study of the flame response results showed that:

- In compressible simulations with excitation longitudinal acoustic modes resulting from the reduced radial domain size occur, impacting the pressure as well as the heat release fluctuations. The resulting flame response is not representative for the transverse chamber mode.
- The incompressible approach successfully suppresses the formation of acoustic eigenmodes. By a harmonic density modulation, the issue of incompressible flow dynamics is considerably mitigated.

A discussion of FTF modeling led to the conclusions that:

- If the excitation simulations adequately represent the effect of the chamber acoustics on the flame, the corresponding heat release amplitude distribution can directly be used for the FTF modeling.
- The excitation pressure distribution is the appropriate choice for the coupling of the flame response to the perturbation simulations. However, its usage requires knowledge of the flame's response to the excitation pressure without significant disturbances.

For further development of the flame response modeling, detailed validation data for the flame's dynamic behavior are required.

Stability Prediction Acoustic perturbation simulations including flame feedback yielded the following findings for the components' impact on the stability prediction:

- The c-s and c-i mean flow models provide similar stability predictions. For some cases the strength of the flame response's impact on the stability is lower for the c-κ approach, due to the different distribution of the isentropic coefficient.
- The compressibility model used in the flame response calculations can alter the system's stability prediction from stable to severely unstable.
- The FTF modeling choices have a tremendous impact on the predicted damping rates.

Overall Assessment and Prospects On the basis of the componentwise analysis, an assessment of the methodology's current state and further perspectives is given in the following.

The perturbation analysis is currently the most mature part of the stability assessment. A procedure to determine the amount of numeric stabilization required for the modal analysis is available for both two- and three-dimensional simulations. By using Bloch functions two-dimensional simulations of transverse modes are conducted, which allows for finer computational grids and thus a higher grid-independence of the results.

An adequate representation of the rocket engine flames via cost-efficient RANS-simulations is possible as well. However, the specification of the appropriate turbulent Schmidt number is crucial, which can for example be based on experimental data.

The high uncertainties in the mean flow and the flame response modeling prohibit an application of the stability assessment procedure in its current form. Effectively addressing these issues requires additional validation data: Currently, the only validation data for the chamber's thermoacoustic behavior are the system's stability behavior. While flame radiation images give qualitative insight into the mechanisms of the flame response, even with a thorough selection of the evaluation models, the level of detail required for a direct validation of the flame response calculation cannot be reached. So the validation of the thermoacoustic prediction currently can only be based on the overall system's stability. Given the considerable amount of uncertainty in the procedure's different components, the result of such a top-level validation is no reliable indicator for the approache's soundness. Even if the overall stability behavior is reproduced correctly, for instance an underestimation of passive damping due to the one-dimensional mean flow might compensate for a too weak flame response.

For the flame response validation, getting the necessary detailed insight into the flow processes from an experiment seems hardly possible. In this case, data from an Large Eddy Simulation would be a valuable reference. However, the chamber dynamics need to be correctly reproduced by the LES, which is currently not the case (cf. Sec. 3.1.2). For the mean flow, experimental studies covering the impact of cross-streamwise gradients on the acoustics of a passive configuration can be used to gain validation data.

While the structure underlying the stability assessment procedure constitutes a reasonable concept for the efficient simulation of rocket engine acoustics, further development needs to be undertaken in order to obtain a reliable tool for stability predictions.

A LEE Pressure Equation

The derivation of the LEE pressure equation 2.34 is shown step by step in the following. First, the derivation of the sensible internal energy equation 2.33 from the total energy conservation equation 2.18 is addressed. That equation is transformed into a pressure equation using the ideal gas EOS 2.5. Thereupon, the linearization and manipulation of Eq. 2.33 leading to Eq. 2.34 is outlined.

The starting point for the derivations is the non-diffusive form of the total energy conservation Equation:

$$\frac{\partial\left(\rho E\right)}{\partial t}+\nabla\cdot\left[\boldsymbol{u}\left(\rho E+p\right)\right]=0 \quad . \tag{2.32}$$

Inserting Eq. 2.17 and rearranging while noting that

$$\begin{aligned}\boldsymbol{u}\cdot\nabla\left(\frac{\boldsymbol{u}\cdot\boldsymbol{u}}{2}\right)&=\boldsymbol{u}\cdot\left[\left(\boldsymbol{u}\cdot\nabla\right)\boldsymbol{u}+\boldsymbol{u}\times\left(\nabla\times\boldsymbol{u}\right)\right]\\&=\boldsymbol{u}\cdot\left(\boldsymbol{u}\cdot\nabla\right)\boldsymbol{u}\end{aligned} \tag{A.1}$$

gives

$$\begin{aligned}&\rho\frac{\partial\Delta e_s}{\partial t}+\rho\boldsymbol{u}\cdot\nabla\Delta e_s+p\nabla\cdot\boldsymbol{u}+\left(\Delta e_s+\frac{1}{2}\boldsymbol{u}\cdot\boldsymbol{u}\right)\underbrace{\left(\frac{\partial\rho}{\partial t}+\nabla\cdot\left(\rho\boldsymbol{u}\right)\right)}_{=0,\ \text{Eq. 2.11}}\\&\qquad+\rho\boldsymbol{u}\cdot\underbrace{\left(\frac{\partial\boldsymbol{u}}{\partial t}+\left(\boldsymbol{u}\cdot\nabla\right)\boldsymbol{u}+\frac{1}{\rho}\nabla p\right)}_{=0,\ \text{Eq. 2.12}} \qquad .\\&\qquad=-\frac{\partial\left(\rho h_f^0\right)}{\partial t}-\nabla\cdot\left(\rho\boldsymbol{u}h_f^0\right)\end{aligned} \tag{A.2}$$

After dropping the terms that become zero due to mass (Eq. 2.11) and momentum conservation (Eq. 2.12), Eq. 2.33 is obtained:

$$\rho\frac{\partial \Delta e_s}{\partial t} + \rho\boldsymbol{u}\cdot\nabla\Delta e_s + p\nabla\cdot\boldsymbol{u} = -\left(\frac{\partial \rho h_f^0}{\partial t} + \nabla\cdot\left(\rho\boldsymbol{u}h_f^0\right)\right) \quad . \tag{2.33}$$

For the further modification of Eq. 2.33 the differential of the linearized sensible energy is required. From Eq. 2.9b its general form follows as

$$d\Delta e_s = \underbrace{\int_{T_{ref}}^{T} dc_v d\check{T}}_{d\Gamma} + c_v dT \quad . \tag{A.3}$$

and the temperature differentials can be replaced according to the thermal ideal gas EOS 2.5a

$$\frac{dp}{p} = \frac{dT}{T} + \frac{d\rho}{\rho} + \frac{dR}{R} \quad . \tag{A.4}$$

Due to the assumption of the local fluid properties being constant in time, the expressions obtained from Eq. A.3 and A.4 for temporal derivatives differ from those of spatial gradients. The respective terms are given in Tab. A.1.

Next, a pressure equation is derived from Eq. 2.33. Thereto the energy differentials Eq. A.5a and A.5b are inserted into Eq. 2.33 and the temperature is replaced via Eq. 2.5a, A.6a and A.6b. Noting that $\partial\phi/\partial t = \partial\phi'/\partial t$ the following pressure equation is obtained:

$$\begin{aligned}\frac{c_v}{R}\left(\frac{\partial p}{\partial t} - \frac{p}{\rho}\frac{\partial \rho}{\partial t}\right) + \frac{c_v}{R}p\boldsymbol{u}\cdot\left(\frac{1}{p}\nabla p - \frac{1}{\rho}\nabla\rho - \frac{1}{R}\nabla R\right) + \rho\boldsymbol{u}\cdot\nabla\Gamma + p\nabla\cdot\boldsymbol{u} \\ = -\left[\frac{\partial(\rho h_f^0)}{\partial t} + \nabla\cdot\left(\rho\boldsymbol{u}h_f^0\right)\right] \quad .\end{aligned} \tag{A.7}$$

Expressing c_v by κ and R, adding and subtracting $\frac{p}{\kappa-1}\nabla\cdot\boldsymbol{u}$ and rearranging

ϕ	Δe_s	T
ϕ'	$c_v T'$ (A.5a)	$\frac{p'}{\bar{\rho} R} - \frac{1}{\bar{\rho}^2} \frac{\bar{p}}{R} \rho'$ (A.6a)
$\nabla \bar{\phi}$	$c_v \nabla \bar{T} + \underbrace{\int_{T_{ref}}^{\bar{T}} \frac{1}{\kappa - 1} \nabla R - \frac{R}{(\kappa - 1)^2} \nabla \kappa d\check{T}}_{\nabla \bar{\Gamma}}$ (A.5b)	$\bar{T} \left(\frac{1}{\bar{p}} \nabla \bar{p} - \frac{1}{\bar{\rho}} \nabla \bar{\rho} - \frac{1}{R} \nabla R \right)$ (A.6b)
$\nabla \phi'$	$c_v \nabla T' + \underbrace{\frac{1}{\kappa - 1} \nabla R T' - \frac{R}{(\kappa - 1)^2} \nabla \kappa T'}_{\nabla \Gamma'}$ (A.5c)	$\frac{T'}{\bar{T}} \nabla \bar{T} + \frac{1}{\bar{\rho} R} \left(\nabla p' - \nabla \bar{p} \frac{p'}{\bar{p}} \right) - \frac{p}{\bar{\rho}^2 R} \left(\nabla \rho' - \nabla \bar{\rho} \frac{\rho'}{\rho} \right)$ (A.6c)

Table A.1: Differentials for sensible internal energy Δe_s and temperature T following Eq. A.3 and A.4

results in

$$\frac{1}{\kappa - 1} \left(\frac{\partial p}{\partial t} + \boldsymbol{u} \cdot \nabla p - \frac{p}{\rho} \underbrace{\left(\frac{\partial \rho}{\partial t} + \boldsymbol{u} \cdot \nabla \rho + \rho \nabla \cdot \boldsymbol{u} \right)}_{=0} + p \nabla \cdot \boldsymbol{u} - \frac{p}{R} \boldsymbol{u} \cdot \nabla R \right)$$
$$+ \rho \boldsymbol{u} \cdot \nabla \Gamma + p \nabla \cdot \boldsymbol{u} = - \left[\frac{\partial (\rho h_f^0)}{\partial t} + \nabla \cdot \left(\rho \boldsymbol{u} h_f^0 \right) \right] \quad . \tag{A.8}$$

After using the continuity equation, the final form of the pressure equation reads:

$$\begin{aligned} &\frac{\partial p}{\partial t} + \boldsymbol{u} \cdot \nabla p - \frac{p}{R} \boldsymbol{u} \cdot \nabla R + (\kappa - 1) \rho \boldsymbol{u} \cdot \nabla \Gamma + \kappa p \nabla \cdot \boldsymbol{u} \\ &\quad = -(\kappa - 1) \left[\frac{\partial (\rho h_f^0)}{\partial t} + \nabla \cdot \left(\rho \boldsymbol{u} h_f^0 \right) \right] \quad . \end{aligned} \tag{A.9}$$

So far, the only simplification that has been applied since starting from the non-diffusive total energy conservation equation 2.32 is the time-independece of the fluid properties R and κ due to the usage of Eq. A.6a and A.5a.

Now the linearization is performed. Combining Eq. A.5c with Eq. A.6a gives

$$(\kappa-1)\bar{\rho}\overline{\boldsymbol{u}}\cdot\nabla\Gamma' = \frac{1}{R}\left(p'-\frac{\overline{p}}{\overline{\rho}}\rho'\right)\boldsymbol{u}\cdot\nabla R-\frac{1}{\kappa-1}\left(p'-\frac{\overline{p}}{\overline{\rho}}\rho'\right)\overline{\boldsymbol{u}}\cdot\nabla\kappa \quad . \tag{A.10}$$

Inserting Eq. A.10 into Eq. A.9 results in

$$\begin{aligned}
&\frac{\partial p'}{\partial t}+\overline{\boldsymbol{u}}\cdot\nabla p'+\boldsymbol{u}'\cdot\nabla\overline{p}+\kappa\left(\overline{p}\nabla\cdot\boldsymbol{u}'+p'\nabla\cdot\overline{\boldsymbol{u}}\right)\\
&\quad+\frac{1}{R}\left(-\frac{\overline{p}}{\overline{\rho}}\overline{\boldsymbol{u}}\rho'-\boldsymbol{u}'\overline{p}+R(\kappa-1)\left(\boldsymbol{u}'\overline{\rho}+\overline{\boldsymbol{u}}\rho'\right)\int_{T_{ref}}^{\overline{T}}\frac{1}{\kappa-1}d\check{T}\right)\cdot\nabla R\\
&\quad-\frac{1}{\kappa-1}\left(p'-\frac{\overline{p}}{\overline{\rho}}\rho'\right)\overline{\boldsymbol{u}}\cdot\nabla\kappa-R(\kappa-1)\left(\boldsymbol{u}'\overline{\rho}+\overline{\boldsymbol{u}}\rho'\right)\cdot\int_{T_{ref}}^{\overline{T}}\frac{1}{(\kappa-1)^2}\nabla\kappa d\check{T}\\
&\quad=-(\kappa-1)\left[\frac{\partial(\rho h_f^0)}{\partial t}+\nabla\cdot\left(\rho\boldsymbol{u}h_f^0\right)\right] \quad .
\end{aligned} \tag{A.11}$$

For a temperature independent isentropic coefficient this simplifies to

$$\begin{aligned}
&\frac{\partial p'}{\partial t}+\overline{\boldsymbol{u}}\cdot\nabla p'+\boldsymbol{u}'\cdot\nabla\overline{p}+\kappa\left(\overline{p}\nabla\cdot\boldsymbol{u}'+p'\nabla\cdot\overline{\boldsymbol{u}}\right)\\
&\quad+\frac{1}{R}\left(-\frac{\overline{p}}{\overline{\rho}}\overline{\boldsymbol{u}}\rho'-\boldsymbol{u}'\overline{p}+R(\overline{T}-T_{ref})\left(\boldsymbol{u}'\overline{\rho}+\overline{\boldsymbol{u}}\rho'\right)\right)\cdot\nabla R\\
&\quad-\frac{1}{\kappa-1}\left(\left(p'-\frac{\overline{p}}{\overline{\rho}}\rho'\right)\overline{\boldsymbol{u}}+R(\overline{T}-T_{ref})\left(\boldsymbol{u}'\overline{\rho}+\overline{\boldsymbol{u}}\rho'\right)\right)\cdot\nabla\kappa\\
&\quad=-(\kappa-1)\left[\frac{\partial(\rho h_f^0)}{\partial t}+\nabla\cdot\left(\rho\boldsymbol{u}h_f^0\right)\right]'
\end{aligned} \tag{A.12}$$

and after replacing $\overline{T}$ via the ideal gas equation of state 2.5a the final form of the pressure fluctuation equation is

$$\begin{aligned}
&\frac{\partial p'}{\partial t} + \overline{\boldsymbol{u}} \cdot \nabla p' + \boldsymbol{u}' \cdot \nabla \overline{p} + \kappa \left(\overline{p} \nabla \cdot \boldsymbol{u}' + p' \nabla \cdot \overline{\boldsymbol{u}} \right) - \frac{1}{\kappa - 1} \left(\boldsymbol{u}' \overline{p} + \overline{\boldsymbol{u}} p' \right) \cdot \nabla \kappa \\
&\qquad + T_{ref} \left(\boldsymbol{u}' \overline{\rho} + \overline{\boldsymbol{u}} \rho' \right) \cdot \left(\frac{R}{\kappa - 1} \nabla \kappa - \nabla R \right) \\
&\qquad = -(\kappa - 1) \left[\frac{\partial (\rho h_f^0)}{\partial t} + \nabla \cdot \left(\rho \boldsymbol{u} h_f^0 \right) \right]' \quad .
\end{aligned} \tag{A.13}$$

B Radiation

Conversion between wave length specific and wave number specific spectral radiation intensity:

$$I = \int_{\nu_s}^{\nu_e} I_\nu d\nu = \int_{1/\nu_s}^{1/\nu_e} I_\lambda d\lambda = -\int_{\lambda_s}^{\lambda_e} I_\lambda d\left(\frac{1}{\nu}\right) = \int_{\lambda_s}^{\lambda_e} \frac{1}{\nu^2} I_\lambda d\nu \qquad \text{(B.1)}$$

and thus

$$I_\nu = \frac{1}{\nu^2} I_\lambda = \lambda^2 I_\lambda \quad . \qquad \text{(B.2)}$$

C Incompressible Flow Dynamics

During the development of the pressure excitation procedure in Sec. 4.3.1.3.2 the response of a one-dimensional, incompressible flow to a volumetric mass and the associated momentum sources is studied. The analytic solutions for the cases of spatially and temporally constant density (Sec. C.1) as well as spatially non-constant density that fluctuates harmonic in time (Sec. C.2) are derived in the following.

The common setup for both cases is a duct of cross-sectional area A with a constant mass flow inlet and a constant pressure outlet:

$$\dot{m}\big|_{x=0} = \dot{m}_0 \tag{C.1a}$$

$$p\big|_{x=L} = p_{out} \quad . \tag{C.1b}$$

As the flow is one-dimensional,

$$\frac{\partial \phi}{\partial r} = \frac{\partial \phi}{\partial \theta} = 0, \quad u_r = u_\theta = 0 \tag{C.2}$$

holds. The mass source is calculated as (cf. Sec. 4.3.1.3.2)

$$\mathcal{S}'_m = \frac{1}{c^2}\left(\frac{\partial p'_t}{\partial t} + u_x \frac{\partial p'_t}{\partial x}\right) \tag{4.59}$$

from the target pressure fluctuation

$$p'_t = |\hat{p}|_t \psi_x \sin(\omega t) \quad . \tag{4.71}$$

The momentum source that corresponds to the mass source (Eq. 4.59) is obtained by evaluating Eq. 4.68 for one-dimensional flow (Eq. C.2), yielding

$$\mathcal{S}'_{u,x} = \mathcal{S}_m u_x \quad . \tag{C.3}$$

Based on Eq. 2.11 and Eq. 2.12 along with Eq. C.2 the inviscid mass and continuity equations with source terms are obtained as

$$\frac{\partial \rho}{\partial t} + u_x \frac{\partial \rho}{\partial x} + \rho \frac{\partial u_x}{\partial x} = \mathcal{S}_m \tag{C.4}$$

and

$$\frac{\partial u_x}{\partial t} + u_x \frac{\partial u_x}{\partial x} = -\frac{1}{\rho}\frac{\partial p}{\partial x} + \mathcal{S}_{u,x} \quad . \tag{C.5}$$

As there is no mean source in the flow but just the fluctuating source terms,

$$\mathcal{S}_\phi = \mathcal{S'}_\phi \tag{C.6}$$

holds in Eq. C.4 and C.5. With the above prerequisites the analytic solutions for the constant density (Sec. C.1) and harmonically oscillating density (Sec. C.2) are derived.

C.1 Constant Density

Constant flow density is described as

$$\frac{\partial \rho}{\partial t} = 0 \ , \quad \nabla \rho = 0 \quad . \tag{C.7}$$

Inserting Eq. C.7 along with Eq. C.6 into the one-dimensional continuity equation C.4 yields

$$\frac{\partial u_x}{\partial x} = \frac{1}{\rho}\mathcal{S}'_m \quad . \tag{C.8}$$

By integration of Eq. C.8 under usage of the mass flow inlet boundary condition Eq. C.1a, the velocity distribution is obtained as

$$u_x = \frac{1}{\rho}\left(\frac{\dot{m}_0}{A} + \int_0^x \mathcal{S}'_m d\check{x}\right) \quad . \tag{4.77a}$$

From Eq. 4.77a the temporal and spatial velocity derivatives can be calculated:

$$\frac{\partial u_x}{\partial t} = \frac{1}{\rho}\int_0^x \frac{\partial \mathcal{S}'_m}{\partial t} d\check{x} \tag{C.9a}$$

$$\frac{\partial u_x}{\partial x} = \frac{1}{\rho}\mathcal{S}'_m \quad . \tag{C.9b}$$

Inserting Eq. C.9 into the momentum equation C.5 under usage of Eq. C.6 gives

$$\frac{\partial p}{\partial x} = -\rho \frac{\partial u_x}{\partial t} \tag{C.10}$$

and after integration under consideration of the outlet pressure boundary condition Eq. C.1b:

$$p = p_{out} + \int_x^L \int_0^{\check{\check{x}}} \frac{\partial \mathcal{S}'_m}{\partial t} d\check{x} d\check{\check{x}} \quad . \tag{4.74b}$$

C.2 Harmonic Density Fluctuations

The harmonically varying density is modeled as

$$\rho = r\hat{h}o + \frac{1}{c^2} p'_t \tag{4.79}$$

with the spatially and temporally constant mean part $r\hat{h}o$. Inserting Eq. 4.71 into Eq. 4.59 yields the mass source term

$$\mathcal{S}'_m = \frac{1}{c^2} \frac{\partial p'_t}{\partial t} + u_x \frac{1}{c^2} \frac{\partial p'_t}{\partial x} \quad . \tag{C.11}$$

Inserting Eq. 4.79 and Eq. C.11 along with Eq. C.6 in the one-dimensional continuity equation C.4 yields a zero velocity gradient:

$$\frac{\partial u_x}{\partial x} = 0 \quad . \tag{C.12a}$$

Integrating Eq. C.12a under consideration of the inlet boundary condition Eq. C.1a gives the expression for the velocity

$$u_x = u_x|_{x=0} = \frac{\dot{m}}{A \, \rho|_{x=0}} \tag{C.12b}$$

with the temporal derivative

$$\frac{\partial u_x}{\partial t} = - \frac{u_x}{\rho|_{x=0} \, c^2} \left. \frac{\partial p'_t}{\partial t} \right|_{x=0} \quad . \tag{C.12c}$$

Inserting Eq. C.12 along with the source term Eq. C.11 into the momentum equation Eq. C.5 and integrating under consideration of Eq. C.1b yields the pressure distribution in the flow:

$$\begin{aligned} p &= p_{out} - \int_x^L \left(\rho \frac{\partial u_x}{\partial t} + u_x \mathcal{S}'_m \right) d\check{x} \\ &= p_{out} - \frac{\partial u_x}{\partial t} \int_x^L \rho d\check{x} + \frac{u_x}{c^2} \int_L^x \frac{\partial p'_t}{\partial t} d\check{x} + \frac{u_x^2}{c^2} + \int_L^x \frac{\partial p'_t}{\partial \check{x}} d\check{x} \\ &= p_{out} + \frac{u_x}{c^2} \left. \frac{\partial p'_t}{\partial x} \right|_{x=0} \left(\frac{1}{\rho|_{x=0}} \int_x^L \rho d\check{x} + \int_L^x \psi d\check{x} \right) + \frac{u_x^2}{c^2} p'_t \quad . \end{aligned} \tag{C.13}$$

Bibliography

[1] F. E. C. Culick. *Overview of Combustion Instabilities in Liquid-Propellant Rocket Engines*, chapter Instability Phenomenology and Case Studies, pages 3–37. AIAA, 1995.

[2] D. T. Harrje. Liquid Propellant Rocket Combustion Instability. Technical Report NASA-SP-194, NASA, 1972.

[3] M. Schmid. *Thermoakustische Kopplungsmechanismen in Flüssigraketentriebwerken.* PhD thesis, Technische Universität München, 2014.

[4] L. Crocco and S. I. Cheng. *Theory of Combustion Instability in Liquid Propellant Rocket Motors.* Butterworths Science Publication, 1956.

[5] G. P. Sutton and O. Biblarz. *Rocket Propulsion Elements.* John Wiley & Sons, New York, 7th edition, 2001.

[6] W. Armbruster, J. S. Hardi, D. Suslov, and M. Oschwald. Injector-Driven Flame Dynamics in a High-Pressure Multi-Element Oxygen-Hydrogen Rocket Thrust Chamber. *Journal of Propulsion and Power*, 35(3):632–644, 2019.

[7] F. E. C. Culick and P. Kuentzmann. Unsteady Motions in Combustion Chambers for Propulsion Systems. *NATO RTO-AG-AVT-039, AGARDograph*, 2006.

[8] J. Hardi, S. Webster, and M. Oschwald. Response of a Reacting Cryogenic Oxygen Jet to Transverse Acoustic Forcing. In *Space Propulsion*, 2016.

[9] M. Barrére and F. A. Williams. Comparison of Combustion Instabilities Found in Various Types of Combustion Chambers. *Symposium (International) on Combustion*, 12(1):169–181, 1969.

[10] J. E. Pieringer. *Simulation Selbsterregter Verbrennungsschwingungen in Raketenschubkammern im Zeitbereich*. PhD thesis, Technische Universität München, 2008.

[11] A. Török. *Computation of the Thermoacoustic Driving Capability of Rocket Engine Flames with Detailed Chemistry*. PhD thesis, Technische Universität München, 2015.

[12] M. Schulze. *Linear Stability Assessment of Cryogenic Rocket Engines*. PhD thesis, Technische Universität München, 2016.

[13] M. Schulze and T. Sattelmayer. Linear Stability Assessment of a Cryogenic Rocket Engine. *International Journal of Spray and Combustion Dynamics*, 9(4):277–298, 2017.

[14] G. K. Batchelor. *An Introduction to Fluid Dynamics*. Cambridge Mathematical Library. Cambridge University Press, 2000.

[15] S. Gordon and B. J. McBride. Computer Program for Calculation of Complex Chemical Equilibrium Compositions and Applications - I. Analysis, 1994. NASA RP-1311.

[16] R. Ewert and W. Schröder. Acoustic Perturbation Equations Based on Flow Decomposition via Source filtering. *Journal of Computational Physics*, 188(2):365–398, 2003.

[17] M. K. Myers. Transport of Energy by Disturbances in Arbitrary Steady Flows. *Journal of Fluid Mechanics*, 226:383–400, 1991.

[18] L. Vingert, P. Gicquel, and D. Lourme et al. *Fundamental Mechanisms of Combustion Instabilities*, chapter Part 2, pages 145–399. AIAA, 1995.

[19] M. F. Modest. *Radiative Heat Transfer*. Elsevier, 3rd edition, 2013.

[20] U. Boltendahl. *Spektroskopische Bestimmung der Temperatur- und OH-Konzentrationsverteilung in einer Laminaren H2-O2-Diffusionsflamme.* PhD thesis, RWTH Aachen, 1974.

[21] T. Fiala. *Radiation from High Pressure Hydrogen-Oxygen Flames and its Use in Assessing Rocket Combustion Instability.* PhD thesis, Technische Universität München, 2015.

[22] T. Fiala and T. Sattelmayer. Assessment of Existing and New Modeling Strategies for the Simulation of OH^* Radiation in High-Temperature Flames. *CEAS Space Journal*, 8(1):47–58, 2016.

[23] M. Ó Conaire, H. J. Curran, J. Simmie, W. Pitz, and C. K. Westbrook. A Comprehensive Modeling Study of Hydrogen Oxidation. *International Journal of Chemical Kinetics*, 36(11):603–622, 2004.

[24] T. Kathrotia, M. Fikri, M. Bozkurt, M. Hartmann, U. Riedel, and C. Schulz. Study of the H+O+M Reaction Forming OH^*: Kinetics of OH^* Chemiluminescence in Hydrogen Combustion Systems. *Combustion and Flame*, 157(7):1261–1273, 2010.

[25] M. Tamura, P. A. Berg, J. E. Harrington, J. Luque, J. B. Jeffries, G. P. Smith, and D. R. Crosley. Collisional Quenching of CH(A), OH(A), and NO(A) in Low Pressure Hydrocarbon Flames. *Combustion and Flame*, 114(3):502–514, 1998.

[26] M. Schulze, T. Fiala, and T. Sattelmayer. Radiation-Based Validation of Combustion Simulations and Comparison to Heat Release in Rocket Engines. In *54th AIAA Aerospace Sciences Meeting*, 2016.

[27] I. E. Gordon, L. S. Rothman, C. Hill, R. V. Kochanov, Y. Tan, P. F. Bernath, M. Birk, V. Boudon, A. Campargue, K. V. Chance, B. J. Drouin, J.-M. Flaud, R. R. Gamache, J. T. Hodges, D. Jacquemart, V. I. Perevalov, A. Perrin, K.P. Shine, M.-A. H. Smith, J. Tennyson, G. C. Toon, H. Tran, V. G. Tyuterev, A. Barbe, A. G. Csaszar, V. M. Devi, T. Furtenbacher, J. J. Harrison, J.-M. Hartmann, A. Jolly, T. J. Johnson, T. Karman, I. Kleiner, A. A. Kyuberis, J. Loos, O. M. Lyulin, S. T. Massie, S. N. Mikhailenko, N. Moazzen-Ahmadi, H. S. P. Müller,

O. V. Naumenko, A. V. Nikitin, O. L. Polyansky, M. Rey, M. Rotger, S. W. Sharpe, K. Sung, E. Starikova, S. A. Tashkun, J. Vander Auwera, G. Wagner, J. Wilzewski, P. Wcislo, S. Yu, and E. J. Zak. The HITRAN2016 Molecular Spectroscopic Database. *Journal of Quantitative Spectroscopy and Radiative Transfer*, 203:3–69, 2017.

[28] L. S. Rothman, I. E. Gordon, R. J. Barber, H. Dothe, R. R. Gamache, A. Goldman, V. I. Perevalov, S. A. Tashkun, and J. Tennyson. HITEMP, the High-Temperature Molecular Spectroscopic Database. *Journal of Quantitative Spectroscopy and Radiative Transfer*, 111(15):2139–2150, 2010.

[29] J. Diederichsen and H. G. Wolfhard. Spectrographic Examination of Gaseous Flames at High Pressure. *Proceedings of the Royal Society of London. Series A, Mathematical and Physical Sciences*, 236(1204):89–103, 1956.

[30] A. G. Gaydon. *Spectroscopy and Combustion Theory*. Chapman & Hall Limited, 1942.

[31] P. Padley. The Origin of the Blue Continuum in the Hydrogen Flame. *Transactions of the Faraday Society*, 56:449–454, 1960.

[32] M. Vanpee and R. J. Mainiero. The Spectral Distribution of the Blue Hydrogen Flame Continuum and its Origin in Hydrogen-nitric Oxide Flames. *Combustion and Flame*, 34:219–230, 1979.

[33] S. Gröning, J. S. Hardi, D. Suslov, and M. Oschwald. Injector-Driven Combustion Instabilities in a Hydrogen/Oxygen Rocket Combustor. *Journal of Propulsion and Power*, 32(3):560–573, 2016.

[34] S. Gröning, M. Oschwald, and T. Sattelmayer. Selbst Erregte Tangentiale Moden in einer Raketenbrennkammer unter Repräsentativen Bedingungen. In *61. Deutscher Luft- und Raumfahrtkongress*, 2012.

[35] S. Gröning, D. Suslov, M. Oschwald, and T. Sattelmayer. Stability Behaviour of a Cylindrical Rocket Engine Combustion Chamber Operated with Liquid Hydrogen and Liquid Oxygen. In *5th European Conference for Aeronautics and Space Sciences*, 2013.

[36] S. Gröning, J. Hardi, D. Suslov, and M. Oschwald. Influence of Hydrogen Temperature on the Stability of a Rocket Engine Combustor Operated with Hydrogen and Oxygen. *CEAS Space Journal*, 9(1):59–76, 2017.

[37] S. Gröning, D. Suslov, Justin Hardi, and M. Oschwald. Influence of Hydrogen Temperature on the Acoustics of a Rocket Engine Combustion Chamber Operated with LOX/H2 at Representative Conditions. In *Space Propulsion*, 2014.

[38] S. Gröning, Justin Hardi, D. Suslov, and M. Oschwald. Analysis of Phase Shift Between Oscillations of Pressure and Flame Radiation Intensity of Self-excited Combustion Instabilities. In *6th European Conference for Aeronautics and Space Sciences*, 2015.

[39] S. Gröning, J. S. Hardi, D. Suslov, and M. Oschwald. Measuring the Phase Between Fluctuating Pressure and Flame Radiation Intensity in a Cylindrical Combustion Chamber. In *EUCASS Book Series - Advances in AeroSpace Sciences*, volume 11, pages 425–446, 2019.

[40] A. Urbano, L. Selle, G. Staffelbach, B. Cuenot, T. Schmitt, S. Ducruix, and S. Candel. Large Eddy Simulation of a Model Scale Rocket Engine. In *9th Mediterranean Combustion Symposium*, 2015.

[41] A. Urbano, L. Selle, G. Staffelbach, B. Cuenot, T. Schmitt, S. Ducruix, and S. Candel. Large Eddy Simulation of a Model Rocket Engine. In *Proceedings of the 3rd REST Workshop on Combustion Instability Modeling*, 2014.

[42] A. Urbano, L. Selle, G. Staffelbach, B. Cuenot, T. Schmitt, S. Ducruix, and S. Candel. Exploration of Combustion Instability Triggering Using Large Eddy Simulation of a Multiple Injector Liquid Rocket Engine. *Combustion and Flame*, 169:129–140, 2016.

[43] A. Urbano, Q. Douasbin, L. Selle, G. Staffelbach, B. Cuenot, T. Schmitt, S. Ducruix, and S. Candel. Study of Flame Response to Transverse Acoustic Modes from the LES of a 42-Injector Rocket Engine. *Proceedings of the Combustion Institute*, 36(2):2633–2639, 2017.

[44] A. Urbano and L. Selle. Driving and Damping Mechanisms for Transverse Combustion Instabilities in Liquid Rocket Engines. *Journal of Fluid Mechanics*, 820:R2, 2017.

[45] T. Schmitt, G. Staffelbach, S. Ducruix, S. Gröning, J. Hardi, and M. Oschwald. Large Eddy Simulations of a sub-Scale Liquid Rocket Combustor: Influence of Fuel Injection Temperature on Thermo-Acoustic stability. In *7th European Conference for Aeronautics and Aerospace Sciences*, 2017.

[46] D. Eiringhaus, H. Riedmann, and O. Knab. Demonstratorbeschreibung TCD2 - v1.0. Technical report, ArianeGroup, 2017.

[47] D. Eiringhaus, H. Riedmann, and O. Knab. Demonstratorbeschreibung TCD3 - v1.0. Technical report, ArianeGroup, 2017.

[48] A. Chemnitz, N. Kings, and T. Sattelmayer. Modification of Eigenmodes in a Cold-Flow Rocket Combustion Chamber by Acoustic Resonators. *Journal of Propulsion and Power*, 35(4):765–779, 2019.

[49] G. A. Mensah and J. P. Moeck. Efficient Computation of Thermoacoustic Modes in Annular Combustion Chambers Based on Bloch-Wave Theory. In *The American Society of Mechanical Engineers Turbo Expo 2015: Turbine Technical Conference and Exposition*, volume 4B: Combustion, Fuels and Emissions, 2015. GT2015-43476.

[50] J. Donea and A. Huerta. *Finite Element Methods for Flow Problems*, chapter Stabilization Techniques, pages 59–65. John Wiley & Sons, Chichester, 2005.

[51] M. Schulze. Linearized Euler and Navier-Stokes Equations for the Determination of the Acoustic Scattering Behavior of Area Expansion and Orifice. Master's thesis, Technische Universität München, 2011.

[52] W. C. Ullrich and T. Sattelmayer. Transfer Functions of Acoustic, Entropy and Vorticity Waves in an Annular Model Combustor and Nozzle for the Prediction of the Ratio Between Indirect and Direct Combustion Noise. In *21th AIAA/CEAS Aeroacoustics Conference*, 2015.

[53] G. J. Le Beau, S. E. Ray, S. K. Aliabadi, and T. E. Tezduyar. SUPG Finite Element Computation of Compressible Flows with the Entropy and Conservation Variables Formulations. *Computer Methods in Applied Mechanics and Engineering*, 104(3):397–422, 1993.

[54] A. Chemnitz and T. Sattelmayer. Acoustic Characterization of Virtual Thrust Chamber Demonstrators. Annual Report SFB/TRR40, DFG SFB Transregio 40, 2018.

[55] A. Chemnitz and T. Sattelmayer. Calculation of the Thermoacoustic Stability of a Main Stage Thrust Chamber Demonstrator. In *Notes on Numerical Fluid Mechanics and Multidisciplinary Design*, pages 235–247. Springer International Publishing, 2021.

[56] E. Truckenbrodt. *Fluidmechanik*. Springer, 4th edition, 1999.

[57] A. Chemnitz and T. Sattelmayer. Influence of Radial Stratification on Eigenfrequency Computations in Rocket Combustion Chambers. In *8th European Conference for Aeronautics and Space Sciences*, 2019.

[58] M. Schmid and T. Sattelmayer. Influence of Pressure and Velocity Perturbations on the Heat Release Fluctuations for Coaxial GH2/GO2 Injection. In *4th European Conference for Aeronautics and Space Sciences*, 2011.

[59] ANSYS. *Fluent User's Guide*, 17.0 edition, 2017.

[60] ANSYS. *Fluent Customization Manual*, 17.0 edition, 2017.

[61] A. Chemnitz, T. Sattelmayer, C. Roth, O. Haidn, Y. Daimon, R. Keller, P. Gerlinger, J. Zips, and M. Pfitzner. Numerical Investigation of Reacting Flow in a Methane Rocket Combustor: Turbulence Modeling. *Journal of Propulsion and Power*, 34(4):864–877, 2017.

[62] A. Chemnitz, N. Kings, M. Schulze, and T. Sattelmayer. Numerical Investigation of Eigenmode Damping Rates in a Single Element Rocket Combustion Chamber. In *International Symposium on Space Technology and Science*. 2017.

[63] ANSYS. *Fluent Theory Guide*, 17.0 edition, 2017.

[64] B. E. Launder and D. B. Spalding. *Lectures in Mathematical Models of Turbulence*. London: Academic Press, 1972.

[65] M. Wolfshtein. The Velocity and Temperature Distribution in One-Dimensional Flow with Turbulence Augmentation and Pressure Gradient. *International Journal of Heat and Mass Transfer*, 12(3):301–318, 1969.

[66] G. Soave. Equilibrium Constants From a Modified Redlich-Kwong Equation of State. *Chemical Engineering Science*, 27(6):1197–1203, 1972.

[67] A. Chemnitz and T. Sattelmayer. Efficient Modeling of the Radiative Transport of OH* Emissions in Diffusion Flames. Technical report, DFG SFB Transregio 40, 2019.

[68] M. Zahn. URANS-Simulations for the Analysis of O2/H2-Flame Dynamics under Supercritical Conditions. Master's thesis, Technische Universität München, 2013.